1G-model tests on the long-term cyclic pile response in clay

Are Reiakvam

Master Thesis in Geosciences
Geohazards and Geomechanics
60 credits

Department of Geosciences
Faculty of Mathematics and Natural Sciences

UNIVERSITY OF OSLO

June 2020

1G-model tests on the long-term cyclic pile response in clay

Are Reiakvam

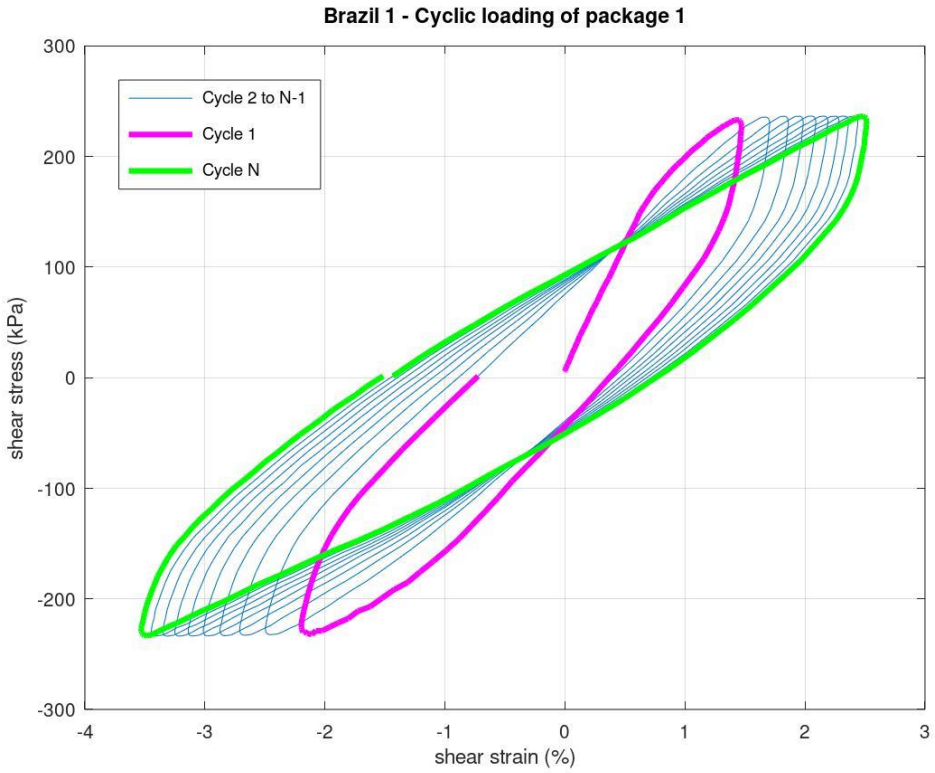

Master Thesis in Geosciences
Geohazards and Geomechanics
60 credits

Department of Geosciences
Faculty of Mathematics and Natural Sciences

UNIVERSITY OF OSLO

June 2020

2020

Qualitative study on long-term cyclic loading of pile responses in clay

Are Reiakvam

http://www.duo.uio.no/

Trykk: Reprosentralen, Universitetet i Oslo

Abstract

With much attention drawn to replace oil- and gas-based energy production with cleaner alternatives, energy production from offshore windmills has particularly been considered over the recent years. As offshore windmills are exposed to different types of external cyclic loads it is necessary to consider their pile-foundations and the pile response on surrounding soil during cyclic loading. A newly developed P-Y apparatus at Norwegian Geotechnical Institute (NGI) is used in this qualitative study to investigate the long-term cyclic pile responses in clay-based soils.

Four experimental tests were conducted on two types of specimen-materials; kaolin clay and Brazilian marine clay. A model pile, to simulate the cyclic lateral movements, was inserted in the soil specimens for testing. The soil specimens were tested with multiple cyclic loading parcels, with few numbers of cycles and continuous consolidation throughout the experiments. A targeted cyclic pressure was maintained throughout all the cyclic parcels within an experimental test. Relevant parameters were collected after testing to generate cyclic parameters to be studied for stiffness development and damping.

This research reveals that short-termed cyclic loading weakens the soil, denoted by lowered stiffness, accumulation of cyclic displacements and hysteretic damping-development. Additionally, the cyclic strain rate diminishes for each cyclic iteration within a cyclic parcel. For long-term cyclic loading however, the overall stiffness of the soil is observed to increase, likely due to material densification and lessening of pore pressure accumulation over time. Furthermore, axial strain rates are seen to decrease over the course of the experiments.

For long-term stiffness development it is shown that both initial- and end stiffnesses of each cyclic parcel tend to show a strain-hardening behaviour. As such, this could appoint to a general improvement of the post-cyclic shear strength of the soil.

Preface

This master thesis is a one-year project within the discipline Geohazards and Geomechanics, at the Department of Geosciences, University of Oslo. The project has been performed at the Norwegian Geotechnical Institute (NGI) in Oslo. It is a part of an on-going project at NGI, including the *Wave Loads and Soil Support for Extra-Large Monopiles* (WAS-XL) project and the *REDucing cost of offshore WINd by integrated structural and geotechnical design 2* (REDWIN 2) project.

Acknowledgment

I wish to express sincere gratitude toward my supervisor, Hendrik Sturm, for letting me be a part of this exciting project at NGI. Additionally, I wish to thank him for all the support, the meetings, the feedbacks and the follow-ups throughout this project, including the "mini-lectures" about geotechnics. I also wish to express thankfulness to my co-supervisor, Elin Skurtveit, for her feedbacks and follow-ups during this project.

I would also like to thank the staff at NGI's laboratory and at the department of Marine Geotechnics for their inputs and discussions regarding my project. I would especially give a big thanks to Tariq Abdu for his guidance, assistance and patience regarding the laboratory part of this study.

I additionally wish to thank my family and friends for all the support yet again during such a stressful time, as this will be my second master thesis. An extra appreciation is given to Linn M. E. for her reviews on some of the chapters herein.

Finally, I cannot underscore enough my sincere gratitude and love to my dear Ståle, who during this year has been a fantastic supporter and has always been there for me during stressful times.

Contents

Nomenclature

Abbreviations

DSS – direct simple shear

FLS – fatigue limit state

LL – liquid limit

MPT – Multi purpose testware

NGI - Norwegian Geotechnical Institute

OCR – over consolidation ratio

PI – plasticity index

PL – Plastic limit

SCTD - Soil Conductor Testing Device

SLS – serviceability limit state

Upper case symbols

D – pile diameter

F_{cyc} – cyclic force

F_L – Maximum lateral force of pile

$F_{\tau max}$ – Maximum shear force

G – secant stiffness

H – height

H_{pc} – height after pre-consolidation

L – pile length

N_p – ultimate bearing capacity factor

P_u – ultimate lateral resistance per unit pile length

S_u – undrained shear strength

T_p – Normalised loading period

Lower case symbols

c' – cohesion

c_v – coefficient of consolidation

m – mass

p'_c – consolidation pressure

p_{cy} – cyclic pressure

r – radial distance from pile

r_0 – pile radius

t – time

t_p – cyclic loading period

u – pore pressure

y – lateral displacement

z – depth

Greek letter symbols

α – roughness factor

γ - strain

γ_a – average shear strain

γ_{cyc} – cyclic shear strain

$\gamma_{p\ -}$ total strain

Δw – area of hysteretic loop

δ – unit weight

δ' – effective unit weight

δ_w – unit weight of water

σ' – effective normal stress

σ'_f – normal stress at failure

σ'_{oc} – over consolidation stress

σ_v – vertical stress

σ'_v – effective vertical stress

τ – shear stress

τ_0 – initial shear stress

τ_a – average shear stress

τ_{cyc} – cyclic shear stress

τ_f – shear stress at failure

τ_{max} – maximum shear stress

φ – friction angle

Ψ – triangular area beneath secant stiffness, G

Chapter 1

Introduction

1.1 Background

In recent years there has been ambitious plans and solutions regarding substituting oil and gas-based energy production in favour of more clean and renewable electrification. The goal is to reduce the amount of carbon emissions and to reduce pollution. Hence a large focus and demand on renewable energy and its potentials have been heavily declared (Statkraft, 2019). One of the most discussed topics in relation to this is the development of sustainable windmill farms. It is envisioned that the world will become more dependent on wind-powered energy, from both offshore- and onshore based energy production, in the foreseeable future (Statkraft, 2019).

Particular attention has been directed to the energy production from offshore winds. Offshore windmills are able to harness these winds for cleaner energy production (Statkraft, 2019). For it to be cost-efficient and sustainable to develop and maintain these it is necessary to consider the foundation design and its implicit challenges (Andersen, 2015; Kallehave et al., 2015).

There exist several types of foundation designs for offshore windmills (Figure 1.1). One of these types is the monopile, with its foundation design involving a cylindrical steel tube with a large diameter. Due to its robustness and easy to employ by conventional impact driving, it is the most used foundation type for offshore windmills. It is also sublime for water depths ranging from near shore to depths of at least 35 meters (Kallehave et al., 2015).

Offshore monopiles are often prone to different types of cyclic wave loading, such as fair-weather waves, storm waves, strong winds, drifting ice-sheets, and even earthquakes. Secondary resonance, as a response to applied cyclic wave loading, may also cause further cyclic loading. These cyclic loads can occur continuously, seasonally or as a single event (Semblat and Pecker, 2009; Andersen et al., 2013; Andersen, 2015). The loading commonly produces irregular cyclic displacement amplitudes, varying from one wave to the next wave. The duration and number of cycles the offshore monopile experiences depends on the cycles' origin and their amplitudes (Andersen, 2015).

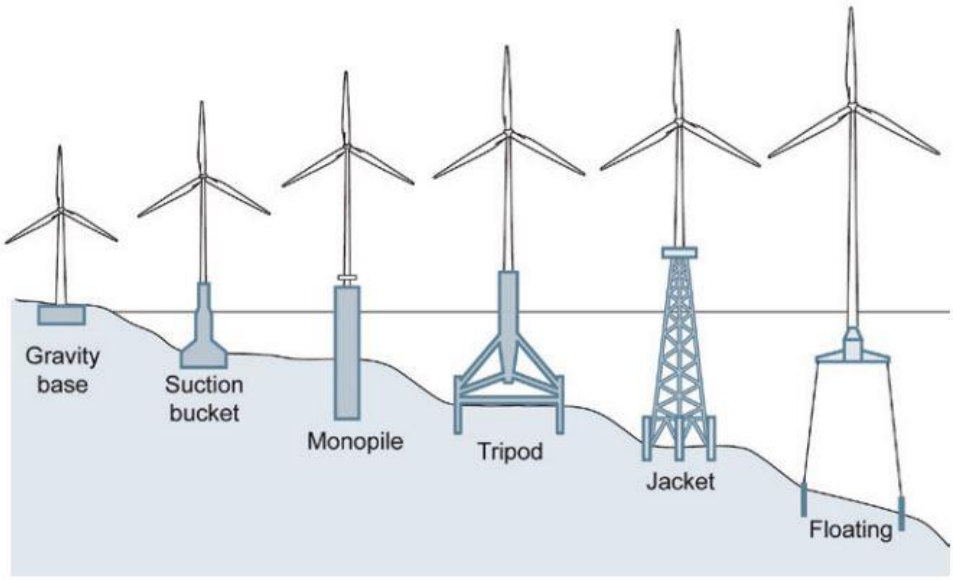

Figure 1.1 – Types of foundation designs for offshore windmills. For this thesis the monopile-foundation will be emphasized. From World Steel Association (2012).

The cyclically loaded pile may influence the surrounding soil by altering the soil properties and weakening the soil. This can lead to fatigue damages to the pile and cause accumulated pile displacements over time. The displacements can pose a challenge for the serviceability limit state (SLS) design. Additionally, stress changes around the pile may also be changed due to the soil-structure interaction, which can affect the bearing capacity of the pile. As such, for foundation design purposes one must consider these challenges (Andersen, 2015).

Soil responses from cyclic loading is commonly modelled with the use of lateral load-displacement springs. As this approach possesses limitations and uncertainties it cannot be properly used for fatigue analyses of engineering structures (such as windmills or offshore well conductors). Such fatigue analyses deal with assessing the structures fatigue limit state (FLS) and fatigue stresses caused by cyclic loading (Jardine et al., 2012; Zakeri et al., 2017).

Hence, a newly developed apparatus by the Norwegian Geotechnical Institute's (NGI), the P-Y apparatus, aims at collecting P-Y (pressure-displacement) data and hysteretic damping, to better evaluate the fatigue limit state design of engineering structures (Zakeri et al., 2017). Both displacement controlled- and load controlled tests are possible with this device (Zakeri et al., 2017; Støren, 2018). It also has the potential to serve as an aid for SLS assessments of engineering structures (Støren, 2018).

1.2 Aim and motivation

The main goal of this thesis is to qualitatively investigate the long-term effects of two-way cyclic pile response in clay-based soils with the use of NGI's newly developed P-Y apparatus.

To reach this goal, the objectives of this study are to:

- Assess the soil stiffnesses both during and after cyclic testing
- Study the effects of continuous consolidation during and after cyclic testing

This will be achieved by accomplishing fatigue analyses on two types of soil materials. Four experimental tests, with several, but short-duration cyclic parcels, will be performed, to determine the stiffness evolution. The testing will be accompanied by continuous axial consolidation both during and between cyclic testing. These analyses will provide a more realistic insight on the soil-structure interaction between a pile and its surrounding soil over the pile's loading history. This study can thus be viewed as an analogue to the behaviour of monopile-foundations for offshore structures, exposed to external loading.

1.3 Focus of work

Since this thesis will be a qualitative study on the cyclic loading development of clays, much of the focus will be dedicated to the experiments and the developments throughout the experiments. Less focus will thus be given to geotechnical calculations, although some calculations in the study is inevitable.

Chapter 2

Literature

This chapter will provide background information concerning soil mechanics and cyclic loading. It begins by presenting some base definitions relevant for this study, which will be described briefly. Furthermore, main ideas concerning the topics of mechanics and cyclic loading will be presented thereafter. Finally, some geotechnical aspects of cyclic loading will be mentioned.

2.1 Definitions

A soil's **effective unit weight** (δ') is defined by its saturated unit weight (δ) subtracted from the unit weight of water (δ_w; Equation 2.1), where the latter is equal to 9.81 kN/m^3 (McCarthy, 2007; Wesley, 2010).

$$\delta' \left[\frac{\text{kN}}{m^3}\right] = \delta \left[\frac{\text{kN}}{m^3}\right] - \delta_w \left[\frac{\text{kN}}{m^3}\right] \tag{2.1}$$

Soils in their natural state are inflicted by static loading from overburden soils and structures, causing vertical stress to increase with depth. The **in-situ vertical stress** (σ_v) with depth (z) is defined as (Equation 2.2; Craig, 2004):

$$\sigma_v \left[kPa = \frac{\text{kN}}{m^2}\right] = \delta \left[\frac{\text{kN}}{m^3}\right] * z\ [m] \tag{2.2}$$

Pore fluids in a soil-medium collect in the voids between the soil grains, and the amount of occupied void space in relation to total void space within the soil skeleton defines the soil saturation. The pore fluids exert an internal **pore pressure** (u), expressed as a static pore pressure component (u_s) within the soil by counteracting external stress. When the vertical stress increases, pore pressure increases, if no drainage is allowed, by an added excess pore pressure component (u_e) to the static pore pressure component (Equation 2.3). This formula expresses that increasing the pore pressure reduces the **effective stress** (σ'_v) in the soil (Equation 2.4; Craig, 2004).

$$u\ [kPa] = u_s[kPa] + u_e[kPa] \tag{2.3}$$

$$\sigma'_v[kPa] = \sigma_v\,[kPa] - u\,[kPa] \quad (2.4)$$

The **shear strength** of a material is equal to the amount of shear stress at failure (τ_f), i.e. when a shear fracture develops. The shear strength of soils is commonly expressed as (Equation 2.5):

$$\tau_f[kPa] = c'[kPa] + \sigma'_f[kPa] * \tan\varphi \quad (2.5)$$

Where c' is the soil cohesion, σ'_f is the effective normal stress at failure and φ is the friction angle (Craig, 2004). Shear strength of a soil however is dependent on its level of saturation. During undrained conditions, meaning soil is fully saturated and drainage is restricted during testing, the friction angle (φ) can be considered as zero and hence the **undrained shear strength** (S_u) is equal to its soil cohesion (Wesley, 2010). When pressure is thus applied, no volume change takes place, and instead excess pore pressure is building up with a similar amount to the pressure change (Wesley, 2010). During drained conditions, the soil behaves more or less as a frictional material (Craig, 2004).

The Skempton-relation (Equation 2.6) indicates that the ratio between undrained shear strength (S_u) and the effective vertical stress (σ'_v) can be related by the soil's **plasticity index** (PI; Craig, 2004; Wesley, 2010):

$$\frac{S_u}{\sigma'_v} = 0{,}11 + 0.0037 * PI \quad (2.6)$$

When the soil gets exposed to stresses, a certain yield shear stress is needed before any permanent deformation takes place. The yield stress is termed as 'elastic limit'. Before the yield stress occurs, the soil experiences a linear elastic deformation, defined as **elastic strain**. After surpassing the elastic limit, irreversible deformation takes place, where **plastic strain** accumulates with increasing pressure (see Figure 2.1). **Strain-hardening** is observed if the accumulated plastic strain continues to increase with increasing shear stress. The opposite effect is denoted **strain-softening** (see Figure 2.1). By unloading after applying the pressure, the elastic strain is subtracted from the total strain, thus remaining with the plastic strain deformation. (Fossen, 2016).

Certain properties of a soil, such as liquid limit, plastic limit and plasticity index, can provide an overall indication of its behaviour when exposed to external stresses. These properties rely on the water content in the soil. **Liquid limit** (LL) of a clay indicates the amount of water needed to make the material behave more as a liquid rather than plastic. **Plastic limit** (PL)

denotes the water content needed to make the clay behave truly plastic, with no fracturing of it when deformed (Wesley, 2010). **Plasticity index** (PI) reflects the plastic state of the soil over a range of water contents. As such, it follows Equation 2.7 by:

$$PI = LL - PL \tag{2.7}$$

Both PI and LL can be related in a plasticity chart, to determine the soil's engineering properties (Wesley, 2003, 2010).

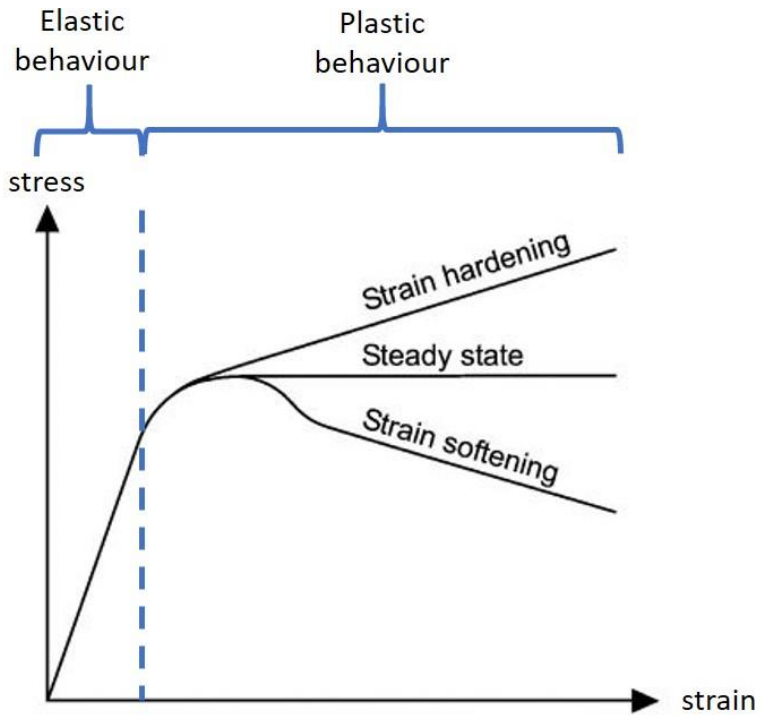

Figure 2.1 – Conceptual stress-strain diagram of elastic and plastic behaviour. Modified from Neuzil (2003).

Cyclic loading of a soil is commonly associated with horizontal stresses, inflicted by lateral movement of a structure within the soil. The infliction of cyclic loading can be decomposed into two types of shear stresses (see Figure 2.2); **average shear stress** (τ_a; also called static shear stress) and **cyclic shear stress** (τ_{cyc}). The former is usually constant and is the sum of two components (Equation 2.8); initial shear stress (τ_o; shear stresses existing in the soil prior to installation of a structure) and added shear stress ($\Delta\tau_a$), from settlement of structure (Andersen, 2015). Average shear stress can also be viewed as an average stress of the maximum- and minimum shear stresses within a cycle.

$$\tau_a = \tau_0 + \Delta\tau_a \tag{2.8}$$

Cyclic shear stress is produced by the lateral loads, and it fluctuates about the average shear stress. Cyclic loading can be loaded in several directions, but in this thesis two-way (bilateral) loading is considered. Two-way cyclic shear stress imply movement in both positive and negative direction of its original position. The stresses produced by cyclic loading depends on the amplitude, number of cycles and frequency (Andersen, 2015; Sheil and McCabe, 2017). Cyclic loading produces total strains (permanent strain; γ_p), which can be demonstrated as a sum of accumulating **average shear strain** (γ_a) and **cyclic shear strains** (γ_{cyc}) with progressive number of cycles (see Figure 2.2; Andersen, 2015).

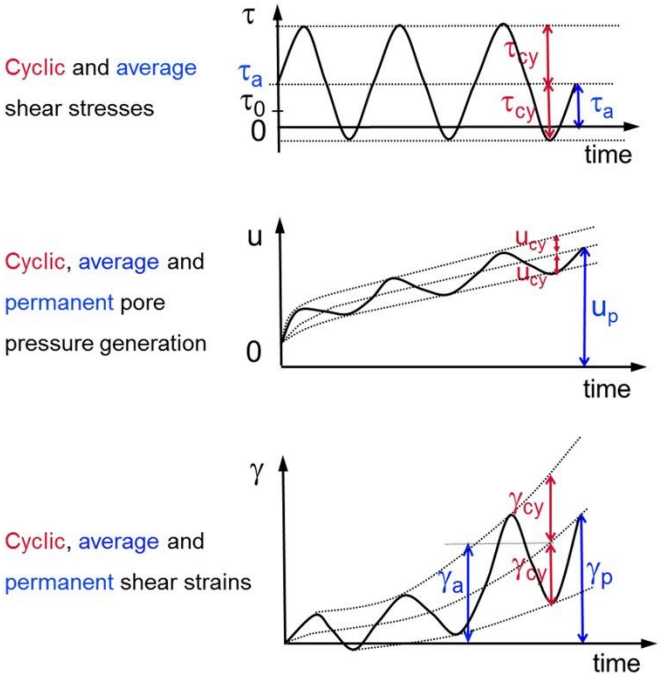

Figure 2.2 – Conceptual diagrams of average shear- and cyclic shear components. τ – shear stress; τ_a – average shear stress; τ_c – cyclic shear stress; τ_o – initial shear stress; u – pore pressure; u_p – permanent pore pressure; u_a – average pore pressure; u_{cy} – cyclic pore pressure; γ – strain; γ_a – average shear strain; γ_{cy} – cyclic shear strain; γ_p – permanent shear strain. From Andersen (2015).

Stress-strain relationship of cyclic loading can be modelled with **cyclic loops**, with the same principles of elastic and plastic strains (Skelton et al., 1997; Ibarra et al., 2005; Paul et al., 2011). Cyclic loading implies unloading-reloading curves are generated for each cycle, developing hysteretic loops (see Figure 2.3). In a two-way loading setting, the hysteretic curves overlap both the compressional- and tensional regions in the stress-strain diagrams, where unloading occurs from peak compression to peak tension. In an idealized, so-called Masing loop,

hysteretic curve, the following reloading phase mimics the unloading phase to complete a hysteretic loop (Chiang, 1999). In reality, the loops change over time as a result of change of 'elastic limit' and stiffness degradation of the material (Skelton et al., 1997; Ibarra et al., 2005). Generally, in such hysteretic stress-strain diagrams secant modulus and hysteretic damping can be explored. **Secant stiffness** (G) is defined as the modulus connecting two points on the stress-strain curve and is useful for assessing the stiffness of a material (McCarthy, 2007). In cyclic loops, the modulus can be the connection between origin and the maximum peaks, or the minimum and maximum peak for each cycle (see Figure 2.3a). The hysteretic **damping** can be related to the area of the hysteretic loops (Δw) with the triangular area, where G acts as the hypotenuse (see Figure 2.3b). The evolution of damping for each passing cycle can be used for studying the energy dissipation occurring within the material (Ashmawy et al., 1995; Semblat and Pecker, 2009).

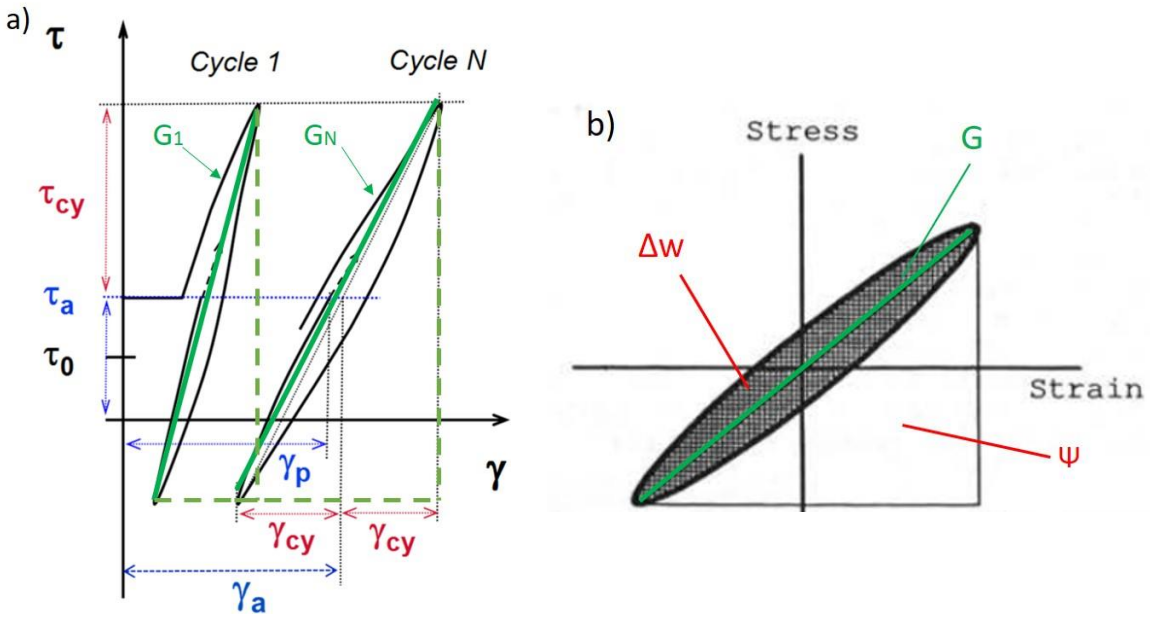

Figure 2.3 – a) Example of cyclic loops. Green lines indicate the secant stiffness (G), connecting the maximum and minimum peaks of the cyclic loops. It is evident that the slope of G changes for each iteration. Modified from Andersen (2015). b) Area of loop (Δw) indicating the damping, along with the secant stiffness (green line). Ψ is the area of triangle below the secant stiffness. Modified from Ashmawy et al. (1995).

2.2 Compaction and consolidation processes

The term 'compaction' implies a mechanical process, in which soil is made denser by the use of dynamic energy. In regard to undrained shear strength, increasing the density causes higher

undrained shear strength. No loss of water occurs during this process, but instead leads to collapse of air voids in the soil. Soil compaction is dependent on the water content and the saturation level within the soil. If the water content becomes too high, compaction could lead to soil-softening, since the water will likely lubricate the disturbed grains (Wesley, 2010).

Consolidation involves the process of removing water in addition to shrinking the soil volume by static loading. Vertical loading onto a soil, such as the weight of a pile or a building, causes ground settlements due to a combination of elastic and plastic strains. Over time, in an undrained setting the total settlement is higher, compared to the total settlement in a drained setting (McCarthy, 2007; Wesley, 2010). The consolidation behaviour can be studied in a semi-logarithmic consolidation curve with vertical stress displayed on the logarithmic axis (see Figure 2.4). For a near-surface soil specimen experiencing consolidation for the first time, it deforms in a linear uniform manner with increasing vertical stress. This phase is referred to as the normal consolidation, following an approximate linear slope (normal-consolidation modulus). During unloading of the consolidated sample, some of the acquired elastic strain is removed, causing some swelling of the soil. As the soil already has experienced irreversible void collapse and remoulding, the unloading path is indicated by a new slope, gentler than the normal consolidation-slope. By reapplying the load, the same gentle slope is followed back to its previous maximum load. If further increasing load is applied beyond this initial maximum stress, the normal-consolidation slope is followed (see Figure 2.4; Craig, 2004; McCarthy, 2007; Wesley, 2010). In reality, the reloading path does not explicitly coincide with the unloading path. But for simplicity, these paths are commonly treated as an average slope. Such reloading cases are also valid for over-consolidated soils, in which soils have previously been exposed to higher in-situ stress (σ'_{OC}), compared to their present state (Wesley, 2010). The over-consolidation ratio (OCR) for these types of soils can be found by (Equation 2.9):

$$OCR = \frac{\sigma'_{OC}}{\sigma'_{v}} \tag{2.9}$$

Such cases are relevant for soils and rocks which have experienced isostacy, overburden removal or dry soils which have been later exposed to permanent groundwater table (Craig, 2004).

To obtain the consolidation curve for a soil specimen, along with its characteristic moduli, an oedometer can be used. The device applies known incremental vertical loading onto a known initial height of undisturbed sample, where also the time is monitored. Porous stone lids above

and below the soil sample allows for drainage of expelled pore water during compression. For each incremental load parcel, the vertical strain is registered to the point when the sample remains undeformed, before a new load parcel is increased and applied to register a new height change (McCarthy, 2007; Wesley, 2010).

The process described above depicts the primary consolidation, involving grain redistribution, expulsion of pore water and void collapse, thus changing the soil skeleton. When a constant effective stress is applied some strain continues to develop, even after dissipation of pore pressure. This secondary consolidation is likely a result of some re-adjustments of the soil grains occurring as a delayed response of compression (McCarthy, 2007; Wesley, 2010).

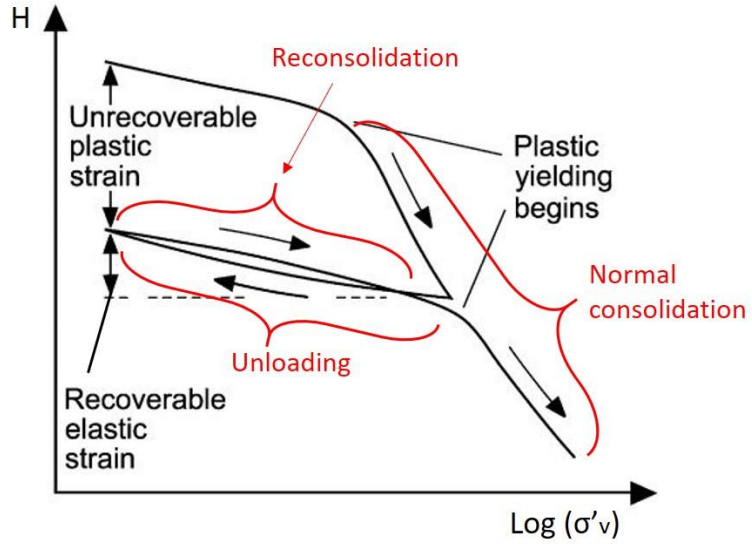

Figure 2.4 – Idealised semi-logarithmic consolidation curve. By applying vertical load, the soil will deform plastically, by following the normal consolidation. When loading is removed, the unloading phase is followed. As reloading takes place again, reconsolidation occurs at a lower slope compared to the normal consolidation. H – soil height; σ'_v – effective vertical stress. Modified from Neuzil (2003).

2.3 Cyclic loading

As previously mentioned, the effects of cyclic loading are determined by the sum of average shear stresses and cyclic shear stresses, along with the number of cycles. To fully assess the cyclic shear strength of a material, parameters such as cyclic, average and permanent shear strains, permanent pore pressure, volumetric strain, damping and post cyclic static shear strength needs to be taken into consideration. These parameters are thus a function of the different shear stresses and number of cycles applied (Andersen, 2015).

In undrained and saturated settings, cyclic loading causes the pore pressure to increase in the soil. Lateral stress applied to the soil skeleton will be transferred to the pore fluids due to the volumetric constriction from restricted drainage. As such, the effective stress in the soil overall lowers (see Figure 2.5). Additionally, the movements also remould the soil structure by softening, hence weakening the soil (Heidari et al., 2014; Andersen, 2015). The cyclic shear strength is defined as when the average shear strain or cyclic shear strain reaches 15%, or in other words, when the displacement reaches 15% of the structure's diameter (Jardine et al., 2012; Andersen, 2015; Zhang et al., 2019). However, an intermediate sum of these strains can also account for failure. Contour diagrams can be used to study the accumulated strains for each category, in addition to the number of cycles to reach failure (see Figure 2.6). Generally, it is evident that by applying high cyclic shear stresses, fewer cycles and lower static shear stress are required to reach failure. Hence, the total strain accumulation could then be higher than the set 15% strain limit within each category. On the other hand, the contour diagram also implies that the number of cycles has less significance as long as the cyclic shear stresses remain low. The undrained static shear strength then becomes more dependent on the applied static shear stress (Andersen, 2015). The amount of strain produced by a certain shear stress is also reliant on the over-consolidation ratio. The strain rate is seen to respond more slowly with increasing OCR of the soil (Andersen, 2015).

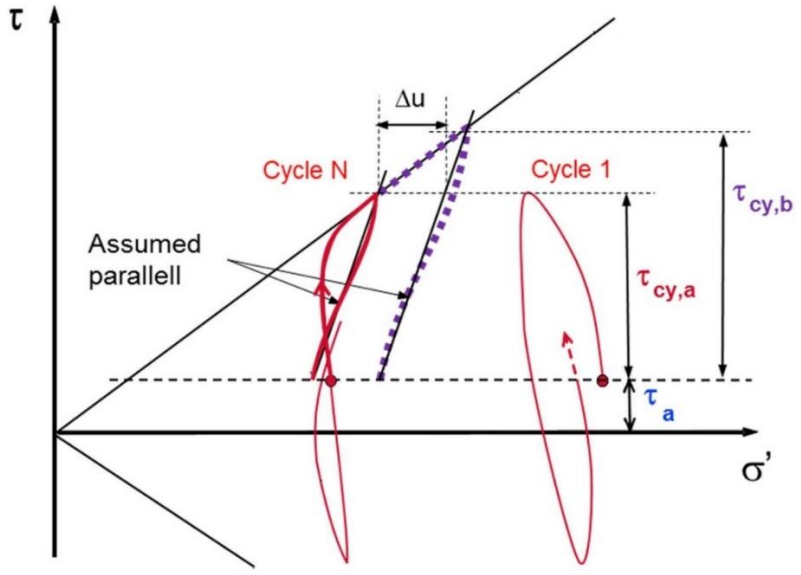

Figure 2.5 – Principle of triaxial test of cyclic loading. After N cycles, the initial cycle has been displaced leftward due to lowered effective stress. Here it also shown an example of when initial cyclic shear stress ($\tau_{cy,a}$) is increased higher cyclic shear stress ($\tau_{cy,b}$). τ – shear stress; σ' – effective normal stress; Δu – pore pressure change. Modified from Andersen (2015).

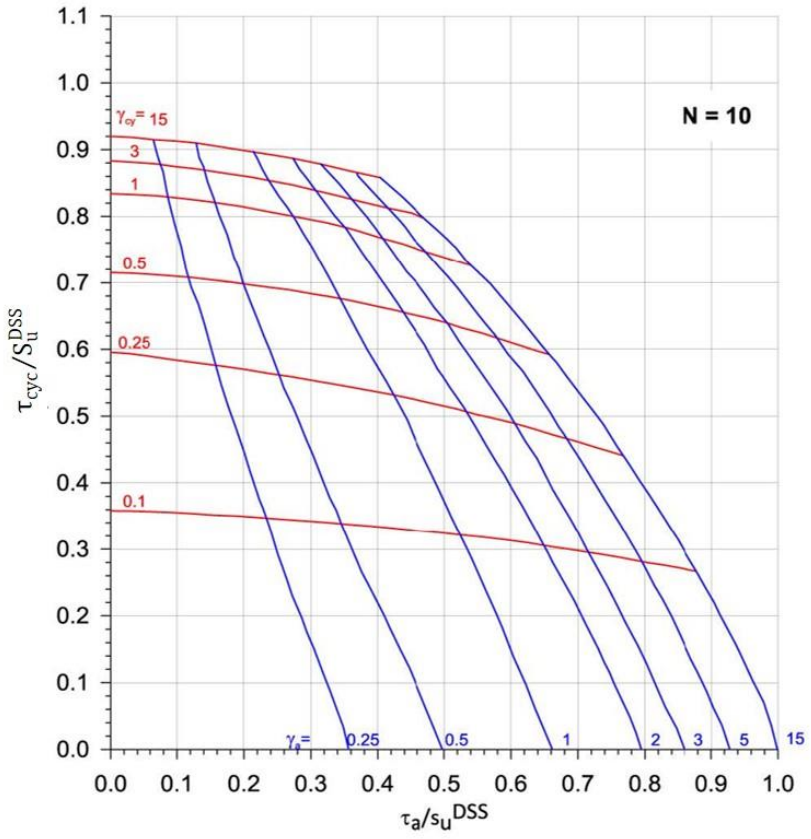

Figure 2.6 – Example of a cyclic contour diagram produced after a cyclic DSS (direct simple shear)-test with N = 10 cycles. Modified from Zhang et al. (2019).

For a monopile experiencing cyclic movements, radial stresses are applied to the surrounding soils, causing local remoulding. The stress distribution of such loading diminishes with depth, thus forming a wedge-shaped stress field around the pile (see Figure 2.7; Karlsrud and Nadim, 1990; Memarpour et al., 2012; Heidari et al., 2014; Sheil and McCabe, 2017). No difference in stress distribution by cyclic movements of a closed-end pile versus an open-end pile has been noted (Karlsrud and Nadim, 1990). Free-standing open end monopile exposed to cyclic loading will experience the largest horizontal displacements, which will dissipate with depth. The movement produces a gap formation behind the displaced pile near the surface. For each cyclic iteration the gap continues to further develop. As a result, the cyclic shear stress is also transferred downward and deflects to the opposite direction of the active shear stress near the surface. For a two-way cyclic setting, this causes the wedge-shaped stress field (see Figure 2.8; Karlsrud and Nadim, 1990; Memarpour et al., 2012). Moreover, this is similarly observed with cyclic failure, where failure near the top continues to be develop downward with progressing cyclicity (Jardine et al., 2012).

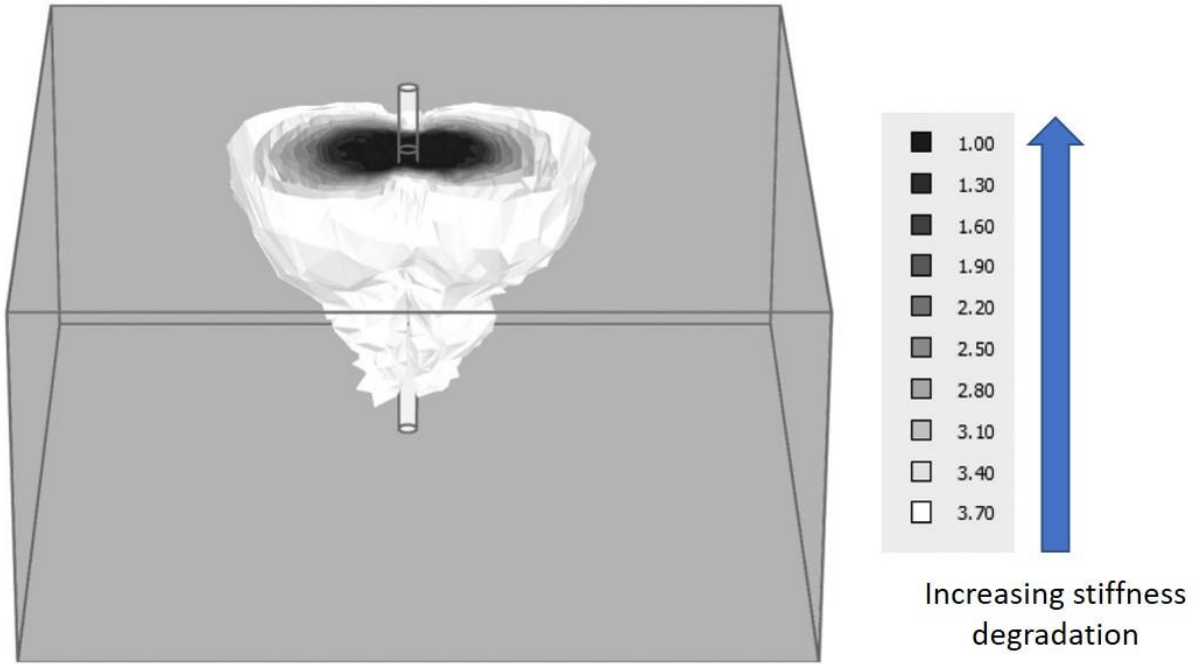

Figure 2.7 – Soil degradation about a moving pile. Modified from Sheil and McCabe (2017).

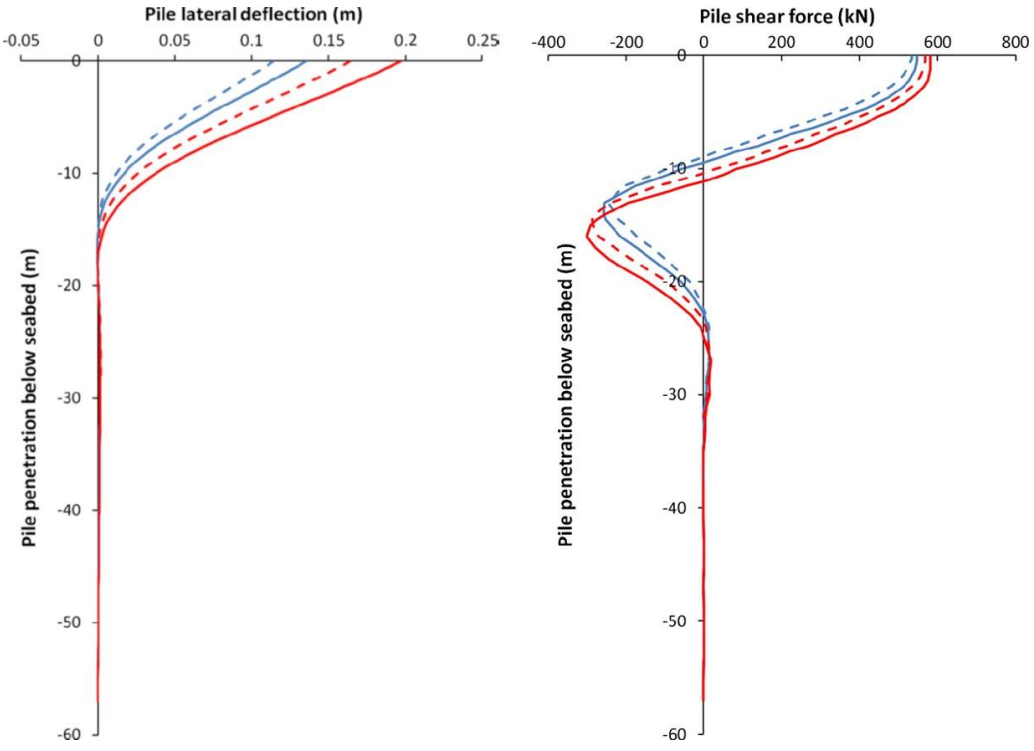

Figure 2.8 – Typical axial pile response with depth, in relation to lateral displacement (left) and shear forces (right). Although the pile remains stationary approximately near 17 meters depth, some large shear forces still exist at this depth. Modified from Memarpour et al. (2012).

2.4 Geotechnical aspects of cyclic design

By performing pile installations into soils, zonal soil disturbances are expected to develop. These zones are associated with altered soil properties, as a result of pile installation (see Figure 2.9; Karlsrud and Nadim, 1990). According to Karlsrud and Nadim (1990), the radial zone (zone A) proximal to the pile is characterised by highly disturbed and remoulded soil, displaying relatively high shear strength. The outer radial zone (zone B), encircling zone A, is the disturbed zone, where the shear strength close to zone A is sharply reduced and increases toward the outer zone C. The latter zone is recognised as the undisturbed zone where the soil is unaffected by the pile installation.

The bearing capacity of a pile refers to how much load can be applied to the structure before it fails. As external forces, generating lateral stress onto the structure, are imminent, lateral loading resistance must be considered for foundation-design. The bearing capacity depends on factors such as slenderness ratio (H/L; H – height; L - pile length), shaft resistance along the pile and soil properties (for example grain size distribution and plasticity; Karlsrud and Nadim, 1990; Andersen, 2009; Knappett and Craig, 2012; Zhang and Andersen, 2017). To study the soil-structure interaction it is common to model the behaviour as dynamic P-Y springs, where it is represented by a series of moving uncoupled springs between soil wall and structure along the depth of the structure, when exposed to lateral stresses (Boulanger et al., 1999; Zhang et al., 2019). For a certain level within the depth, the corresponding spring reproduces the lateral deformation when the pile is subjected to a certain cyclic pressure (p_{cy}) for N number of cycles. This stress-strain relationship is analogous to simple shearing of a soil element, when the cyclic stress (τ_{cyc}) for same number of cycles fulfils the equation within Figure 2.10 (Zhang et al., 2019). From this principle it is possible to scale the cyclic P-Y relationship from laboratory measurements to develop lateral pile response for design purposes (Zhang and Andersen, 2017).

The ultimate lateral resistance per unit pile length (P_u) is found according to Equation 2.10,

$$P_u = N_p * S_u * D \tag{2.10}$$

where N_p is the ultimate bearing capacity factor and D is the pile-diameter (Arroyo et al., 2015; Zhang and Andersen, 2017). Factor N_p depends on the interface roughness factor (α) by Equation 2.11.

$$N_p = 9 + 3 * \alpha \tag{2.11}$$

The variable α is assumed to be equal to 1 for fully rough piles (Zhang and Andersen, 2017).

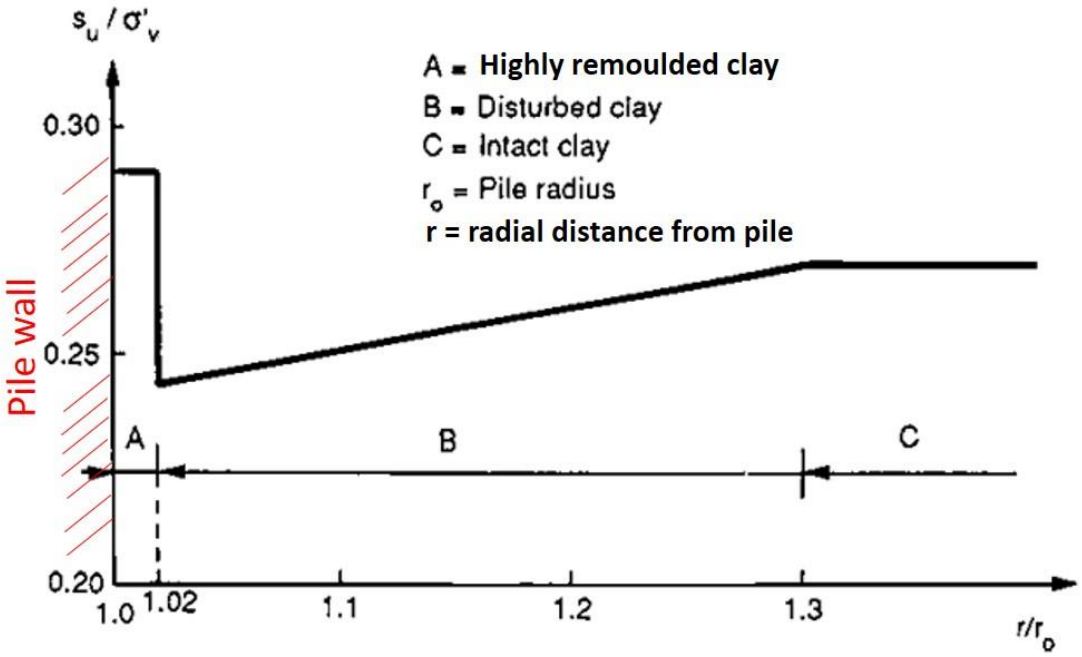

Figure 2.9 – Shear strength distribution of clay around a pile, relative to the vertical effective stress, after pile installation. Modified from Karlsrud and Nadim (1990).

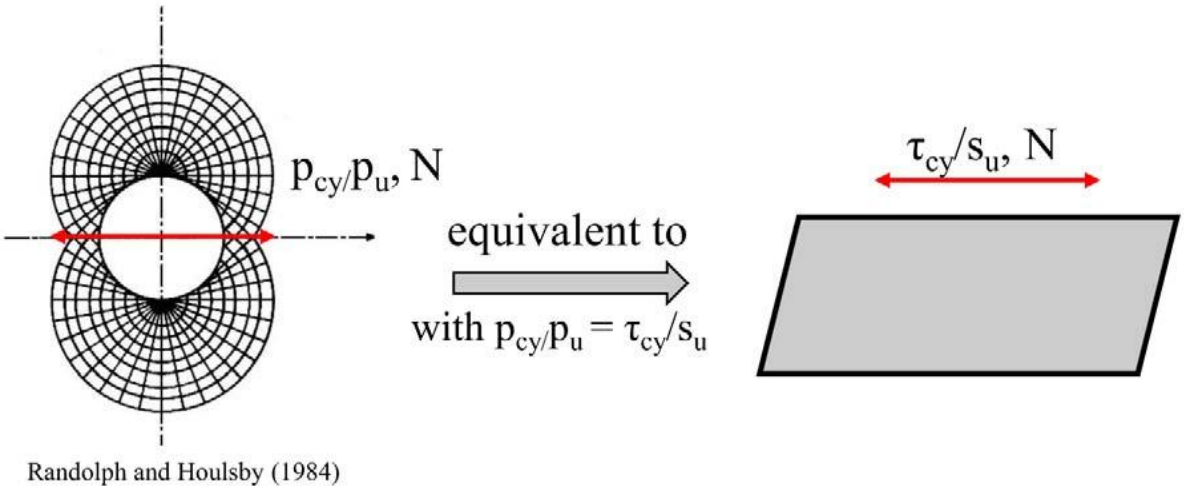

Figure 2.10 – Principle of cyclic stress-strain relationship being equivalent to direct simple shearing. Red arrows indicate direction of lateral movements. From Zhang et al. (2019). Left part of figure, with axial view of the pile, is from Randolph and Houlsby (1984).

Fatigue state refers to the initial degradation of structure under cyclic loading, with developing minor fractures, which can then evolve to an ultimate failure. Over time, the application of cyclic stresses cause bending and axial stresses on to the structure (see Figure 2.8), thus accumulating fatigue damages. As such, fatigue analysis can be performed to investigate the

structure's fatigue limit, reached before its limit of cyclic strength (Zakeri et al., 2016). In some occurrences, if the lateral deflection is too severe or the pile-end is rather shallow, cyclic forces can cause rotation of the entire pile, including its bottom end. The resulting strain will then cause a rotational failure (or scoop) near the bottom of the pile (see Figure 2.11; Zhang and Andersen, 2019).

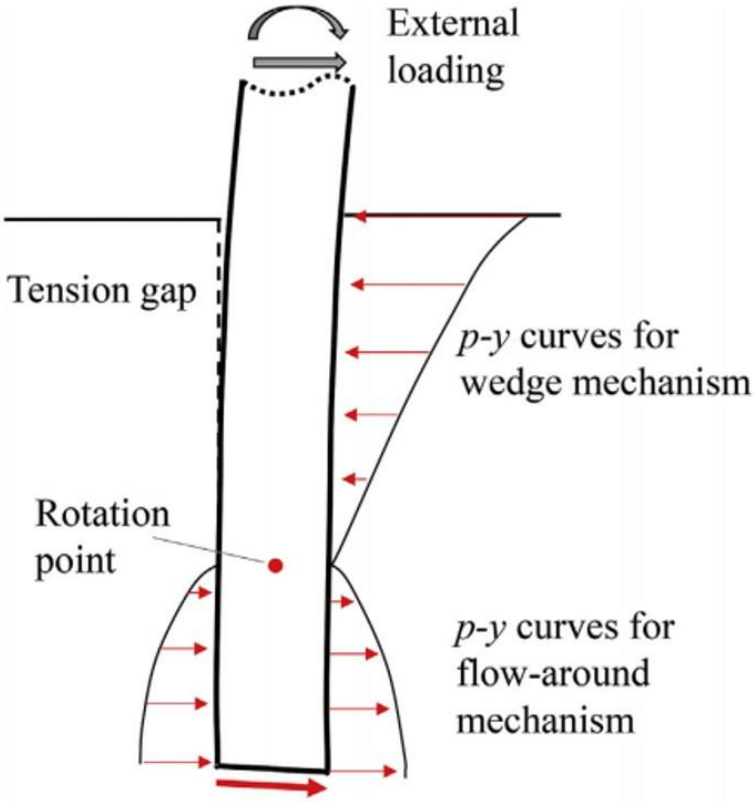

Figure 2.11 – Conceptual model of cyclic loading and pile-response. From Zhang and Andersen (2019).

Chapter 3

Methods

A description of equipment, software and the different steps of procedure will be presented in this chapter.

3.1 P-Y apparatus

The cyclic testing and consolidation are executed with NGI's P-Y apparatus (see Figure 3.1). The idea behind this device is to obtain pile responses exposed to cyclic loading, as well as soil damping, related to these responses. It is primarily used to study the cyclic loading effects and obtain fatigue analyses on well conductors, used in the offshore oil and gas industry. The idea could also be further extended to offshore monopile foundations of windmills (Zakeri et al., 2017; Støren, 2018).

The device is suitable for assessing the soil-pile interaction in "undisturbed" fine-grained soil specimens, such as clay and marine sediments. By "undisturbed" soil specimen, it means soil samples collected in the field, which can be used directly in the apparatus. Cyclic loads and -durations can be simulated to act as external loading force on the pile, and hence establish a soil resistance-displacement relationship (Zakeri et al., 2017).

The device is able to measure lateral pile response by exerting lateral movements onto a model pile, situated in the confined soil specimen. The measurements are registered by transducers, which detects both displacements and loads from lateral movement of a pile. From these measurements it is possible to establish a cyclic p-y response of the soil. Further from this p-y response it is possible to obtain previously mentioned cyclic parameters, such as secant stiffness, damping and cyclic shear strain. The apparatus can also measure the consolidation loads applied to the soil sample, along with axial displacement. Additionally, the apparatus is able to perform pre-consolidation of a specimen to obtain a desired stress state and/or specimen height. The pre-consolidation can be accomplished in a stepwise phase, where bolts on either side of the soil chamber allows for stress-interlock of the soil specimen. Hence, one can simply

adjust the pre-consolidation stress whilst preserving the stress in the soil specimen. The apparatus also allows for cyclic testing to be performed both with and without constant consolidation load applied. This can be used to study, for example effects of settlement, in combination with lateral pile response.

The main parts of the apparatus include a cylindrical soil chamber for the test specimen, end caps to seal each side of the soil chamber, a pile rod, an MTS-hydraulic actuator for controlling the cyclic displacements and -forces, air pressure piston for axial consolidation, and transducers. The soil chamber holds the soil specimen which will be tested for pile response. The soil chamber is made of a steel tube with coated Teflon on the inside of the chamber. This chamber acts as a confinement for the soil specimen. The model pile represented in this device is a cylindrical steel rod. The steel rod is situated in the centre of the soil specimen within the soil chamber. As both ends of the steel rod protrudes out of both sides of the soil chamber, lateral movements of it are purely translational. Hence, no rotational element of the pile needs to be considered (such as the case in Figure 2.11).

The hydraulic actuator is the main component used for cyclic loading, by generating the lateral movements. The movements can either be load-controlled or displacement-controlled, and also involve monotonic testing. The hydraulic actuator is connected to the test specimen by two push/pull rods that are attached to the pile rod within the specimen itself and a back rod, fastened to the actuator (see Figure 3.2). This attachment causes the lateral movements of the hydraulic actuator to be transferred onto the pile rod in the soil specimen. It is the responding movements on this pile which is being registered for pile response.

Three transducers are secured to the apparatus during testing; one measuring the axial consolidation force and -displacement (axial transducer), the two others measure the lateral forces and -displacements of the pile rod on either side (left- and right lateral transducers) of the specimen. As the pull/push rods are attached to the model pile, these pull/push rods are also moving simultaneously with the model pile. The lateral transducers are placed in contact with these pull/push rods, while being firmly attached to the apparatus. It is these movements and the loads that are registered.

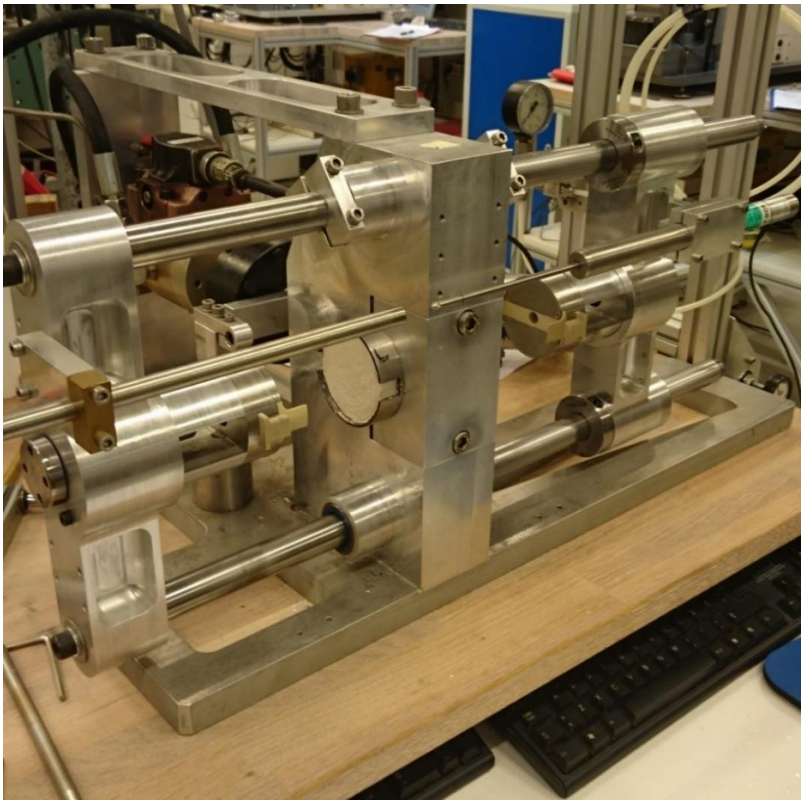

Figure 3.1 - The P-Y apparatus. Clay sample within the soil chamber, without the model pile inserted, is seen in the middle of the photo.

3.2 Software and logging

The cyclic test-measurements and logging were done on the software ModLab, by using the script "Soil Conductor Testing Device" (SCTD) at NGI's laboratory. This also includes logging of the specimens' pre-consolidation.

The specifications and performance of the cyclic load-testing were executed on the MTS Model 793.10 MultiPurpose Testware (MPT). With this software, one can design tests by applying commands and controls to an external controller (MTS Systems Corporation, 2011). The external controller in this case is the MTS hydraulic actuator. The test design involves determining the number of cyclic parcels to use for testing, one-way or two-way cyclicity, number of cycles within each parcel, their amplitudes and frequency. Also, the shape of the cycles may be determined, for example by using sinusoidal or box-shaped waves. The software also allows for monotonic test-setup, either as a stand-alone test or at the end of cyclic testing. In this software it is possible to determine whether to use load-controlled or displacement-controlled cyclic testing. During load-control, one determines the maximum- and minimum

cyclic load amplitudes for each cycle, and thus measuring the cyclic displacement generated. For displacement-controlled testing, the maximum- and minimum displacements are determined beforehand on the MPT. As such, the cyclic loads are measured.

The specifications for the relevant cyclic test are employed into a script on the MPT-software. In the script, the sine wave function was selected, where the bilateral (two-way) movement is implemented. This causes the hydraulic actuator to move the back rod from its initial position toward the positive direction (push) toward a peak, and then shift to the negative direction (pull), passing through the initial point and further into a negative peak. From here the back rod is pushed back to its initial position, and a new cycle begins by repeating the same procedure. It is within the sine wave function where one can specify the number of cycles to be performed, whether the test should be load-controlled or displacement-controlled, amount of force (N) or displacement (mm) to be implemented in the parcel, and the cycle period. All parcel-scripts ended with a ramp function, where any remaining displacement-offsets of the back rod causes it to be shifted back to its original position. It is important before executing the test to consider the set displacement limit. Due to the design of the apparatus, a maximum displacement for the hydraulic actuator is 4 mm. Exceeding this value will potentially damage the apparatus (Støren, 2018). As such, the limit was adjusted to be lower (commonly ca. 2 mm). Thresholding this pre-determined limit will then cause shut-down of the hydraulic actuator and the script is stopped. When performing load-controlled cyclic testing it is vital to continuously observe the experiment. If the shear strength of the sample is over-estimated, failure of the soil specimen may occur, hence displacement will become too large.

When cyclic testing is executed the MPT-software visualizes both the command-signals and produced output-signals for the user to infer whether the signals are acceptable or not. To achieve satisfactory performance of the MTS-hydraulic actuator, it is necessary to calibrate certain tuning parameters through MPT, such as P-gain, I-gain and dither amplitude. These parameters can aid to lower the error between the actuator's command and its performance. P-gain controls how fast the system responds to the input-command; too low P-gain causes slow responds of a command. Contrary, too high will make the system unstable and produces unpredictable output-signals. The I-gain controls the mean response of the system over time during performance. If this gain is too high oscillations may occur. The dither amplitude controls the actuator system's response to improve low amplitude signals (MTS Systems Corporation, 2009; Støren, 2018). As the tuning parameters selected are not uniform in all tests, they are included in the cyclic specifications for each test, summarised in previous chapter.

Consistently, the sampling rate during axial consolidation was set at 10 seconds, to not overload the log-file and to reduce the file-size. During cyclic loading the rate was lowered to 0.01 seconds, to achieve high resolution of each cycle.

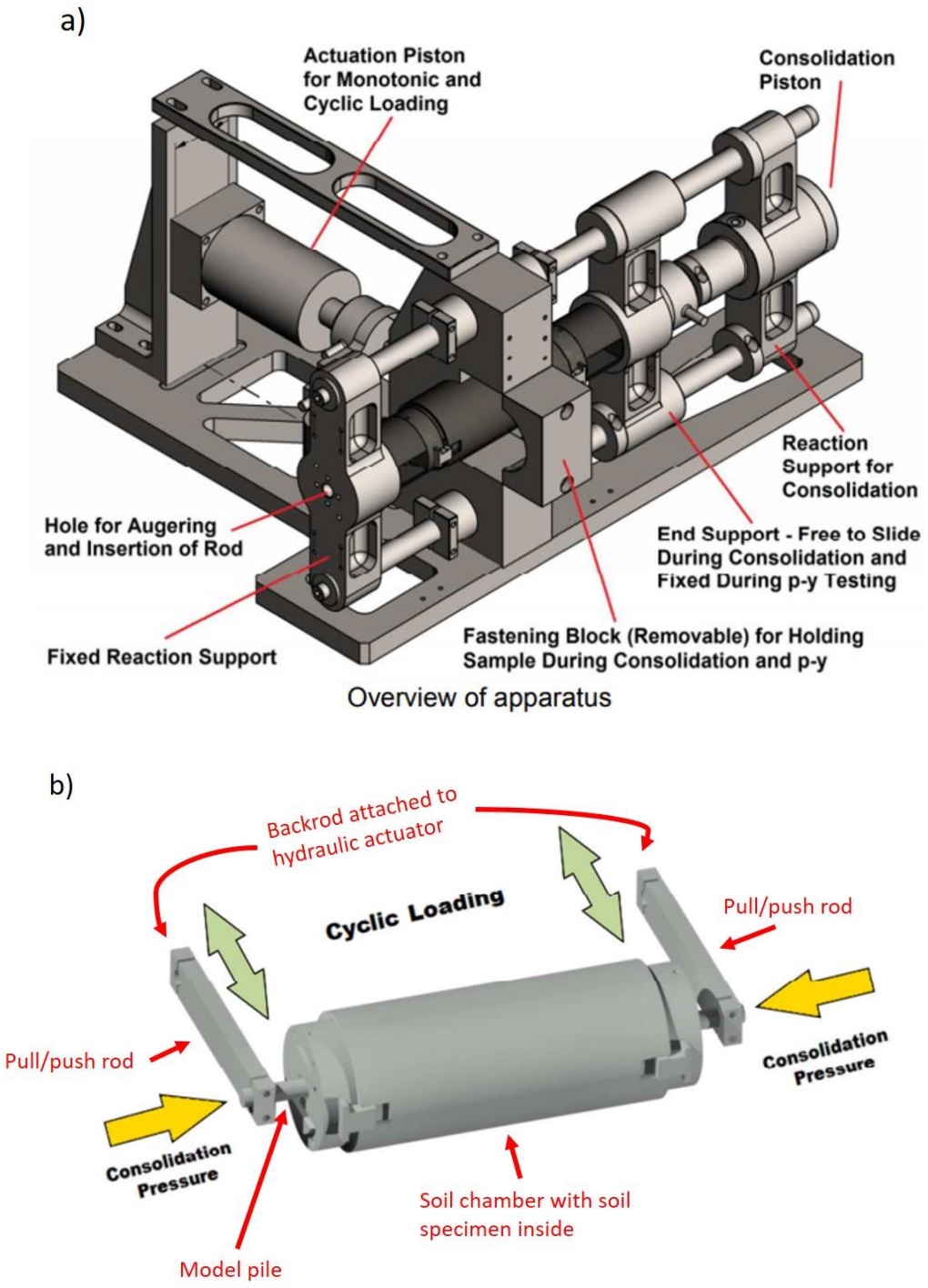

Figure 3.2 – The P-Y apparatus. a) an overview of the apparatus, indicating its main components. b) Detailed overview of the soil chamber and surrounding components, and direction of the forces applied to the soil specimen. Both figures are modified from Zakeri et al. (2017).

3.3 Methodology

The laboratory phase of the cyclic testing will be presented in this section. The outline of the workflow is presented in Figure 3.3, and each phase will be thoroughly explained. The initial phase and the computational phase encompass the evaluation part of this study and will not be explained in this chapter. However, these will be further presented in Chapter 4.

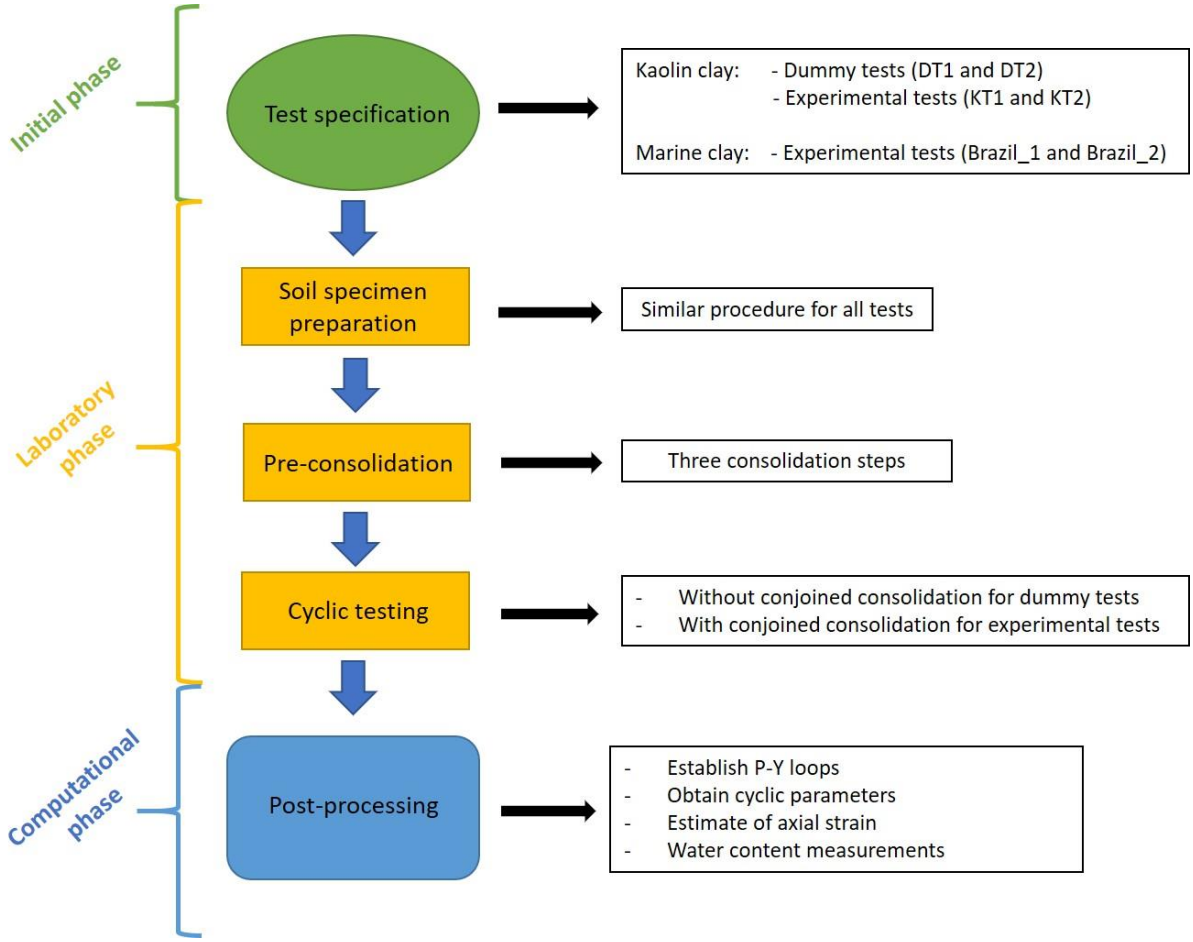

Figure 3.3 – Outline of the workflow for the experiments. The initial phase involves determining the test specifications for each test and will be presented in the next chapter. The laboratory phase involves three steps; soil specimen preparation, pre-consolidation and cyclic testing. The computational phase is the last step, where measured raw data is processes and calculated. This will also be thoroughly explained in the next chapter.

3.3.1 Soil specimen preparation

All specimens were prepared for testing at the laboratory of NGI. The preparation method is similar for both materials used in this project. One exception is the collection process of different materials. For the kaolin clay, the specimens were already prepared by Støren (2018). In her study, the kaolin was prepared into a slurry with mixture and water, and then consolidated to 80 kPa in two separate batches, to achieve a desired firmness. After consolidation, the batches were then sliced into squared prism, having the dimensions of 9x9 cm in both length and width. The height of the batches varied with one having the height of 14.8 cm and the other a height of 21.5 cm. The sliced kaolin specimens were then wrapped into airtight plastic bags, along with a soaked tissue to preserve the humidity (Støren, 2018). For the Brazil clay, the specimen was enclosed in a plastic tube-casing with sealed ends. To extract a specimen, the tube ends were removed, and a vertical piston was used to push out the topmost part of the soil material. A sufficient height of specimen was extracted to have enough material for both the build-in of the soil chamber and for reference sample used for water content measurement.

The build-in of material into the soil chamber encompasses cutting the specimen to fit inside the soil chamber (see equipment-specifications in Table 3.1). This involves less disturbance of the soil specimen as possible, by carefully cutting it with a wire to have sufficient amount of material to fill the soil chamber. The soil chamber was slightly lubricated inside to remove friction between the soil material and the Teflon coating during build-in. The soil chamber can be equipped with a cylindrical ring-blade, having sharp edges on one of its rims. The soil chamber is then firmly attached to a frame stand, with the ring-blade pointing downward (see Figure 3.4). A slightly lubricated, flat disk is placed below the soil chamber, where the soil specimen is placed. It is important make sure that the downward part of the specimen is placed faced down onto the disk. To build the specimen inside the chamber, the chamber is lowered and pushed incrementally downward into the specimen. During each incremental stop, excess material collected outside the soil chamber is scraped off with a knife. As the chamber reaches the bottom the soil specimen is situated inside the soil chamber. Some surplus material protrudes out the other end of the chamber. This surplus was sliced of and used as a reference for water content measurement. To ensure appropriate specimen height inside the soil chamber a spatula is placed above the soil chamber to scrape of any excessive height. This process also smooths out the surface on the soil specimen. The height is satisfactory when the specimen surface is located just below the inclined rim on the soil chamber. The soil chamber, with the

soil specimen inside, can then be carefully removed from the frame stand. Before placing the chamber into the P-Y apparatus, the chamber was weighted, and the specimen height was measured manually with a ruler.

For the upcoming sections it is recommended for the reader to refer to Figure 3.2 to follow the components of the P-Y apparatus.

Table 3.1 – Equipment specifications for the specimen.

Height of soil specimen	~100 mm
Diameter of soil chamber	68 mm
Weight of soil chamber	650.19 g

3.3.2 Installation of soil specimen into the P-Y apparatus

When the soil chamber is placed in the device, the fastening block is placed on the front to secure the chamber in place. Then the end supports on either side of the soil specimen is pushed toward the specimen to place the end caps onto the specimen ends. The end supports are then fixed into place by bolts on the top of either side of the soil specimen. This is to prevent the end supports to move during set-up. On the end supports there is a hole where the clay specimen can be cored at the centre with an auger to fit the steel rod (model pile) inside (see Figure 3.5). After this has been completed, the specimen is ready for the pre-consolidation phase.

3.3.3 Pre-consolidation

The pre-consolidation is performed with an air pressure piston, attached to the reaction support of the P-Y apparatus (see Figure 3.2). The consolidation piston is fixed into place by bolts. A valve controls the amount of air pressure to be applied to the piston. When the desired axial load is applied and touches the right-hand side of the end support, the bolts of this end support is opened, thus allowing movement during consolidation. As the other end support still remain fixed it is these end supports which directly apply the consolidation load onto the soil specimen. Both the consolidation force and -displacement are then immediately monitored and logged in

the ModLab-software on a logging file. The consolidation is done in three steps, by increasing incrementally the load. For the two first steps, the consolidation was performed over one day for each step, whereas for the last step the duration occurred over at least two days. Between each consolidation step the applied consolidation load it is increased by turning the valve to reach a desired load.

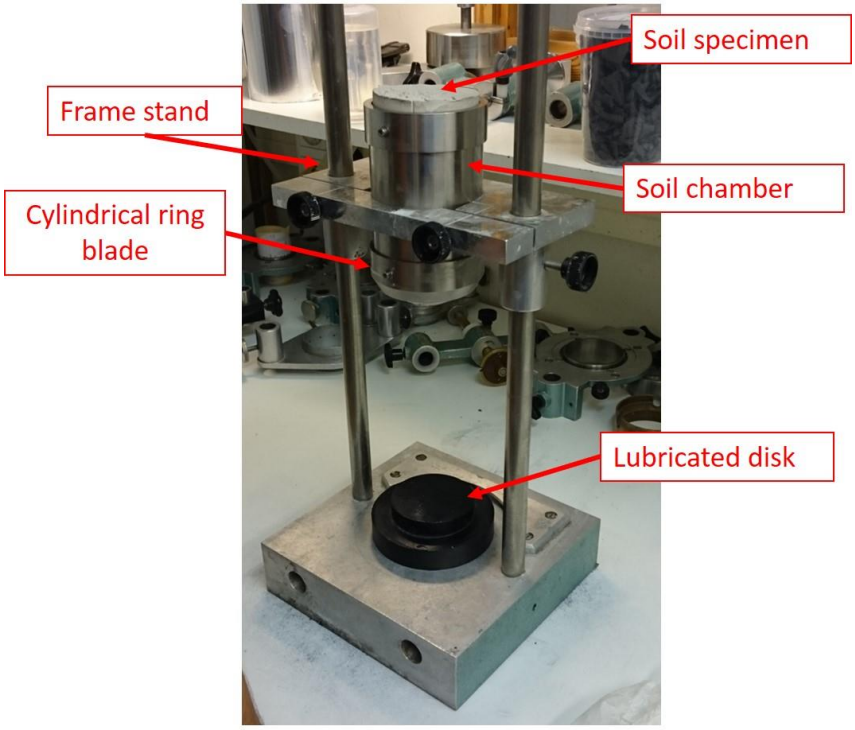

Figure 3.4 – Build-in of soil specimen into the soil chamber, with denoted tools to aid less disturbance of the soil specimen.

Figure 3.5 - Soil chamber (left photo) with kaolin specimen inside. The centre has been cored to fit the model pile inside (right photo).

3.3.4 Cyclic testing

After completing the axial pre-consolidation, the specimen is then ready to be equipped for cyclic testing. Before this step however the moving end support must be secured into place and logging paused, to avoid data-noise during set-up which could transmit to the logging file. The pump of the hydraulic actuator is also warmed up before equipping the soil specimen for cyclic testing. This warm-up is activated through the MPT-software.

The hydraulic actuator is connected to the model pile by a back-rod, which is also attached to the pull/push rods on the model pile (see Figure 3.2). It is important that the installation of these rods do not apply pressure onto the model pile within the soil specimen, as this could disturb the soil specimen before cyclic testing. To correctly adjust the push/pull rods there must be a 10 mm gap between each pull/push rod and the back rod-clamp on the hydraulic actuator. Screws on the back rod and pull/push rods must be firmly attached to both hydraulic actuator and cylindrical chamber, to prevent sluggish movements and erroneous results. On the other hand, they must also be similarly attached, so that the lateral forces are close to zero. This could be consulted by the MPT-monitor, which surveys the force and position of the hydraulic actuator.

The lateral transducers register the movement of the push/pull rods, with their pin-points touching the pull-push rods. These transducers are connected to the apparatus through their separate transducer-rods. The space between the lateral transducers, should be 191 mm wide. This is to correct for false deformation, involving flexural bending of the model pile (Zakeri et al., 2017; will be presented in more detail in the next chapter). The correction is done to avoid erroneous delays and misleading measurement. As they are installed with the appropriate space in between, they must be firmly screwed to their lateral transducer-rods. After installing the transducers some displacement offset of the pin-points are imminent. Hence, before executing the cyclic testing it is important to reset their displacement offsets, to start their measurement from a zero position.

The specifications for the cyclic testing are entered into MPT software. For each cyclic parcel that wish to be studied, one must design an individual script to set the parcel's specifications. All parcel-scripts ended with a ramp function, where any remaining displacement-offsets of the back rod causes it to be shifted back to its original position. With the exception of the dummy tests, the cyclic testing is conjoined with continuous axial consolidation over several days. This

requires that the interlock of the end support to be unlocked, to allow continuing consolidation displacement. When the script for cyclic testing is ready to be initiated, logging is resumed on the ModLab software, right before the testing starts.

After completing the cyclic test, the specimen, along with the soil chamber, is removed from the P-Y apparatus, and re-weighted to estimate the amount of material loss after testing. Some material- and porewater loss is expected during performance, especially during axial consolidation (see Figure 3.6). The sample is then carefully pushed out from the soil chamber and sliced into approximate three equal parts. For the kaolin-based specimens the slices were weighted, then stored in an oven to dry for several days. Afterward, they were re-weighted to estimate the water content. With the Brazil-tests the slices were further divided and sampled into two parts; one sampled near the core of the model pile and the other proximal to the walls of the soil chamber. To check for their water contents they were weighted, dried in an oven for several days and then re-weighted again.

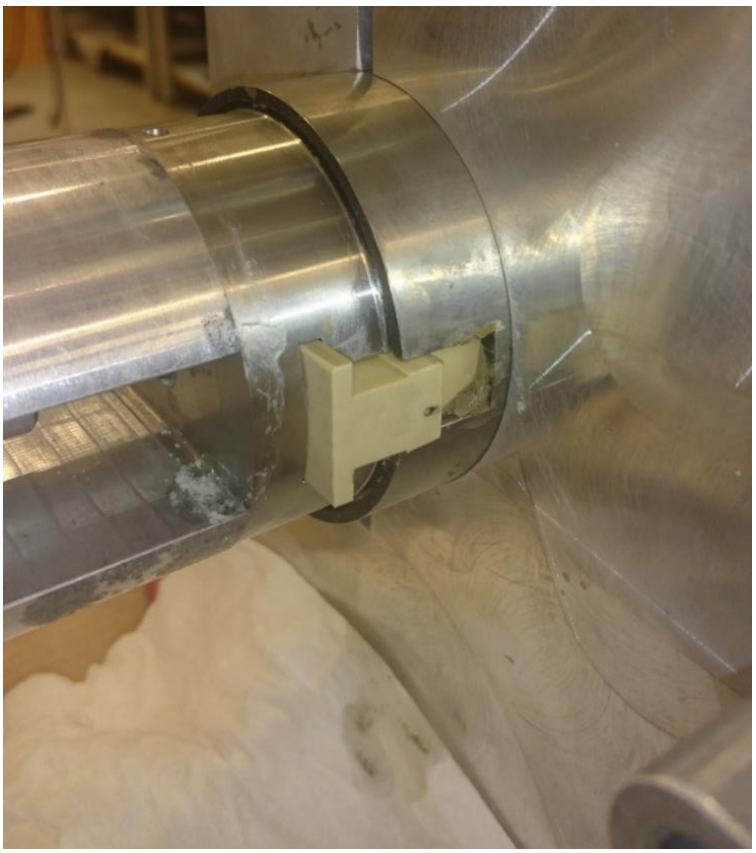

Figure 3.6 - Material squeezed out between the soil chamber and the end cap. Some wet stains on a tissue are observed below the end cap.

Chapter 4

Evaluation

For this project, a total of six tests were executed. The first four tests were tested on a remoulded and pre-consolidated kaolin clay. Two of these are dummy tests, whereas the two others are for experimental study. The four kaolin-based specimens are denoted "DT" for dummy tests and "KT" for experimental test, followed by their test number. The remaining tests (Brazil_1 and Brazil_2) were done on marine material from Carcará field in Santos Basin, offshore Brazil (Norwegian Geotechnical Institute, 2019).

The purpose of the dummy tests, DT1 and DT2, was to become familiar with the P-Y apparatus, as well as to understand the behaviour of cyclic loading and consolidation. For these tests five cyclic parcels, with different loads and numerous cycles within each, was performed.

For both KT1 and KT2 the purpose was to study the cyclic behaviour and consolidation of kaolin. The cyclic testing involves several, but short cyclic parcels, along with continuous axial consolidation. In KT2 the specifications were replicated but with different axial consolidation stress. Relative to the consolidation stress given in KT1, the consolidation stress was lowered during cyclic testing of KT2.

In the Brazil-samples, the specification-procedure is repeated, as that performed with KT1 and KT2. The purpose of these tests is to study the cyclic behaviour of marine clay and compare this behaviour with that developed in the kaolin-tests. In Brazil_2 the vertical consolidation and cyclic shear stresses were increased, relative to the specifications in Brazil_1.

A general overview of the tests with their purposes is summarised in Table 4.1.

Table 4.1 – General overview of the cyclic tests and their purposes.

Test ID	Material	Consolidation (kPa)	Number of parcels	Main number of cycles	Purpose
DT1	Kaolin	-	5	1000	Familiarise with the P-Y apparatus
DT2	Kaolin	-	5	1000	Repeat test of DT1; familiarise with the P-Y apparatus
KT1	Kaolin	120	7	100	Study long-term effects of cyclic loading on kaolin
KT2	Kaolin	100	12	20	Study long-term effects of cyclic loading on kaolin; reducing both consolidation and number of cycles relative to KT1
Brazil_1	Marine clay	80	11	10	Study long-term effects of cyclic loading on marine clay; repeat procedure of KT2, but with reduced consolidation and number of cycles
Brazil_2	Marine clay	100	12	10	Study long-term effects of cyclic loading on marine clay; repeat procedure of Brazil_1, but with increased consolidation

4.1 Materials and their properties

The kaolin, namely reconstituted Prestige-NY kaolin, is a mixture consisting of 70% kaolinite, 22% quartz and 8% nordstrandite (Carotenuto et al., 2018; Støren, 2018). It had been pre-consolidated to 80 kPa beforehand by Støren (2018). As the clay was prepared and consolidated from a slurry in two separate batches, the consolidation loads and measured axial strain were given (see appendix F in Støren, 2018). From this, a semi-logarithmic consolidation curve was constructed and thus finding the normal consolidation modulus (see Figure 4.1). Soil parameters of this mixture are summarised in Table 4.2.

The Brazil marine clay was collected from well EQ19463-BH-18, cored from a depth of 10-11 m below seabed by Equinor. This material is mainly clay-based, with a high fine content between 90-95 % (Norwegian Geotechnical Institute, 2019). Both the normal consolidation- and the reconsolidation moduli were obtained from a consolidation curve for the marine clay localised at 7 meters depth. No consolidation curve was available for 10-11 meters depth. Thus, the obtained moduli are assumed to be similar to that obtained from 7 meters depth. Soil parameters of this material is summarised in Table 4.3.

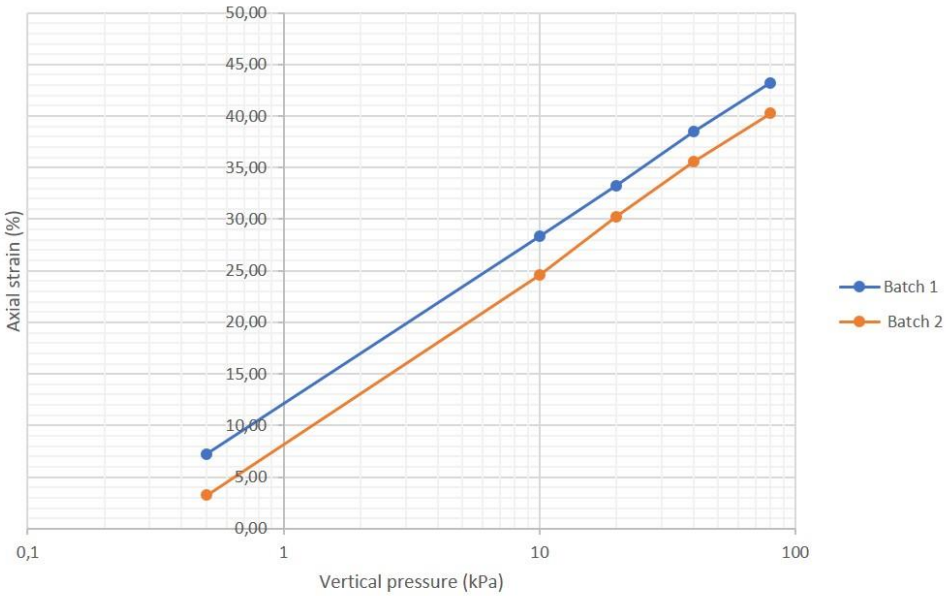

Figure 4.1 - Consolidation curve of Prestige-NY kaolin. Obtained from appendix F, Støren (2018), and used to determine the normal consolidation modulus of kaolin.

Table 4.2 – Soil parameters of kaolin-mixture (from Carotenuto et al., 2018 and Støren, 2018). The normal consolidation modulus was determined from consolidation results of prepared kaolin (see appendix F in Støren, 2018).

c_v [m^2/s] (from 7 meters depth)	0.2e-6
Clay content [%]	55.7
Liquid limit, LL [%]	56.1
Plastic limit, PL [%]	28.0
Plasticity index, PI [%]	28.1
Normal consolidation modulus	15.58

Table 4.3 – Soil parameter of marine clay in Brazil-samples (from Norwegian Geotechnical Institute, 2019). The moduli were determined from consolidation curves presented within the report of Norwegian Geotechnical Institute, 2019.

Effective unit weight [kN/m^3]	5.5
Soil depth, z [m]	10 < z < 11
In-situ effective vertical stress, σ'_v [kPa]	55
Undrained shear strength, S_u [kPa]	20
c_v [m^2/s]	0.8e-7
Clay content [%]	57.4
Silt content [%]	39.3
Liquid limit, LL [%]	94
Plastic limit, PL [%]	36
Plasticity index, PI [%]	58
Normal consolidation modulus	25.87
Reconsolidation modulus	2.06

4.2 Evaluating drainage during one cycle

To be able to evaluate the drainage during cyclic loading it is necessary to consider the diameter of model pile (D), the coefficient of consolidation (c_v) and the cyclic loading period (t_p). The evaluation is determined by the normalised loading period (T_p; Equation 4.1; Li et al., 2019), which may suggest whether pore pressure response during cyclic loading needs to be considered. The normalised loading period can thus provide an indication on, for example,

whether the cyclic loading period may drain the soil completely or perhaps not at all (see Figure 4.2; Li et al., 2019). It is then possible from Equation 4.1 to re-structure it to obtain the maximum cyclic loading period needed to achieve a certain drainage. The maximum loading periods for the different materials and the model pile in this study (D), to remain undrained during one cycle, are presented in Table 4.4.

$$T_p = t_p[s] * \frac{c_v\,[m^2/s]}{D^2\,[m]} \tag{4.1}$$

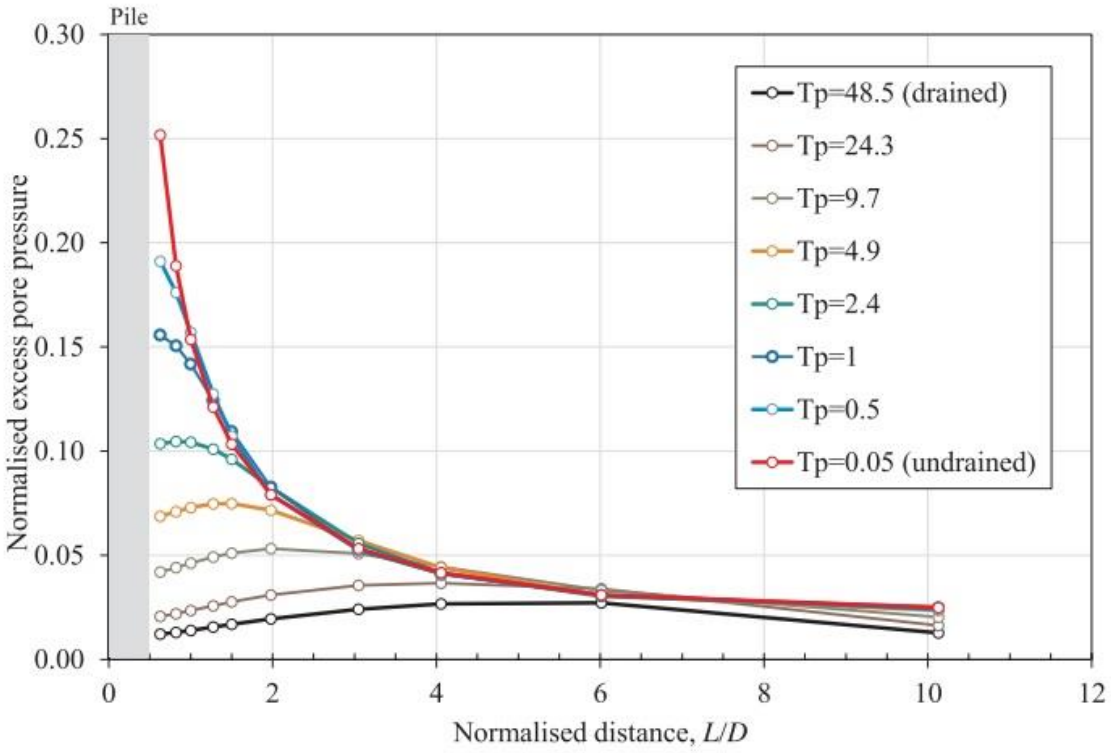

Figure 4.2 – Pore pressure responses at peak of cyclic loading as a function of the normalised distance from pile and the normalised loading period. D – pile diameter; L – pile length. Modified from Li et al. (2019).

Table 4.4 – Calculated maximum cyclic loading period for each material used to remain undrained during one cycle. The calculation is based upon Equation 4.1.

Material	Maximum cyclic loading period, t_p (s)
Kaolin	25
Marine clay	62.5

4.3 Assumptions

For this thesis a base-assumption about soil saturation is made. It will be assumed for all specimens involved that they will remain fully saturated during their entire testing phase. This will include all steps during initial phase and the laboratory phase of the procedure. As such, it is possible to only consider undrained shear strength in this study.

4.4 Test specifications

All specimens are to be pre-consolidated in three incremental steps before cyclic testing is performed. This incremental consolidation is done to reach a specific axial stress without altering the soil skeleton and preserving the full saturation level in the soil specimen. Additionally, it is also necessary to surpass the reconsolidation phase to let the specimen consolidate normally. This is to validate that cyclic testing will be more representative for realistic soil behaviour. Thus, a target consolidation load (σ'_c) must be decided. To evaluate the pre-consolidation loads to use depends on the final step of pre-consolidation, where the largest consolidation (target) load is performed. The first load is 25% of the target and the second load makes up 50% of the target load.

Determining the cyclic pressure to select for cyclic testing depends mainly on the test design and what wishes to be studied. Whether axial consolidation shall be accompanied with the cyclic testing or not is also a factor. Generally, to perform a cyclic fatigue analysis, it is important that the cyclic pressures do not exceed the ultimate lateral resistance of the pile, as this will lead to failure of sample. By using the principle displayed in Figure 2.10 (Zhang et al., 2019), an exceedance of cyclic shear stress in an undrained soil would also threshold the undrained shear strength, causing it to fail. For all experiments an average shear stress of zero will be executed, thus only the cyclic shear stresses need to be considered. Setting of the fatigue limit to investigate the cyclic behaviour was deemed to be 80% of the undrained shear strength, thus defining the maximum shear stress (τ_{max}) to be set.

The corresponding maximum shear force ($F_{\tau max}$) of the maximum shear stress is obtained with the parameters of the model pile used for cyclic testing (see Table 4.5) and the consolidation height of sample after finished pre-consolidation. The roughness factor is assumed to be fully

rough, thus equal to 1 (Støren, 2018). By multiplying $F_{\tau max}$ and the ultimate bearing capacity factor of the pile (N_p; see Equation 2.11) the maximum lateral force (F_L) of the pile is obtained (Equation 4.2).

Table 4.5 - Relevant parameters for the model pile used in the cyclic experiments.

Model pile diameter, D [mm]	10
Roughness factor, α	1
Bearing capacity factor, N_p	12

$$F_L\,[N] = N_p * F_{\tau_{max}}\,[N] \tag{4.2}$$

It is the maximum lateral force that will define the two-cyclic amplitude, namely command-amplitude, used for cyclic testing. The finalised targeted cyclic pressure (p_{cy}) is then determined based on the height after pre-consolidation (H_{pc}) and the maximum lateral force (Equation 4.3). During the course of cyclic testing this cyclic pressure is targeted throughout the experiment. However, since axial consolidation will accompany the experimental tests throughout cyclic loading, thus changing the specimen height before each cyclic testing, the force of the cyclic amplitudes must be adjusted accordingly to maintain the targeted cyclic pressure (p_{cy}; see Equation 4.3).

$$p_{cy}\,[kPa] = \left(\frac{F_L\,[N]}{D\,[m] * H_{pc}\,[m]}\right) * 1000 \tag{4.3}$$

4.4.1 Kaolin clay specimens

From Støren (2018), the S_u/σ'_v-ratio for the kaolin clay is determined as 0.21. Only for the second kaolin-test, KT2, were cyclic specifications determined by calculations from height changes. For each experimental kaolin-test, Table 4.6 summarises an overview of the target consolidation-load, their assumed undrained shear strengths, anticipated and studied maximum shear stress, along with targeted cyclic shear stress. No targeted cyclic shear stress is given for KT1, due to varying cyclic load applied to it, see its test description below.

Table 4.6 – Overview of targeted consolidation-load, assumed undrained shear strengths, anticipated and studied τ_{max} and targeted cyclic shear stress of the experimental kaolin-tests.

Test ID	End-target σ'_c [kPa]	Assumed S_u [kPa]	Anticipated τ_{max} [kPa]	Studied τ_{max} [kPa]	Target p_{cy} [kPa]
KT1	120	25.2	20.2	11.4	-
KT2	100	21	16.8	19.6	235.29

4.4.1.1 DT1 and DT2

The dummy tests were performed without axial consolidation during the cyclic testing, meaning the soil specimens remained at constant height after pre-consolidation.

The specifications for DT1 are provided in Table 4.7. Each parcel consists of thousand cycles, sharing equal command-amplitude. Each parcel increases in amplitude toward the last parcel, where it falls back to similar amplitude specified in parcel 2.

The specifications for DT2 are found in Table 4.8. The same specifications for both consolidation and cyclic load testing are the same as that given in DT1. This was due to incomplete performance of DT1, thus a repeat of the same test was arranged. No axial consolidation was allowed during testing.

4.4.1.2 KT1

The purpose of this test was to study the cyclic behaviour of the sample with several, but short cyclic parcels along with continuous axial consolidation. The test specifications are given in Table 4.9.

The setup of this test is different, compared to the dummy tests. It includes seven cyclic parcels, with similar number of cycles and continuous axial consolidation during- and between cyclic testing. A hundred cycles were set for each parcel. The two first parcels were tested with a cyclic load amplitude of 125 N. Then the cyclic load amplitude was incremented for each parcel up until parcel 7, as it remained with the same specs as parcel 6. The consolidation time in-between the cyclic testing varied between six to thirty minutes. Experimental testing of KT1 ended after about three hours.

When initiating the cyclic testing a very low cyclic amplitude was selected. This was done to tread carefully and investigate the development as the cyclic testing progressed, due to uncertainties of overestimating the undrained shear strength.

4.4.1.3 KT2

Twelve cyclic parcels were performed for this test. The setup is comparable to KT1, but with even shorter parcels. Additionally, the testing had a duration of several days, with axial consolidation both during and between cyclic testing. Test specifications are provided in Table 4.10. Two cyclic parcels were tested each day. The succeeding parcel on the same day was tested after three to six hours of consolidation. The test was initially to be tested with hundred cycles per parcel but was reduced to twenty cycles after the initial parcel. The cyclic shear stress to be maintained throughout the experiment was based on the specimen height after pre-consolidation and the maximum shear force.

Although the studied τ_{max}, based on the maximum shear force ($F_{\tau max}$), is higher than the anticipated τ_{max}, based on the S_u/σ'_v-ratio, this can be explained by experience from the previous experiment, KT1. Due to low response from the first few parcels in KT1 it was decided to increase the cyclic amplitude, and hence the cyclic pressure.

Table 4.7 - Consolidation and cyclic loading specifications of DT1. Writings in red were steps not performed due to incomplete performance.

Test ID - DT1							
Axial consolidation		Stress (kPa)		Force (N)		Duration (hours)	
1.step		30		109.0		20	
2.step		60		217.9		72	
3.step		120		435.8		47	
Axial consolidation during cyclic testing?				No			
Cyclic parcels	Two-way cyclic amplitude (N)	Number of cycles	Frequency (Hz)	P-gain	I-gain	Dither amplitude	Day no.
Parcel 1	50	1000	0.25	95	9.5	0.45	1
Parcel 2	80	1000	0.25	95	9.5	0.45	1
Parcel 3	125	1000	0.25	95	9.5	0.45	1
Parcel 4	200	1000	0.25	95	9.5	0.45	1
Parcel 5	80	1000	0.25	95	9.5	0.45	1

Table 4.8 - Consolidation and cyclic loading specifications of DT2.

Test ID - DT2							
Axial consolidation	Stress (kPa)		Force (N)		Duration (hours)		
1.step	30		109.0		18		
2.step	60		217.9		24		
3.step	120		435.8		125		
Axial consolidation during cyclic testing?			No				
Cyclic parcels	Two-way cyclic amplitude (N)	Number of cycles	Frequency (Hz)	P-gain	I-gain	Dither amplitude	Day no.
Parcel 1	50	1000	0.25	95	9.5	0.45	1
Parcel 2	80	1000	0.25	95	9.5	0.45	1
Parcel 3	125	1000	0.25	95	9.5	0.45	1
Parcel 4	200	1000	0.25	95	9.5	0.45	1
Parcel 5	80	1000	0.25	95	9.5	0.45	1

Table 4.9 - Consolidation and cyclic loading specifications of KT1.

Test ID - KT1								
Axial consolidation		Stress (kPa)		Force (N)		Duration (hours)		
1.step		30		109.0		21		
2.step		60		217.9		24		
3.step		120		435.8		74		
Axial consolidation during cyclic testing?				Yes (120 kPa)				
Cyclic parcels	Cyclic pressure (kPa)	Two-way cyclic amplitude (N)	Number of cycles	Frequency (Hz)	P-gain	I-gain	Dither amplitude	Day no.
Parcel 1	136.61	125	100	0.25	95	9.5	0.45	1
Parcel 2	136.64	125	100	0.25	95	9.5	0.45	1
Parcel 3	164.02	150	100	0.25	95	9.5	0.45	1
Parcel 4	218.70	200	100	0.25	95	9.5	0.45	1
Parcel 5	273.40	250	100	1	95	9.5	0.45	1
Parcel 6	328.11	300	100	1	95	9.5	0.45	1
Parcel 7	328.40	300	100	1	95	9.5	0.45	1

Table 4.10 - Consolidation and cyclic loading specifications of KT2.

Test ID – KT2								
Axial consolidation			Stress (kPa)		Force (N)		Duration (hours)	
1.step			25		90.8		21	
2.step			50		181.6		26	
3.step			100		363.2		25	
Axial consolidation during cyclic testing?					Yes (100 kPa)			
Cyclic parcels	Cyclic pressure (kPa)	Two-way cyclic amplitude (N)	Number of cycles	Frequency (Hz)	P-gain	I-gain	Dither amplitude	Day no.
Parcel 1	235.29	220	100	1	50	5	0.45	1
Parcel 2	235.29	220	20	1	50	5	0.45	1
Parcel 3	235.29	220	20	1	50	5	0.45	2
Parcel 4	235.29	208	20	1	50	5	0.45	2
Parcel 5	235.29	206	20	1	50	5	0.45	3
Parcel 6	235.29	206	20	1	50	5	0.45	3
Parcel 7	235.29	205	20	1	50	5	0.45	4
Parcel 8	235.29	205	20	1	50	5	0.45	4
Parcel 9	235.29	204	20	1	50	5	0.45	5
Parcel 10	235.29	204	20	1	50	5	0.45	5
Parcel 11	235.29	203	20	1	50	5	0.45	6
Parcel 12	235.29	203	20	1	50	5	0.45	6

4.4.2 Marine clay specimens

From the NGI-report (Norwegian Geotechnical Institute, 2019), the liquid limit, plasticity index, silt content, unit weight and the undrained shear strength of the marine clay are provided. The ratio of S_u/σ'_v for the marine clay is determined as 0.36. Since a fatigue analysis is to be conducted the ratio assumed is 0.3, to remain certain of not reaching the undrained shear strength when performing the cyclic tests. Table 4.11 summarises the end-target loads used in the Brazil-tests, along with assumed undrained shear strength, maximum shear stresses and cyclic shear stress. Since calculations were done to estimate the specifications, there are no differences between the studied τ_{max}, and anticipated τ_{max}, estimated from the S_u/σ'_v-ratio.

Table 4.11 – Targeted consolidation load, estimated undrained shear strengths, maximum shear stresses and cyclic shear stresses used for the two marine clay specimens.

Test ID	End-target σ'_c [kPa]	Assumed S_u [kPa]	τ_{max} [kPa]	Target p_{cy} [kPa]
Brazil_1	80	24	19.2	230.40
Brazil_2	100	30	24	291.37

4.4.2.1 Brazil_1

The purpose of this test was to replicate the same specifications and setup as those in KT2, to compare the effects on marine clay and kaolin clay. Test specifications are found in Table 4.12.

The setup is similar to that given in KT2, however some changes were done regarding axial consolidation loading, number of cycles and testing-repetition. The consolidation loading for each step was reduced to 80% of the loading done in KT2. Ten cycles were performed on each parcel. On the first day only one cyclic parcel was performed. On day 2 and 3 two cyclic parcels were performed. Subsequently on the following days only one cyclic test was performed each day. Continuous axial consolidation was performed both during and in between cyclic testing. Cyclic amplitudes were also adjusted accordingly to the specimen's height.

4.4.2.2 Brazil_2

The specifications for Brazil_2 are in summarised in Table 4.13. The consolidation loading was increased 20% compared to that given in Brazil_1. One cyclic parcel, with ten cycles, was tested each day. The cyclic amplitudes were regulated as the sample height changed during continuous consolidation.

Table 4.12 - Consolidation and cyclic loading specifications of Brazil_1.

Test ID – Brazil_1								
Axial consolidation			Stress (kPa)		Force (N)		Duration (hours)	
1.step			20		72.6		19	
2.step			40		145.2		24	
3.step			80		290.4		72	
Axial consolidation during cyclic testing?					Yes (80 kPa)			
Cyclic parcels	Cyclic pressure (kPa)	Two-way cyclic amplitude (N)	Number of cycles	Frequency (Hz)	P-gain	I-gain	Dither amplitude	Day no.
Parcel 1	230.40	205	10	1	50	5	0.45	1
Parcel 2	230.40	204	10	1	50	5	0.45	2
Parcel 3	230.40	204	10	1	70	7	0.45	2
Parcel 4	230.40	203	10	1	95	9.5	0.45	3
Parcel 5	230.40	203	10	1	95	9.5	0.45	3
Parcel 6	230.40	202	10	1	95	9.5	0.45	4
Parcel 7	230.40	202	10	1	95	9.5	0.45	5
Parcel 8	230.40	201	10	1	95	9.5	0.45	6
Parcel 9	230.40	200	10	1	95	9.5	0.45	7
Parcel 10	230.40	200	10	1	95	9.5	0.45	8
Parcel 11	230.40	199	10	1	95	9.5	0.45	9

Table 4.13 - Consolidation and cyclic loading specifications of Brazil_2.

Test ID – Brazil_2								
Axial consolidation			Stress (kPa)		Force (N)		Duration (hours)	
1.step			25		90.8		21	
2.step			50		181.6		26	
3.step			100		363.2		25	
Axial consolidation during cyclic testing?					Yes (100 kPa)			
Cyclic parcels	Cyclic pressure (kPa)	Two-way cyclic amplitude (N)	Number of cycles	Frequency (Hz)	P-gain	I-gain	Dither amplitude	Day no.
Parcel 1	291.37	265	10	1	95	9.5	0.45	1
Parcel 2	291.37	264	10	1	95	9.5	0.45	2
Parcel 3	291.37	263	10	1	95	9.5	0.45	3
Parcel 4	291.37	262	10	1	95	9.5	0.45	4
Parcel 5	291.37	261	10	1	95	9.5	0.45	5
Parcel 6	291.37	261	10	1	95	9.5	0.45	6
Parcel 7	291.37	260	10	1	95	9.5	0.45	7
Parcel 8	291.37	260	10	1	95	9.5	0.45	8
Parcel 9	291.37	259	10	1	95	9.5	0.45	9
Parcel 10	291.37	259	10	1	95	9.5	0.45	10
Parcel 11	291.37	258	10	1	95	9.5	0.45	11
Parcel 12	291.37	258	10	1	95	9.5	0.45	12

4.5 Post-processing of the measured data

This step involves processing of the acquired raw data to collect relevant cyclic parameters, cyclic loops and consolidation data. Most of the processing was performed by using mathematical tool-software, mainly GNU Octave (version 5.2.0) and Microsoft Excel.

The raw data were reduced to extract relevant columns for both the vertical consolidation and the cyclic testing. For vertical consolidation, the displacement (mm) and forces (N) were extracted to obtain the consolidation history, including the axial strain (mm) within each cyclic parcel. The amount of axial strain was determined according to Equation 4.4, with an estimation of primary consolidation-endpoint, before secondary consolidation took place. Settlement rate of intervals was obtained by collecting the height change between two parcels, divided by the amount of time in between (Equation 4.5).

$$Axial\ strain\ [mm] = H_{start\ cycle\ 1} - H_{end\ cycle\ N} \quad (4.4)$$

$$Axial\ strain\ rate\ [mm/s] = \frac{H_{start\ \text{cycle}\ 1,parcel\ i} - H_{end\ cycle\ N,parcel\ i-1}}{t_{start\ \text{cycle}\ 1,parcel\ i} - t_{end\ cycle\ N,parcel\ i-1}} \quad (4.5)$$

The data for cyclic testing were reduced and assembled to obtain the lateral normalised displacement and cyclic pressures. For the tests KT1, KT2, Brazil_1 and Brazil_2 each cyclic parcel had to be processed individually to remove any operational set-up effects, varying for each cyclic testing. To obtain the correct normalised lateral displacement one must account for the flexural bend of the model pile (Zakeri et al., 2017). Thus, an average was taken from both left-sided and the right-sided displacement (Equation 4.6), then corrected for the elastic strain of the model pile with the measured cyclic force (F_{cyc}; Equation 4.7; Norwegian Geotechnical Institute, n.d.).

$$y_{average}\ [mm] = \frac{y_{left}\ [mm] + y_{right}\ [mm]}{2} \quad (4.6)$$

$$y\ [\%] = \frac{y_{average}[mm] - (-1.63681 * 10^{-6} * H\ [mm] + 3.7 * 10^{-4}) * F_{cyc}\ [N]}{10} * 100 \quad (4.7)$$

The processed cyclic data was prepared for the DLP-script, generated by NGI. This script calculates the stress-strain relationship for each point in a cycle during testing. Hence, cyclic loops for each parcel is graphed, which can further be studied for their corresponding cyclic parameters. The parameters include secant stiffness, damping, average- and cyclic shear strain of each curve. The secant stiffness of a cycle (G) is based upon Equation 4.8, whereas the relative secant stiffness of a cycle is calculated as the secant stiffness of the current cycle (G_n), divided by the first secant stiffness of the first cycle (G_1) in the parcel (Equation 4.9). The average shear strain and cyclic shear strain are calculated according to Equations 4.10 and 4.11, respectively. Equations 4.8-11 is based upon the presented frameworks of Andersen (2009,

2015). The soil damping is based on the area of current hysteretic loop (Δw) divided by the area of the right-angled triangle (Ψ), in which the secant stiffness (G) makes up the hypotenuse and ends in origin (Equation 4.12; Richart and Wylie, 1977).

$$G\ [MPa] = \frac{\frac{\tau_{cyc\ max} - \tau_{cyc\ min}}{1000}}{\frac{\gamma_{cyc\ max} - \gamma_{cyc\ min}}{100}} \tag{4.8}$$

$$Relative\ secant\ stiffness = \frac{G_n}{G_1} \tag{4.9}$$

$$\gamma_{average}[\%] = \frac{\gamma_{cyc\ max} + \gamma_{cyc\ min}}{2} \tag{4.10}$$

$$\gamma_{cyc}\ [\%] = \frac{\gamma_{cyc\ max} - \gamma_{cyc\ min}}{2} \tag{4.11}$$

$$Damping\ [\%] = \frac{\Delta w}{\Psi} \tag{4.12}$$

The water content measurements after drying the sliced specimens are calculated according to Equation 4.13.

$$Water\ content\ [\%] = \frac{m_{wet}\ [g] - m_{dry}\ [g]}{m_{wet}\ [g]} * 100 \tag{4.13}$$

Chapter 5

Results

5.1 Results of the kaolin-based samples

The cyclic results of the kaolin-based tests are given in Appendix A. A selection of representative figures is presented in this chapter. Results of the consolidation of each specimen are found in Appendix B. Four kaolin-based tests were tested for their cyclic behavior. DT1, DT2, KT1 and KT2 were all load-controlled. DT2, KT1 and KT2 were executed fully, whereas DT1 was only performed halfway. All tests were tested with zero average load, i.e. constant average load. Appendix C includes photographs of the samples after cyclic testing was completed. This appendix however does not include the tests DT1 and DT2. Measurements of water content and material loss of each sample is included in Appendix D.

In all kaolin samples, the texture of the clay was observed to have altered from a semi-soft texture before loading, to a firmer texture in post-experiment.

5.1.1 DT1

5.1.1.1 Consolidation results

The consolidation results of DT1 are enclosed in Appendix B1. The sample decreased from its original length of 101 mm to approximately 95 mm before cyclic testing.

5.1.1.2 Cyclic results

Originally, this specimen was to be treated with five parcels, with increasing load-parcel up to parcel 5, where it would decrease back to a lower pressure. Vertical consolidation during cyclic testing was not performed. As failure of the sample occurred during cyclic parcel 4, only the results of the first three parcels will be presented. All test-results of DT1 are enclosed in Appendix A1.

The secant stiffness-development of DT1 is found in Figure 5.1. For each load parcel applied, the stiffness is observed to decrease, with the rate increasing for each increasing load step. Most evident for parcel 2 and 3 is the notion that the rate of reduction of secant stiffness is greatest at the beginning, and further decreases to become constant with time. For parcel 1 this trend is not that evident, but it is observed overall to have a linear rate of decreasing stiffness.

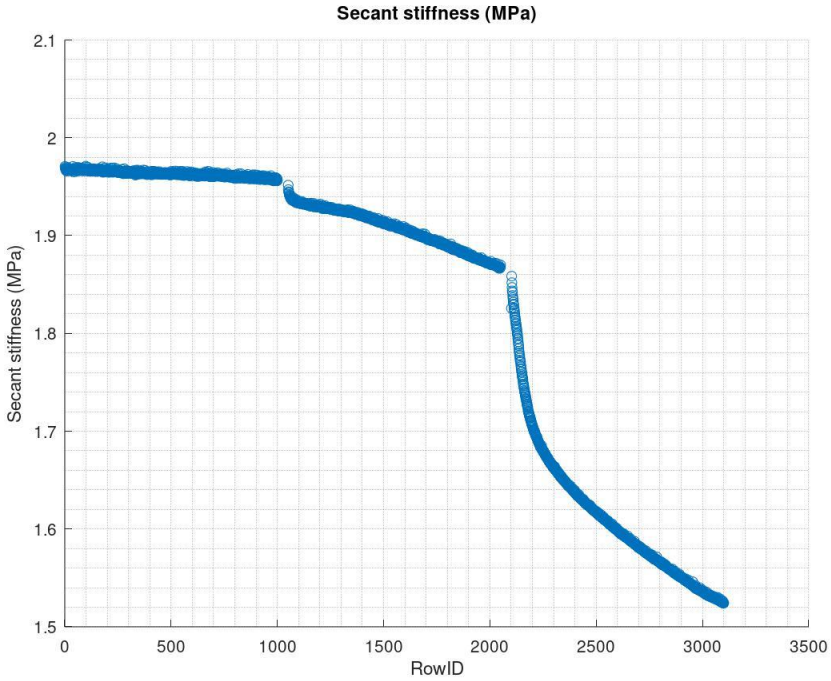

Figure 5.1 - Secant stiffness development of DT1.

5.1.2 DT2

5.1.2.1 Consolidation results

Consolidation results for this test is enclosed in Appendix B2. The pre-cyclic consolidation resulted in height-reduction from 101 mm to 94,2 mm.

5.1.2.2 Cyclic results

The results of DT2 are given in Appendix A2. The main purpose of this test was to replicate the specs given for DT1. No vertical consolidation was implemented during testing.

Figure 5.2 represents the normalised displacement and cyclic pressures during cyclic loading. Erroneous sampling rate was set during the first two loading steps, hence low resolution of these. It is generally observed that the amount of normalised displacement is overall proportional to the cyclic stresses. From the second parcel to the third parcel the displacement

goes from about 0,25% to 0,8%. From here it steadily increases to approximately 0,9%, where it remains stationary during this cyclic parcel. During fourth parcel, with the largest applied cyclic stresses, the displacement is observed to shift from an overall positive direction toward a negative direction. Hence, the cyclic average displacement develops a negative trend. However, the relationship between maximum- and minimum peaks remain constant. In the transition from fourth parcel to fifth parcel an offset is developed, which remains permanent during the final testing.

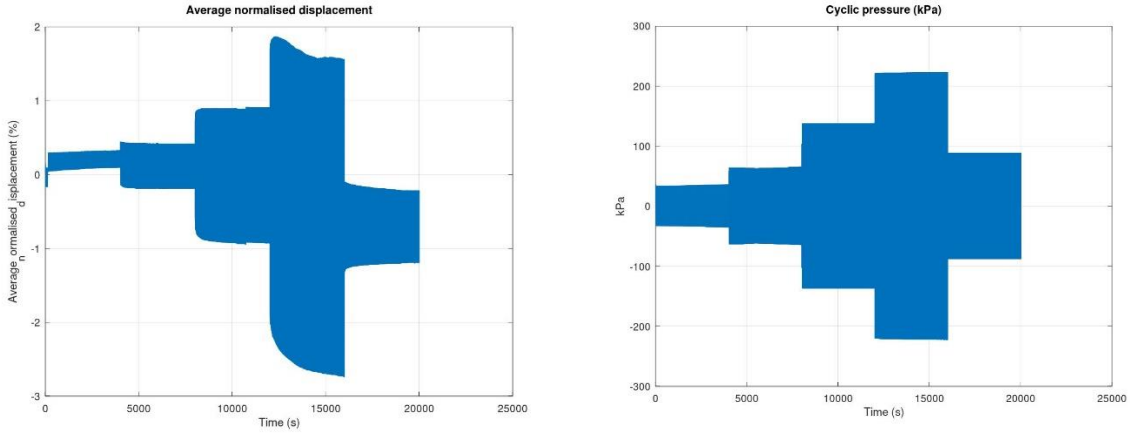

Figure 5.2 - Cyclic displacement and -loads of DT2. Left: Normalised displacement; right: Cyclic pressure.

Figure 5.3 shows the cyclic loops of the cyclic testing of DT2. Parcel 1 and 2 show erroneous curves due to the low sampling rates. It is generally observed for each increasing load parcel the elongation of the curves increases proportionally. In parcel 3 (see Appendix A2) the final cycle is rotated clockwise and slightly elevated in vertical axis, compared to the parcel's first cycle. Likewise, for parcel 4, but with some offset-drifting toward left on the P-Y plot. For parcel 5 (see Appendix A2) however the observation is the opposite; final curve is rotated counter-clockwise relative to initial curve.

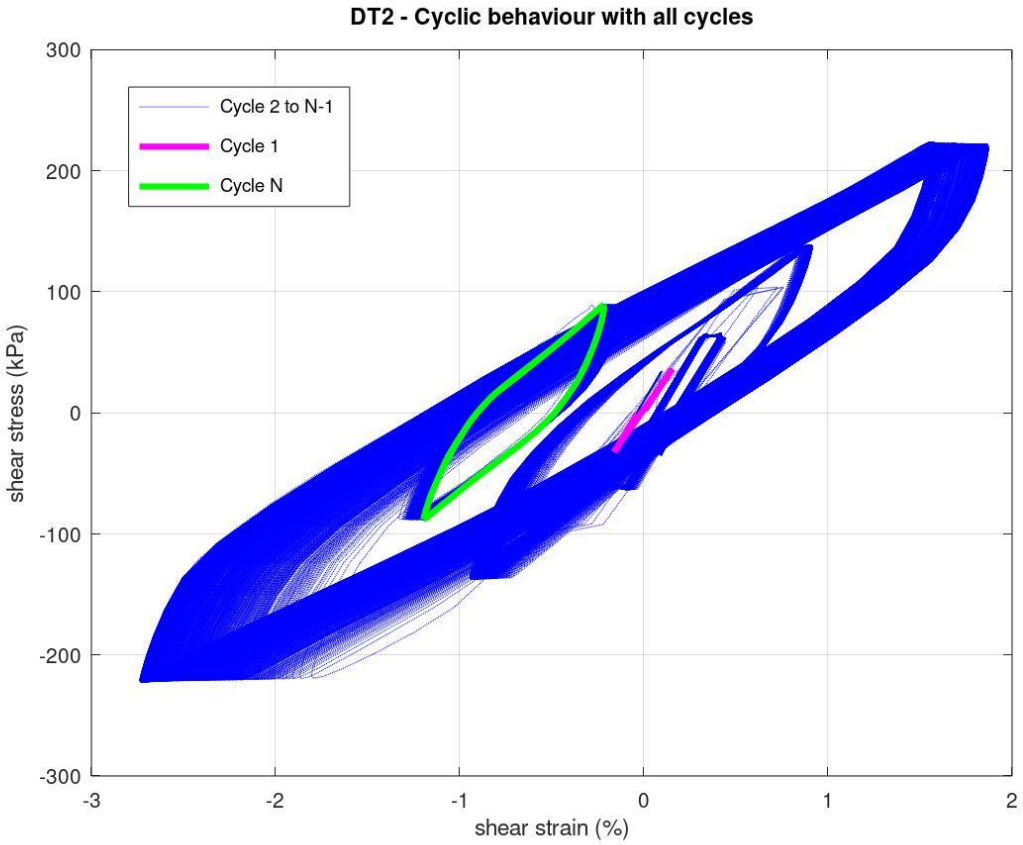

Figure 5.3 - Resulting cyclic loops of the DT2, including the first and last cycles.

Figure 5.4 illustrates the secant stiffness-evolution during the cyclic testing of DT2. Except for parcel 1 and 5, the stiffness is observed to decrease over time, in relation to amount of normalised displacement and cyclic shear stresses. At the onset of parcel 2, 3, and 4 the stiffness decreases exponentially into a stable horizontal trend. Parcel 1 and 5 display the opposite manner, with steadily increase in stiffness during testing.

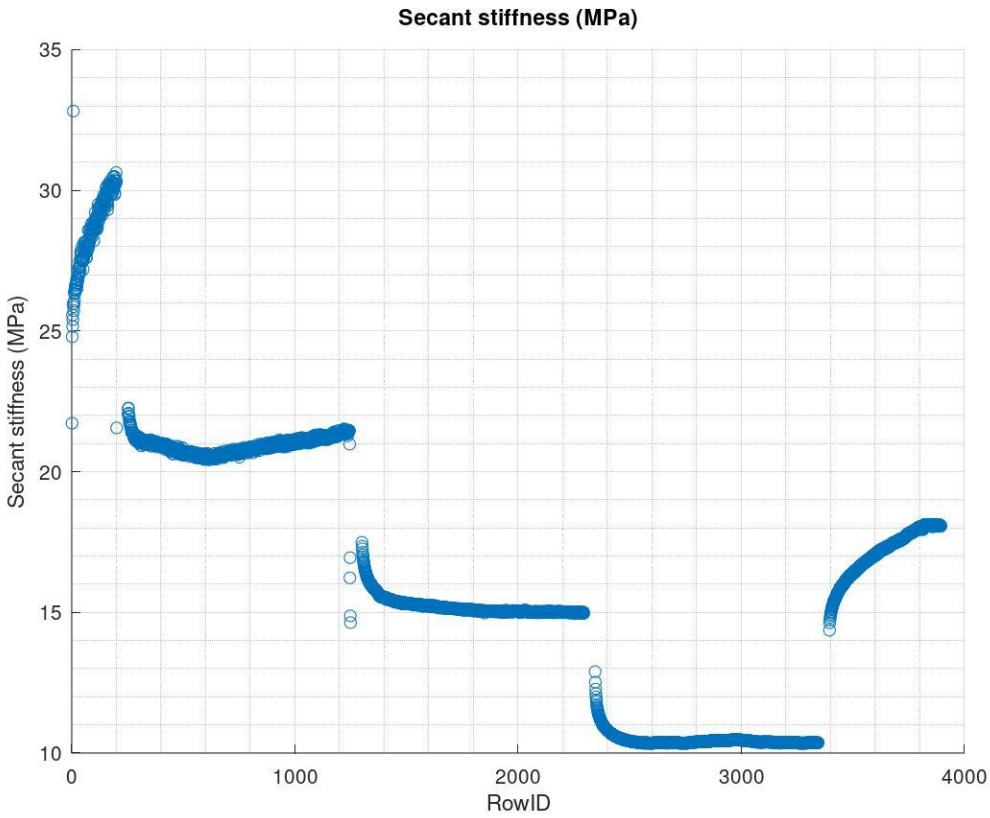

Figure 5.4 - Secant stiffness development of DT2.

5.1.3 KT1

5.1.3.1 Consolidation results

Appendix B3 contains the consolidation results for KT1, along with the axial strain rates. The sample's height decreased from its initial 101 mm to 91,5 mm, before cyclic testing.

5.1.3.2 Cyclic results

The test results of KT1 are given in Appendix A3. The test was performed with seven cyclic packages with intervening periods of continuous consolidation. Between the last five cyclic packages the consolidation period was decreased. Faulty results are encountered in the last two parcels, hence only the first five test-parcels are considered adequate.

Figure 5.5 illustrates the resulting normalised cyclic displacement, along with the cyclic pressures measured in KT1. The magnitude of the normalized displacements is expectedly proportional to the cyclic pressures. For the fifth package the resolution remained low after

consolidation, hence data were not sufficiently collected for this package. It is overall seen a widening tendency, with increased displacement at the end of each cyclic packages. The explanation for the one-sided cyclic behaviour at the beginning of parcel 1 is due to constrained model pile-movement, which was quickly sorted during performance. Consulting the test in Appendix A3, for the sixth parcel, abnormal displacement amounts are observed at the end of the testing. This package starts off with a widening within the sample for each cycle completed, until mid-testing where it eventually escalades. On the contrary, the cyclic pressure is seen to drop during this stage. In the seventh package this becomes more evident with irregular cyclic development. Large, fluctuating cyclic displacement occurs, until it reaches the displacement-limit of the apparatus. At this stage the sample failed, and testing was abruptly shut down.

Figure 5.6 shows the resulting cyclic loops of the KT1's cyclic testing. All parcels indicate an increase of cyclic displacement over time, with increased elongation of the curves. Considering the individual parcels (see parcel-details in Appendix A3) all final cycles show a clockwise rotation from the original position. The difference in resulting normalised displacement from the first cycle and the final cycle increases for each increasing load parcel. The "boomerang"-shaped curves in the beginning of parcel 1 is related to the erroneous constraint registered at the start of cyclic testing.

The secant stiffness-development of KT1 is presented in Figure 5.7. It is overall observed to lower during the duration of the test, by stepping down for each parcel performed. Each individual parcel displays an L-shape, where the stiffness is greatest at the very beginning and gradually lowers and flattens over time. The first part of parcel 1 displays the exception and is related to the constrained lateral movement of the pile. Regarding the damping-rate (Figure 5.8), it is trending to lower slightly over the duration of the experiment. Studying each parcel reveals a slight increase at the very end.

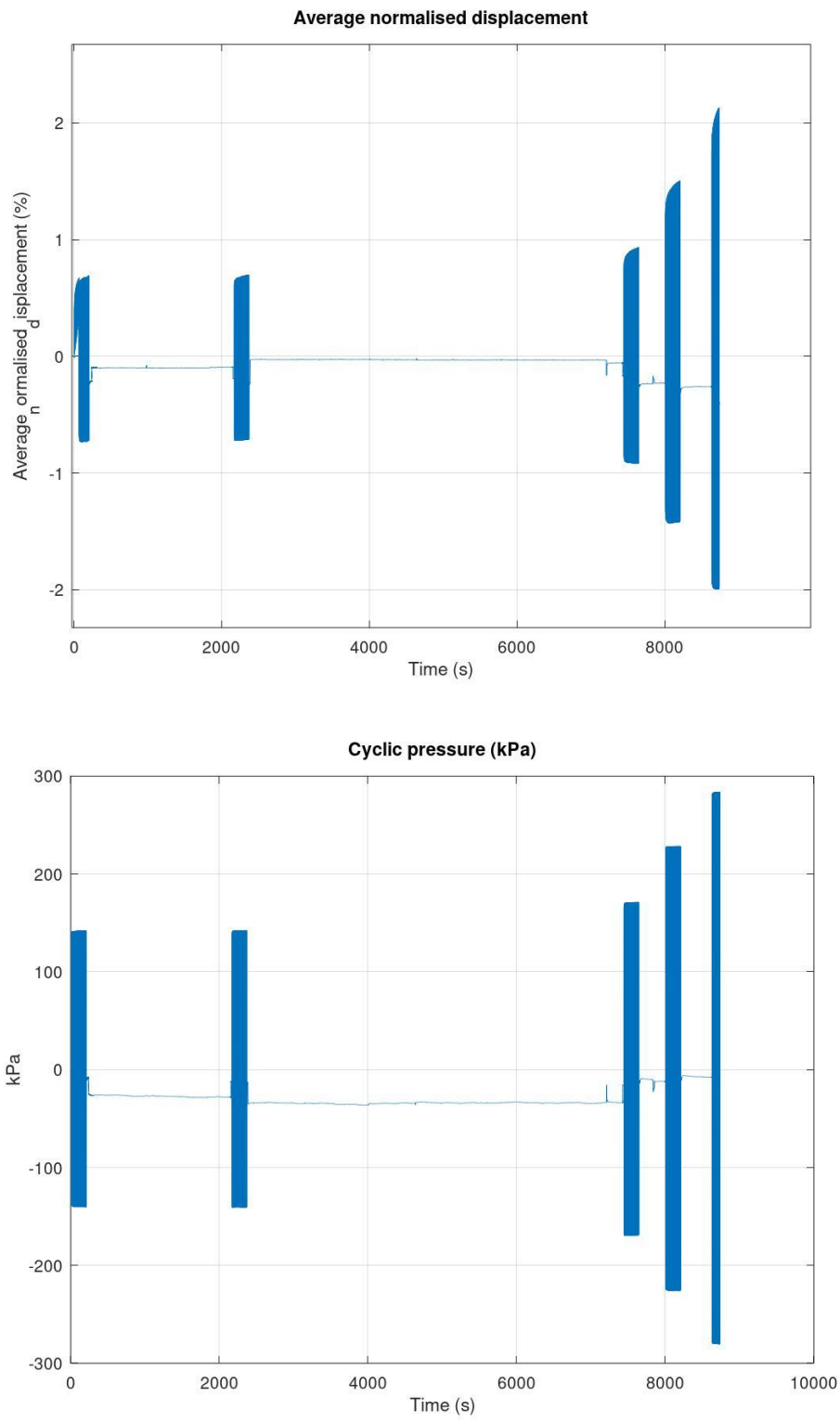

Figure 5.5 - Cyclic displacement and -loads of KT1. Above: Normalised displacement; below: Cyclic pressure.

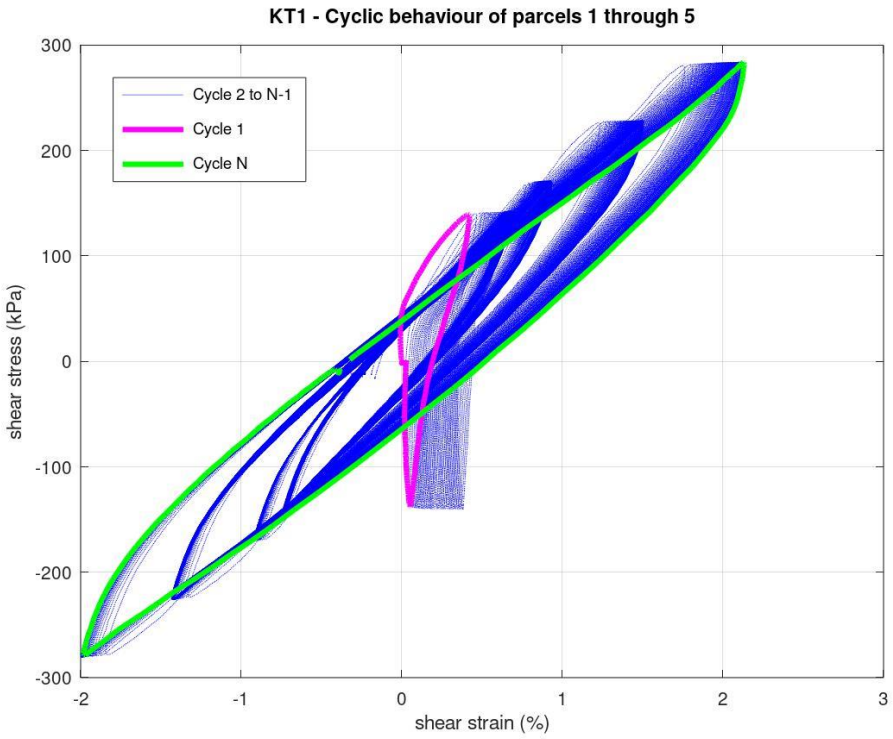

Figure 5.6 - Resulting cyclic loops of the KT1, including the first and last cycles. Only the first five parcels are considered.

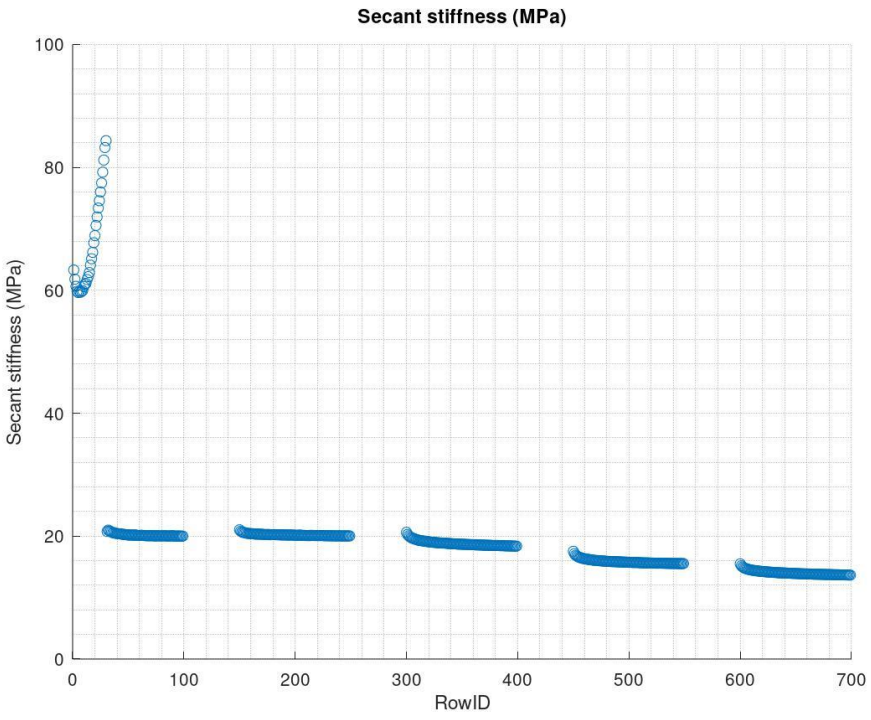

Figure 5.7 - Secant stiffness development of KT1.

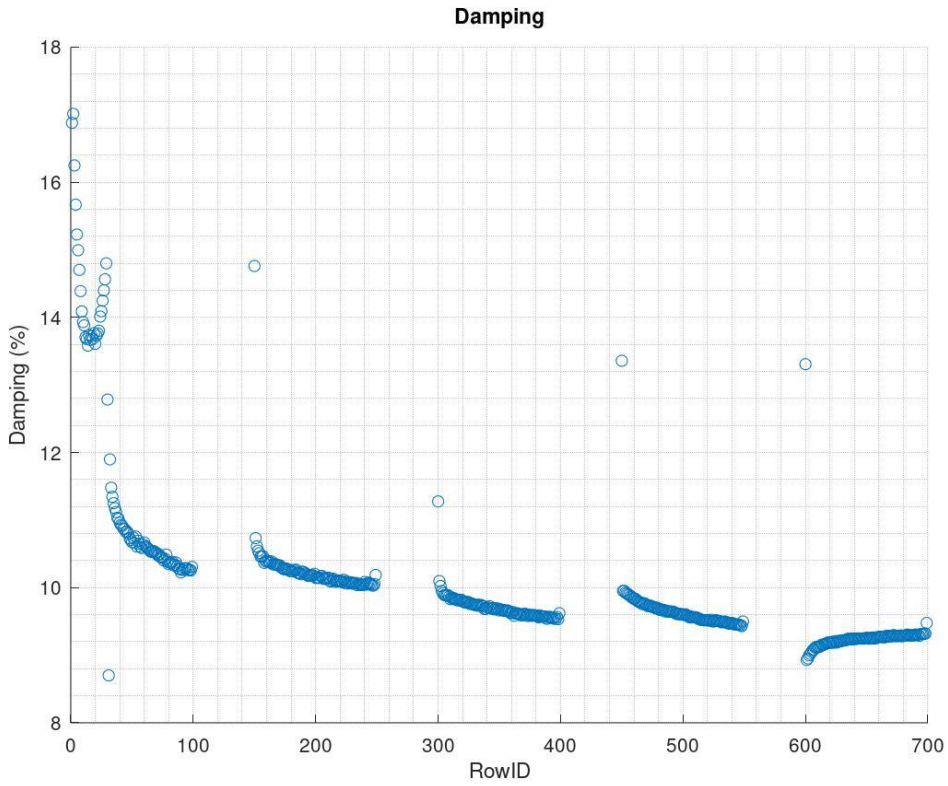

Figure 5.8 - Development of damping in KT1.

5.1.4 KT2

5.1.4.1 Consolidation results

The consolidation results, along with axial strain rates, of KT2 are enclosed in Appendix B4. The total consolidation of the sample, before cyclic testing, went from its original height of 101 mm to 93,5 mm. Consolidation droop is observed between parcel 1 to parcel 11. From parcels 11 and 12 the consolidation was regulated again to appropriate level.

Figure 5.9 displays the axial strain within each cyclic parcel. The first parcel shows the highest amount of axial strain during the experiment, and following parcels are rather small in comparisons, except for parcels 5 and 6. Here the fifth parcel sharply rises, with the subsequent parcel also showing a rather high axial strain, but lesser than the preceding.

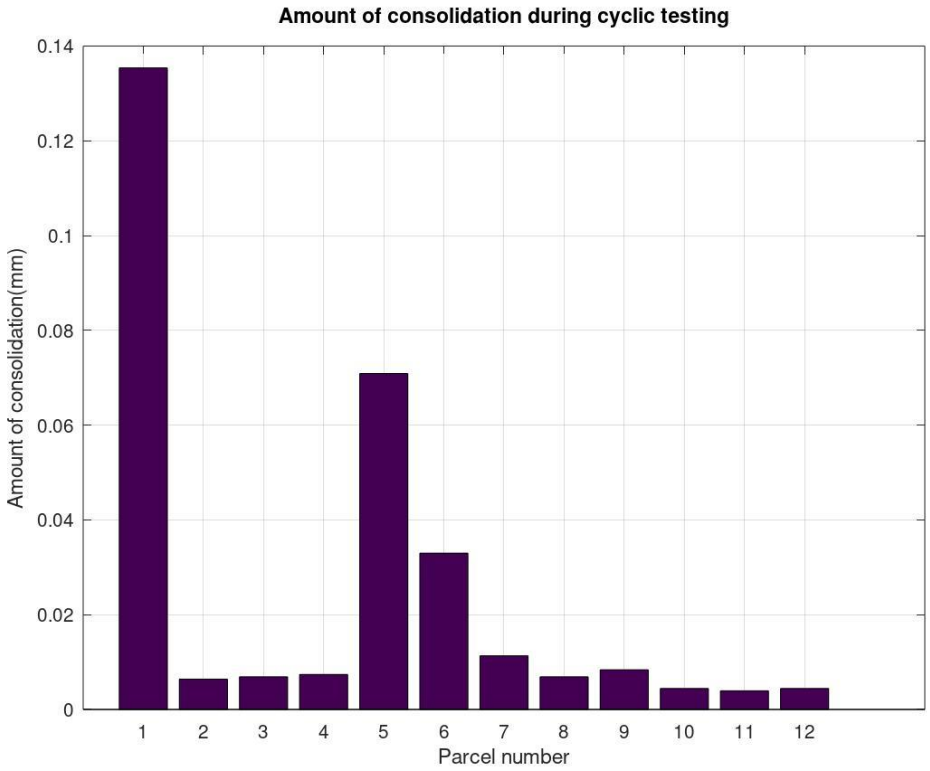

Figure 5.9 - Bar plot showing the amount of consolidation-axial strain within each cyclic parcel of KT2.

5.1.4.2 Cyclic results

Results for the twelve test-parcels of KT2 can be found in Appendix A4. Except for the first three cyclic parcels (1-3), twenty cycles were conducted in each parcel. In the first parcel only sixty-seven out of pre-set hundred cycles were performed. For the second parcel six out of twenty cycles were completed, whereas fourteen cycles out of twenty cycles were carried out in parcel 3. The sample was vertically consolidated during cyclic performance. For both parcel 1 and 2 the termination was related to software interlock, as the displacement toppled the set limit of the apparatus. Appendix C1 includes photos of the sliced sample after cyclic testing. A notable oval-shaped disturbance zone is evident in all slices near the pile, with the longest elongation perpendicular to the direction of the external lateral movements.

A selection of parcels (1, 3, 9 and 12) is presented in Figure 5.10, along with their measured normalized displacements and cyclic pressures. For parcel 1 it is evident that the cyclic development increases over time, with lateral expansion occurring immediately and continues to expand. The opposite is observed in the corresponding pressure-diagram, where the pressure

drops linearly at about same time as the displacement begins to escalate. For parcel 3 the relationship between maximum- and minimum displacement-peaks gradually increases over time; going from 3,25% at the beginning to 3,62% at the end. The corresponding cyclic pressure is overall constant. For parcels 9 and 12 the displacements are observed to increase and widen in the sample. The cyclic pressures in both parcels remain constant throughout testing.

Calculated secant stiffnesses are presented in Figure 5.11. They are observed to decrease over the course of testing. As two tests were coupled per day, it is registered that the second testing on a day displays lower secant stiffness, compared to the previous test on the same day. The damping is presented in Figure 5.12. It is noted that in the two first parcels and the two last parcels the damping differs from the relative constant parcels during mid-testing. First parcel shows increasing damping-rates, whereas in second parcel it starts to lower. The following parcels, 3 and 4, remain similar, at about 10% damping-rate. The rate then increases and remains stationary at about 14-15% in the succeeding parcels. For parcel 10 the damping-rate increases and then drops again in the last parcel. Except for parcels 1 and 11, all parcels show a decreasing rate of damping, with the lowest rate during mid-testing. These parcels however indicate a slight increase in damping at the very end. Parcel 1 displays a build-up in damping. Parcel 11 however shows a high increase in the beginning and then develops lower damping-rate toward the end.

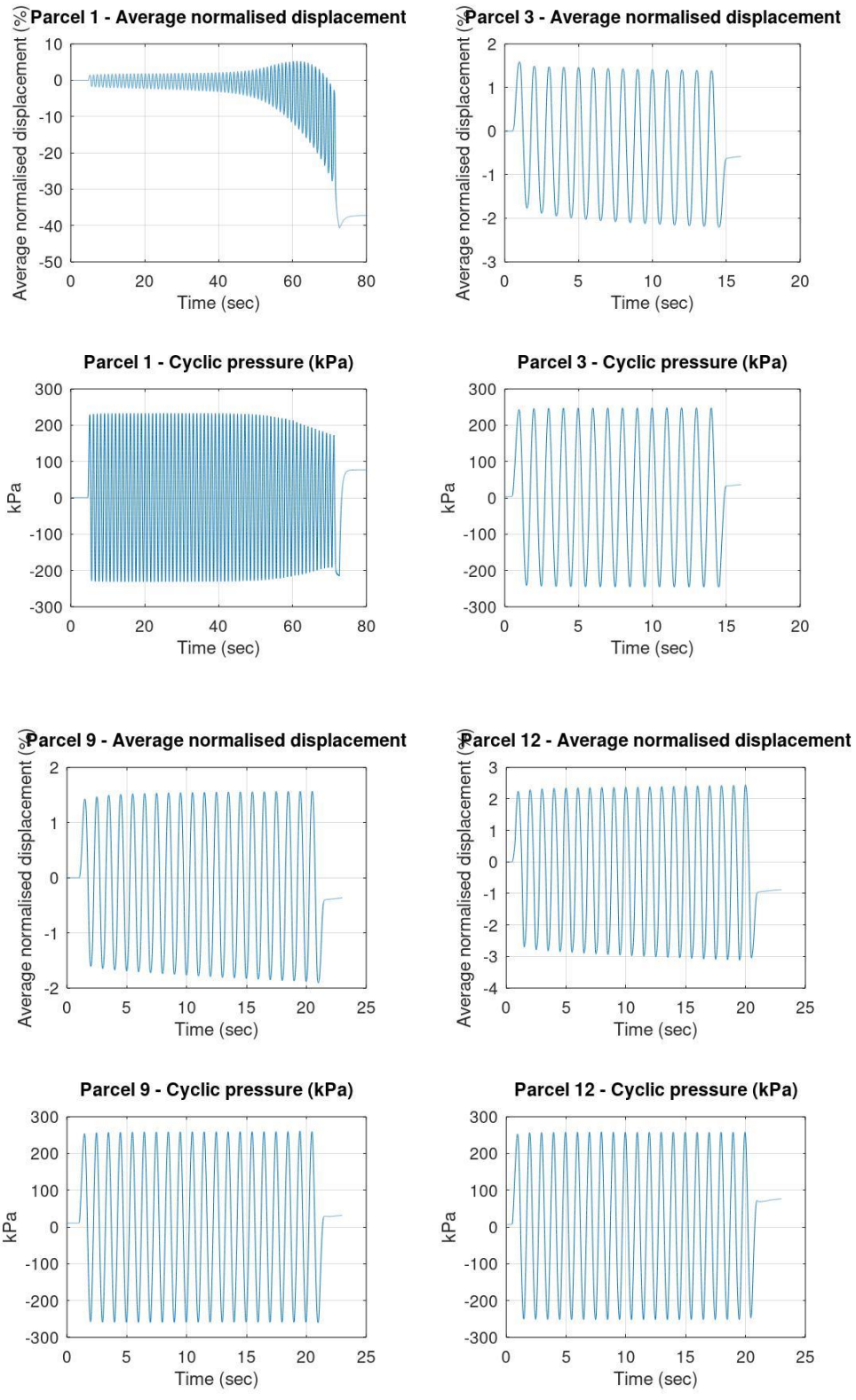

Figure 5.10 - Cyclic displacement and -pressures for selected parcels of KT2.

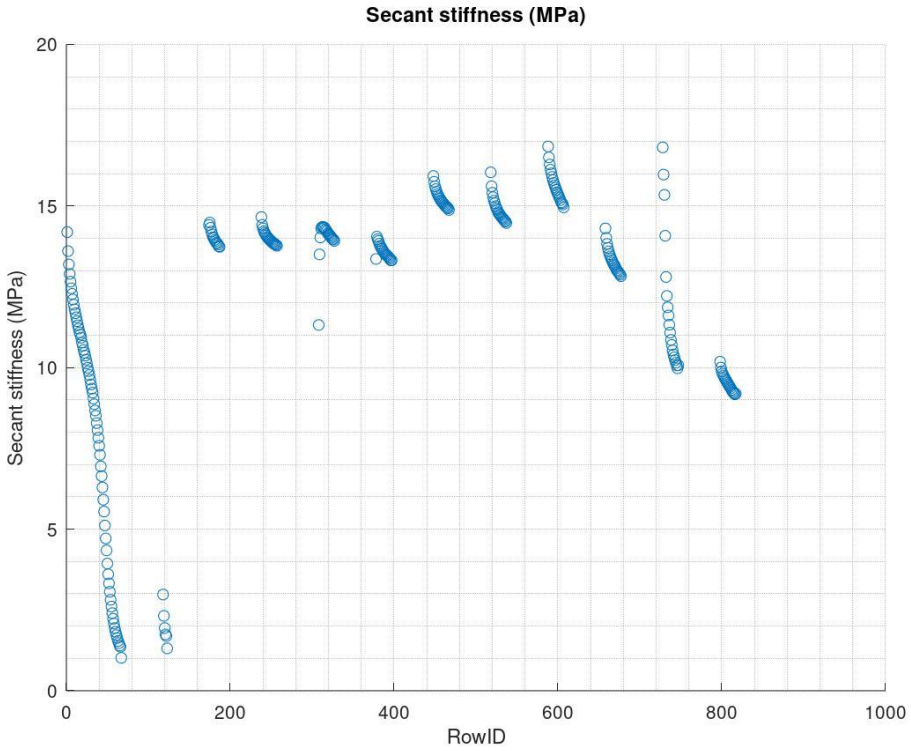

Figure 5.11 - Secant stiffness development of KT2.

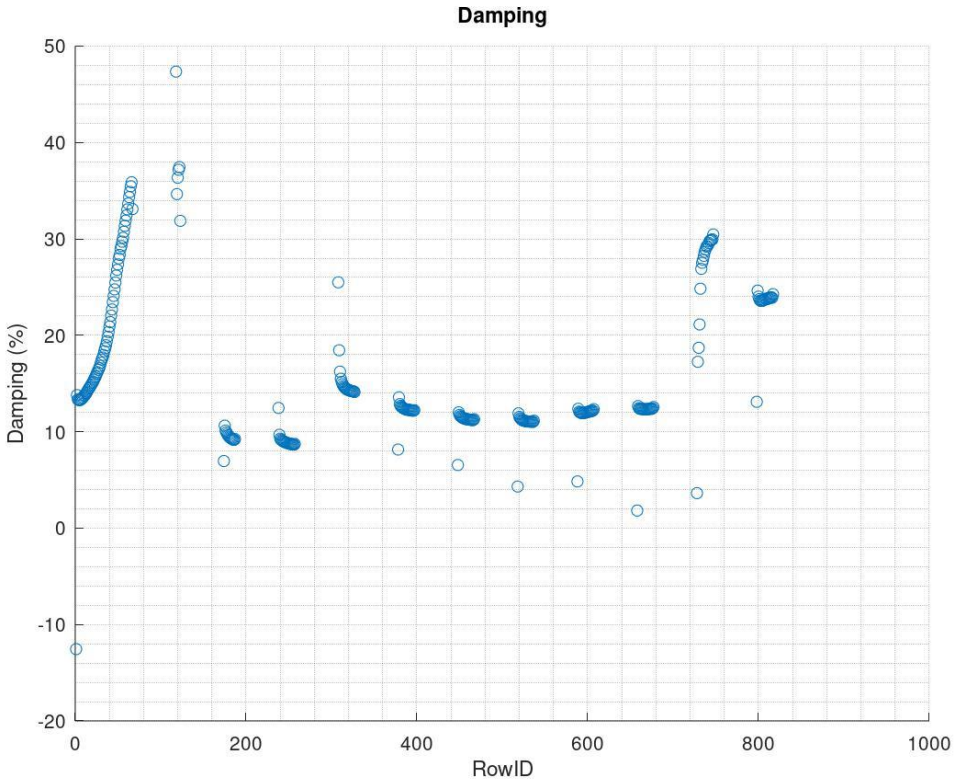

Figure 5.12 - Development of damping in KT2.

5.1.5 Calculated parameters of kaolin-based tests

Table 5.1 includes measurements and calculations of shear stress and its ratio relative to vertical consolidation stress for KT1 and KT2. The first column considers the obtain maximum shear stress (τ_{max}) from the cyclic loops, whereas the second column is based on the Skempton-relation (see Equation 2.6). As the Skempton-relation only relies on the material property, this ratio is the same in both tests.

Table 5.1 – Measured and calculated aspects of shear stress of kaolin-based samples.

Test ID	**Measured τ_{max} from cyclic loops**	**S_u/σ_c; based on Skempton-relation (Equation 2.6)**
KT1	280	0,22
KT2	260	0,22

5.2 Results of the marine clay-based samples

The results from the marine clay samples are presented in Appendix A. Two specimens from the Brazilian offshore were studied for cyclic development. All cyclic tests were done in combination with vertical consolidation. Appendix C2 shows pictures of the sliced sample, along with the direction of external lateral movements. No obvious disturbance-zone was evident near the pile, except within the right-sliced specimen; a faint oval-shaped was noted. The texture of the marine clay was observed to have gone from having a semi-soft texture, before loading, to become firmer after complete cyclic loading experiment.

5.2.1 Brazil_1

5.2.1.1 Consolidation results

The consolidation results of Brazil_1, along with axial strain rates, are in Appendix B5. The sample's initial height (100 mm) was compressed to a final height of 89.2 mm, before cyclic testing.

Figure 5.13 illustrates the amount of vertical consolidation occurring within each cyclic parcel of Brazil_1. Parcel 1 has the largest axial strain of all parcels. The succeeding parcel is almost halved. From here the overall axial strain decreases for each passing parcel. Two notable exceptions apply for parcel 3 and 5, as they both show a heavier reduction of axial strain during cyclic loading, compared to their preceding parcel.

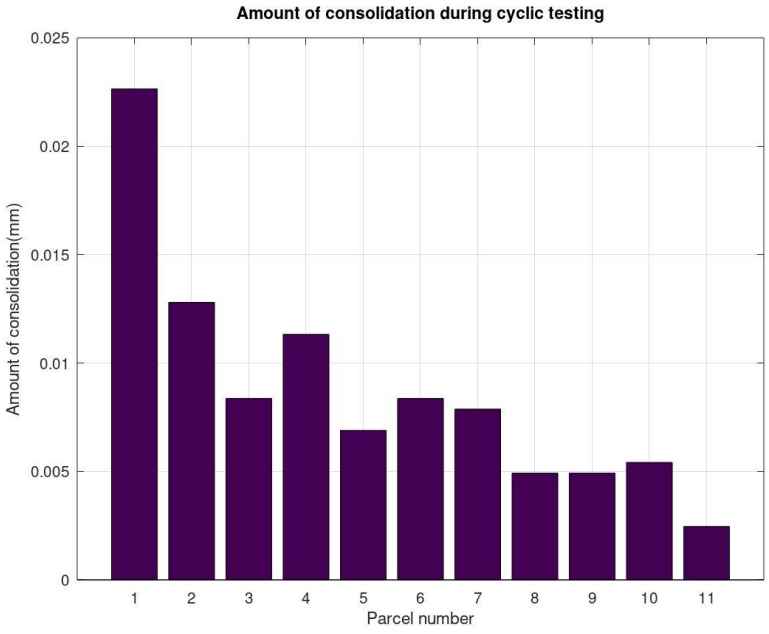

Figure 5.13 – Bar plot showing the amount of consolidation-axial strain within each cyclic parcel of Brazil_1.

5.2.1.2 Cyclic results

Test results of Brazil_1 can be found in Appendix A5. Eleven cyclic parcels were performed, conjoined with vertical consolidation. Pictures of the sliced sample are assembled in Appendix C3, along with the direction of external lateral movements. Only in the right-sliced piece of the sample was it observed a faint, disturbed zone near the pile.

Parcels 1, 4, 7, and 11 are presented in Figure 5.14. In general, all parcels show a tendency of widening of the specimen, as observed from the normalized displacement. The largest displacements are seen to be more drifting toward the negative direction. Parcel 1 starts the test with a linear development of displacement throughout the experiment. Parcel 4, out of all parcels, has the largest widening occurring, with the highest displacement-rate at the beginning and decreases somewhat during the duration. The last cycle develops a total widened

displacement of 6%. In both parcels 7 and 11, the displacement-rates are lowered, especially around midway during testing. Parcel 11 shows the least amount of displacement taking place within the specimen. Regarding the cyclic pressures, all parcels are seen to remain constant and symmetric. Pressure peaks of parcel 1 are lower compared to the other parcels (about 230 kPa for parcel 1, versus 250 kPa for the other parcels).

Figure 5.15 shows the resulting cyclic loops from cyclic testing of Brazil_1. It is observed that for each cyclic iteration the elongation increases, and curves rotate clockwise throughout parcels 1 to 5. From here the rotation shifts to the opposite direction up until parcel 10. During parcel 10 and 11 the initial cycles remain similar, but the final cycle of parcel 10 is slightly more tilted compared to the final cycle of the last parcel (see further details in Appendix A5). The overall response of the cyclic testing show that the specimen has developed increasing cyclic displacement over time, with elongated cyclic loops. At a later stage however, the elongation decreases overall. It must be noted that the maximum and minimum shear stresses observed between parcels 3 to 11 is somewhat higher than the targeted cyclic pressure used prior to testing. The cause of this is not known.

The secant stiffness-development of the eleven parcels of the marine clay sample is given in Figure 5.16. For each parcel the stiffness decreases over the duration of each testing, with the rate of stiffness-degradation decreasing as well. For parcels 3-11 the difference between initial stiffness and end-stiffness is about 2 MPa. The first two parcels illustrate a high initial stiffness. In parcel 3 the stiffness drops significantly, and in parcels onward the stiffness gradually increases over time. From parcel 9 to the end the secant stiffness is observed to become stabilized. Studying the damping-rate of the specimen (Figure 5.17) it is evident that the parameter overall decreases. The damping-rate drops from approximately 16% at its maximum in parcel 1, down to about 9% in parcel 12. In each parcel the damping-rate increases for each cyclicity. But the amount of change in damping-rate between the first and last cycles lowers with each testing.

5.2.2 Brazil_2

5.2.2.1 Consolidation results

All consolidation results, along with axial strain rates, are found in Appendix B6. The total consolidation of the sample, before cyclic testing, went from its original height of 100 mm to 90,9 mm.

Figure 5.18 displays the amount of axial strain occurring within each cyclic parcel of Brazil_2. The largest axial strain is found in parcel 1, and onward it decreases gradually over the course of the experiment. The amount of reduction between each parcel also is seen to diminish. Parcel 8 however indicates a local peak in the bar plot, whereas parcel 11 shows a local minimum, hence deviating from the overall gradual reduction and flattening. Figure 5.19 illustrates the vertical consolidation behaviour of parcel 1 and parcel 12. It is noteworthy that a prominent, oscillating curve is observed at parcel 1, but becomes more distorted in parcel 12. Additionally, the amount of consolidation has drastically lowered in latter parcel, compared to the former.

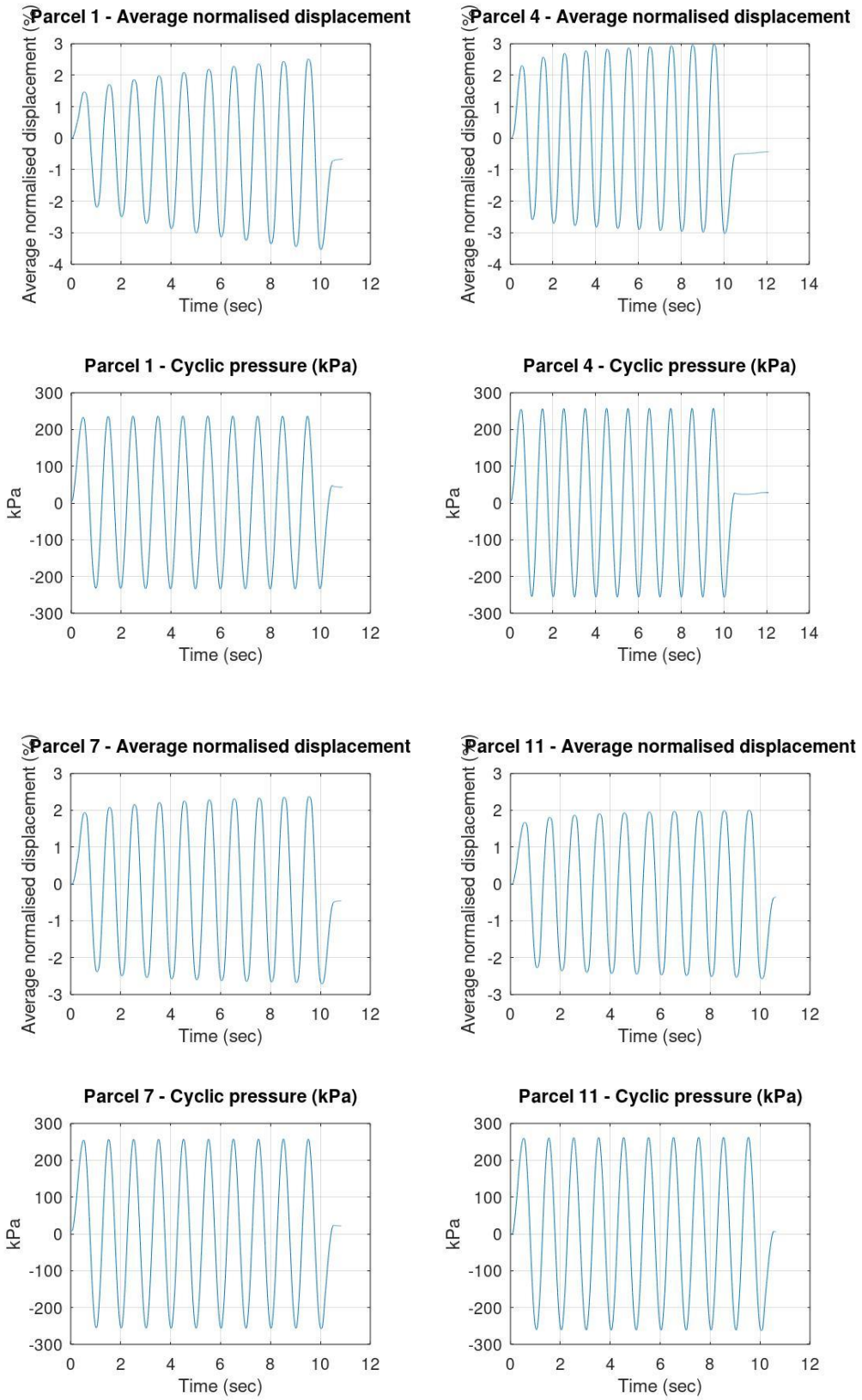

Figure 5.14 - Cyclic displacement and -pressures for selected parcels of Brazil_1.

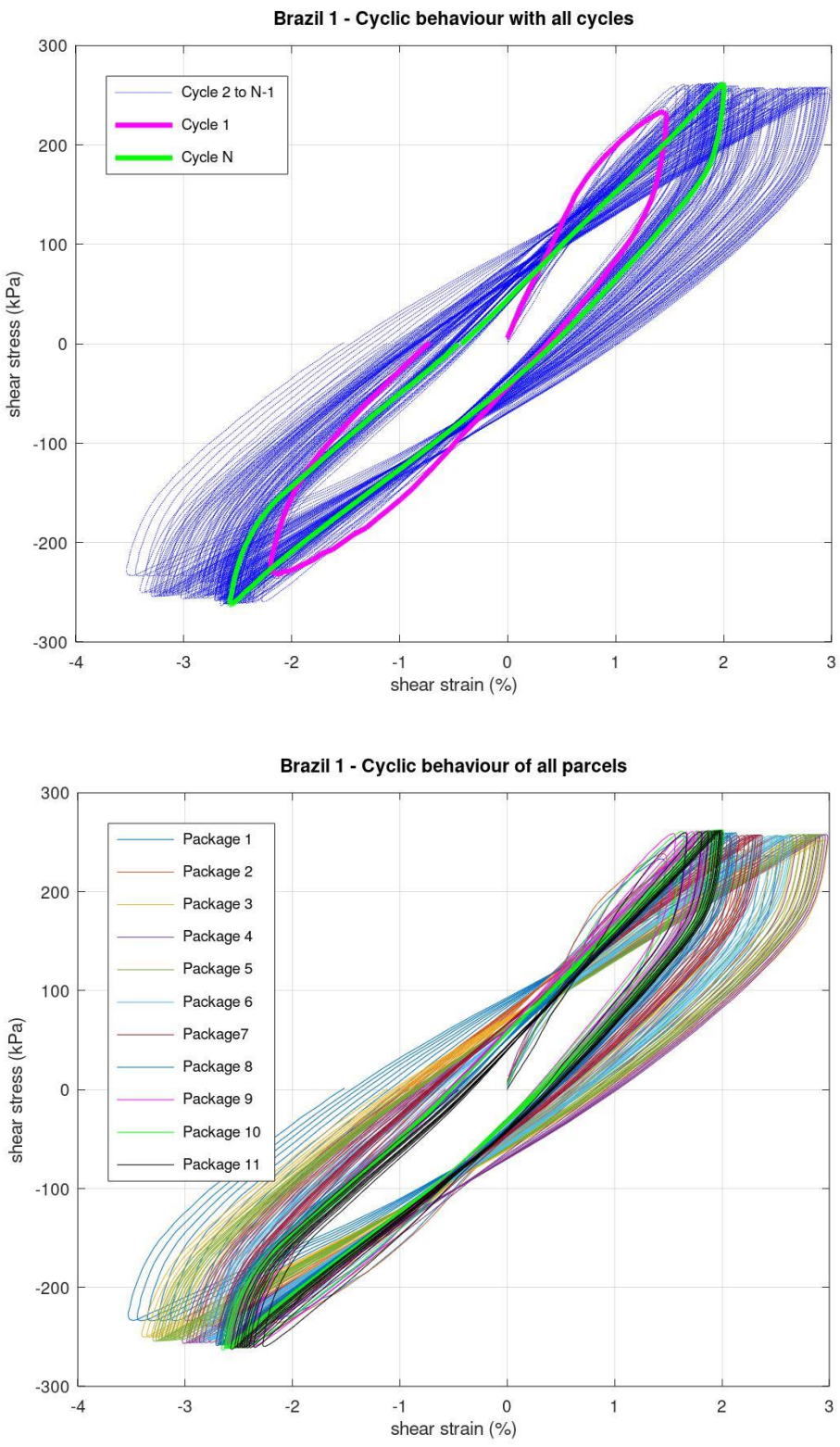

Figure 5.15 - Resulting cyclic loops of the Brazil_1. Above: Complete cyclic history; below: all parcels highlighted.

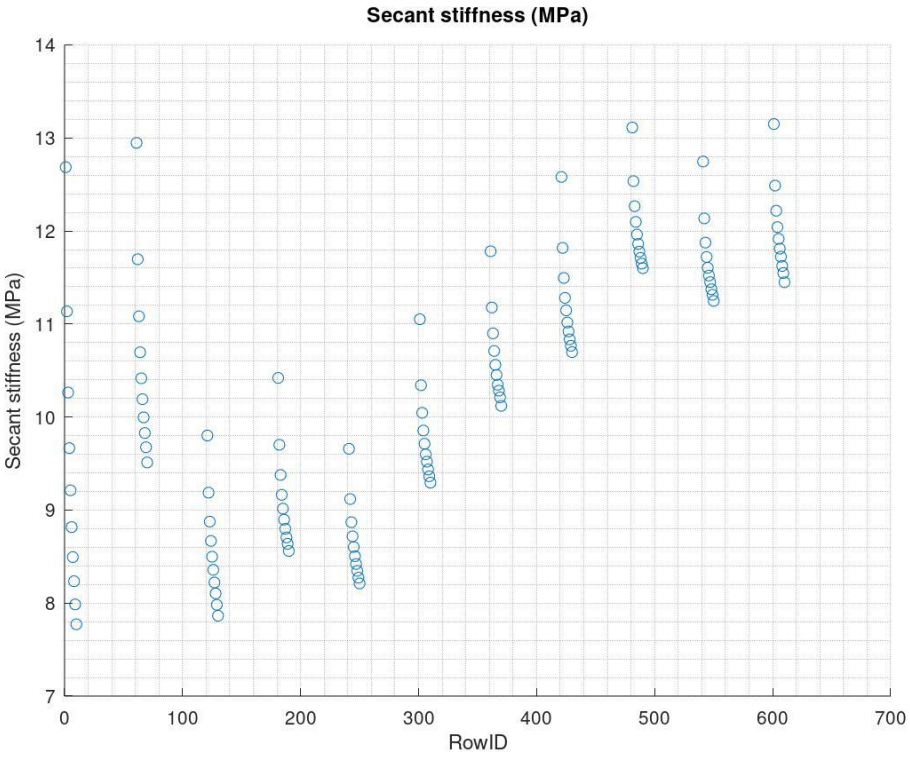

Figure 5.16 - Secant stiffness development of Brazil_1.

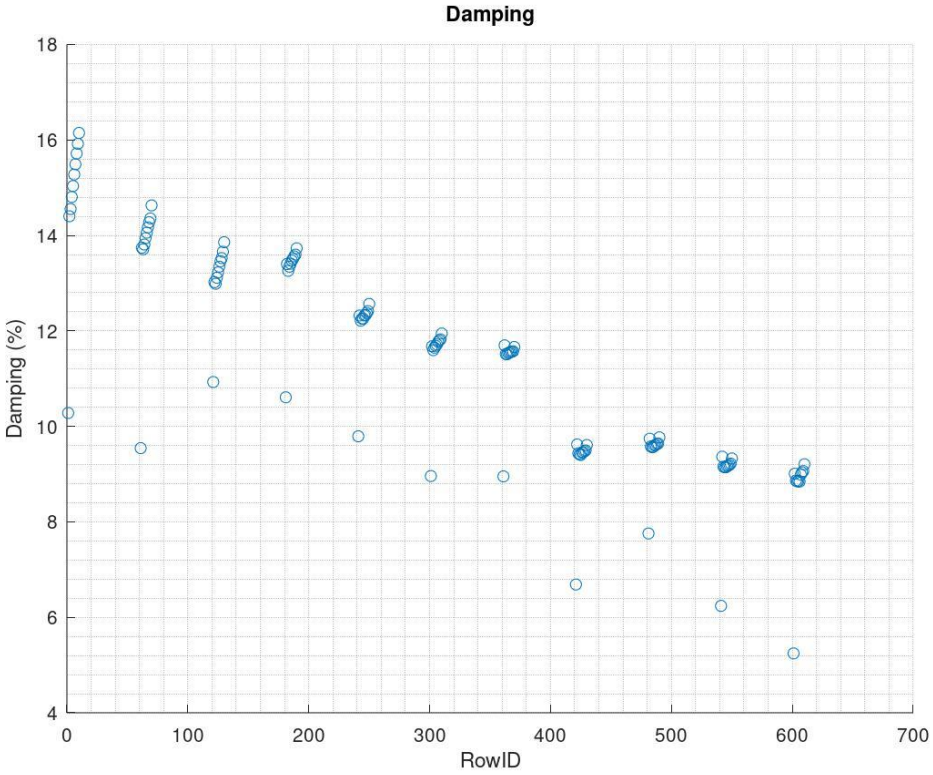

Figure 5.17 – Development of damping in Brazil_1.

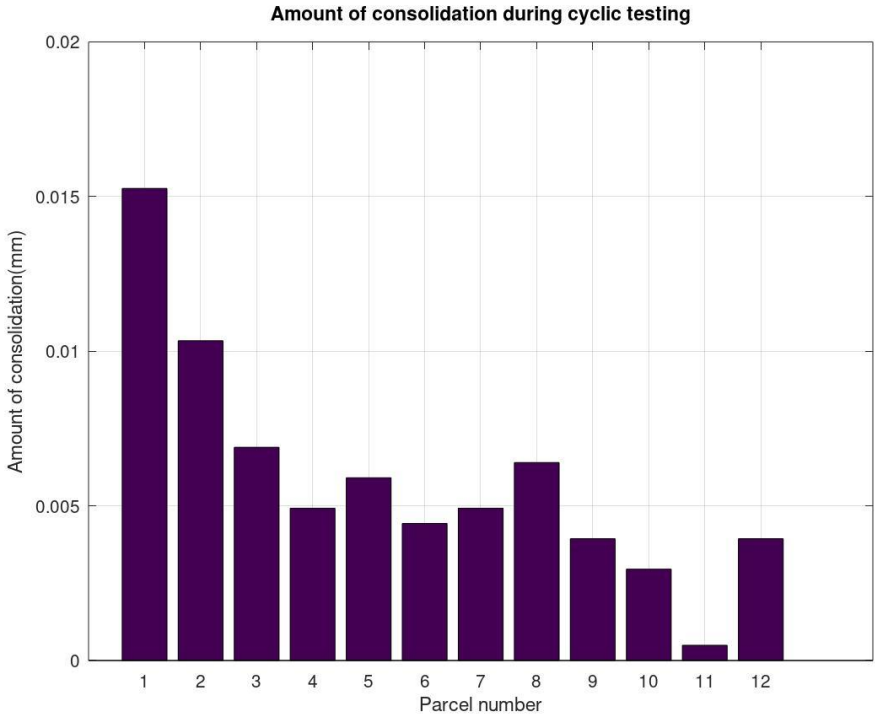

Figure 5.18 - Bar plot showing the amount of consolidation-axial strain within each cyclic parcel of Brazil_2.

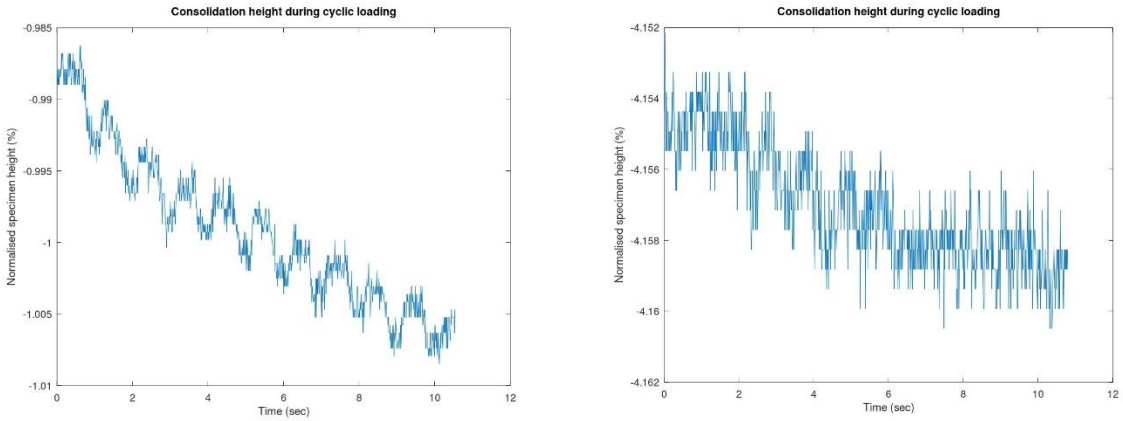

Figure 5.19 – Vertical consolidation behaviour during cyclic parcel 1 (left) and parcel 12 (right) of Brazil_2. Note the amount of consolidation is less prominent on the right figure.

5.2.2.2 Cyclic results

The test results of Brazil_2 is enclosed in Appendix A6. For this test twelve cyclic parcels were performed, with continuous vertical consolidation during the entire testing.

Figure 5.20 illustrates the cyclic displacements and -loading measured in parcels 1,4, 9 and 12. In parcel 1 the maximum displacement-peaks are steadily increasing from approximately 1,5% to 2,4%. During parcel 4 the initial maximum peak increases to about 2% displacement, and ends at approximately 2,4%, hence lowering the rate of normalized displacement. For parcel 9 the measured displacement is overall lowered during the test, with only the last cycle displaying a slight increase compared to first cycle. Similarly, parcel 12 illustrates the same behaviour, but with less cyclic displacements. Regarding the cyclic pressures observed, they display continuous harmonic waves, with increasing amplitudes for each parcel up until parcel 9. Parcel 12 however indicates a slight decrease in cyclic pressures.

Figure 5.21 displays the resulting cyclic loops for Brazil_2. Considering the individual parcels, the development shows a clockwise rotation of loops in all parcels, but with decreasing amount of rotation over time. The difference in normalised displacement between first and last cycles becomes approximately constant in parcel 5 and onward. A cyclic behaviour of this specimen is comparable to previous sample (Brazil_1), with increasing elongation from parcel 1 to parcel 4, then begins decreasing toward the end of testing. One exception is parcel 11, where the strain is observed to exceed above 2%. Compared to parcel 10 and 12, this strain value is much higher. As indicated for the previous test, the maximum and minimum shear stresses observed from the cyclic loops is higher than the targeted cyclic pressure aimed at before testing.

Figure 5.22 illustrates the changing secant stiffness throughout cyclic testing of Brazil_2, in addition to the relative secant stiffnesses of each cycle in relation to the initial stiffness in each parcel. Overall, it is observed to lower at the beginning, before it increases toward the end of the test. Some parcels (8, 10 and 11) show an intervening drop in stiffness in the general trend. Considering the individual parcels, all of them display a lowering stiffness over time. In addition, the amount of stiffness degradation-rate for each cycle reduces over the testing period. Considering the damping-rate parameter of this test (Figure 5.23), each parcel displays a general lowered damping-rate from the first cycle to the last cycle. Over the testing period the damping-rate lowers to parcel 5, where it later increases toward parcel 7. From here it decreases again toward the end of testing. Parcel 12 indicates a slight increase in damping-rate, compared to parcel 11. An overall 2% lowering in damping-rate is calculated for this test.

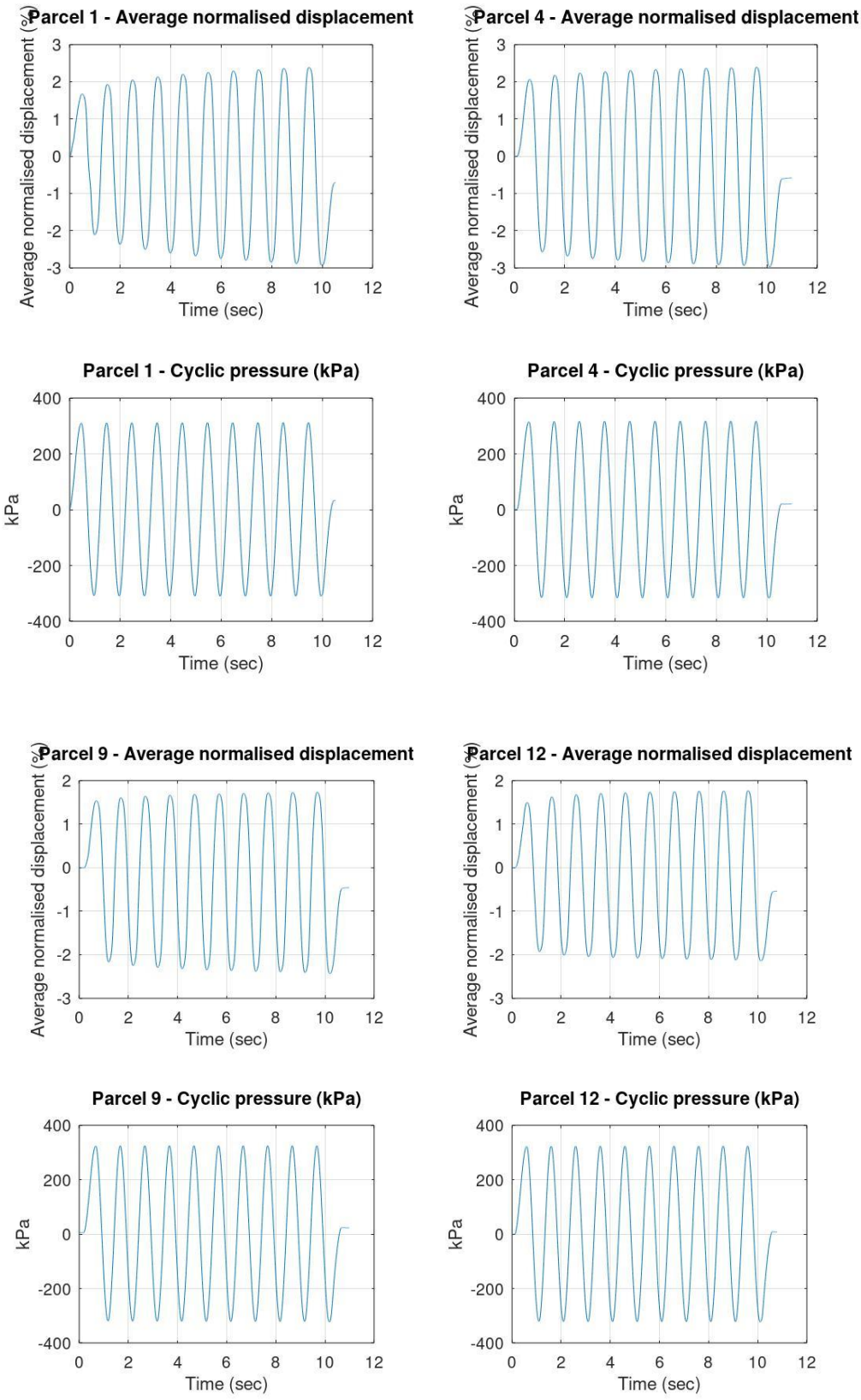

Figure 5.20 - Cyclic displacement and -pressures for selected parcels of Brazil_2.

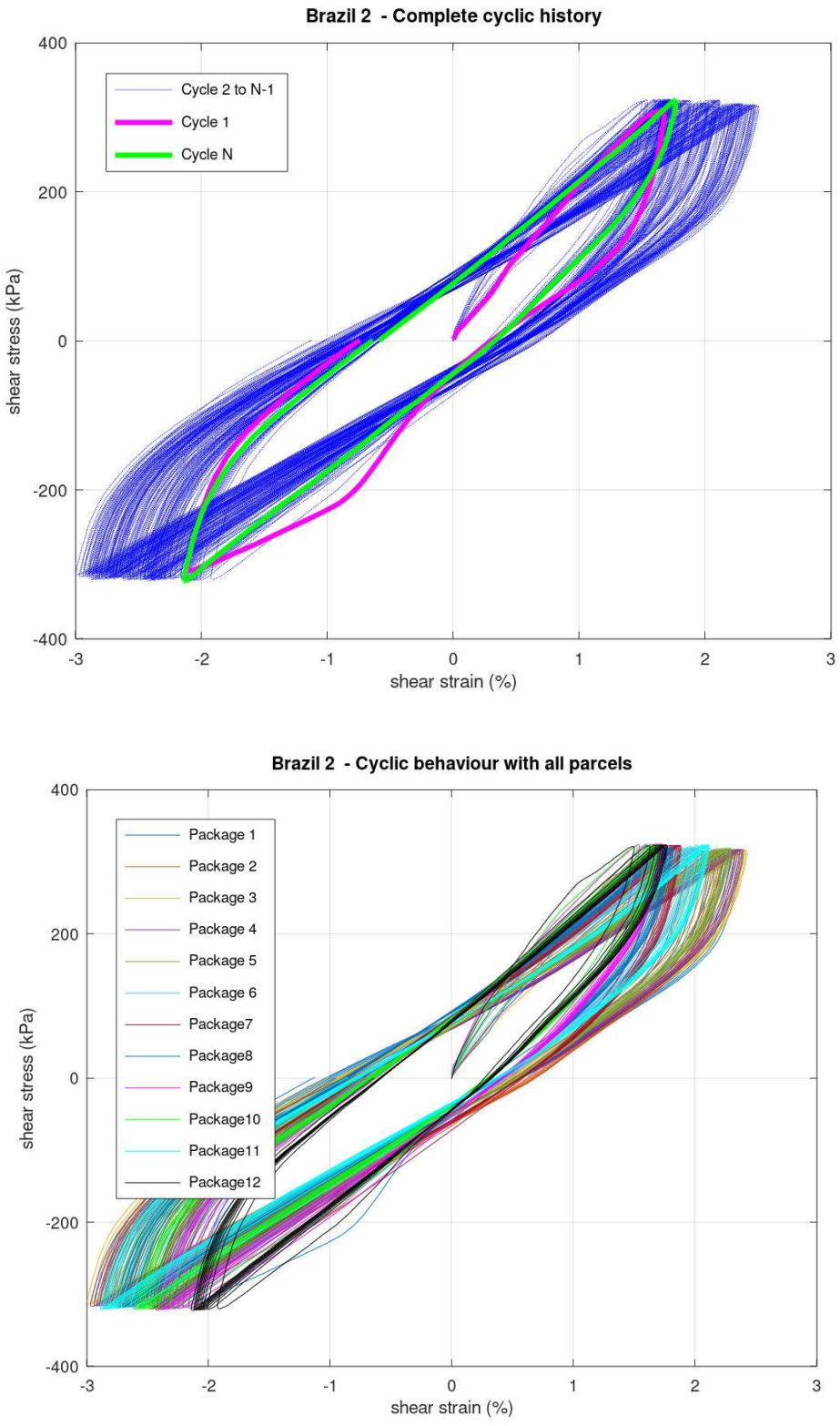

Figure 5.21 - Resulting cyclic loops of the Brazil_2. Above: Complete cyclic history; below: all parcels highlighted.

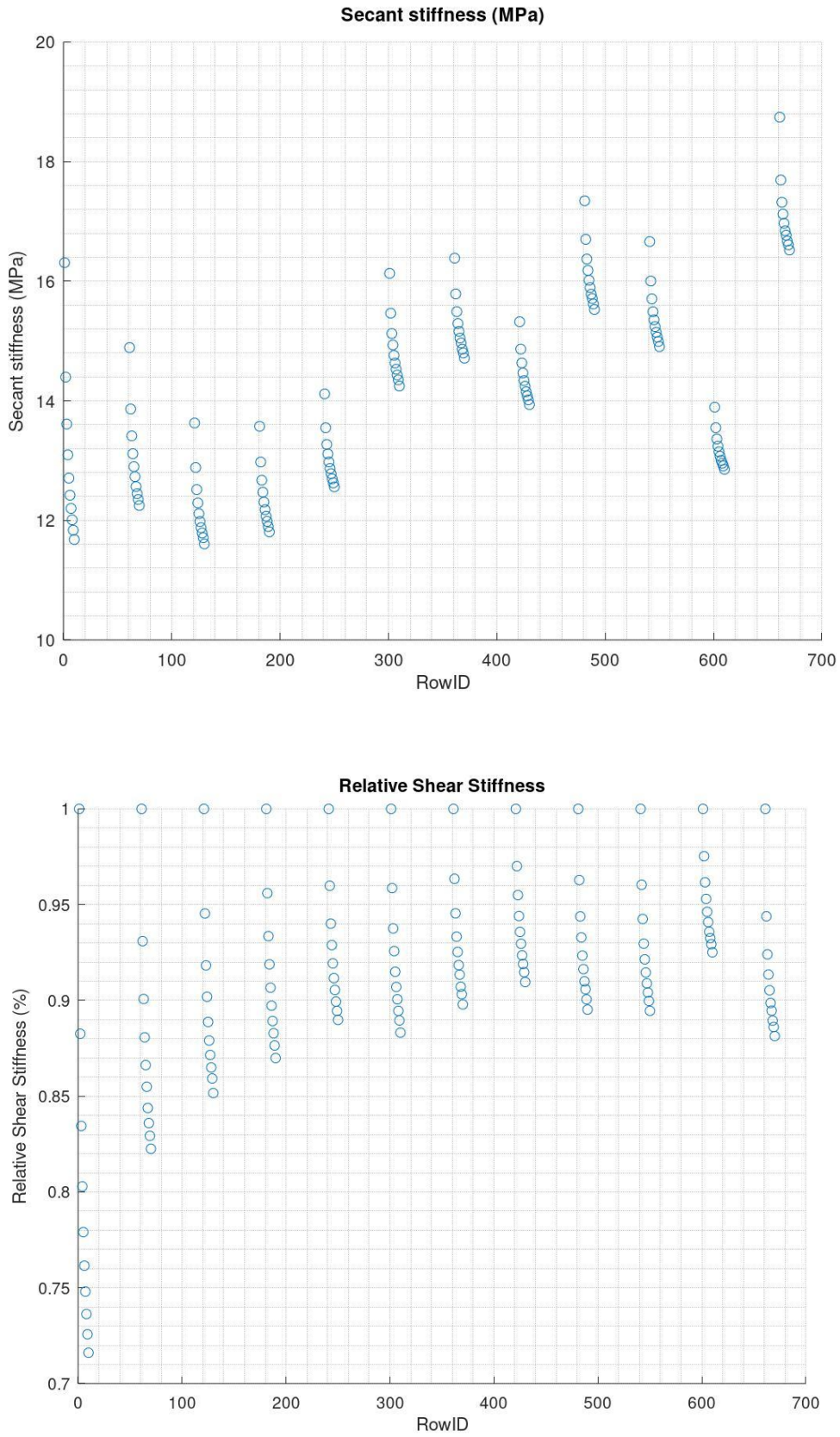

Figure 5.22 – Above: Secant stiffness development of Brazil_2. Below: Relative secant stiffnesses displayed in relation to the initial stiffness at the beginning of each parcel.

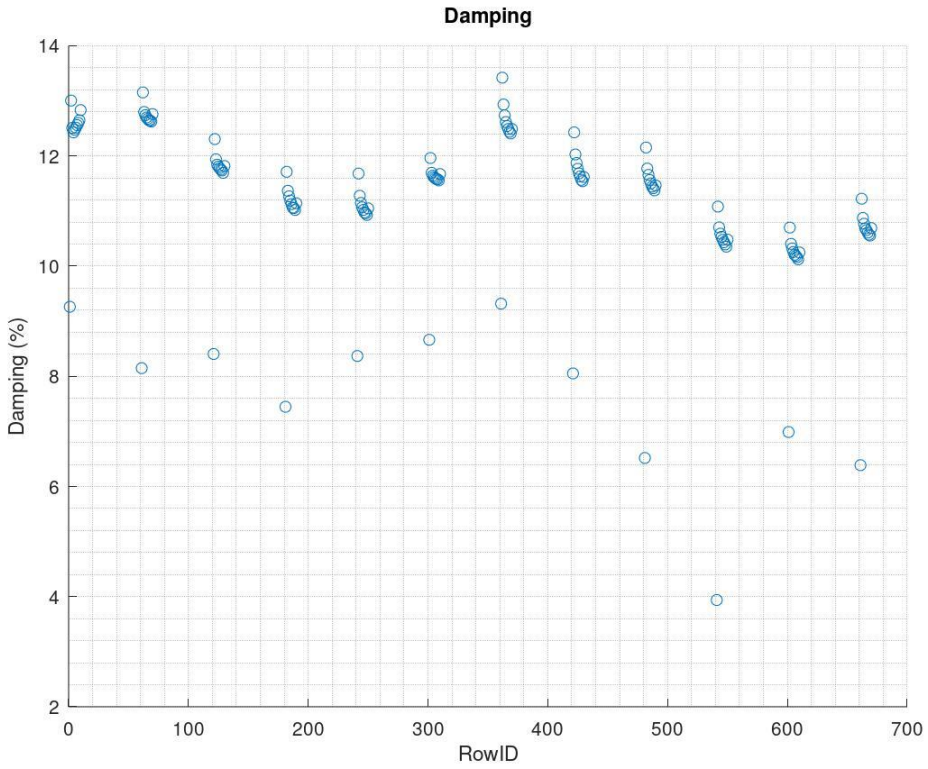

Figure 5.23 - Development of damping in Brazil_2.

5.2.3 Calculated parameters of Brazil-tests

Table 5.2 shows the measurements and calculations of shear stress and its ratio relative to vertical consolidation stress for the Brazil-tests. Similarly, as with kaolin, the Skempton-relation (Equation 2.6) is dependent on material properties. Hence this ratio remains the same for both Brazil-samples.

Table 5.2 – Measured and calculated aspects of shear stress of kaolin-based samples.

Test ID	**Measured τ_{max} from cyclic loops**	**S_u/σ_c; based on Skempton-relation (Equation 2.6)**
Brazil_1	260	0,32
Brazil_2	320	0,32

5.2.4 Water content of Brazil-tests

The water contents of Brazil_1 and Brazil_2 are located in Appendix D5 and D6, respectively. In both tests the water content has decreased over the duration of the experiment. In Brazil_1, no apparent difference is observed when comparing the inner soil (near the model pile) with the outer soil. Likewise can be said about Brazil_2. Generally, the porosity is higher in the middle specimen-slice than in the other slices near the ends. It is interesting to note that some of the lowest water contents are observed on the right side of the specimen. Figure 5.24 illustrates the porosity reduction within both samples. The initial and final porosities were found through direct water content measurements. The final porosities represent the average porosity of all sub-slices. The other porosities were estimated by using the amount of axial strain experienced by the samples during consolidation. For all samples the porosity reduces over the duration of the experiment, with the largest drop occurring between step 2 and 3 of vertical consolidation. For Brazil_2 the porosity continues to decrease, whereas for Brazil_1 some increase is denoted. The observed higher end-porosity in Brazil_1 (Figure 5.24), compared to Brazil_2, could be related to insufficient drying time of the specimen, thus unfortunately masking the real water content of the sample. As both specimens experience axial strain during the entire experiment, it is hence reasonable to interpret that the porosity decreases in both.

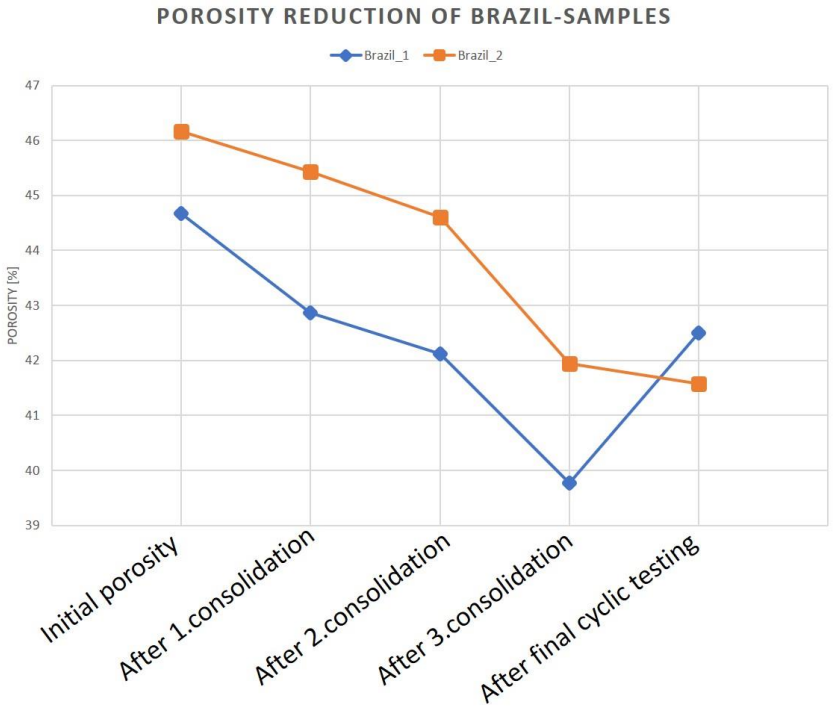

Figure 5.24 – Change of porosity of both Brazil_1 and Brazil_2 during experiment.

Chapter 6

Discussion

6.1 General

The specimens and a majority of the cyclic parcels show a typical cyclic behaviour during loading, with increasing cyclic displacements for each cyclic iteration within a parcel. The amount of cyclic displacement is seen to be linear proportional to the amount of cyclic load, as shown clearly for DT1 and KT1 (see for example Figures 5.2 and 5.5). Comparably, the cyclic loops also reflect the same behaviour, as seen with DT2 and Brazil_1. In the former, the area of the hysteretic loops is proportional to the parcels set in DT2 (see Figure 5.3 and Appendix A2), whereas in the latter the cyclic loops remain relatively similar to each other (see Figure 5.15 and Appendix A5), due to the parcels' similarity.

The study of each cycle, with observation of displacement accumulation at the beginning of each parcel, then flattening toward the end, reveals a gradual stability of cyclic strain-deformation (see for example cyclic strain plot for Brazil_2, Appendix A6). This is observed with lesser displacement accumulation as the parcel progresses. This implies a strain-hardening development of the material. Test DT2 (see cyclic strains in Appendix A2) shows this very clearly, especially parcel 3 and 4, where stabilisation occurs after approximately 150 cycles. The strain changes beyond this point decreases significantly and can thus be considered to remain in a steady-state. The effective stresses of the material decrease during cyclic loading, due to increase of excess pore pressure. As the pile moves laterally, the soil tries to compact but due to the low permeability the soil is expected to generate excess pore pressure (Andersen, 1976; Andersen et al., 2013; Zakeri et al., 2017). As a result, larger lateral strain is registered for each cycle. No gapping seems to take place, as this would be indicated by pinched appearances of the cyclic loops (Heidari et al., 2014).

In many of the cyclic parcels the lateral displacement is observed to be somewhat larger and accumulating in the negative direction (see for example Figures 5.10, 5.14 and 5.20). The same trend appears in the cyclic loops (see Figure 6.1), where the curves accumulate pronounced displacement in the third quadrant of the plot, representing the cyclic response of the minimum

peaks. Few parcels do show displacement accumulation in the positive direction (for example parcel 10 in Brazil_1, Appendix A5). The cyclic pressure measured however (see for example Figure 5.10), indicate no favouring toward the negative side. In other words, the pressure is equal in both positive and negative direction, as is expected by symmetrical loading. This development can be attributed by material's non-linear response, where stiffness deterioration and hysteretic development evolves for each cyclic iteration (Ibarra et al., 2015). This implies that the zero position for each cycle will change over the duration of the cyclic parcel. An alternative explanation could also be related to semi-untightened screws in the positive direction on the push/pull rods, causing delayed and dragged measurements on the lateral transducers. The favouring does occur in the negative direction of most of the parcels, hence this can only be partially explained.

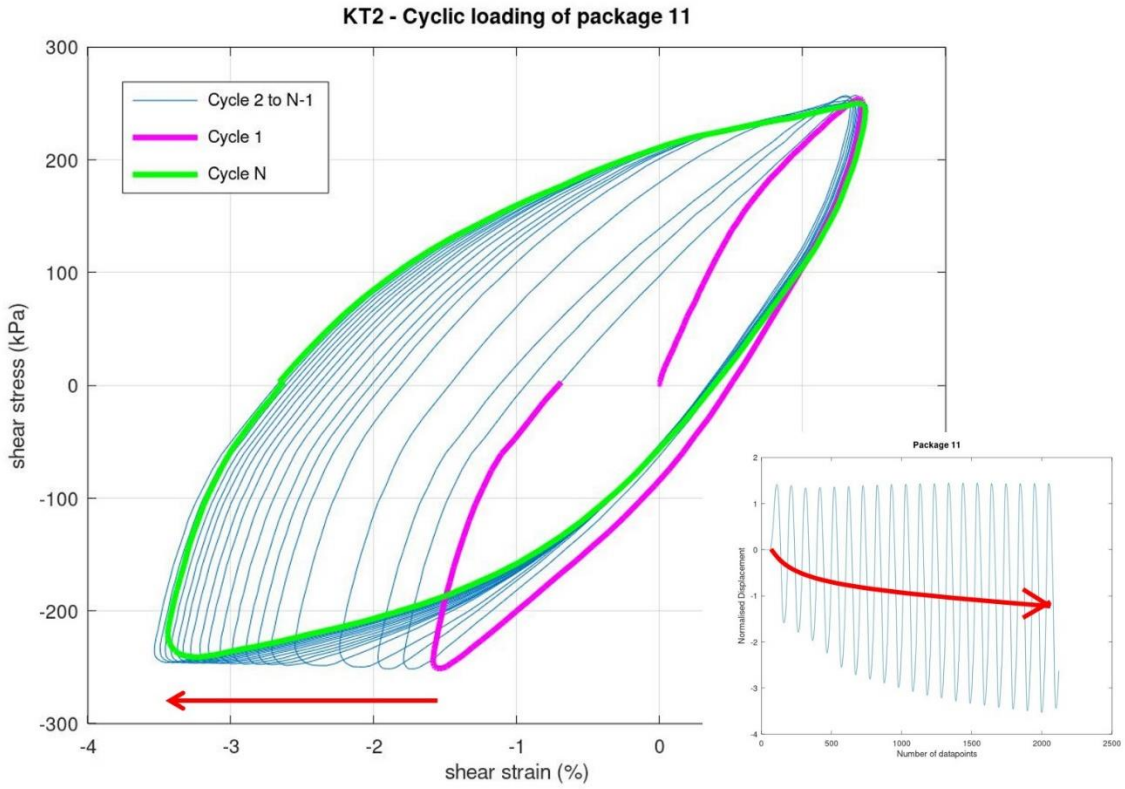

Figure 6.1 – Example of lateral accumulation of parcel 11, KT2, observed during testing, affecting the shapes of cyclic loops. Red arrows indicate the direction of registered movements.

Lateral accumulation in the negative direction over time seems to be caused by the average shear strains accumulated in the tests, when initially zero average loads were to be performed on all samples. This is especially evident in DT2 (see Figure 5.2 and average shear strain-plot of DT2 in Appendix A2), where the accumulation occurs during parcel 4, creating an offset to the next parcel. Slight average shear strains are registered in most parcels, but some display larger developments (for example parcel 7 in KT1 and parcels 1 and 2 in KT2, related to failure, see average shear strain plots in Appendices A3 and A4, respectively). With Brazil_2 (see average shear strain-plot in Appendix A6) all points in each parcel line up with equal spacing, following a linear trend in each parcel. Some bend-shaped average strain development is seen in Brazil_1 (see average shear strain-plot in Appendix A5), probably due to increasing strain development in the positive direction at the beginning, surpassing the more negative strains. It is later overcome by dominating negative strains. On the contrary, the first five parcels of KT1 (see Figure 5.6) display displacement accumulation in a positive direction, which can be linked to a slight drift in the average shear strain. Again, this can be related to operational errors, such as untighten bolts, as the equipment remained interlocked to the sample throughout the day of the experiment.

6.2 Stiffness development

6.2.1 Stiffness development during a cyclic parcel

From the previously discussed section, it is obvious from the previous section discussed that each cyclic iteration within a parcel causes more degradation of the soil, observed with increasing cyclic strains. This can be related to the secant stiffness development in the parcels. For example, in Figure 5.11 it drops for each iteration due to strain-softening. Likewise, the secant stiffness-degradation can be correlated with the cyclic shear stresses, as increasing stress increases cyclic strain, lowering the secant stiffness.

The stiffness degradation tends to increase as a response to larger cyclic strains accumulated, following a typical degradation curve (see Figure 6.2). The increase of stiffness-degradation is postulated from the resulting stiffness after cyclic loading, as it tends to become lower relative to its initial elastic modulus, G_{max} (Adnan and Habib, 2017). The same pattern is also reflected in the individual parcels in the relative stiffness plots (see for example the relative shear stiffness

plot of Brazil_2 in Figure 5.22), where gradual accumulated cyclic displacements cause lowering degradation-ratio between stiffness of current cycle versus the initial stiffness.

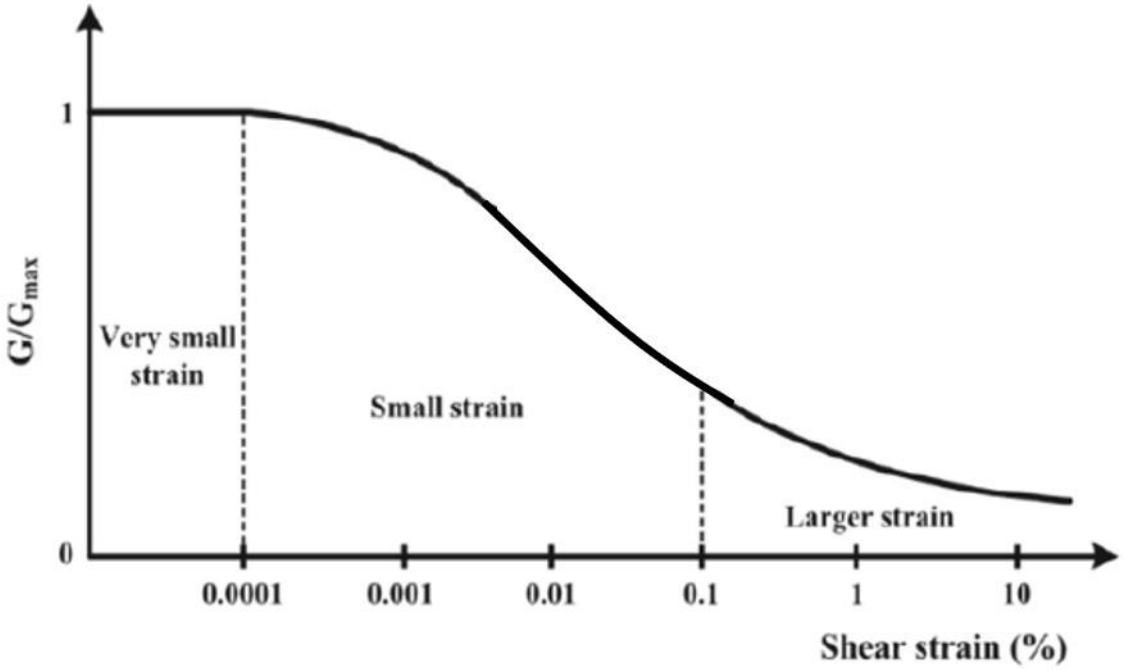

Figure 6.2 – Conceptual stiffness degradation curve. As cyclic strain accumulates the secant stiffness (G) is seen to progressively lower, relative to the maximum secant stiffness (G_{max}). Similar development is also observed with the soil stiffness during cyclic loading in this thesis. Modified from Adnan and Habib (2017).

This can be explained by pore pressure generation, causing a reduction in effective stress in the specimen. Hence the pore pressure development leads to gradual break down of the soil (Andersen, 1976, 1988, 2009). Triaxial studies of cyclic loading on undrained material also reveal this development. The effective stress decreases for each cycle, as a result of increasing pore pressure, see Figure 2.5 (Andersen, 2009). During performance of cyclic loading with clay, tests can be assumed to behave partially undrained during a cycle, as indicated by Støren (2018). To assume undrained conditions within one cycle with the use of the model pile and kaolin, the cycle period must be under 25 seconds for kaolin (Table 4.3; Støren, 2018). Since the maximum period selected in this thesis is 10 seconds, one can thus assume undrained conditions in the performed tests during one cycle. For the marine clay the maximum period is 62.5 seconds to consider one cycle to remain undrained (Table 4.3). With assumed undrained cyclic loads confined within the soil chamber, the lateral pressures cause development of excess porewater pressures, building up with increasing cyclic displacements. Practically however the pore water

of the specimen is allowed to drain both between cyclic parcels as well as during the parcels. The specimens can thus be considered partially drained during these stages.

6.2.2 Axial behaviour during cyclic loading

Considering the cyclic behaviour in company with axial consolidation; although the amount of cyclic displacement increases, the rate of accumulation reduces for each iteration within a parcel (see Figure 6.3). However, as the height of the sample shrinks the amount of accumulated displacement diminishes for each passing parcel. This is likely due to increased stiffness, as a reaction to the axial consolidation. This is also confirmed by the very first initial secant stiffnesses observed in Brazil_1 and Brazil_2 (compare Figures 5.16 and 5.22), with secant stiffnesses equal to 12.6 MPa and 16.4 MPa, respectively. Brazil_1 was performed with a lower consolidation pressure than Brazil_2. For a specimen's material, the undrained shear strength is determined by the effective stresses applied (Wesley, 2010), hence higher axial loads increase the shear strength.

The differences in shear strength in the two materials could be reflected in the material properties of the soil. As the plasticity index and the liquid limit for the Brazil-marine clay is higher than it is for kaolin, the former plots slightly closer to the A-line on a plasticity chart (see Figure 6.4). The A-line generalises soils on whether they have silty or clayey characteristics, thus providing an indication of the material properties. Silty soils tend to have higher shear strengths and little compressibility (Wesley, 2003, 2010). Although the materials used lie close to the A-line, the marine clay lie slightly within the silty clay area. This is also supported by the high silt content found in the marine clay (see Table 3.2). Moreover, considering the Skempton-relation (Equation 2.6), the ratio between undrained shear strength and effective stress increases with increasing plasticity index (PI). As the marine clay possess higher PI than kaolin, it is expected that the ratio increases. It thus implies a higher undrained shear strength found in the marine clay.

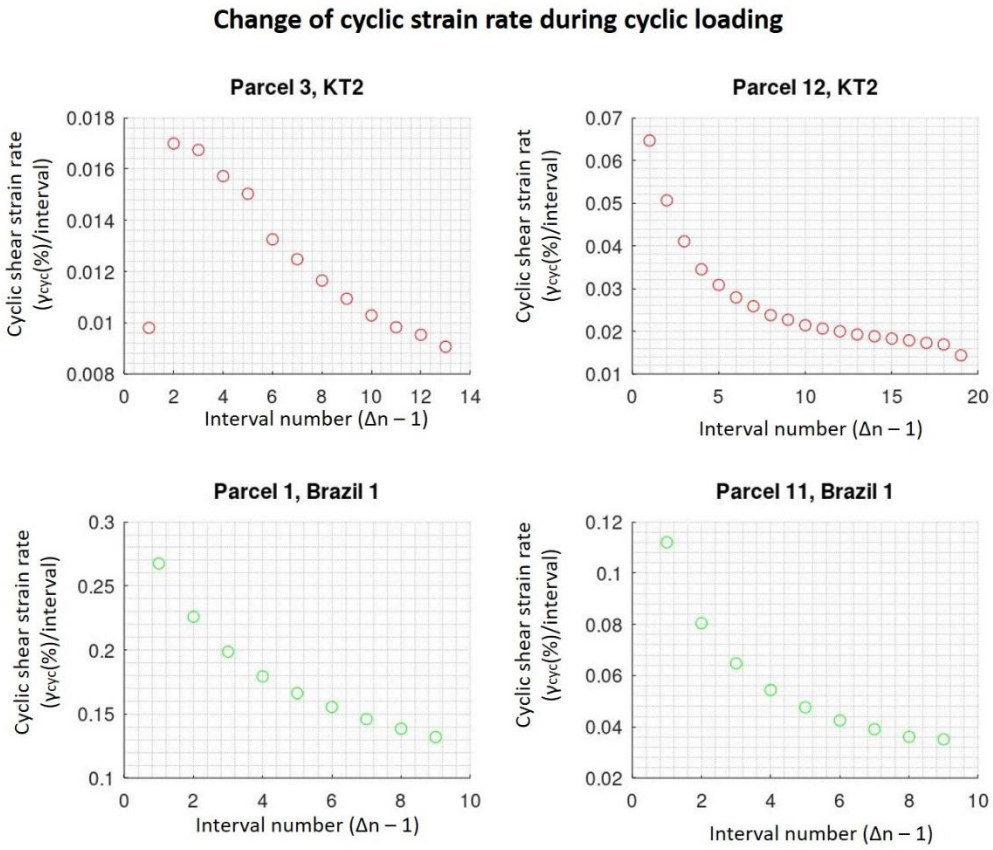

Figure 6.3 – Cyclic strain rate for each passing cycle during cyclic loading. It can be seen that although accumulation of cyclic displacement occurs, less displacement occurs during each iteration.

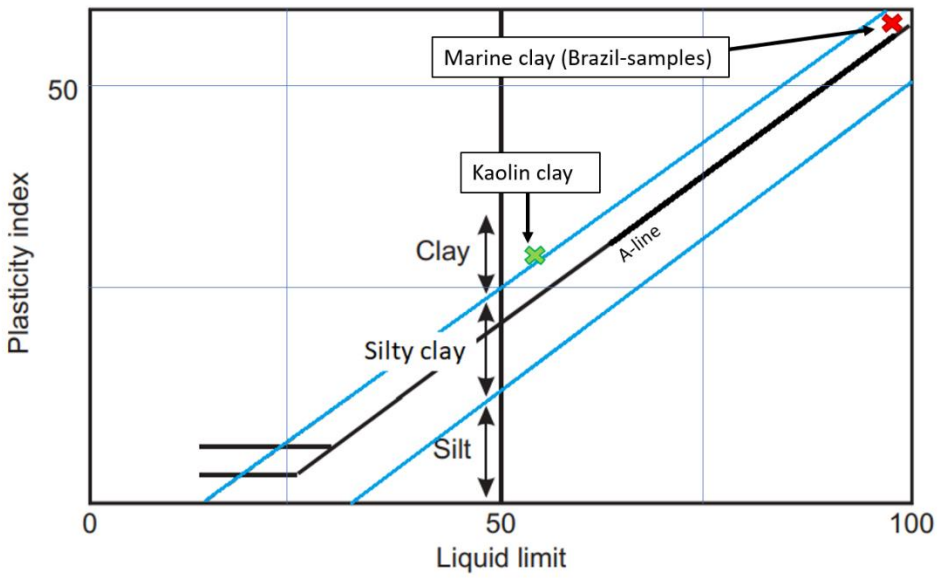

Figure 6.4 – Plasticity chart with positioning of the materials used. Modified after Wesley (2003).

6.2.3 Stiffness development during long-term cyclic loading

The stiffness over time however is observed to increase, especially in Brazil_1 and Brazil_2, see Figures 5.16 and 5.22, respectively. This is additionally evident in their related cyclic loops (Figures 5.15 and 5.21, respectively), with anti-clockwise rotation of cyclic curves throughout the experiment, suggestive of strain-hardening. Over the duration of testing, some water is drained between the parcels, thus lowering the water content (see for example the water content measurements of the specimens in Appendix D). For each cyclic parcel introduced to the experiment, the cyclic strains rely on the previous existing water content and pore pressure. As such, the effective stress increases with pore pressure dissipation.

Another aspect of increasing stiffness can be related to the rise of cohesion in the material. The cohesion tends to develop as the clay becomes firmer and stiffer (Wesley, 2010), and could be related to post-cyclic loading, as the cohesion develops. The latter statement seems to fit clays that have been normally consolidated (Andersen, 1988). Since the clays studied have reached normal consolidation stage, one can assume such a development. Based on the undrained shear strength formula (see Equation 2.5), the increase of cohesion suggests an increasing undrained shear strength over time.

The opposite is evident in some tests (for example in parcels 8-12 in KT2, see Figure 5.11), especially when cyclic parcels were conducted on the same day (see Tables 4.8 and 4.10). The second parcel of the day signify a further reduction of secant stiffness. This could be explained by insufficient pore pressure dissipation after the first test of the day. By continuing cyclic loading, the newly generated pore pressure adds onto the pre-existing pore pressure, causing further reduction of effective stress. The result is weakening of soil strength. A similar cause can likely explain the failure of KT1, displaying excessive lateral displacements (Figure 5.6) and low stiffness (Figure 5.7) toward the end, factors usually related to cyclic failure (Jardine et al., 2012). Considering the testing procedure of KT1, the failure could be related to accumulated pore pressure over the course of testing. As the performance was executed over a single day, not enough time for post-cyclic consolidation between cyclic parcels to sufficiently dissipate the pore pressures could be the issue. Thus, the effective loading reached the failure limit, rather than remain within the fatigue limit.

The localisation of failure is usually predicted to occur between two radial zones, encircling the pile. These radial zones are the same zones postulated from Figure 2.9, as they are characterised

by their typical shear strengths and boundaries, hence influencing the soil's cyclic capacity (Karlsrud and Nadim, 1990; Jardine et al., 2012). Studies on the micro-fabric of clay in relation to soil-pile interaction during cyclic loading have shown a development of well-clustered clay particles, adhering to the pile with well-developed shear fractures (Jardine et al., 2012). As the soil resistance is sharply changed across the boundary between the remoulded clay and disturbed clay failure is likely to be established in this interzone (Karlsrud and Nadim, 1990; Jardine et al., 2012).

6.2.4 Axial strain development during long-term cyclic loading

The axial strains observed can be linked to multiple parameters. One issue is the change of density, postulated in Figure 5.24, relying upon the measured water contents and height changes. Consolidation causes gradual compaction, hence lowering of the void ratio (Westerberg, 1999; McCarthy, 2007; Wesley, 2010). Postulated from the removal of voids, soil compaction may account for the increasing stiffness observed in the samples. Static load compaction tends to orient clay particles perpendicular to the loading direction, as observed with kaolin particles in Sloane and Kell (1966). Additionally, studies have shown that kaolin clay with a dispersed (parallel-oriented) platy microfabric tends to develop higher shear strengths during undrained shearing (Sachan and Penumadu, 2007). The compaction increases the resistance and the soil's bulk density by making it denser (McCarthy, 2007; Wesley, 2010; Brown and Wherrett, 2020), fitting with the observed firmness of the samples after experiments. Studies on kinetic fabric of soil materials indicate a good correlation of macroscopic stiffness anisotropy with the fabric anisotropy (Gu et al., 2013). With increasing stress ratio between maximum principle stress and minimum principle stress, the anisotropic behaviour becomes more apparent. As such, the stiffness in the minimum principle stress directions dissipates in relation to the stiffness in the maximum principle stress direction. This can be attributed to more contact points developing onto grains in the maximum principle stress direction, in addition to increasing contact forces, resisting the pressure. Meanwhile, in the minimum principle stress direction the number of contacts is significantly reduced (Muir Wood et al., 2001; Gu et al., 2013). This idea can possibly be further extended to the previous discussed lateral moving pile-interaction with surrounding clay, where clay proximal to the pile is initially remoulded (see Figure 2.9). With applied cyclic load onto the soil the soil fabric could then further develop this anisotropic behaviour, with local compaction of clay in the cyclic lateral directions.

In all samples, the amount of axial displacement decreases over time as the consolidation stress remains the same. Yasuhara and Andersen (1987) have illustrated this conceptually (Figure 6.5). The first amount of axial strain is always the highest and is likely due to the amount of pore pressure dissipation, related to cyclic strains. As previously mentioned, cyclic loading tends to increase the pore pressure within a sample. By having an axial consolidation load onto a cyclic moving pile, two factors are at play. As the shear modulus of a cyclically-affected soil drops around the pile, the axial stress leads to local static stress redistribution around the affected area. The lowered modulus improves the amount of axial strain. Furthermore, the pore pressures, generated by cyclic applications, dissipates and causes additional volumetric strains (Andersen, 1988). Parcel 1 of Brazil_2 (Figure 5.18) illustrates lower axial strain, compared to parcel 1 of Brazil_1 (Figure 5.13). This can again be linked to the applied loading, with higher cyclic loads performed on Brazil_2. It is more difficult to compare the initial axial strain of KT1 and KT2, due to the drastic weakening of KT2 during parcel 1, but also due to having unequal number of cycles performed on their first parcels.

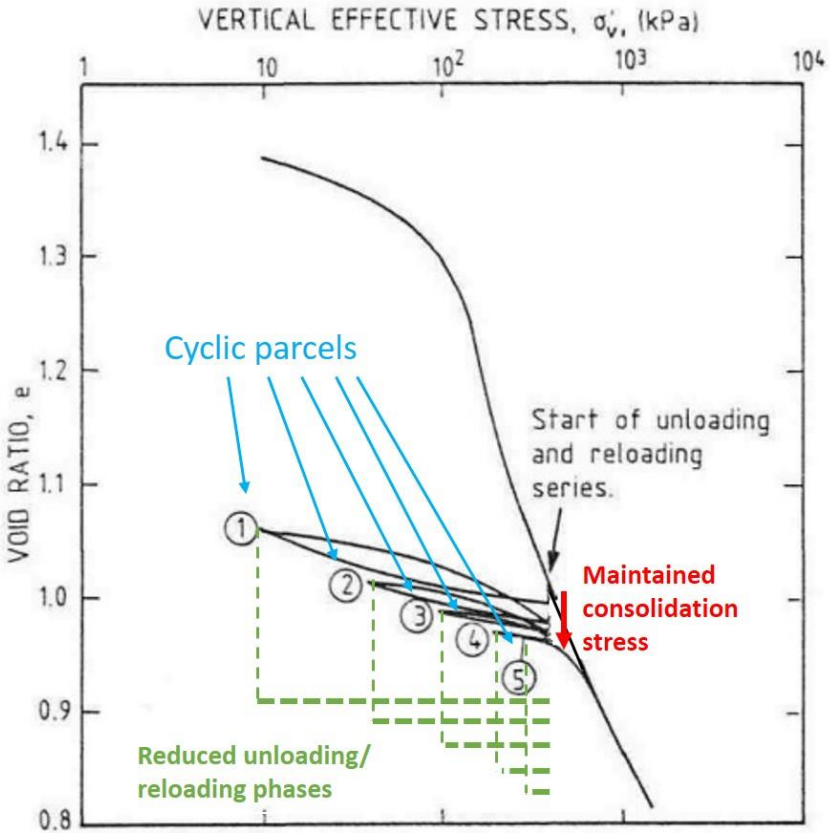

Figure 6.5 – Consolidation curve with applied cyclic parcels during a constant vertical effective stress. After each cyclic parcel the effective stress reduces, but the amount of reduction declines. Likewise can be said about the reloading phases back to total stress, where the path back to normal consolidation stress declines after each parcel performed. Modified from Yasuhara and Andersen (1987).

The behaviour of axial strain during cyclic testing seems to fit very well with the secant stiffness. Similar to the development of cyclic secant stiffness, the amount of axial strain within a second parcel on the same day is reduced (compare parcels 7 and 8, KT2 in Figure 5.9 and parcels 2 and 3, Brazil_1 in Figure 5.13). An explanation of this feature could again be related to not fully dissipated pore pressure, hence excess pressure is still retained. As such, the effective stress is still comparably lower than effective stress with fully dissipated pore pressure, in other words, regained total stress. This may also explain the higher axial strain occurring the next day, as pore pressure dissipation within the specimen is complete (compare parcel 3 and 4, Brazil_1 in Figure 5.13). In Brazil_2, the amount of axial strain (Figure 5.18) also seems to fit well with the secant stiffness development (Figure 5.22). This is especially highlighted with parcel 8, where drop in secant stiffness also corresponds well with the increasing amount of axial strain.

The behaviour of axial strain during cyclic loading displays an oscillating pattern at the beginning, which disintegrates toward the end of testing (see Figure 5.19). This oscillating behaviour could be linked to the disturbed zone, occurring around the model pile, with local swelling and compression of the clay. Considering the consolidation to represent the Z-axis and cyclic loading occurring in the XY-plane; the lateral pile movements causes stress distribution around the model pile in the XY-plane (see Figure 2.7; Karlsrud and Nadim, 1990; Sheil and McCabe, 2017; Zhang and Andersen, 2019). The stress distribution is likely causing the disturbed zone, observed near the model pile on the right side of the specimens (see Appendix C). The oscillating effects could be related to shaft resistance along the model pile. When settlement of soil occurs around a pile, frictional drag is experienced along the pile, causing less settlement near it (Karlsrud and Nadim, 1990; Knappett and Craig, 2012). It is assumed during testing that the sand-blasted model pile displays the highest roughness factor (Støren, 2018).

Another component of the oscillating pattern could be the pore pressures generated. Since pore pressure is allowed to dissipate during post-cyclic consolidation, a similar case could occur near the open ends of the soil chamber during cyclic loading. As the samples experience both shaft resistance and axial strain in combination with reduced effective stress of cyclic loading, this could account for the oscillating axial strains. The elongated disturbed zone is oriented with its long axis normal to the direction of lateral movement along the XY-plane, fitting with that observed by Zakeri et al. (2017). Additionally, soil hardening is also typically occurring in the vicinity of piles due to local densification (Heidari et al., 2014). Since the disturbed zone is most prominent in the right-side of the samples, this could be explained by its proximity to the

consolidation piston. This could be further supported by the observed lowest water content appearing on the right-hand side (see Appendix D). The disintegration of oscillating pattern over time is likely caused by the increasing axial stiffness, with less axial strain occurring between progressive cyclic parcels.

6.2.5 Axial strain rate between cyclic parcels

Likewise for the amount of axial strain, the rate of axial strain for each sample during post-cyclic intervals (see axial strain rates for each sample in Appendix B) also dissipates over time. The axial strain rate within post-cyclic intervals overall lowers in all samples. Some exceptions occur, such as subsequent parcel-interval following a day with two cyclic parcels performed, example the even-numbered intervals in KT2 (see axial strain rate in Appendix B4). Here, the higher rate during, for example, interval 4 reflects a higher average axial strain over time, compared to the rate during interval 5. The axial strain rates herein seem to fit the post-cyclic behaviour described by Yasuhara and Andersen (1987), with alternating lowering and reloading of effective stress. Considering a normal consolidation curve, after applying a cyclic load, the effective stress reduces, yet the axial strain remains. By definition, the sample is then in an over-consolidated state (Yasuhara and Andersen, 1987; Wesley, 2010). The lowering of effective stress occurs during cyclic loading, and the amount of stress-drop decreases for each parcel. After cyclic testing, the sample follows a reconsolidation curve back to the set confined effective pressure (Yasuhara and Andersen, 1987; Andersen, 1988).

Similar natural occurrences of developing shear strengths after shear-induced loading are seen in liquefied soils. Initial liquefaction is due to loss of undrained shear strength, as undrained irregular loading (i.e. ground-vibrations, such as earthquakes or explosions) causes build-up of excess pore pressure. As the pore pressure dissipates, volumetric strains related to ground settlement is imminent (Nagase and Ishihara, 1988; Sitharam et al., 2009). Studies on post-liquefied sand and silt indicate that volumetric strains follow a reconsolidation curve. The reconsolidation strain can be uniquely correlated with the excess pore pressures, generated during irregular loading (Nagase and Ishihara, 1988). However, less strain develops as the relative density of the soil increases (Nagase and Ishihara, 1988; Sitharam et al., 2009). One explanation for increasing shear strength could be attributed by the changed soil fabric after liquefaction (Amini and Trandafir, 2008; Sitharam et al., 2009). This development is similar to

the previously mentioned axial strain, as the samples follows a reconsolidation curve by regaining effective stress after cyclic loading.

6.2.6 Relative shear stiffnesses

Figure 6.6 displays the normalised initial stiffnesses of all tests performed. Although no implicit trend is present it seems as if there could be a tendency of changing stiffness over time. This is especially evident with the Brazil-specimens where stiffness development over time initially decreases, but then start to increase over time. Considering the fact that the first tests of the day in KT2 (odd-numbered parcels) can be considered having fully dissipated pore pressure (resumed its original consolidation stress) from previous cyclic loading, there could be the same tendency here as well. These three tests also indicate that over time their initial stiffness climbs to be slightly higher than their initial stiffness before cyclic testing was performed. The stiffness, as previously discussed, can be related to material densification and soil strengthening, related to axial consolidation and pore pressure dissipation. The first and last initial secant stiffness of the tests summarised in Table 6.1 highlights this development. The low development of KT1 is due to the fact that it eventually failed during its testing performed on the same day.

The relative shear stiffnesses at the end of each parcel of all tests are given in Figure 6.7. Although some scatter present, there is a trend of less and less stiffness degradation over time, and some regaining of stiffness occurring already after the second parcel, compared to the first. This figure also suggests that to reach the same amount of cyclic displacement during the final parcel as that reached in the first, while still maintaining the target pressure, a greater number of cycles are needed to progress the degradation. This number of cycles would also be accounted for the changing rate of cyclic displacement with progressive cyclic loading, as illustrated in Figure 6.3. Progressive amount of axial strain and their expected axial strain rates can also be correlated from this development.

An anticipated trend line has been hypothesised in the figure (grey stippled line in Figure 6.7). The interesting part of it is that it appears they all eventually merge to a ratio about 0.9, apparently independently on their type of material, number of cycles or the consolidation stress. However, though this development appears fascinating, it is difficult to conclude on this based on just the tests performed herein.

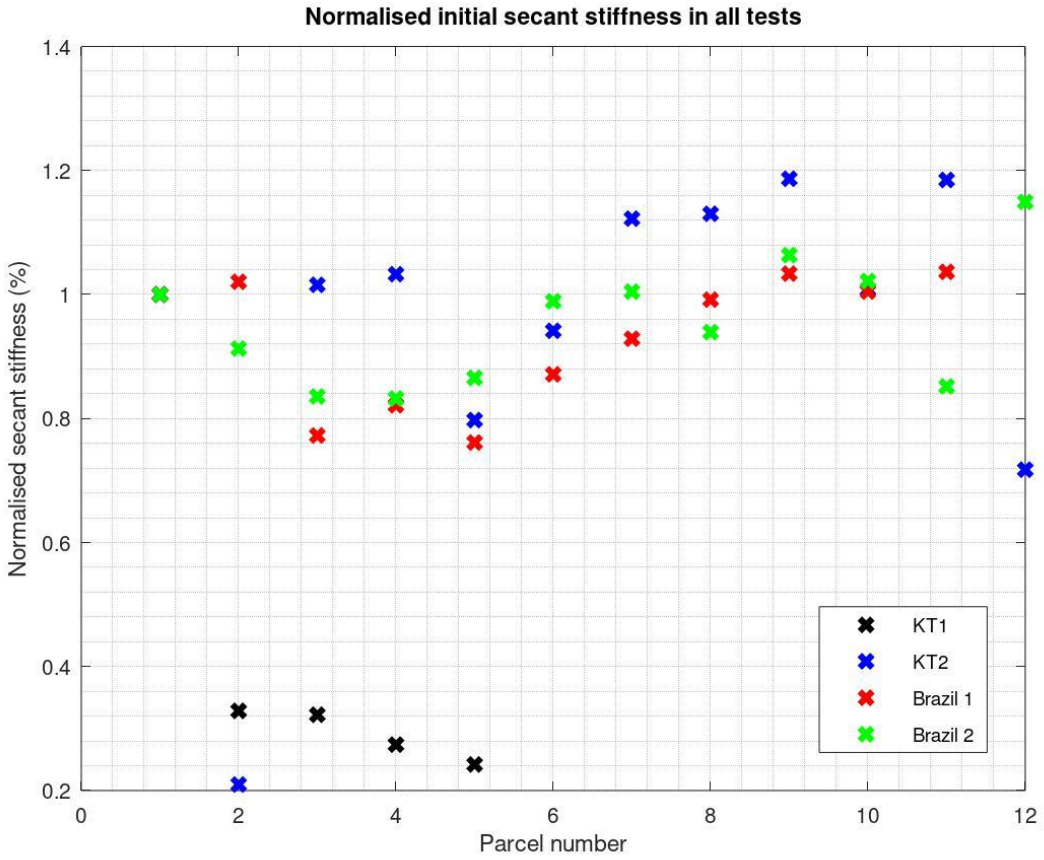

Figure 6.6 – Normalised initial stiffness of all parcels in the tests.

Table 6.1 – Summary table of secant stiffnesses, before and after cyclic testing.

Sample ID	Initial secant stiffness (MPa) of the first parcel of cyclic testing	Initial secant stiffness (MPa) of final selected parcel of cyclic testing
KT1	74	16 (parcel 5)
KT2	14,2	16,8 (parcel 11)
Brazil_1	12,7	13,2 (parcel 11)
Brazil_2	16,4	18,8 (parcel 12)

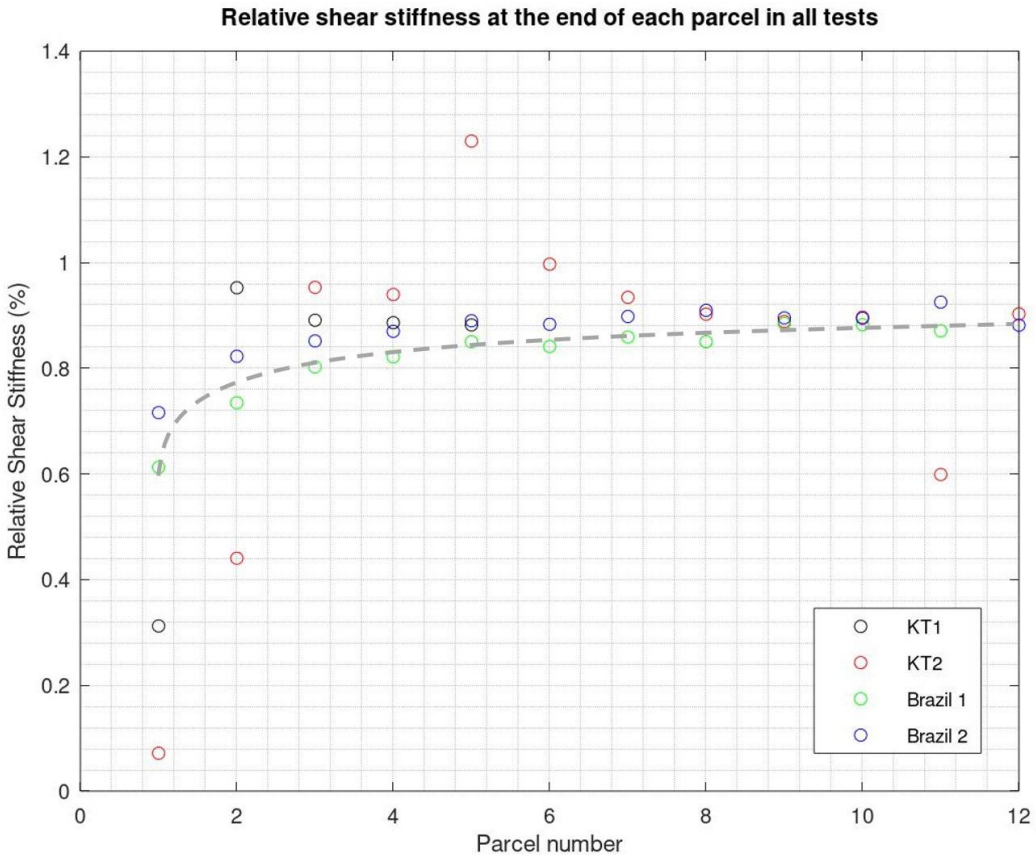

Figure 6.7 – Normalised shear stiffness at the end of all parcels. A hypothetical trend line (grey stippled line) is inserted.

6.3 Damping development

The registered damping appears initially to be negatively correlated with the cyclic secant stiffness (such as in Brazil_1; see Figures 4.16 and 4.17). However, for other tests the opposite is observed, with decreasing damping within the samples with decreasing secant stiffness (for example KT1, Figure 5.8). The higher damping commonly occurs at the beginning, along with lowering secant stiffness, and low damping and high secant stiffness toward the end. As damping reflects the energy absorption of the soil, it can be viewed as a function of cyclic strain development (Bolton and Wilson, 1990; Ashmawy et al., 1995). By comparing the damping behaviour with the secant stiffness (see for example Figures 5.16 and 5.17 of Brazil_1) it is obvious that the damping is high at the beginning of test, where the greatest softening occurs. This can be linked to insufficient strength-development, with large cyclic displacement

amplitudes evolving. Due to the initial softness of the materials, the model pile is allowed to make larger displacement, hence applying more energy onto the soil. This could especially be the case for parcel 11, KT2, in regard to the cyclic loops (see Appendix A4). Likely a set-up error of the model pile caused abrupt cyclic strains and expanded loop development, causing large energy dispersion and damping. Since the stiffness overall develops over time in samples KT2, Brazil_1 and Brazil_2, the damping is observed to be lowering. This indicates an overall build-up of resistance within the soil. This is also supported by the areal reduction in each cyclic loop, as the loops slim and the unloading-reloading modulus becomes more swiftly adapted during progressing cyclic loading (see for example cyclic loops of Brazil_1, Figure 5.15). Similarly, since the rate of damping minimizes during each parcel, it could also reflect a stabilization. This is likely the case in parcels 3-10 in KT2 (see Figure 5.12), where their beginnings mark fluctuating damping to then become flattened. As the stiffening becomes more stabilized during a parcel, this could indicate that energy has lesser impact for continued deformation. The increase in damping within the parcels of Brazil_1 (see Figure 5.17) implies more energy dispersion for each cycle. This could account for higher compaction near the model pile in addition to axial strain. However, progressive parcels indicate that damping eventually becomes rather similar throughout the testing.

When comparing the calculated damping with the amount of consolidation taking place during cyclic loading, the development seems almost impeccable. This is especially evident when comparing the damping of KT2 (Figure 5.12) with its corresponding axial strain (Figure 5.9). Parcel 5 indicates rise in both parameters, whereas the previous parcel shows the opposite. From the results, it does not implicitly indicate that damping is material-dependent. It does however seem to be dependent on the effective pressure, as higher confining pressure lowers the resulting damping. This fits with the ascribed damping-development in relation to increasing shear strength.

6.4 Uncertainties

Following the experiments and discussion of their related results, some insecurities do arise. Firstly, some operational errors have been exposed along the way. These could be attributed to untightened screws during set-up, insufficient sampling rate or erroneous setting on the MTS system. For example, considering test Brazil_2, parcel 11 (se Appendix A6) indicates a much

larger cyclic shear strain observed, than the preceding and the following test. These results could be related to erroneous calibration on the MTS-system, prior to cyclic testing, when connecting the sample to the hydraulic actuator. As such, the connecting procedure caused the model pile within the sample to bend. This produced unregistered loading onto the sample, hence a minor strain or gap was developed near the model pile. This parcel's behaviour is also evident in the secant stiffness (see Figure 5.22, parcel 11), where its stiffness has greatly dropped. Additionally, the favouring strains in the negative direction, evident in almost all parcels tested, could appoint to the performance of the hydraulic actuator. The majority of these observed strains however do not seem to influence the results severely.

Secondly, no pore pressure measurements were performed in combination with other measurements. As such, uncertain porosity-calculations, given in Figure 5.24, are imminent. The pore pressures do tend to increase during cyclic loading, with an increasingly oscillating trend (Andersen, 2009), hence implying reduced effective stress over time. According to Andersen (2009), it is difficult to completely monitor the pore pressure, due to lack of drainage. Moreover, as axial strain is performed on the samples the porosities is naturally expected to decrease, as previously discussed.

Thirdly, it must be mentioned that the cyclic shear stress measured after testing do not match the targeted cyclic pressure prior to testing. In many cases the measured cyclic shear stress was observed to be 10% higher than the target set. The explanation for this however is difficult to assess. It could be related to the post-processing phase, when extraction of cyclic pressures was to be prepared for the DLP-script. Since the cyclic shear stresses are overestimated the secant stiffnesses as well will be overestimated. However, this would still not affect the qualitative study of the stiffness development.

Finally, no oedometric measurements of the actual specimens were performed, to obtain appropriate consolidation curves of both the kaolin and the marine clay. The normal consolidation modulus of kaolin was however obtained from Støren (2018). Although, given the modulus, sample KT1 did eventually fail, likely due to higher number of cycles performed in addition to increasing cyclic pressures. Concerning the marine clay, it originates 10-11 meters below seabed, where neither normal consolidation- and reconsolidation moduli were available for this depth. As such, the moduli and predicted undrained shear strength were based on a given consolidation curve for marine clay located in a shallower level, specifically 7 meters depth.

7. Conclusion

For this study four experimental tests have been conducted to qualitatively investigate the long-term pile responses of cyclic loading in clay.

With the use of the P-Y apparatus the cyclic results adhere to typical cyclic behaviour of soils. Additionally, aspects of both short-term strain-softening and long-term strain-hardening has been presented and discussed.

For each cyclic parcel introduced the stiffness of soil degrades as cyclic loading continues, as a result of pore pressure dissipation. This has been shown with accumulated cyclic displacements and increased hysteretic damping. For each cycle passed however the cyclic strain rate decreases.

Post-cyclic shear strength is likely to improve, as an overall strain-hardening is developed. This can be linked to development of lesser pore pressure generation, and densification of the clay. Discussion of the presented hysteretic damping also conforms to this development. With the tests herein, it is indicated that the resulting stiffness after multiple events of short cyclic loading is slightly higher than its initial secant stiffness.

As for the long-term development of cyclic behaviour over the course of testing, the axial behaviour also shows a similar development. With the cyclic displacements decreasing, also the axial strain decreases over time, as a result of the effects of strain-hardening. After each cyclic parcel performed the effective stress reduces, caused by accumulated pore pressure generation. During the "resting-interval" the effective stress increases as the developed pore pressures dissipates. For each progressing interval the unloading-reloading path shortens, as has been discussed with the axial strain rates presented. This could also suggest that the time to obtain fully dissipated pore pressures, thus reaching the consolidation stress, decreases for each parcel.

The overall long-term development of the stiffness seems to suggest that initial secant stiffness will lower at the beginning, and after further cyclic parcels applied a strengthening of the soil becomes apparent. Similarly, for the end stiffness in each parcel, given enough time for pore pressure dissipation and the same cyclic specifications applied, also these will indicate a strain-hardening development, that eventually, perhaps, will reach a steady-state.

8. Suggestions to future improvements

For future work it is recommended to quantify the stiffness and estimate the shear strengths with similar findings of this qualitative study. Regarding the undrained shear strength, parallel laboratory tasks after cyclic loading, due to the increased firmness and assessed stiffness, can be performed to verify the estimated shear strength. This could involve vane-test or an unconfined compression test. (Wesley, 2010). This could further improve the comparisons of the undrained shear strengths before and after cyclic loading.

It is also recommended to perform only one test per day to ensure that the specimen has fully dissipated the excess pore pressure before a new cyclic testing takes place. This will enhance the quality of the stiffness evolution.

It is also suggested to perform more tests to study the long-term effects of cyclic loading. This could be done by testing with different types of clays, in addition to adjusting the number of cycles to be performed per parcel. It will be especially interesting to study the relative shear stiffnesses at the end of each parcel (similar to Figure 6.7) to see the developments.

References

Adnan, Z., & Habib, M. M. (2017). The Small Strain Effects to the Shear Strength and Maximum Stiffness of Post-Cyclic Degradation of Hemic Peat Soil. *International Journal of Civil and Environmental Engineering*, *11*(9), 1183-1187.

Amini, Z. A., & Trandafir, A. C. (2008). Post-liquefaction shear behavior of Bonneville Silty-Sand. In *Geotechnical Earthquake Engineering and Soil Dynamics IV*, 1-9.

Andersen, K. H. (1976). *Behaviour of clay subjected to undrained cyclic loading*, Behaviour of offshore structures, Norwegian Geotechnical Institute, Norway, 33-44

Andersen, K. H. (1988). *Properties of soft clay under static and cyclic loading.* International Conference on Engineering Problems of Regional Soils, Beijing, China 1988. Proceedings, 11-26.

Andersen, K. H. (2009). *Bearing capacity under cyclic loading – offshore, along the coast, and on land.* The 21st Bjerrum Lecture presented in Oslo, 23 November 2007, Canadian Geotechnical Journal, 2009, 46(5), 513-535, https://doi.org/10.1139/T09-003

Andersen, K. H., Puech, A. A., & Jardine, R. J. (2013). Cyclic resistant geotechnical design and parameter selection for offshore engineering and other applications. In *Proceedings of the TC-209 Workshop, Design for Cyclic Loading: Piles and Other Foundations, Paris. Presses des Ponts.* 1-36.

Andersen, K. H. (2015). Cyclic soil parameters for offshore foundation design. *Frontiers in offshore geotechnics III*, *5*. 5-82

Arroyo, M., Abadías, D., & Coelho, M. (2015). Alternative py curve formulations for offshore wind turbines in clays. In *Third International Symposium on Frontiers in Offshore Geotechnics*, 693-699.

Ashmawy, A. K., Salgado, R., Guha, S., & Drnevich, V. P. (1995). Soil damping and its use in dynamic analyses. *International conferences on recent advances in Geotechnical Earthquake Engineering and Soil Dynamics*, 9, 35-41.

Bolton, M. D., & Wilson, J. M. R. (1990). *Soil stiffness and damping*. Cambridge University Engineering Department, 209-216.

Boulanger, R. W., Curras, C. J., Kutter, B. L., Wilson, D. W., & Abghari, A. (1999). Seismic soil-pile-structure interaction experiments and analyses. *Journal of Geotechnical and Geoenvironmental Engineering*, *125*(9), 750-759.

Brown, K. & Wherrett, A. (2020). *Bulk Density – Measurement*, Soil Quality Pty Ltd, available at: http://www.soilquality.org.au/factsheets/bulk-density-measurement (last visited: 15/04/2020)

Burland, J. B. (1990). On the compressibility and shear strength of natural clays. *Géotechnique*, *40*(3), 329-378.

Carotenuto, P., Carraro, A., Torres, Y. G., Dyvik, R., Andresen, L., & Cassidy, M. (2018). *Characterization of Kaolin under undrained cyclic loading* [In progress].

Chiang, D. Y. (1999). The generalized Masing models for deteriorating hysteresis and cyclic plasticity. *Applied Mathematical Modelling*, *23*(11), 847-863.

Craig, R. F. (2004). *Craig's Soil Mechanics*, 7th. Spon Press, London and New York, 447 pp., 71-135

Fossen, H. (2016). *Structural geology*, 2nd edition, Cambridge University Press, United Kingdom, 510 pp., 110-111

Gu, X., Yang, J., & Huang, M. (2013). DEM simulations of the small strain stiffness of granular soils: effect of stress ratio. *Granular Matter, 15*(3), 287-298. doi: 10.1007/s10035-013-0407-y

Heidari, M., El Naggar, H., Jahanandish, M., & Ghahramani, A. (2014). Generalized cyclic p–y curve modeling for analysis of laterally loaded piles. *Soil Dynamics and Earthquake Engineering*, *63*, 138-149.

Ibarra, L. F., Medina, R. A., & Krawinkler, H. (2005). Hysteretic models that incorporate strength and stiffness deterioration. *Earthquake engineering & structural dynamics*, *34*(12), 1489-1511.

Jardine, R. J., Andersen K. & Puech, A. (2012). Cyclic loading of offshore piles: potential effects and practical design. Keynote Paper. *Proc 7th Int. Conf. on Offshore Site Investigations and Geotechnics*, SUT London, 59-97.

Kallehave, D., Byrne, B. W., LeBlanc Thilsted, C., Mikkelsen, K. K. (2015) Optimization of monopiles for offshore wind turbines. *Phil. Trans. R. Soc. A* 373: 20140100. http://dx.doi.org/10.1098/rsta.2014.0100

Karlsrud, K., & Nadim, F. (1990). Axial capacity of offshore piles in clay. In *Offshore Technology Conference*. Offshore Technology Conference. 405-416.

Knappett, J. A., & Craig, R. F. (2012). *Craig's Soil Mechanics*, 8th. Spon Press, London And New York, 552pp., 327-363. Available at: http://search.ebscohost.com.ezproxy.uio.no/login.aspx?direct=true&db=nlebk&AN=441274&site=ehost-live (last visited: 06/09/2019).

Li, S., Zhang, Y., & Jostad, H. P. (2019). Drainage conditions around monopiles in sand. *Applied Ocean Research*, *86*, 111-116.

McCarthy, D. F. (2007). *Essentials of soil mechanics and foundations – basic geotechnics*, 7th edition, Pearson Education, Inc., New Jersey, 850 pp., 65 + 332-383

Memarpour, M. M., Kimiaei, M., Shayanfar, M., & Khanzadi, M. (2012). Cyclic lateral response of pile foundations in offshore platforms. *Computers and Geotechnics*, *42*, 180-192.

MTS Systems Corporation (2009). *MTS Series 793 Tuning and Calibration*, manual part number: 100- 147-134 E, 216 pp., 19-26 + 67

MTS Systems Corporation (2011). *MTS Model 793.10 MultiPurpose TestWare® and Series 793 Application Software*, manual part number: 100-147-131-H, MTS, 574, 18-19

Muir Wood, D., Lings, M. L., Nash, D. T., & Gajo, A. (2001). Anisotropy of soils: laboratory measurements and constitutive implementation. In *International Conference on soil mechanics and geotechnical engineering*. 321-324.

Nagase, H., & Ishihara, K. (1988). Liquefaction-induced compaction and settlement of sand during earthquakes. *Soils and Foundations*, *28*(1), 65-76.

Neuzil, C. E. (2003). Hydromechanical coupling in geologic processes. *Hydrogeology Journal*, *11*(1), 41-83.

Norwegian Geotechnical Institute (2019). *Detailed Soil Investigation Carcará. Vol. 2: Measured and derived geotechnical parameters and final results*. [Restricted access].

Norwegian Geotechnical Institute (n.d.). *Procedure for evaluation of the p-y tests.* [Unpublished]. Norwegian Geotechnical Institute.

Paul, S. K., Sivaprasad, S., Dhar, S., & Tarafder, S. (2011). Key issues in cyclic plastic deformation: experimentation. *Mechanics of Materials*, *43*(11), 705-720.

Randolph, M. F., & Houlsby, G. T. (1984). The limiting pressure on a circular pile loaded laterally in cohesive soil. *Geotechnique*, *34*(4), 613-623.

Richart, Jr., F. E., & Wylie, E. B. (1977). Influence of Dynamic Soil Properties on Response of Soil Masses, In: Hall, W. J. (editor). *Structural and Geotechnical Mechanics*, Prentice Hall, Englewood Cliffs, New Jersey. 442 pp., 141-162

Sachan, A., & Penumadu, D. (2007). Effect of microfabric on shear behavior of kaolin clay. *Journal of geotechnical and geoenvironmental engineering*, *133*(3), 306-318.

Semblat, J. F. & Pecker, A. (2009). *Waves and Vibrations in Soils: Earthquakes, Traffic, Shocks, Construction works*. IUSS Press, Pavia, Italy. 499 pp., 53-129

Sheil, B. B., & McCabe, B. A. (2017). Biaxial loading of offshore monopiles: numerical modeling. *International Journal of Geomechanics*, *17*(2), 04016050, 1-16.

Sitharam, T. G., Vinod, J. S., & Ravishankar, B. V. (2009). Post-liquefaction undrained monotonic behaviour of sands: experiments and DEM simulations. *Géotechnique*, *59*(9), 739-749.

Skelton, R. P., Maier, H.-J., & Christ, H. J. (1997). The Bauschinger effect, Masing model and the Ramberg–Osgood relation for cyclic deformation in metals. *Materials Science and Engineering: A*, *238*(2), 377-390.

Sloane, R. L., & Kell, T. R. (1966). The fabric of mechanically compacted kaolin. In *Clays and Clay Minerals*. 289-296. Pergamon.

Statkraft, (2019). *Globale energitrender og norske muligheter – Statkrafts Lavutslippsscenario.* Statkraft Lillehammer, 40 pp. Available at: https://www.statkraft.com/globalassets/0-new-external-web/.no/nyheter/lavutslippsscenario/lavutslippsscenario2019.pdf/ (last visited: 11/06/2020)

Støren, A. S. (2018). *Behaviour of piles in clay subjected to cyclic lateral loading* (master thesis). Department of Civil and Environmental Engineering, Norwegian University of Science and Technology

Wang, Y., Lei, J., Gong, X., Wang, Y., & Yang, P. (2018). Post-cyclic undrained shear behavior of marine silty clay under various loading conditions. *Ocean Engineering*, *158*, 152-161

Wesley, L. D. (2003). Residual strength of clays and correlations using Atterberg limits. *Geotechnique*, *53*(7), 669-672, https://doi.org/10.1680/geot.2003.53.7.669

Wesley, L. D. (2010). *Fundamentals of soil mechanics for sedimentary and residual soils*, John Wiley & Sons, Inc., New Jersey, 431 pp.

Westerberg, B. (1999). *Behaviour and Modelling of a Natural Soft Clay – Triaxial testing, constitutive relations and finite element modelling* (doctoral thesis), Luleå University of Technology, 198 pp., 63-72.

World Steel Association (2012). *Steel solutions in the green economy - Wind turbines.* World Steel Association. 16 pp. Available at: https://www.worldsteel.org/en/dam/jcr:41f65ea2-7447-4489-8ba7-9c87e3975aab/Steel+solutions+in+the+green+economy:+Wind+turbines.pdf (last visited: 11/06/2020).

Yasuhara, K., & Andersen, K. H. (1987). Clay behaviour of long-term cyclic loading. In *Proc. 22nd Japan Conf. SMFE*, 2, 535-538

Zakeri, A., Clukey, E. C., Kebadze, E. B., & Jeanjean, P. (2016). Fatigue analysis of offshore well conductors: Part I–Study overview and evaluation of Series 1 centrifuge tests in normally consolidated to lightly over-consolidated kaolin clay. *Applied Ocean Research*, *57*, 78-95.

Zakeri, A., Sturm, H., Dyvik, R., & Jeanjean, P. (2017). Development of novel apparatus to obtain soil resistance–displacement relationship for well conductor fatigue analysis. *Canadian Geotechnical Journal*, *54*(10), 1435-1446.

Zhang, Y., & Andersen, K. H. (2017). Scaling of lateral pile p-y response in clay from laboratory stress-strain curves. *Marine Structures*, *53*, 124-135.

Zhang, Y., & Andersen, K. H. (2019). Soil reaction curves for monopiles in clay. *Marine Structures*, *65*, 94-113.

Zhang, Y., Andersen, K. H., & Jeanjean, P. (2019). Cyclic p-y curves in clays for offshore structures. In *Offshore Technology Conference, OTC-29346-MS*. Offshore Technology Conference. 1-36.

Appendix A – Cyclic results

Appendix A1 – DT1

Cyclic loops and parameters for each cyclic parcel are included.

Cyclic loops

Each plot displays the cyclic behaviour of the kaolin-sample during cyclic loading. No vertical consolidation is taken place.

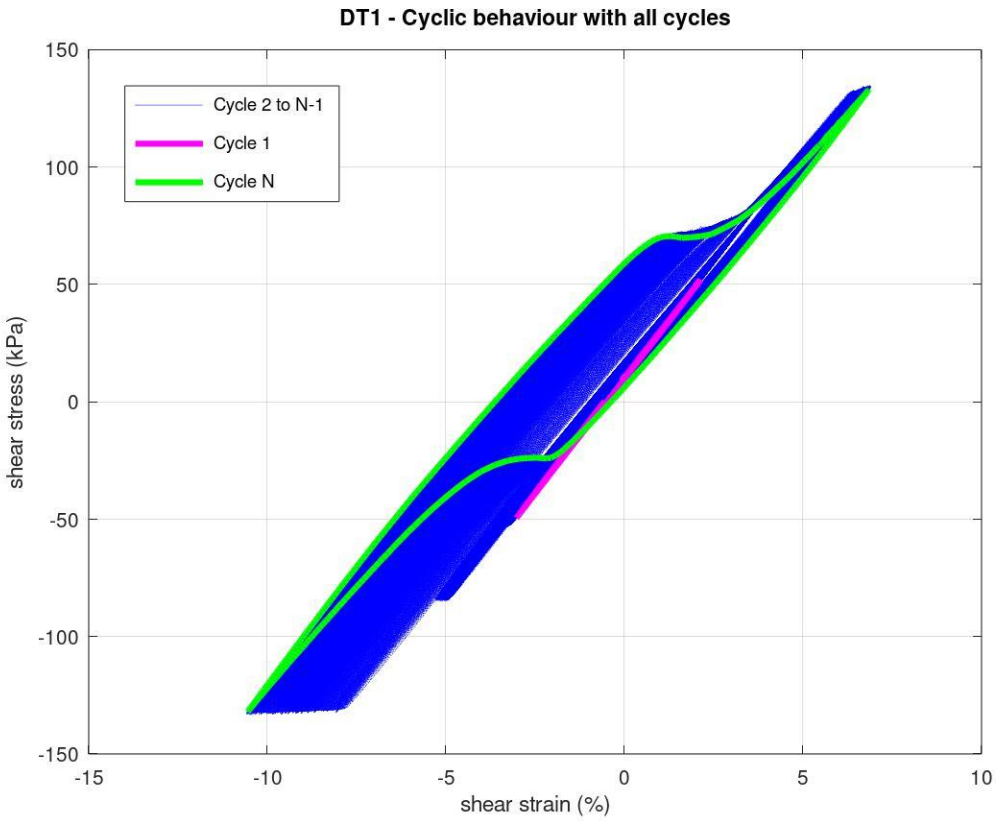

Figure A.1 - Cyclic loading of all parcels.

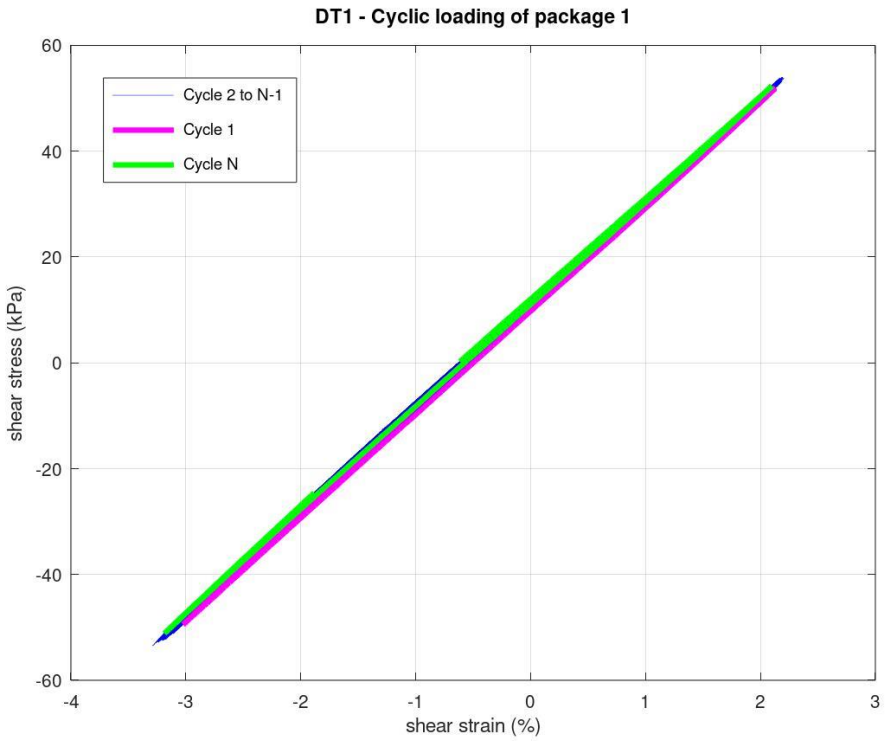

Figure A.2 - Cyclic loading of parcel 1.

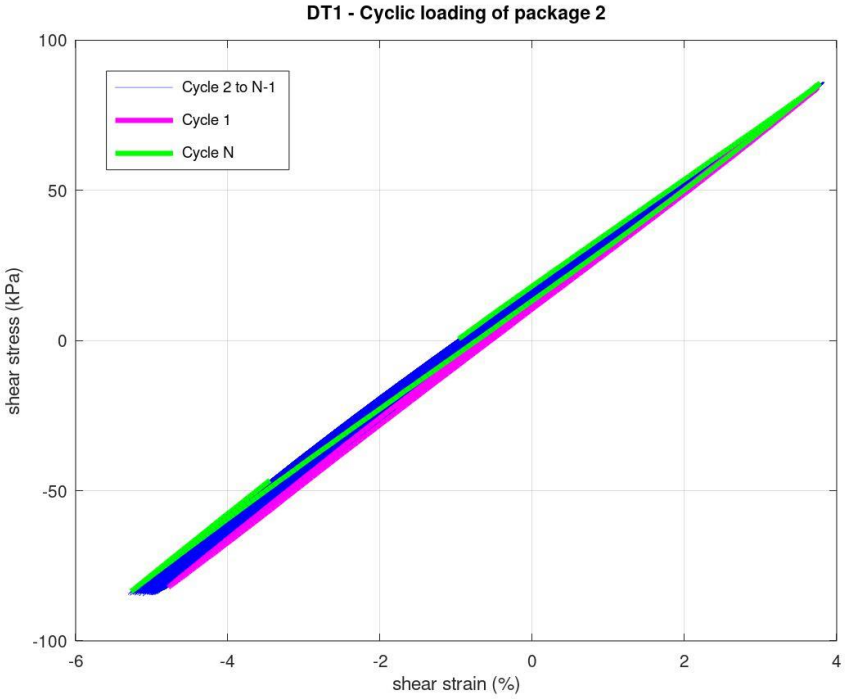

Figure A.3 - Cyclic loading of parcel 2.

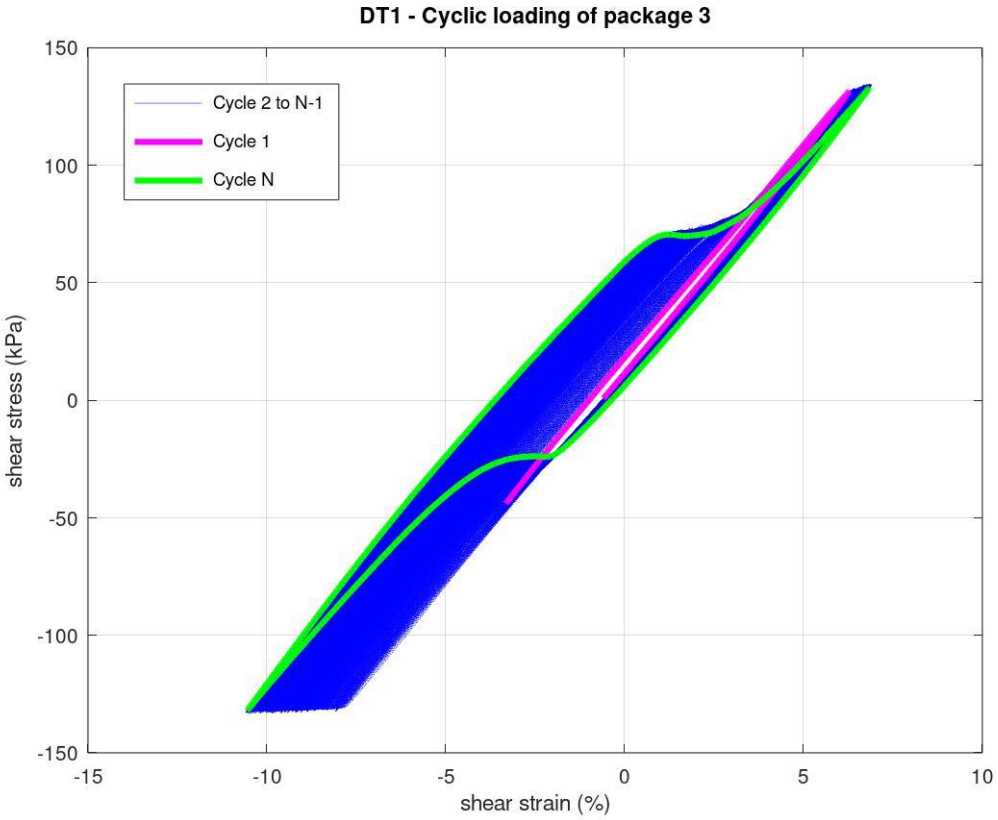

Figure A.4 - Cyclic loading of parcel 3.

Cyclic parameters

Parameters are calculated through the DLP-script, provided by NGI.

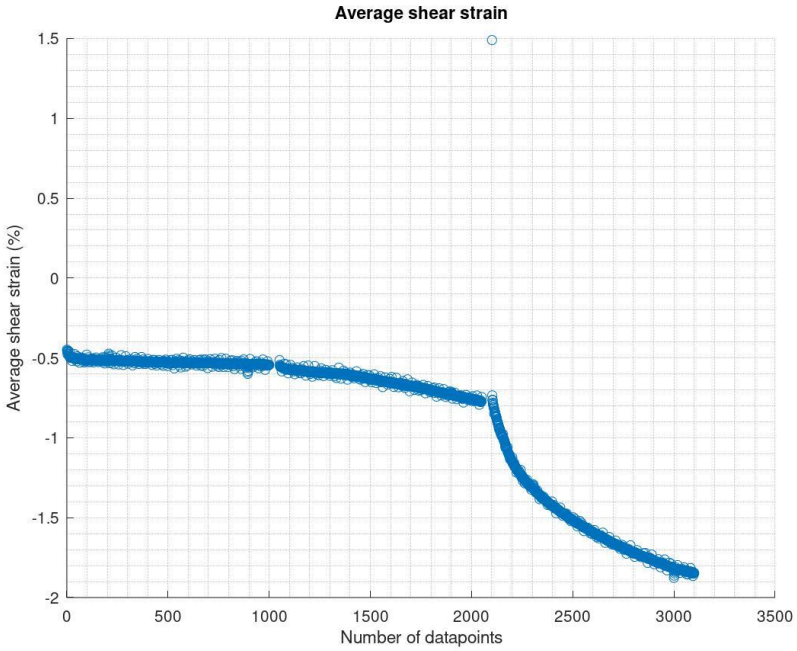

Figure A.5 – Average shear strain.

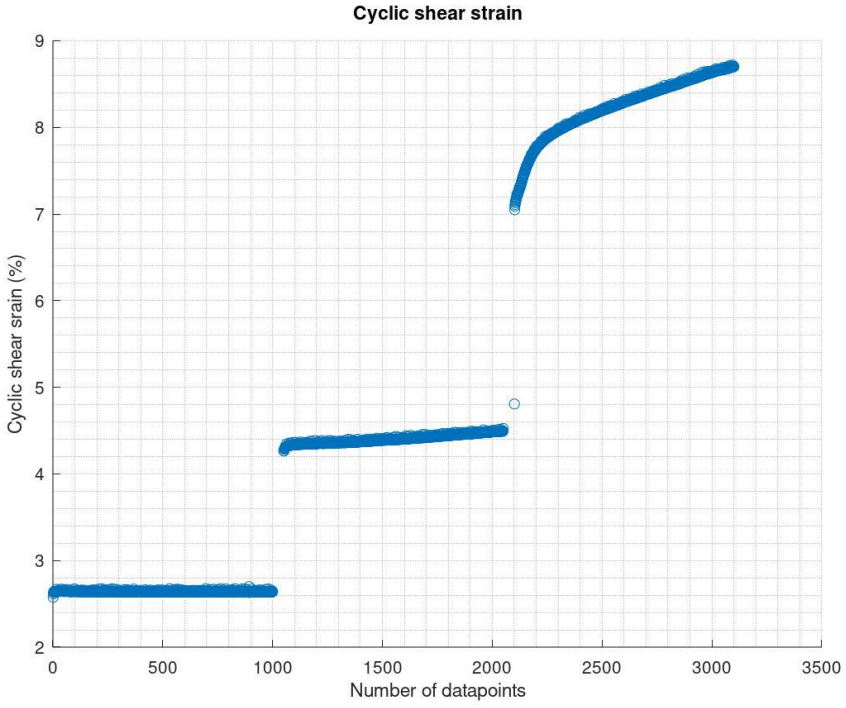

Figure A.6 – Cyclic shear strain.

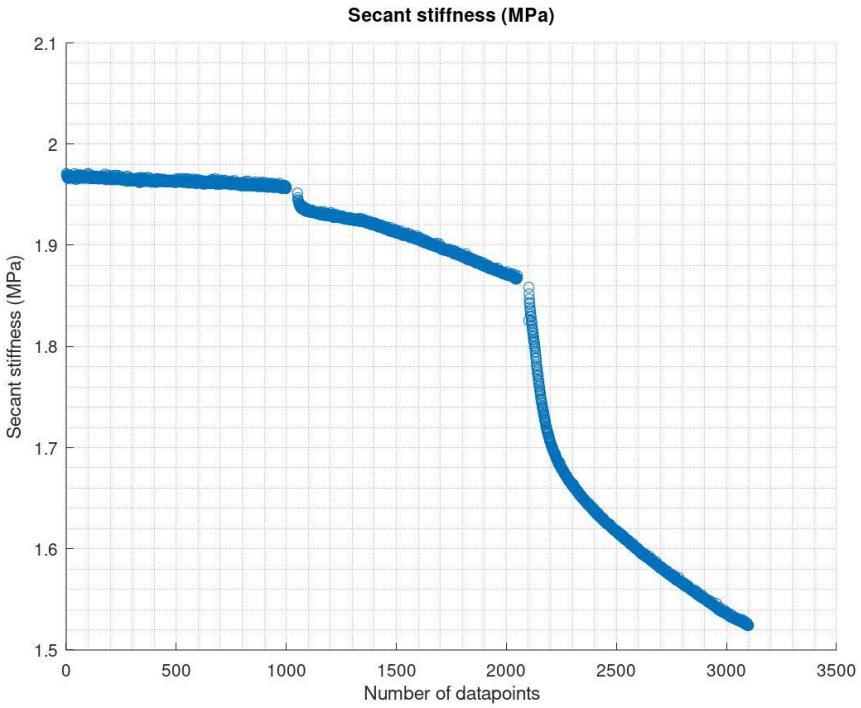

Figure A.7 – Secant stiffness.

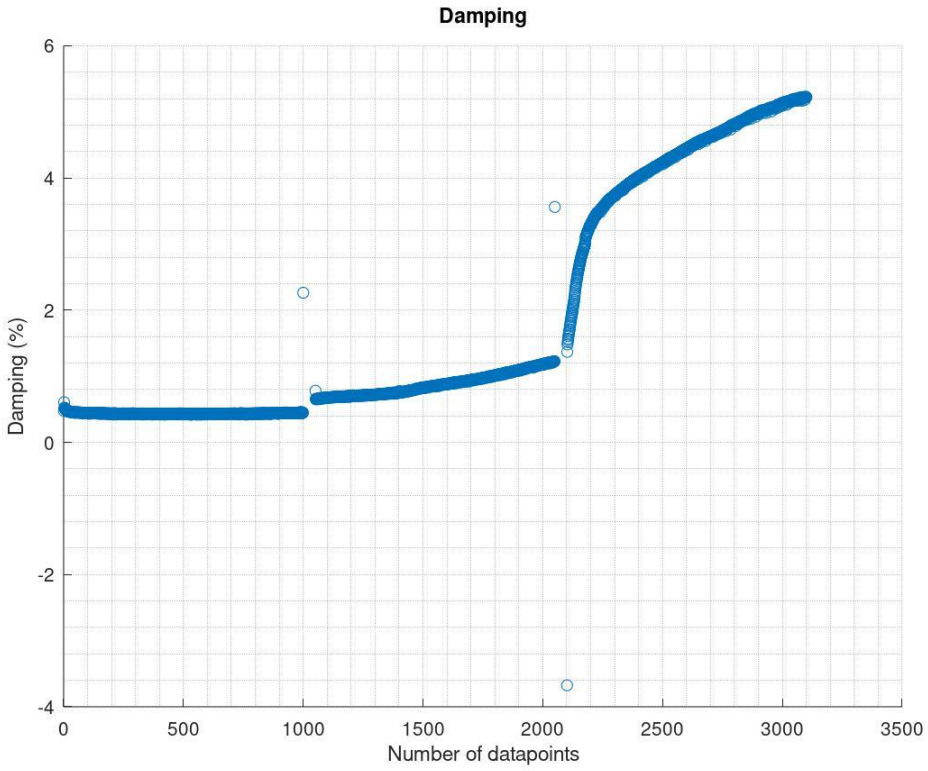

Figure A.8 – Damping.

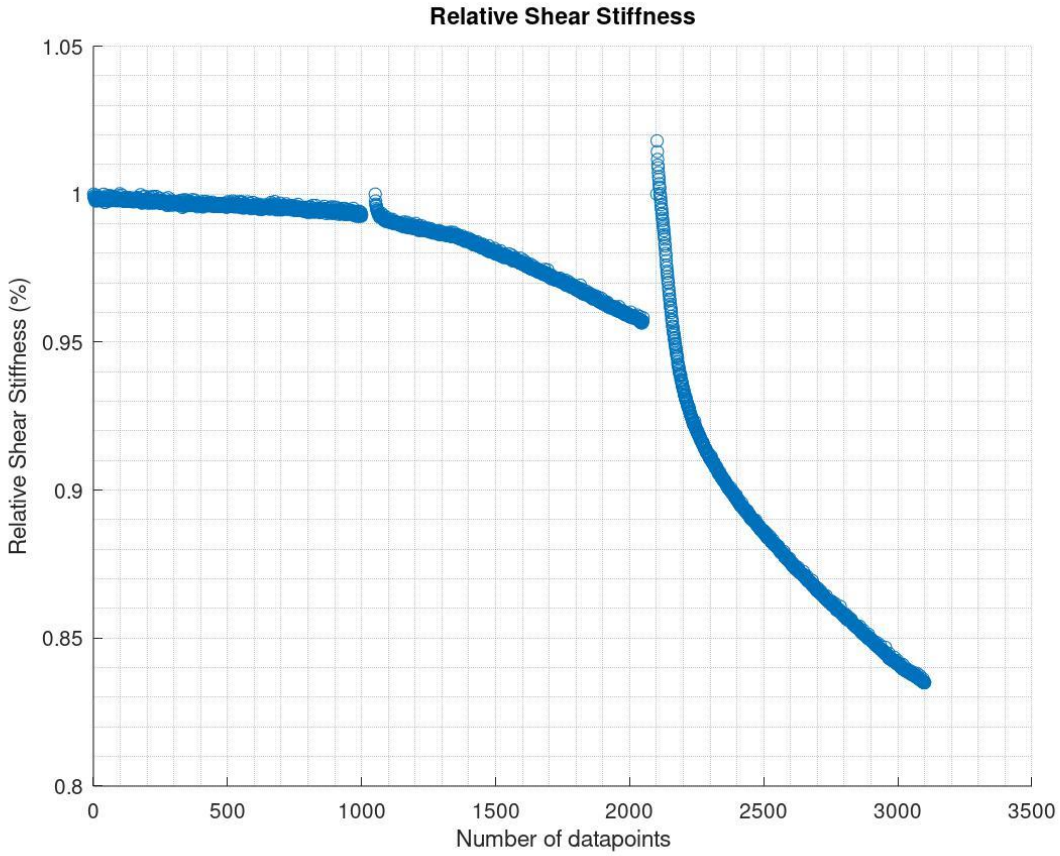

Figure A.9 – Relative shear stiffness.

Appendix A2 – DT2

Cyclic loops and parameters for each cyclic parcel are included.

Cyclic loops

Each plot displays the cyclic behaviour of the kaolin-sample during cyclic loading. No vertical consolidation is taken place.

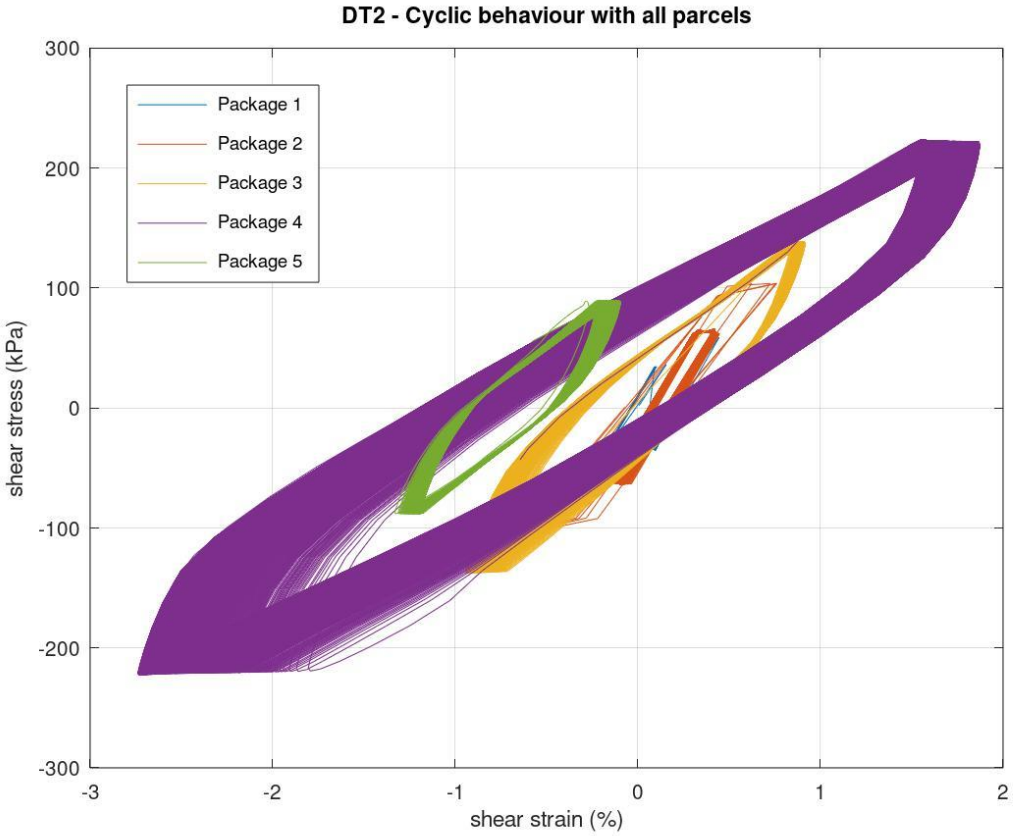

Figure A.10 - Cyclic loading of all parcels.

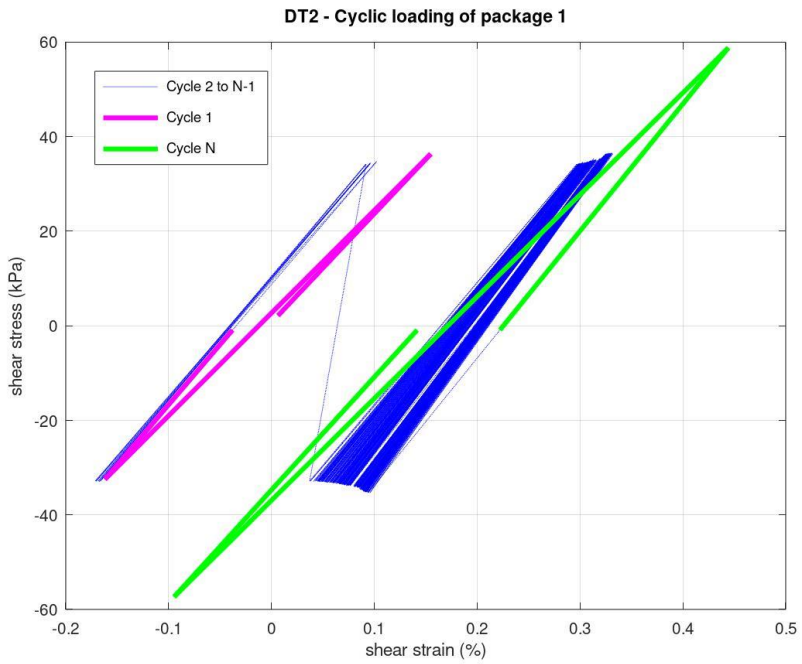

Figure A.11 - Cyclic loading of parcel 1.

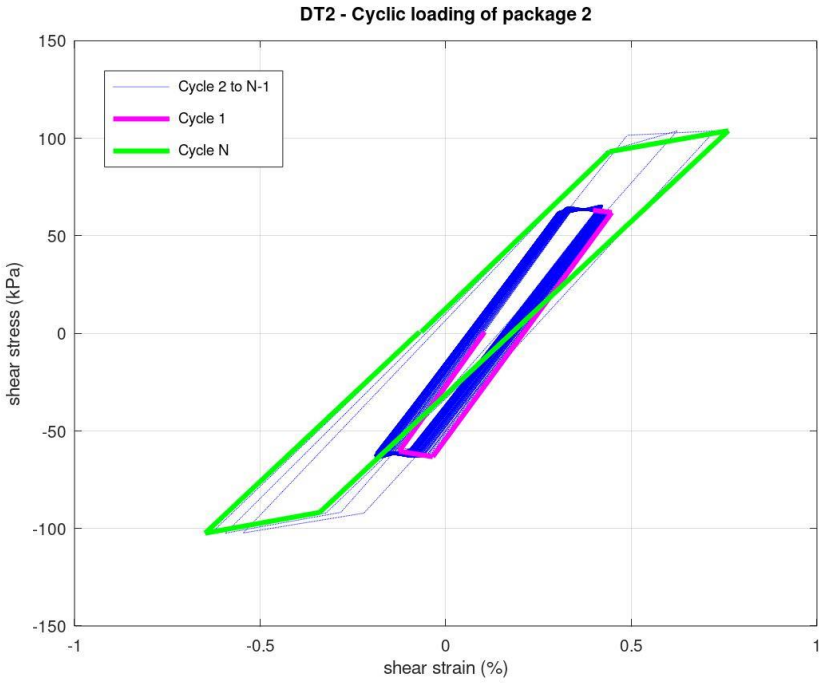

Figure A.12 - Cyclic loading of parcel 2.

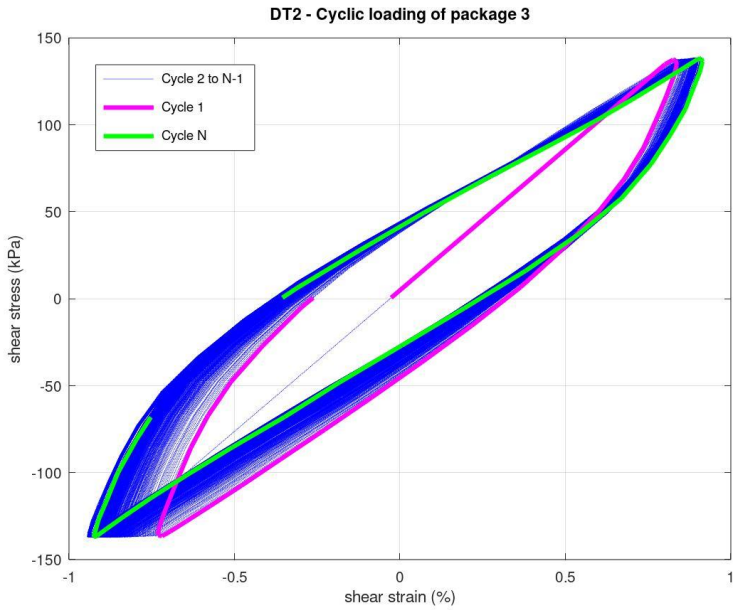

Figure A.13 - Cyclic loading of parcel 3.

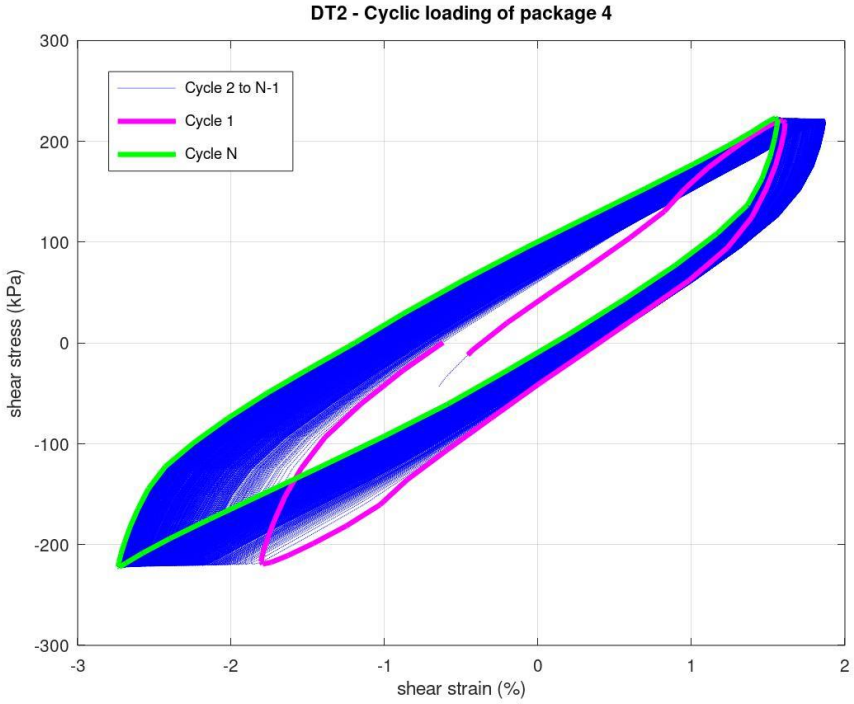

Figure A.14 - Cyclic loading of parcel 4.

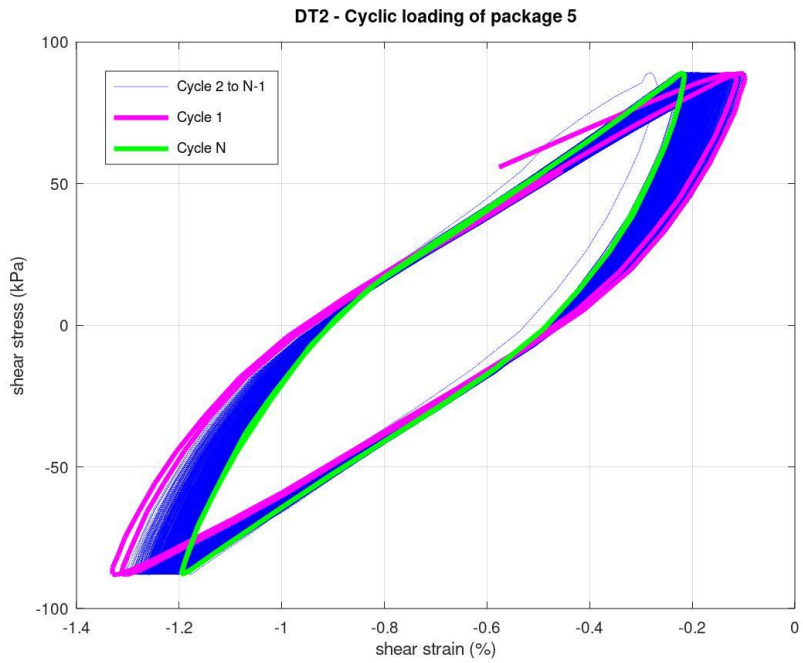

Figure A.15 - Cyclic loading of parcel 5.

Cyclic parameters

Parameters are calculated through the DLP-script, provided by NGI.

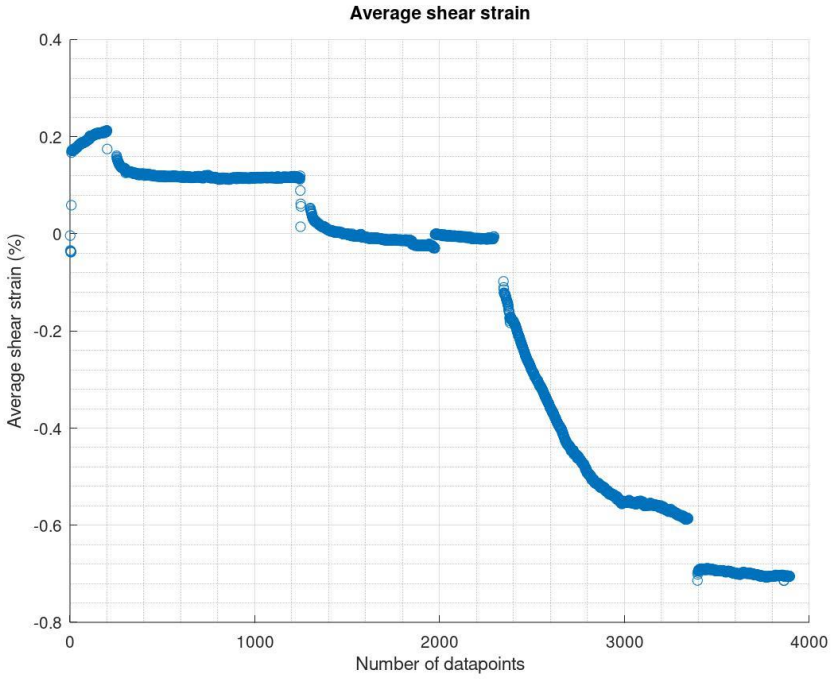

Figure A.16 - Average shear strain.

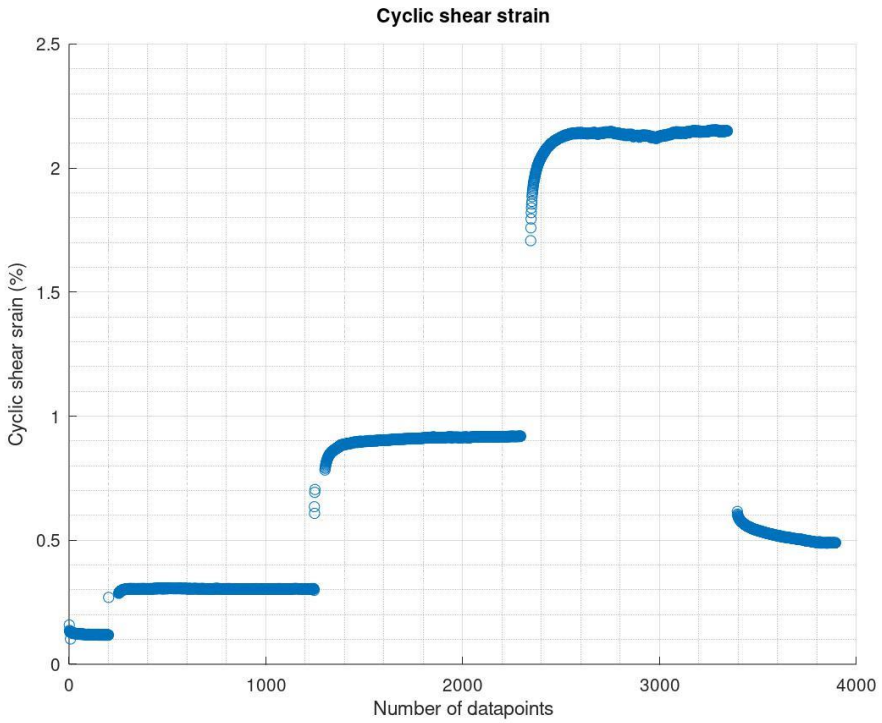

Figure A.17 – Cyclic shear strain.

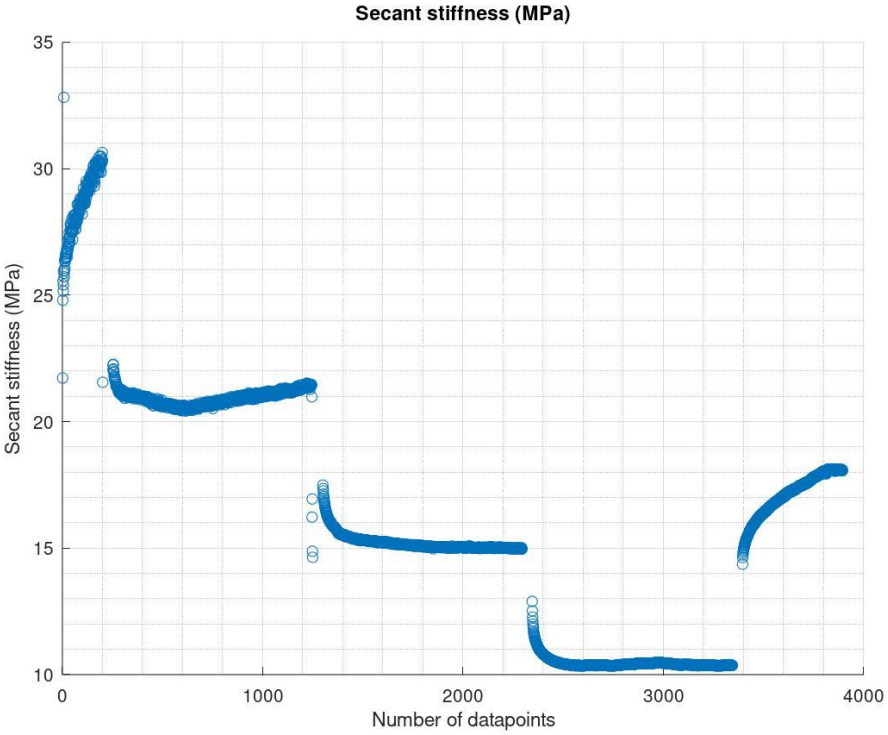

Figure A.18 – Secant stiffness.

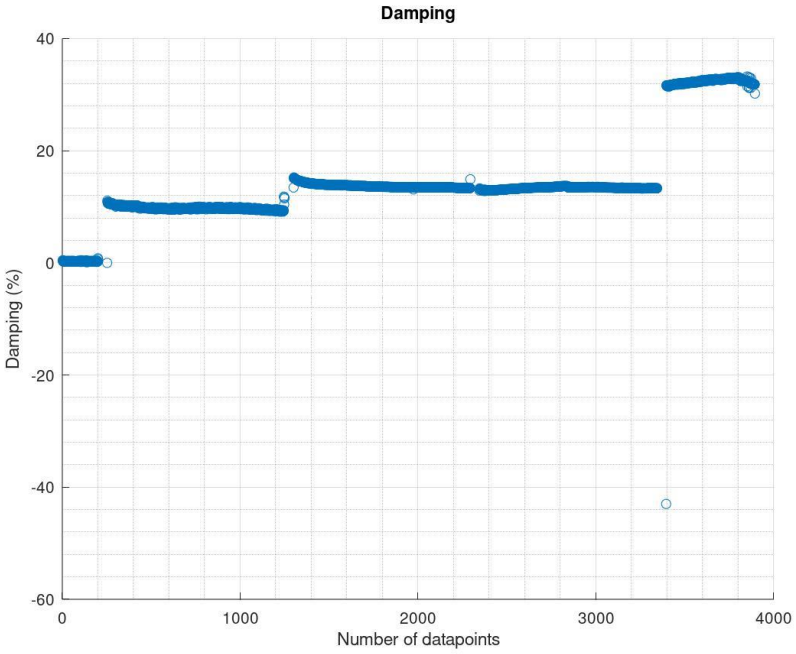

Figure A.19 – Damping

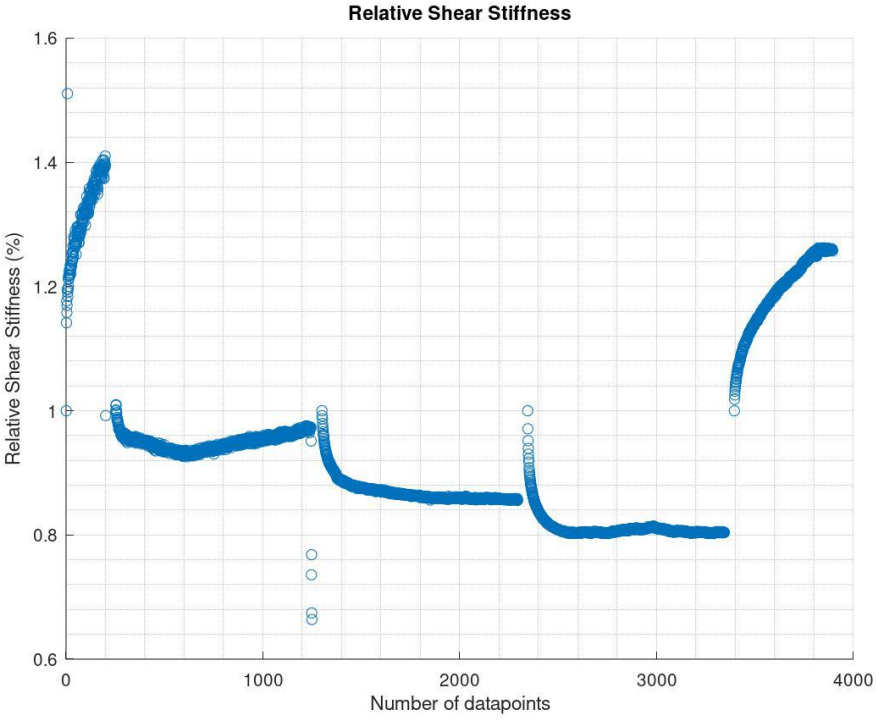

Figure A.20 – Relative shear stiffness.

Appendix A3 – KT1

Cyclic loops and parameters for each cyclic parcel are included.

Cyclic loops

Each plot displays the cyclic behaviour of the kaolin-sample during cyclic loading. Axial consolidation is taken place alongside the cyclic loading.

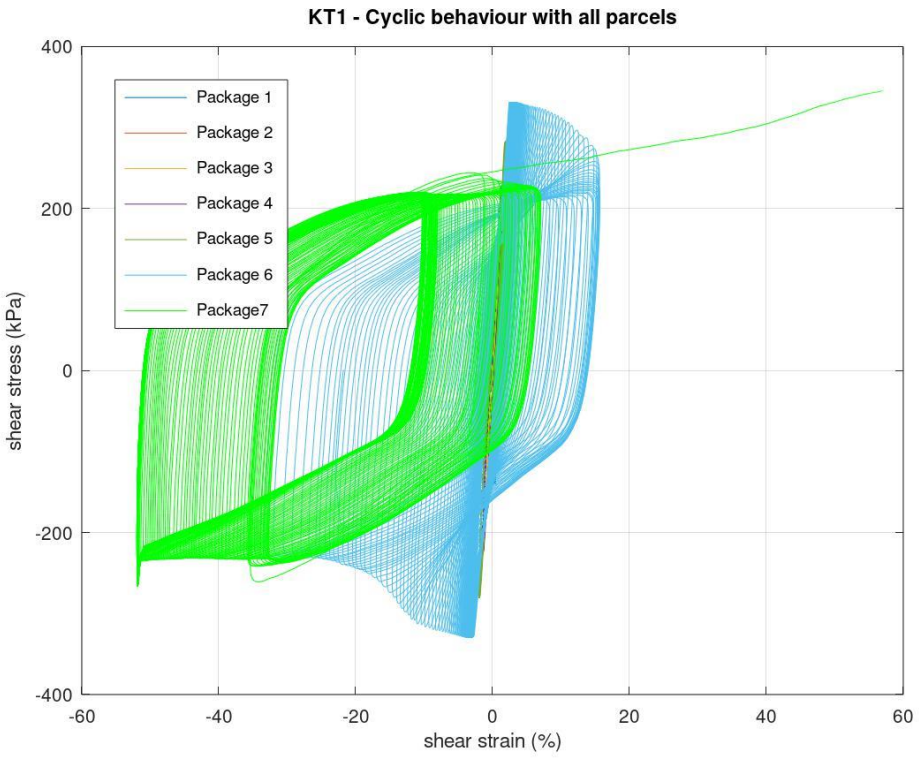

Figure A.21 - Cyclic loading of all parcels.

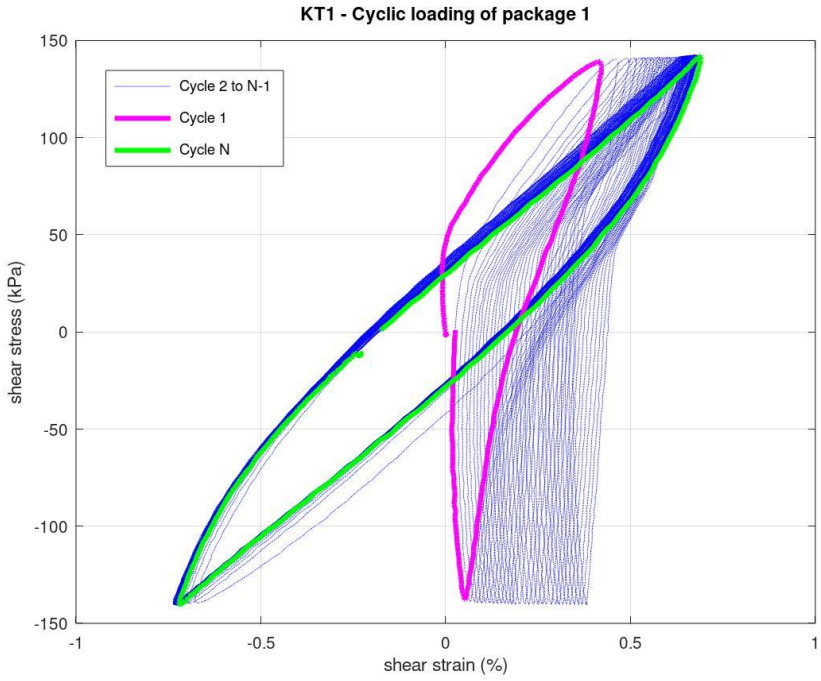

Figure A.22 - Cyclic loading of parcel 1.

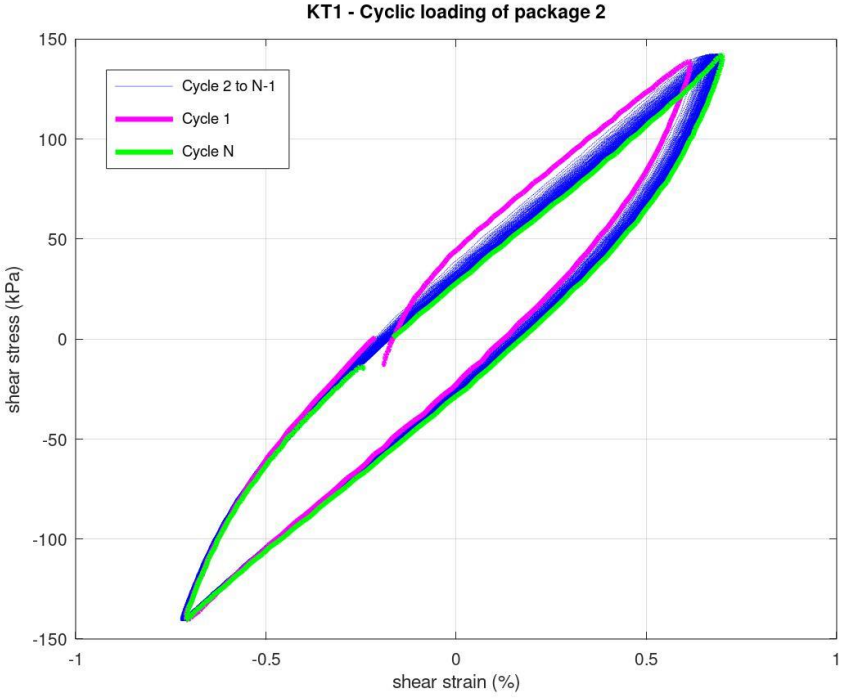

Figure A.23 - Cyclic loading of parcel 2.

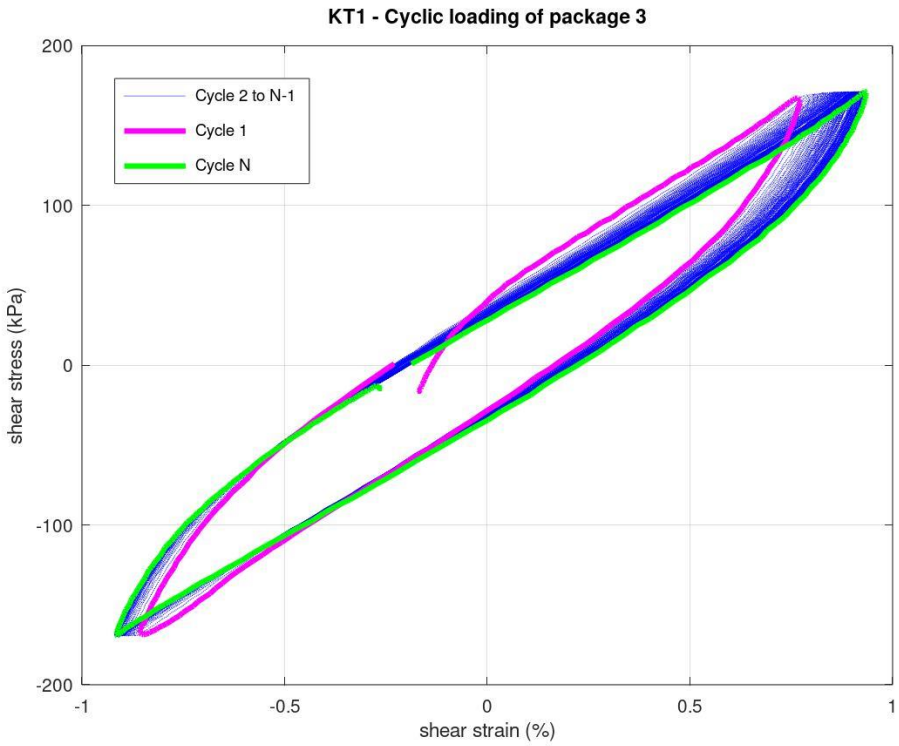

Figure A.24 - Cyclic loading of parcel 3.

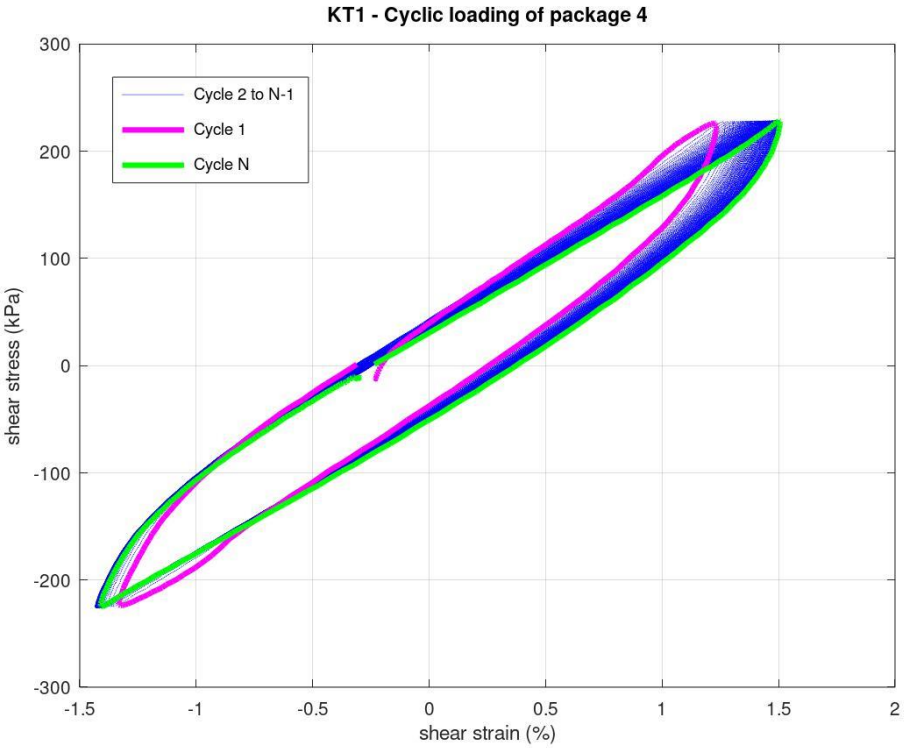

Figure A.25 - Cyclic loading of parcel 4.

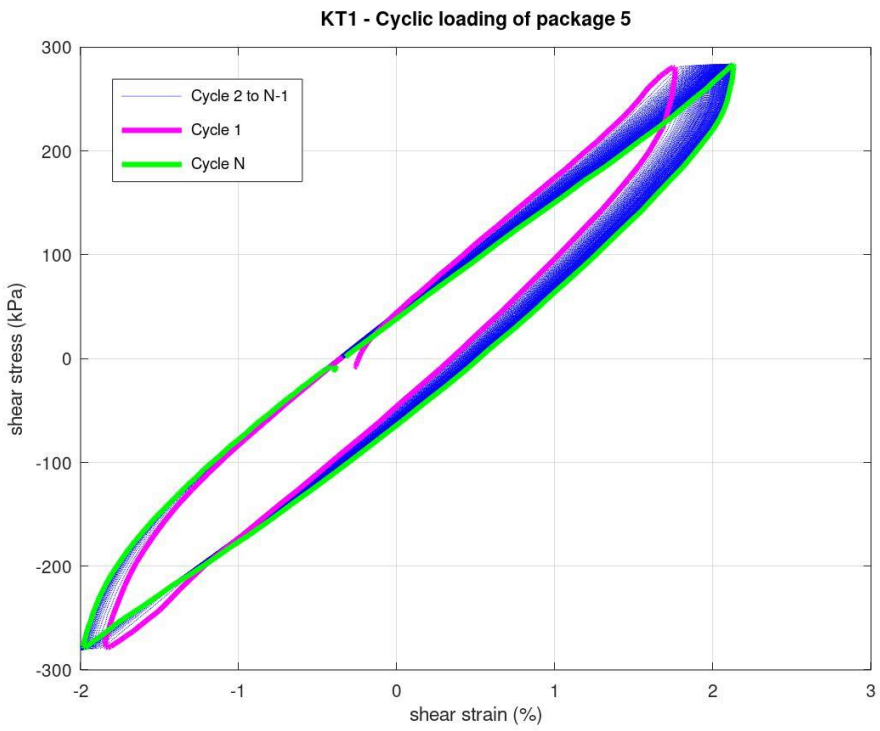

Figure A.26 - Cyclic loading of parcel 5.

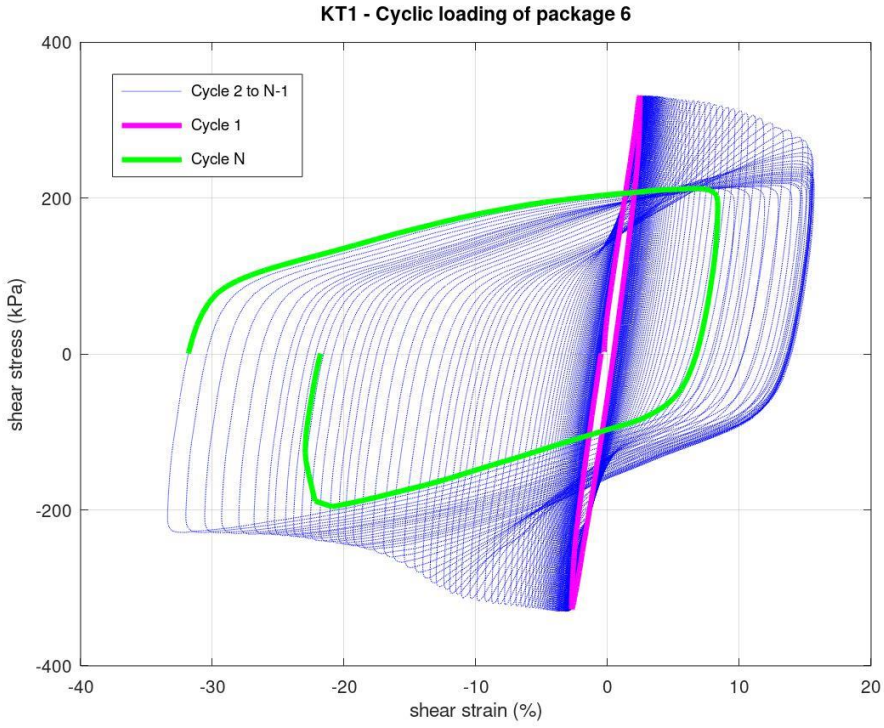

Figure A.27 - Cyclic loading of parcel 6.

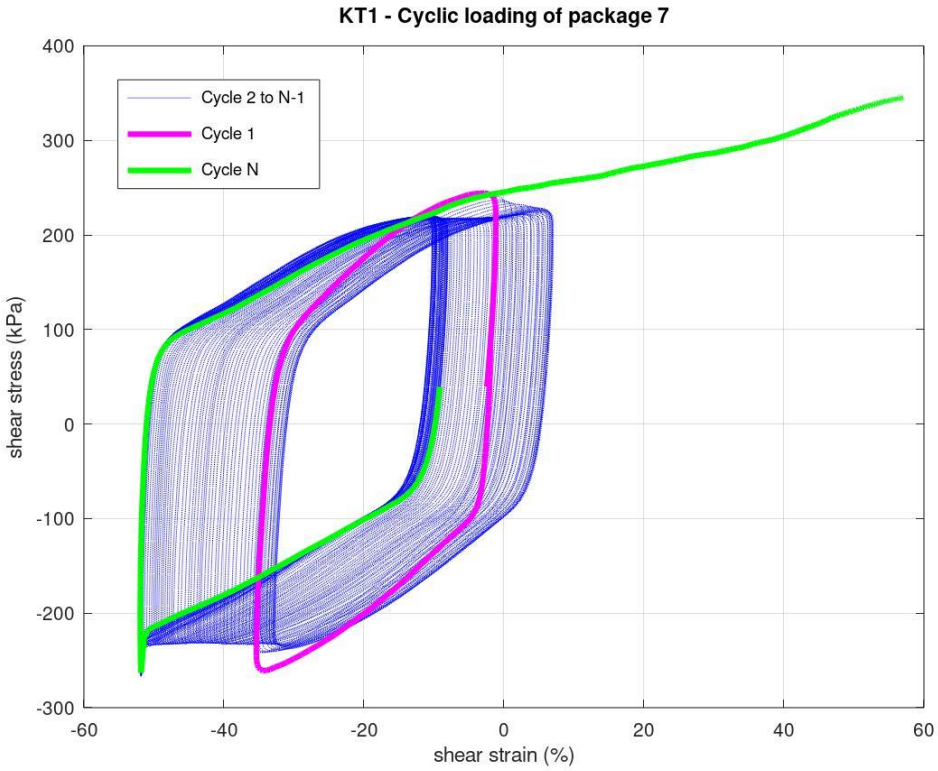

Figure A.28 - Cyclic loading of parcel 7.

Cyclic parameters

Parameters are calculated through the DLP-script, provided by NGI.

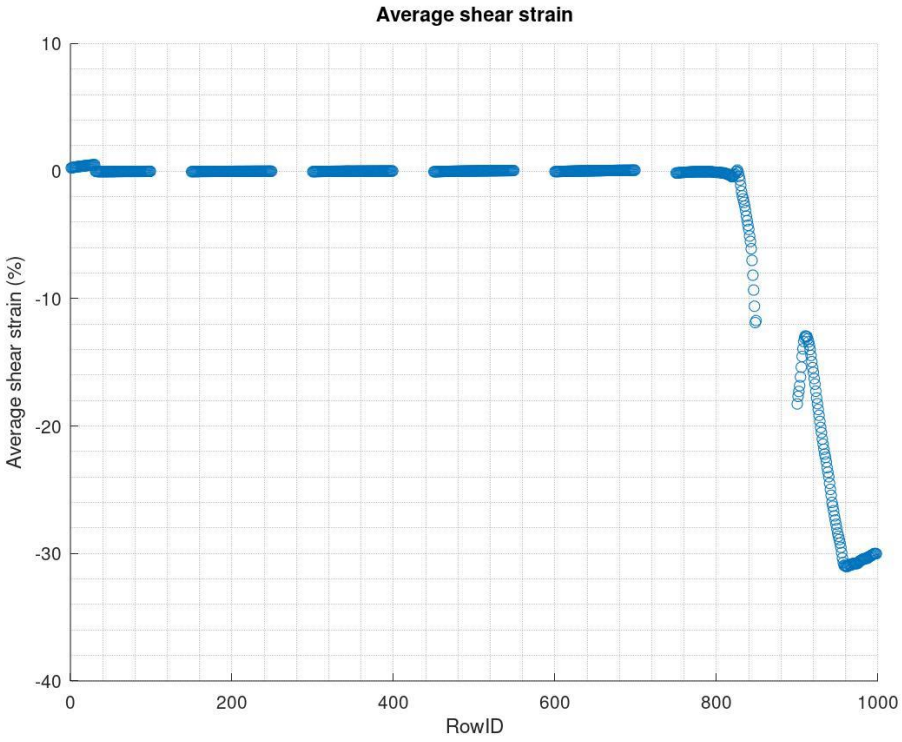

Figure A.29 - Average shear strain.

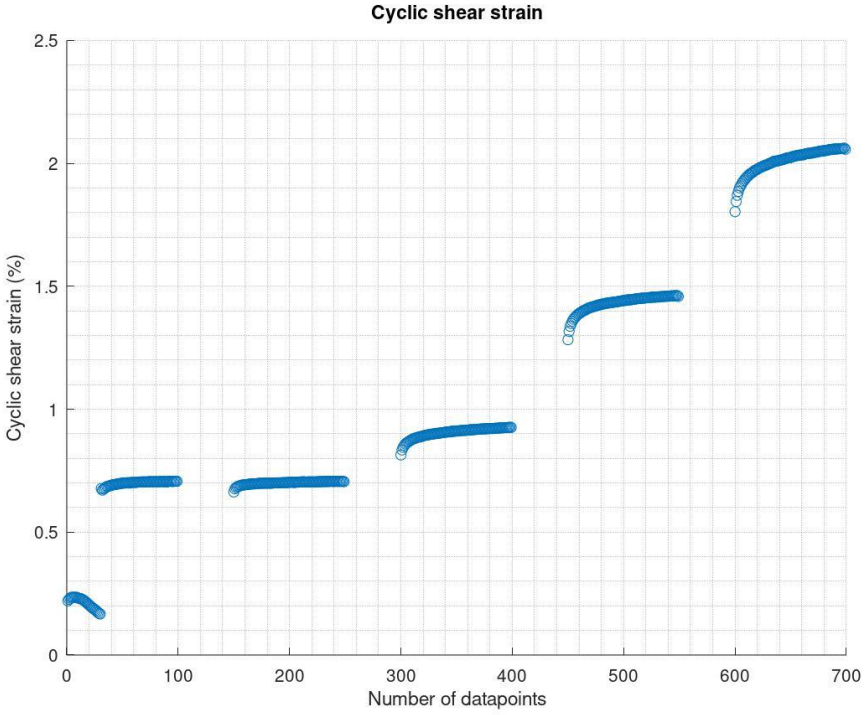

Figure A.30 – Cyclic shear strain.

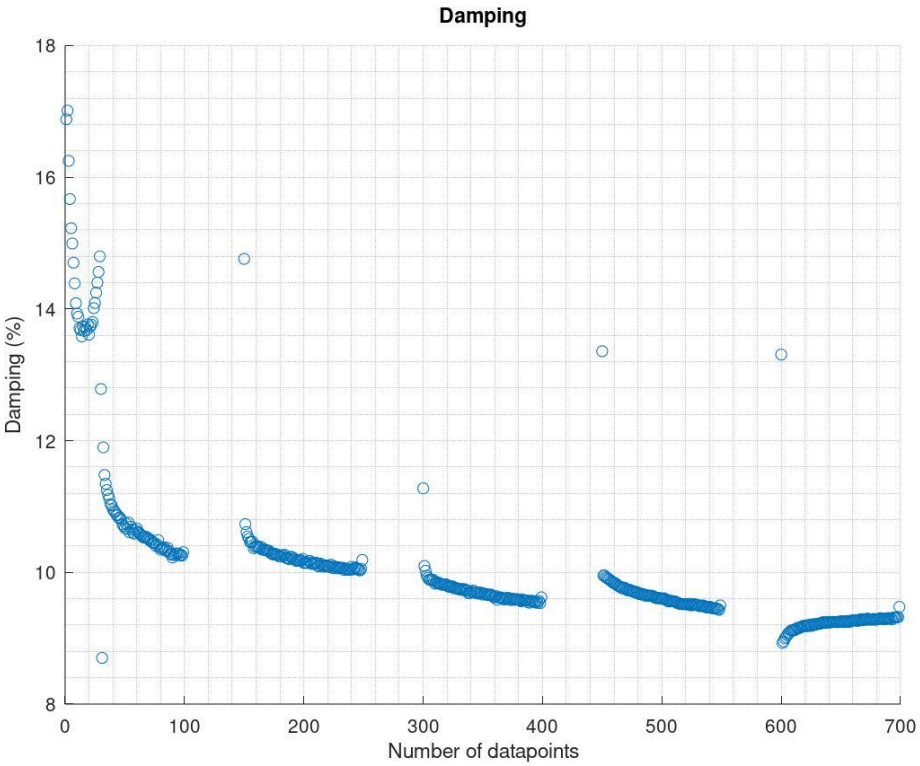

Figure A.31 – Damping.

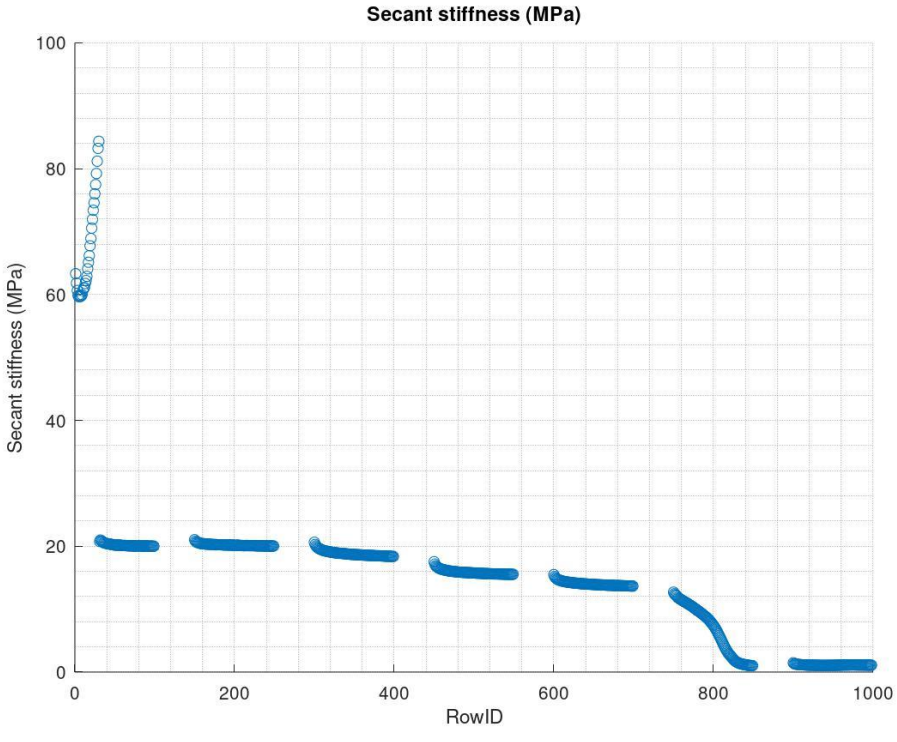

Figure A.32 – Secant stiffness.

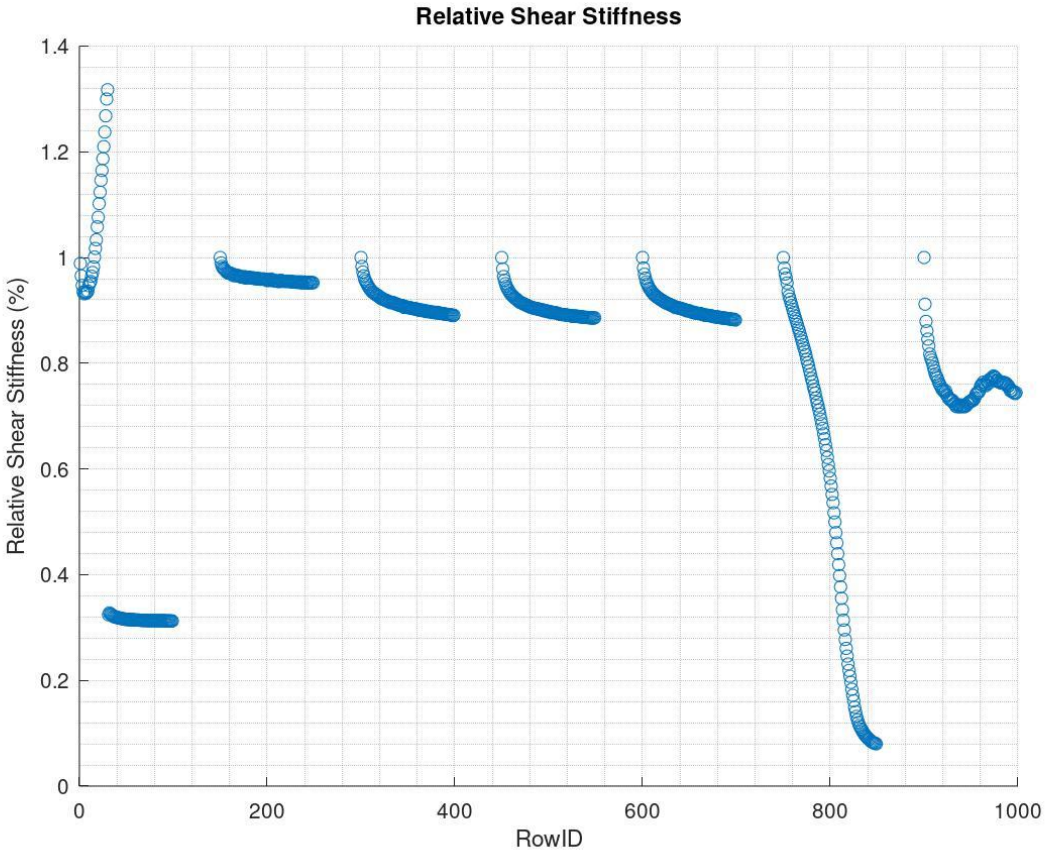

Figure A.33 – Relative shear stiffness.

Appendix A4 – KT2

Cyclic loops and parameters for each cyclic parcel are included.

Cyclic loops

Each plot displays the cyclic behaviour of the kaolin-sample during cyclic loading. Axial consolidation is taken place alongside the cyclic loading.

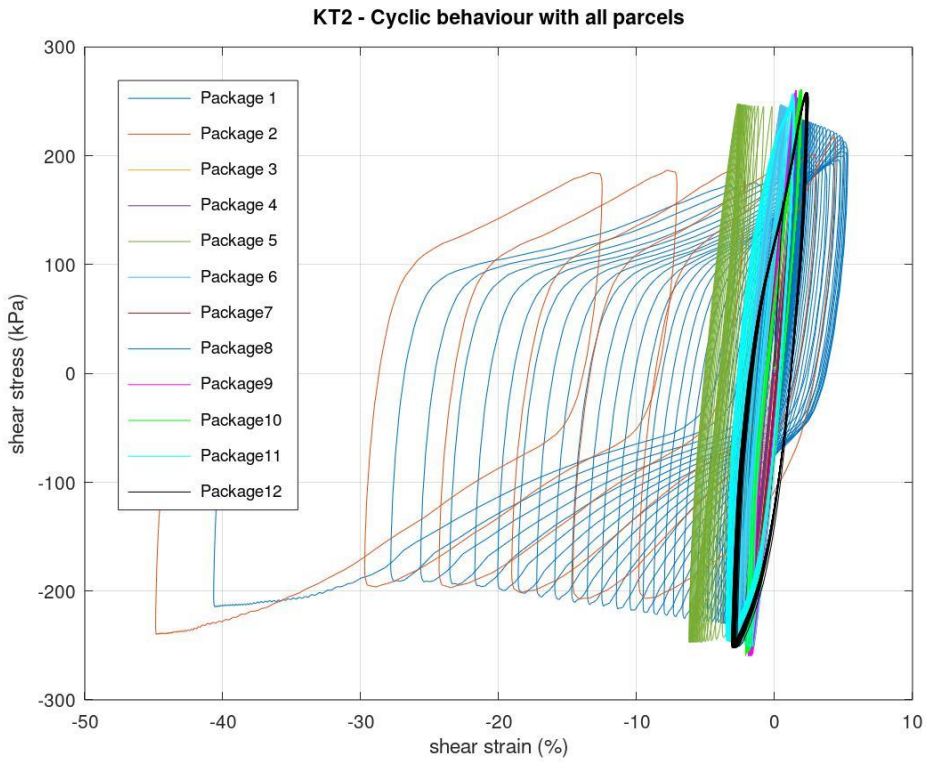

Figure A.34- Cyclic loading of all parcels.

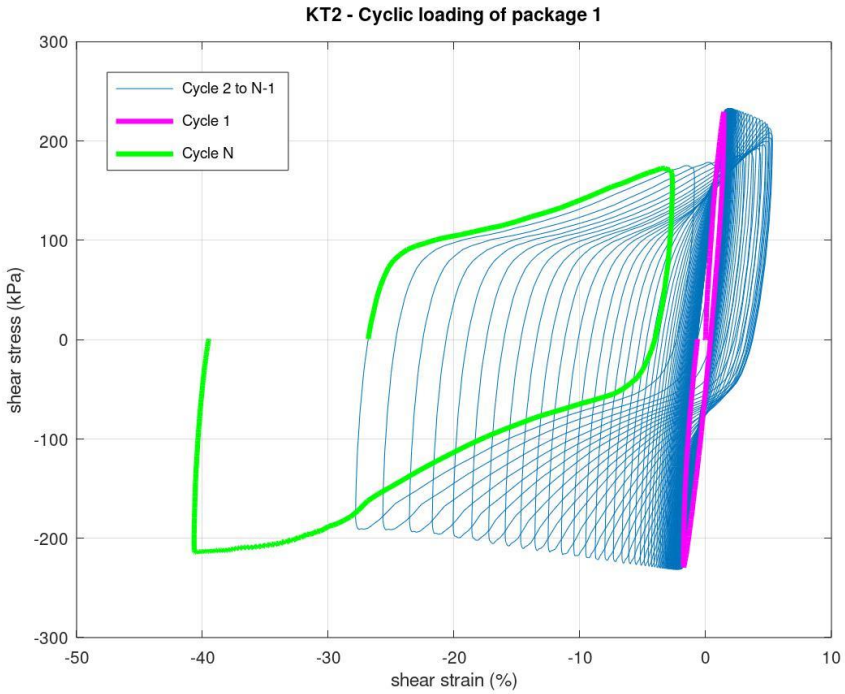

Figure A.35 - Cyclic loading of parcel 1.

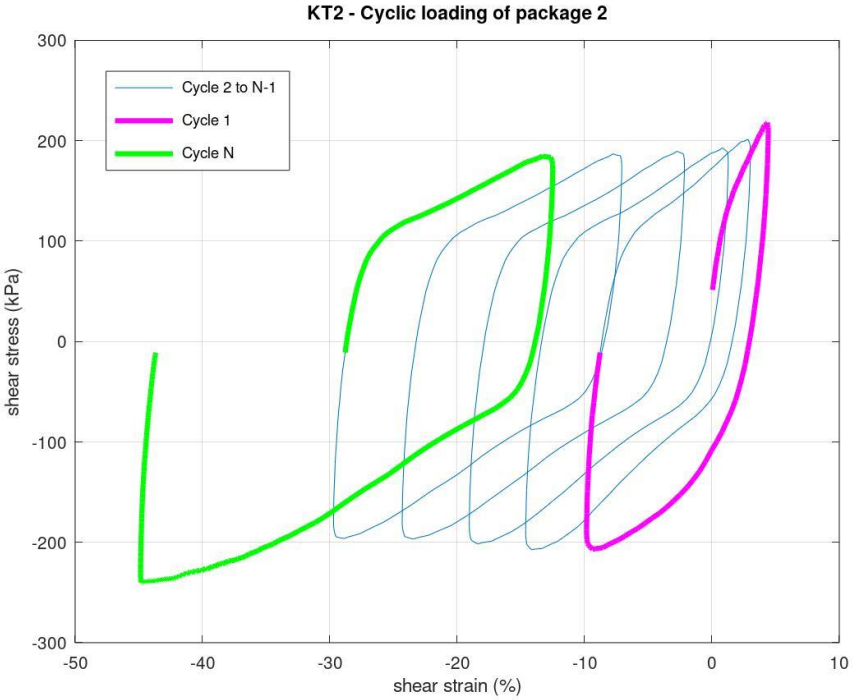

Figure A.36 - Cyclic loading of parcel 2.

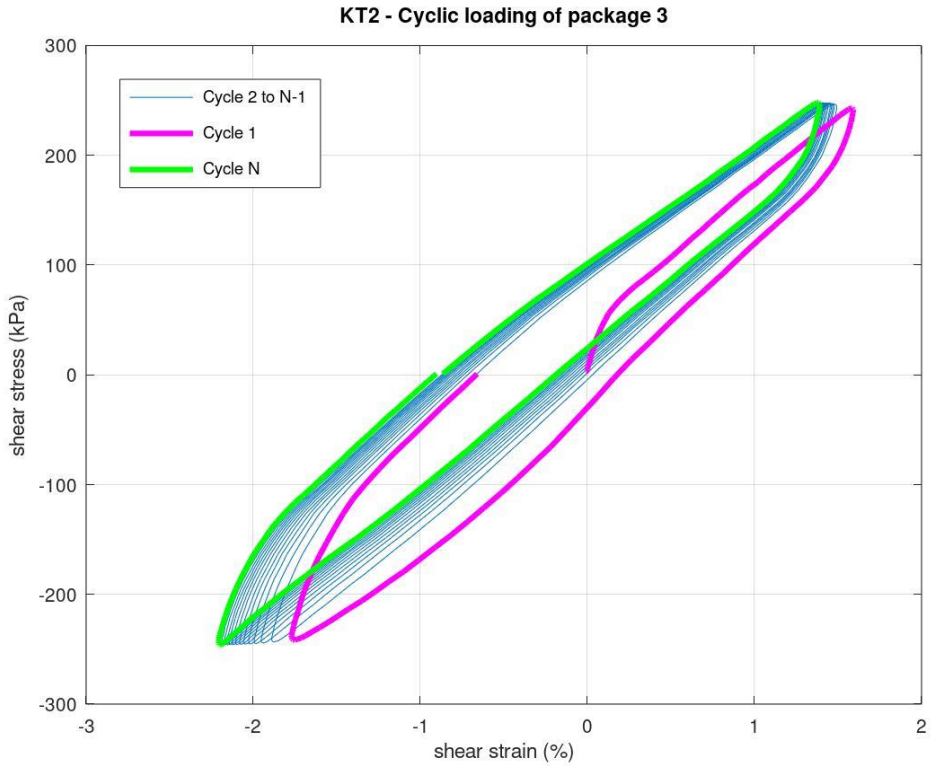

Figure A.37 - Cyclic loading of parcel 3.

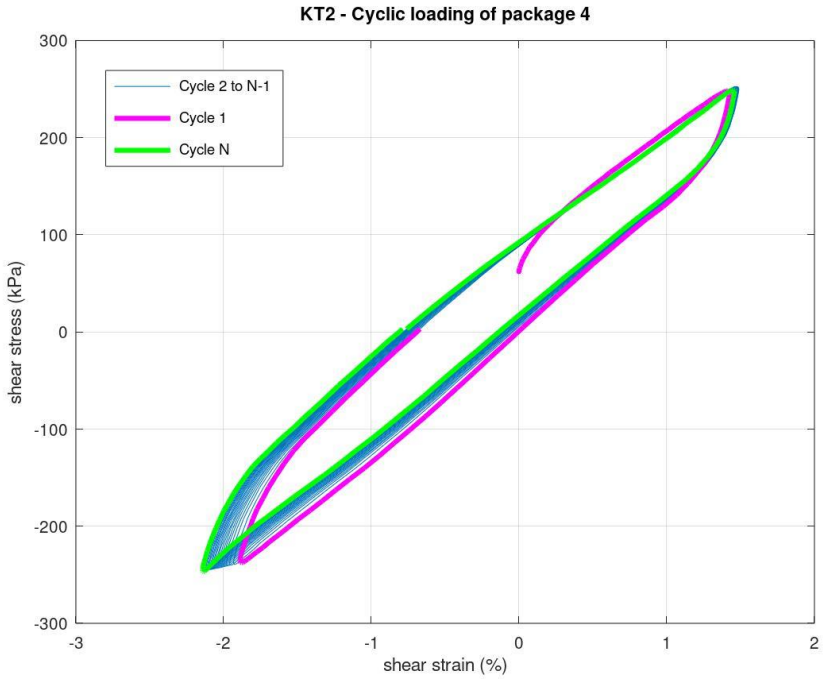

Figure A.38 - Cyclic loading of parcel 4.

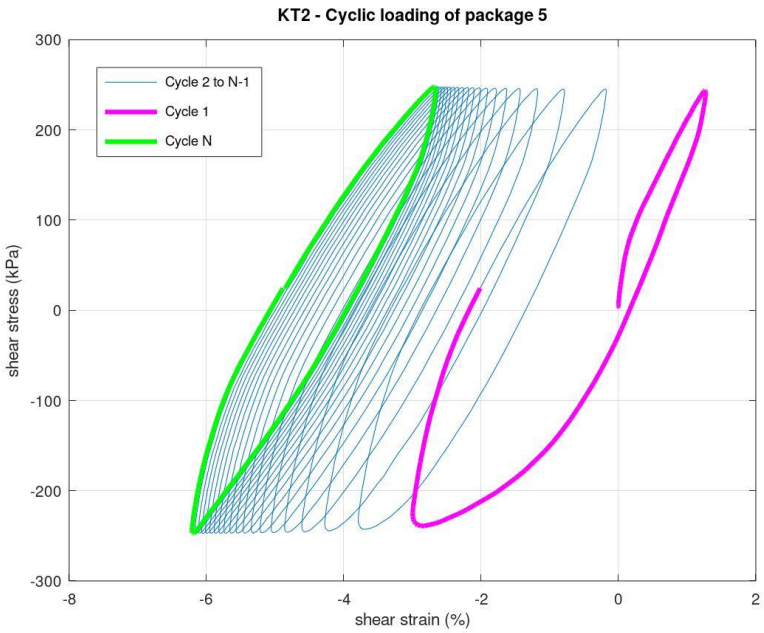

Figure A.39 - Cyclic loading of parcel 5.

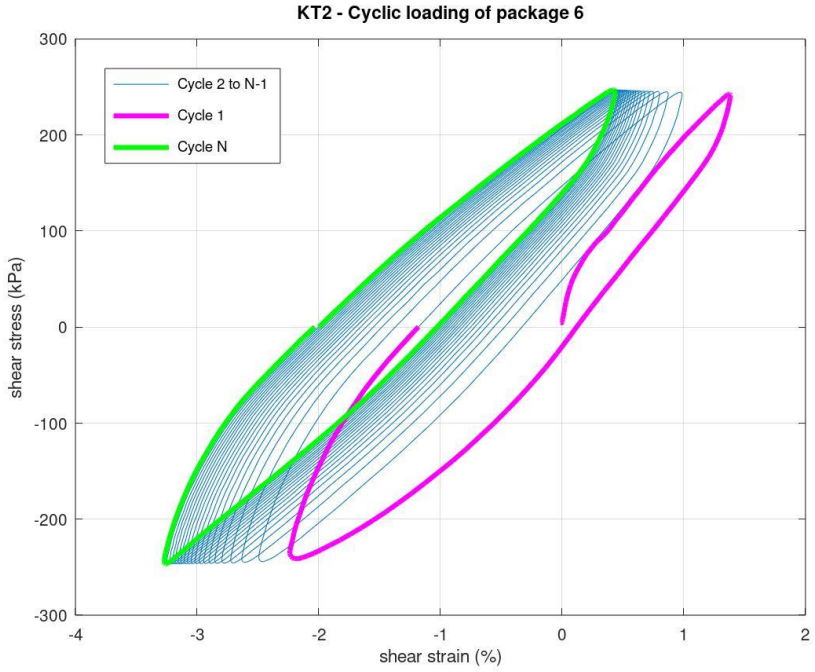

Figure A.40 - Cyclic loading of parcel 6.

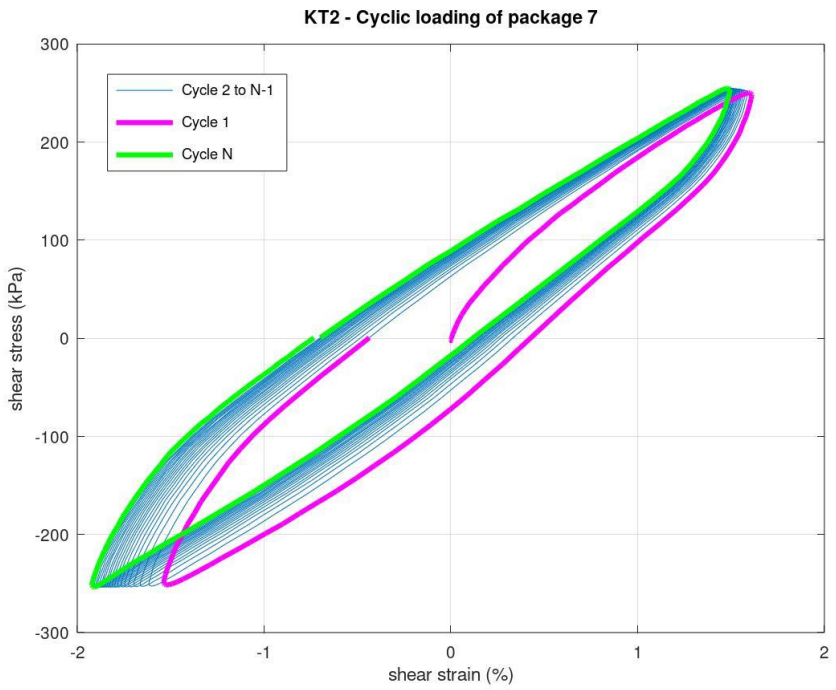

Figure A.41 - Cyclic loading of parcel 7.

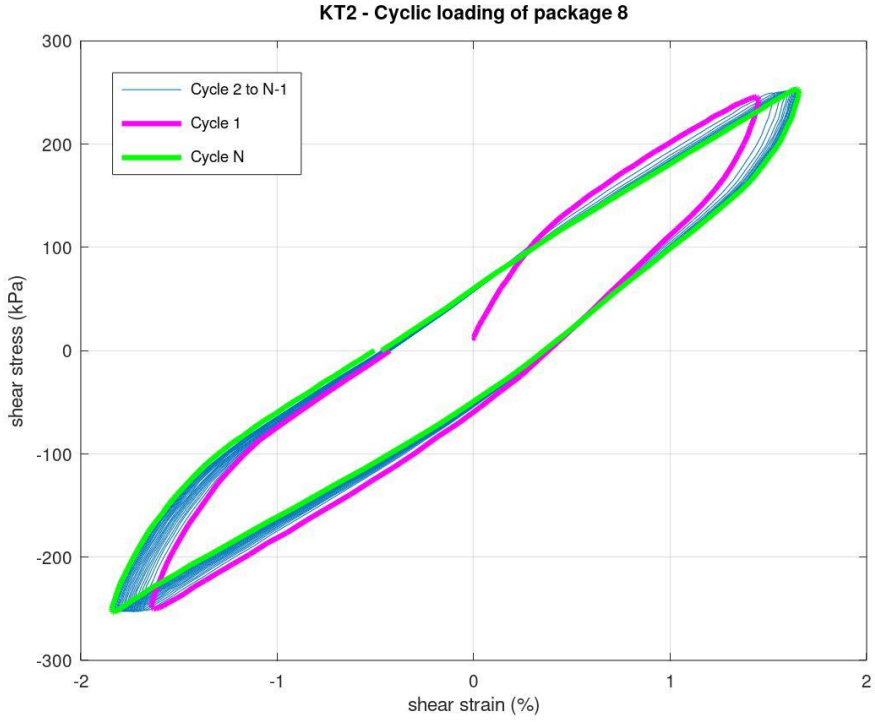

Figure A.42 - Cyclic loading of parcel 8.

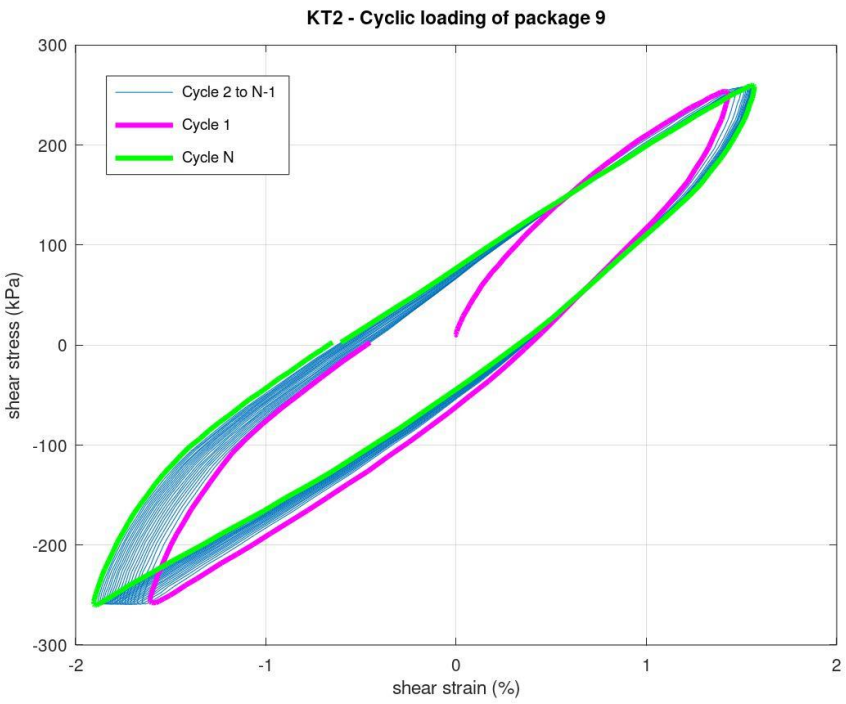

Figure A.43 - Cyclic loading of parcel 9.

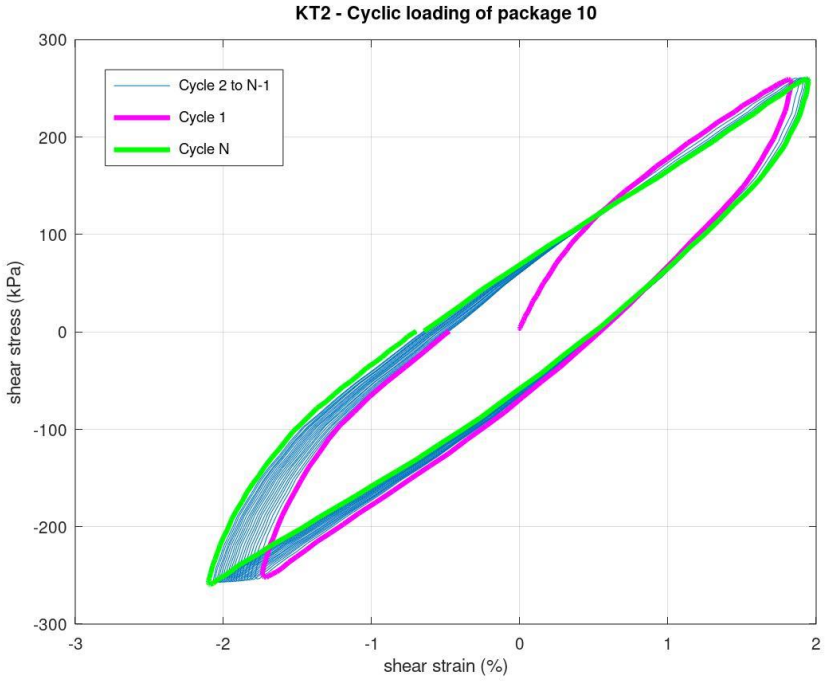

Figure A.44 - Cyclic loading of parcel 10.

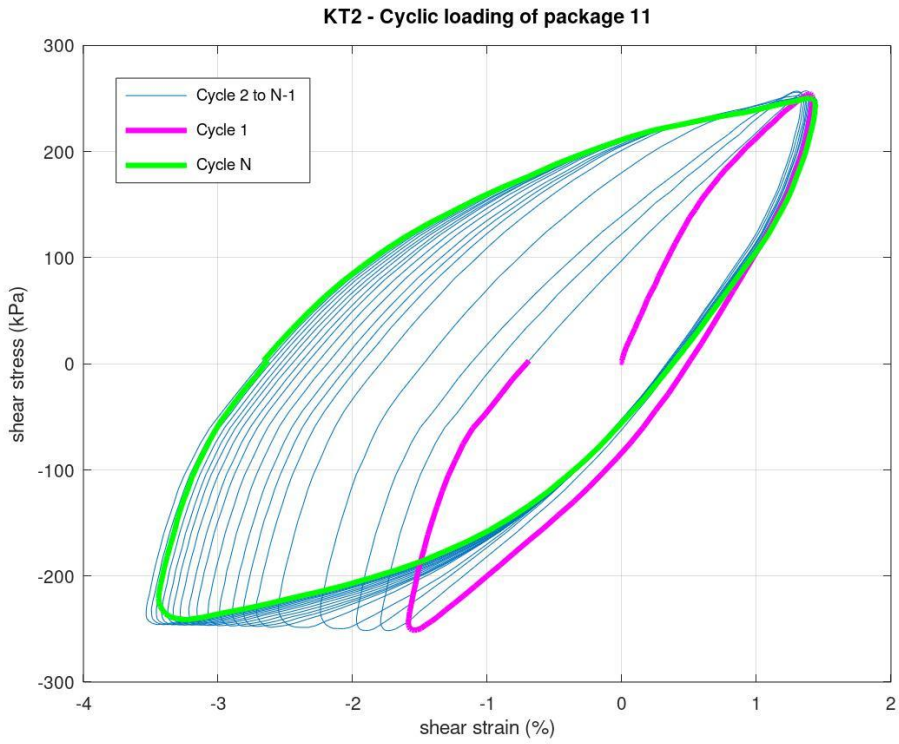

Figure A.45 - Cyclic loading of parcel 11.

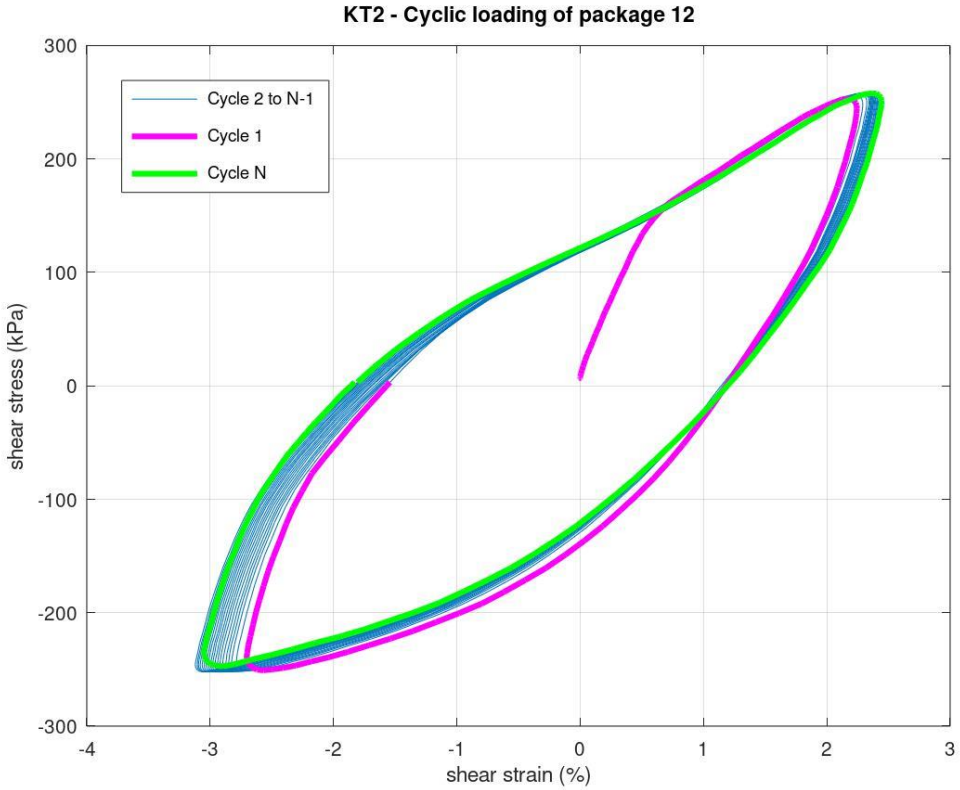

Figure A.46 - Cyclic loading of parcel 12.

Cyclic parameters

Parameters are calculated through the DLP-script, provided by NGI.

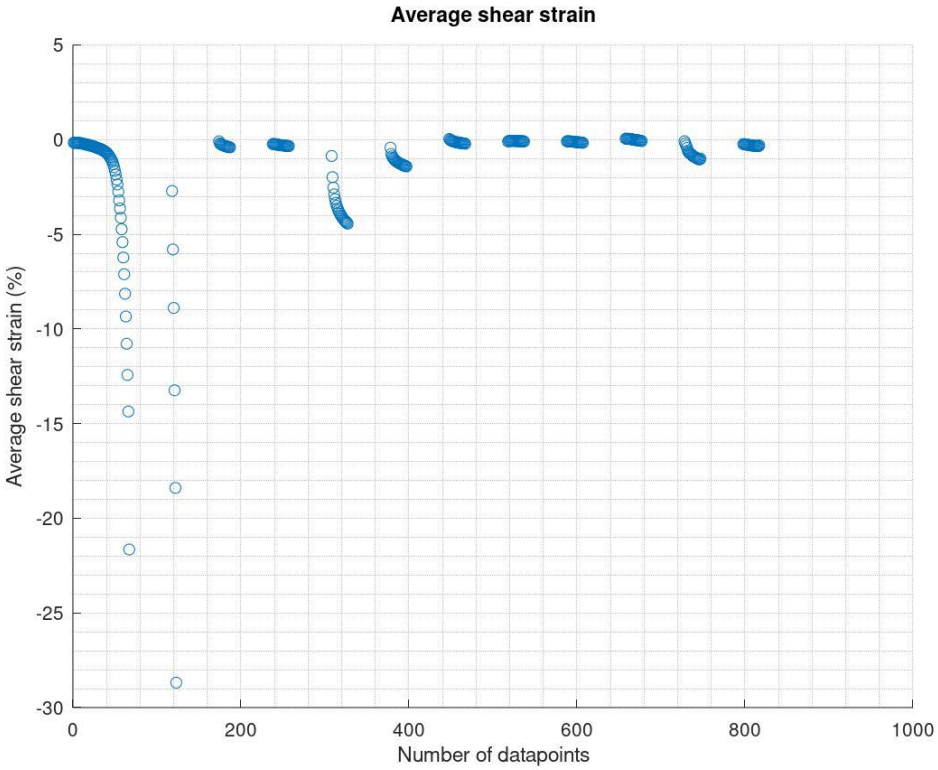

Figure A.47 - Average shear strain.

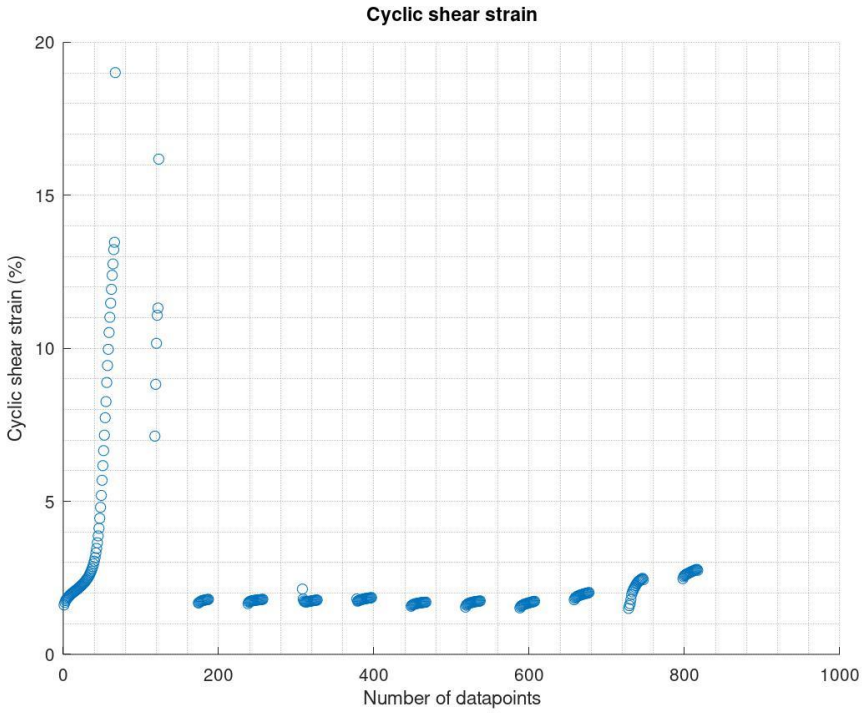

Figure A.48 – Cyclic shear strain.

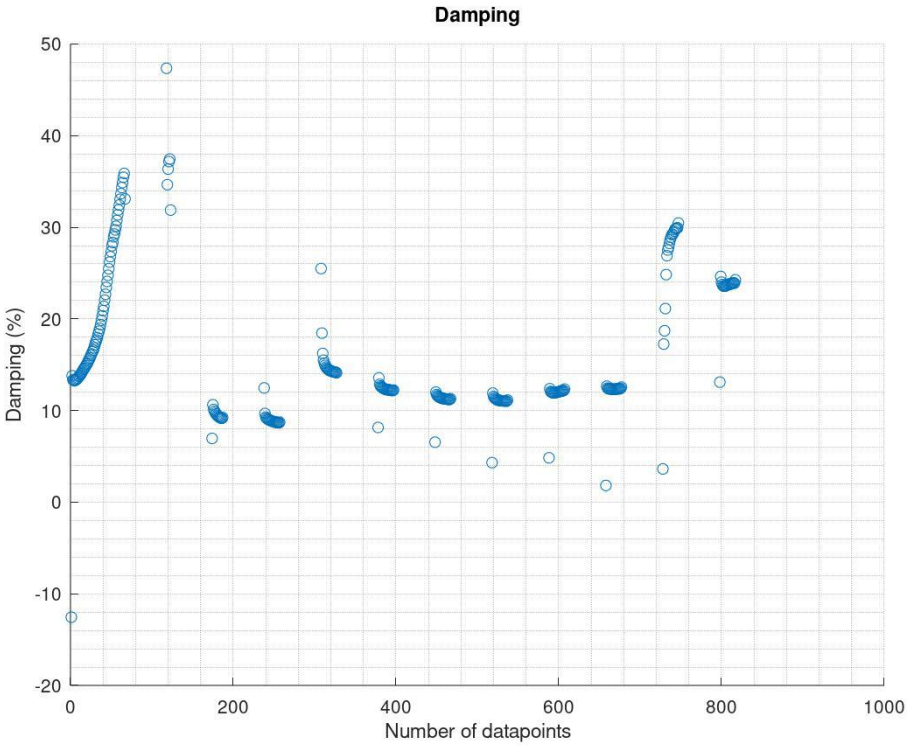

Figure A.49 – Damping.

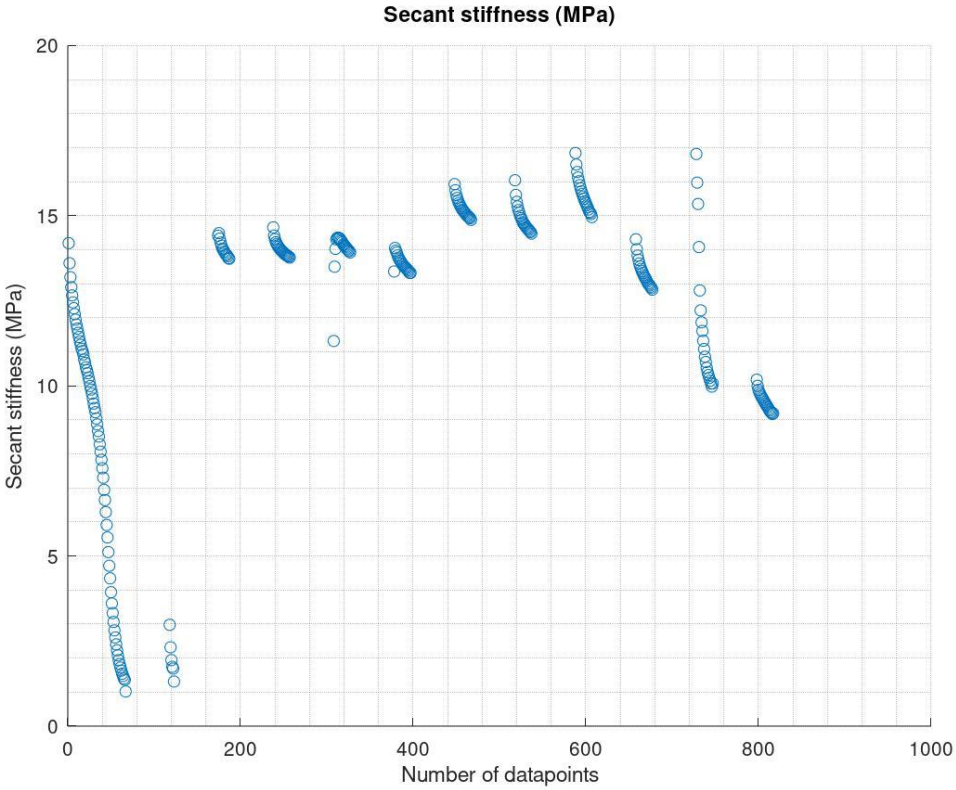

Figure A.50 – Secant stiffness.

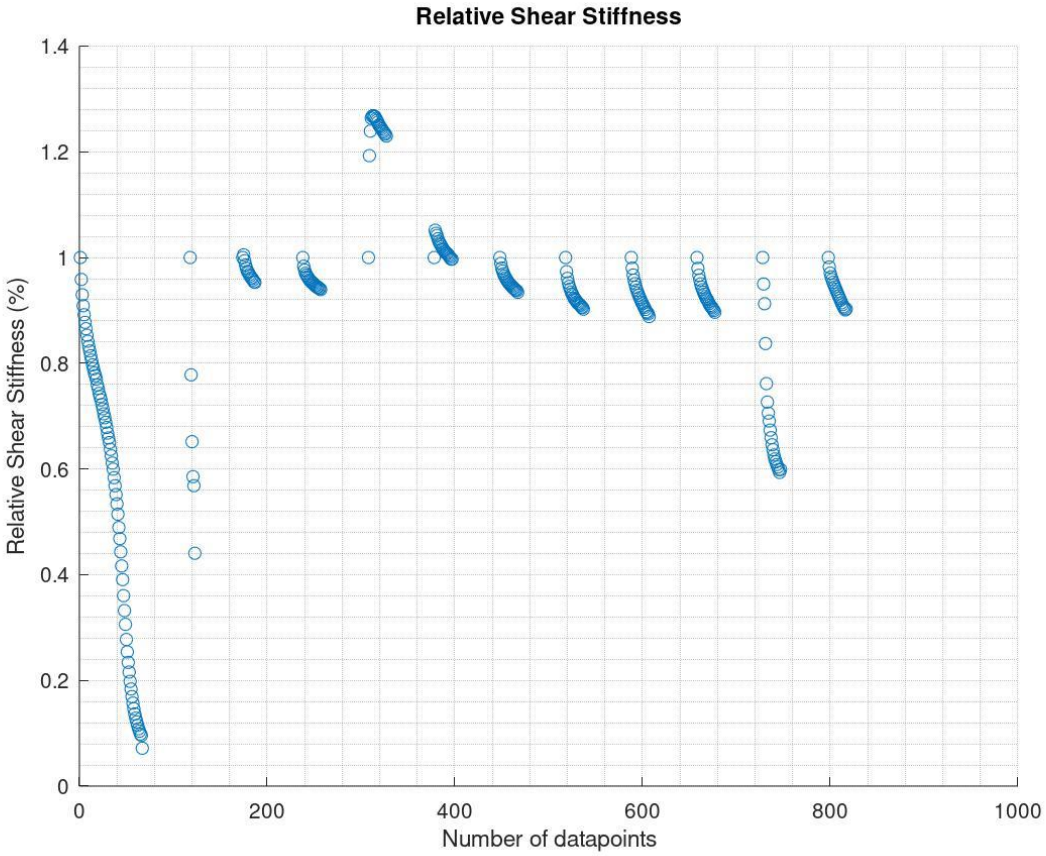

Figure A.51 – Relative shear stiffness.

Appendix A5 – Brazil_1

Cyclic loops and parameters for each cyclic parcel are included.

Cyclic loops

Each plot displays the cyclic behaviour of the kaolin-sample during cyclic loading. Axial consolidation is taken place alongside the cyclic loading.

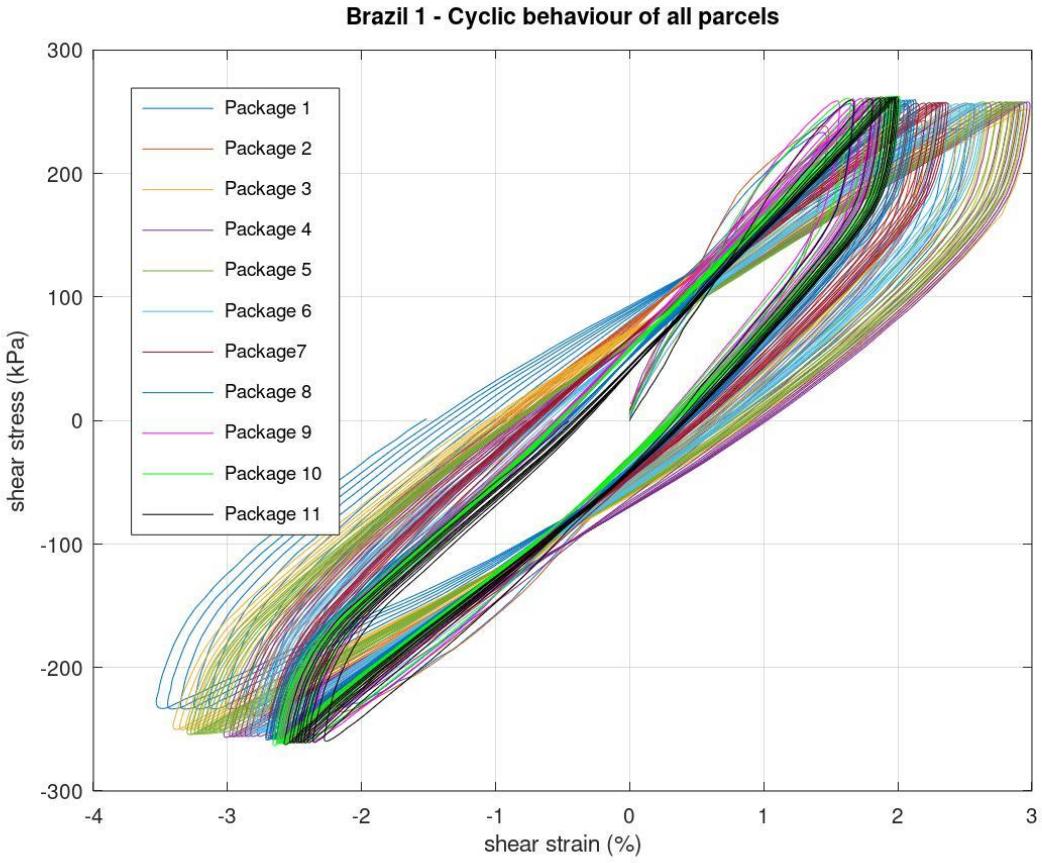

Figure A.52 - Cyclic loading of all parcels.

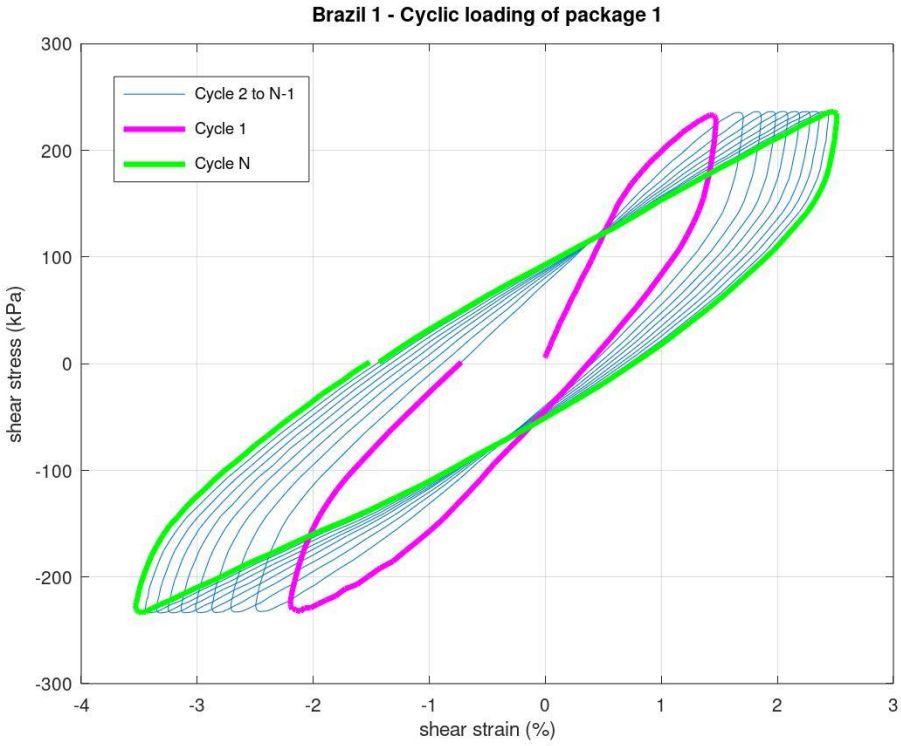

Figure A.53 - Cyclic loading of parcel 1.

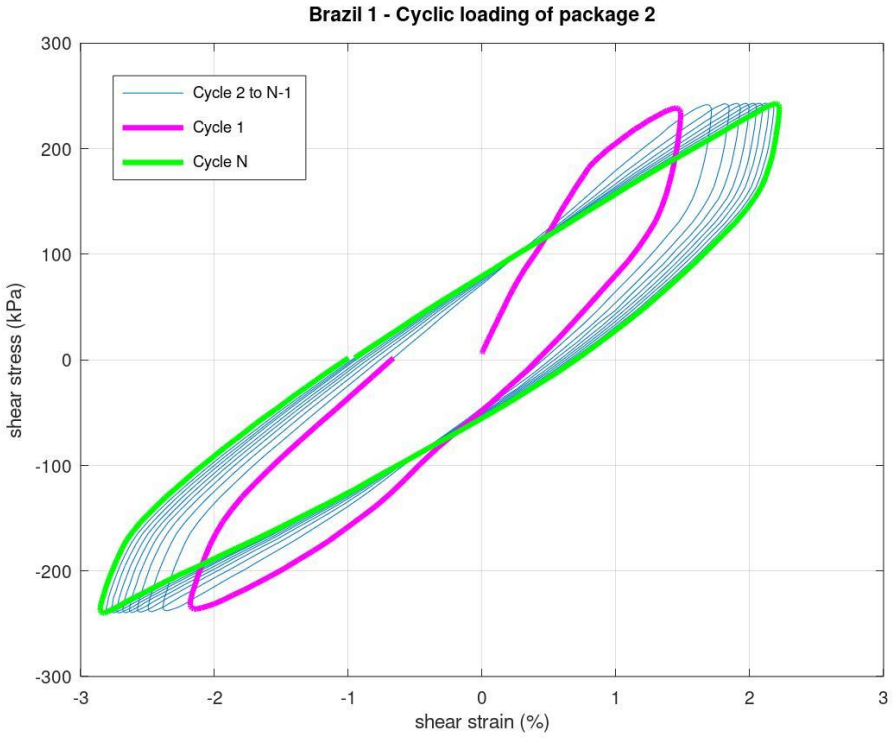

Figure A.54 - Cyclic loading of parcel 2.

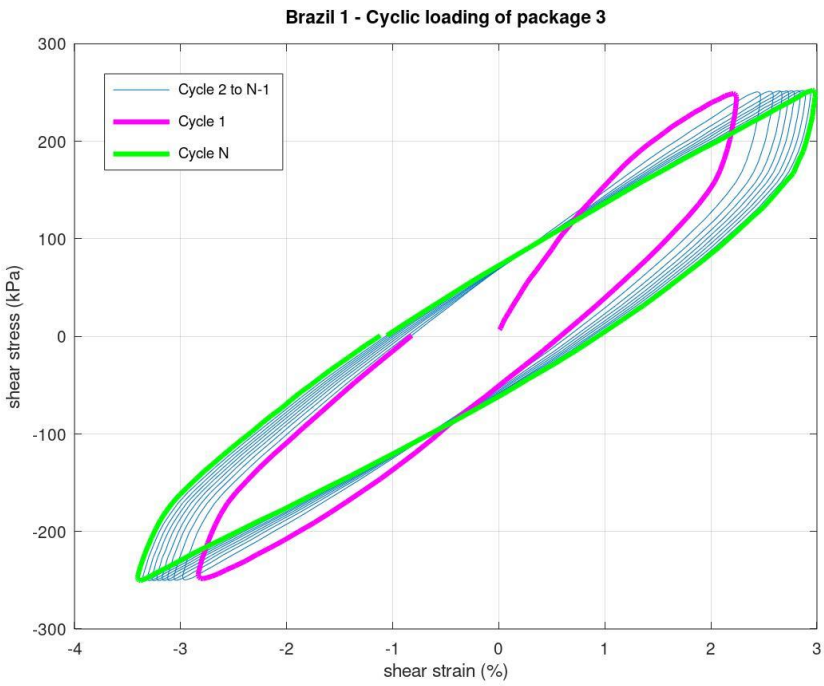

Figure A.55 - Cyclic loading of parcel 3.

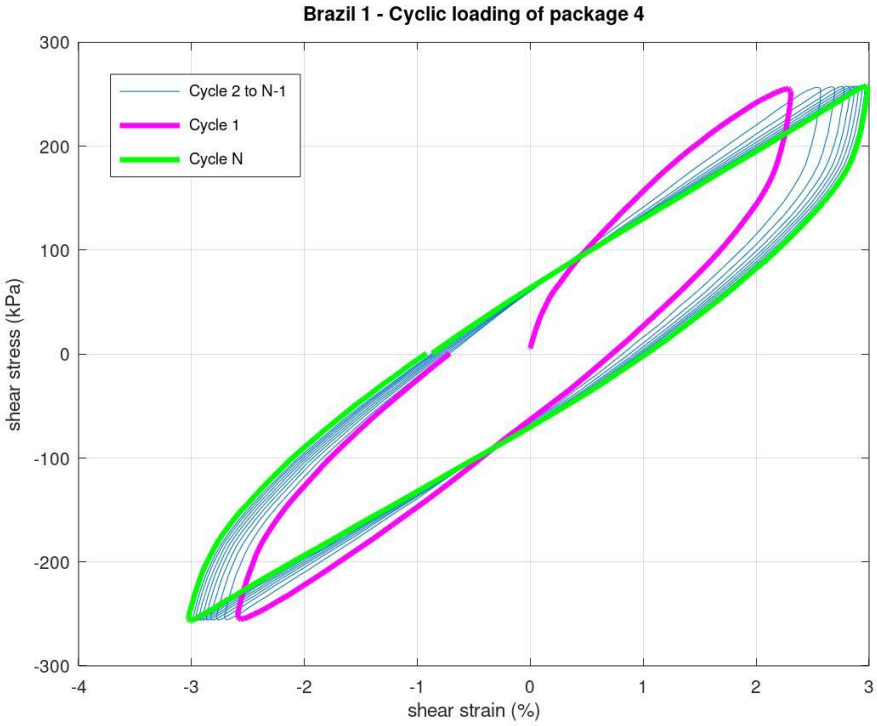

Figure A.56 - Cyclic loading of parcel 4.

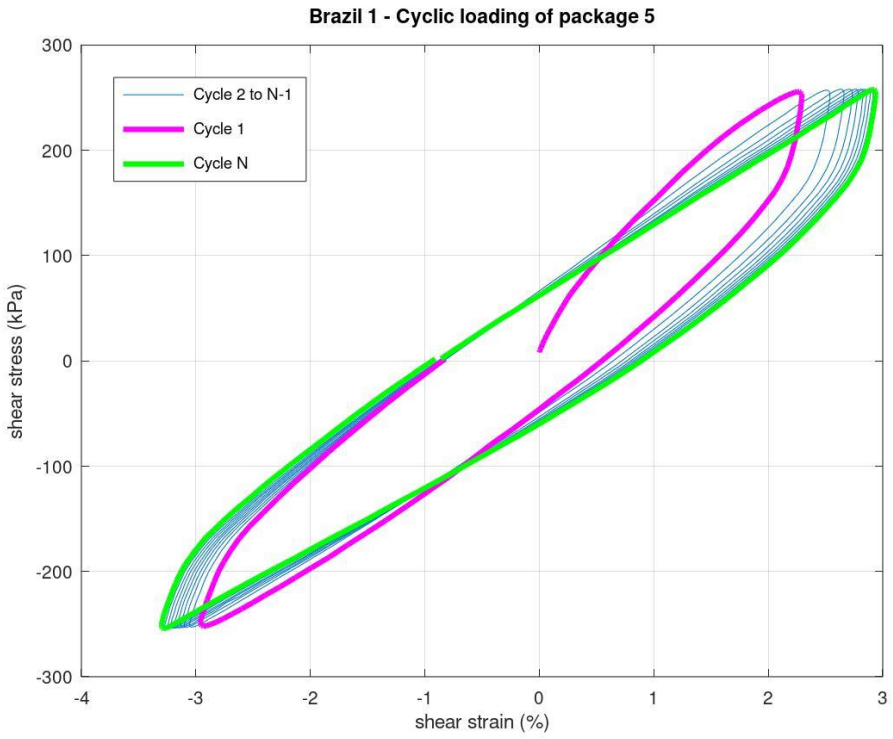

Figure A.57 - Cyclic loading of parcel 5.

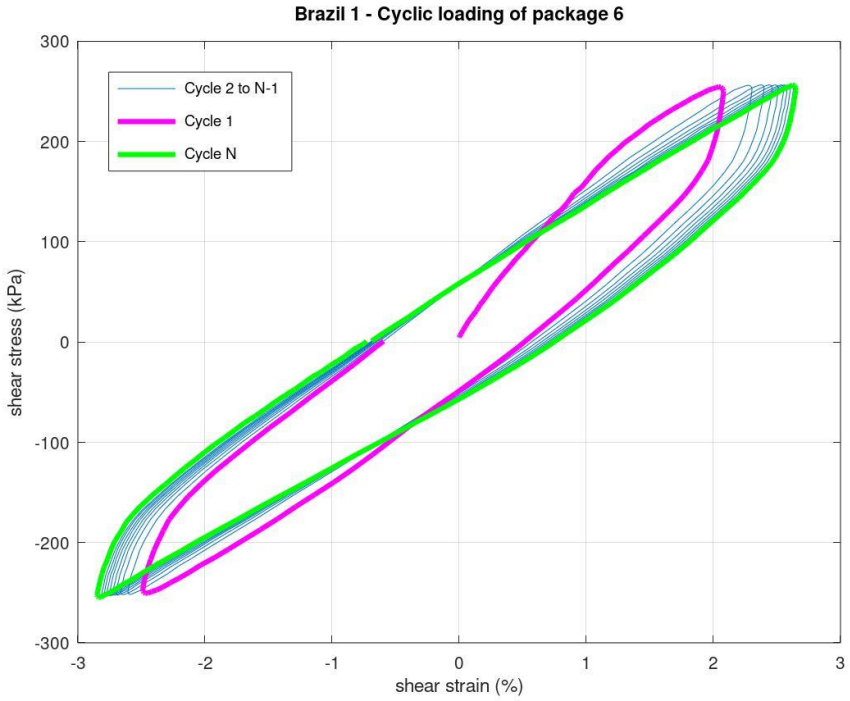

Figure A.58 - Cyclic loading of parcel 6.

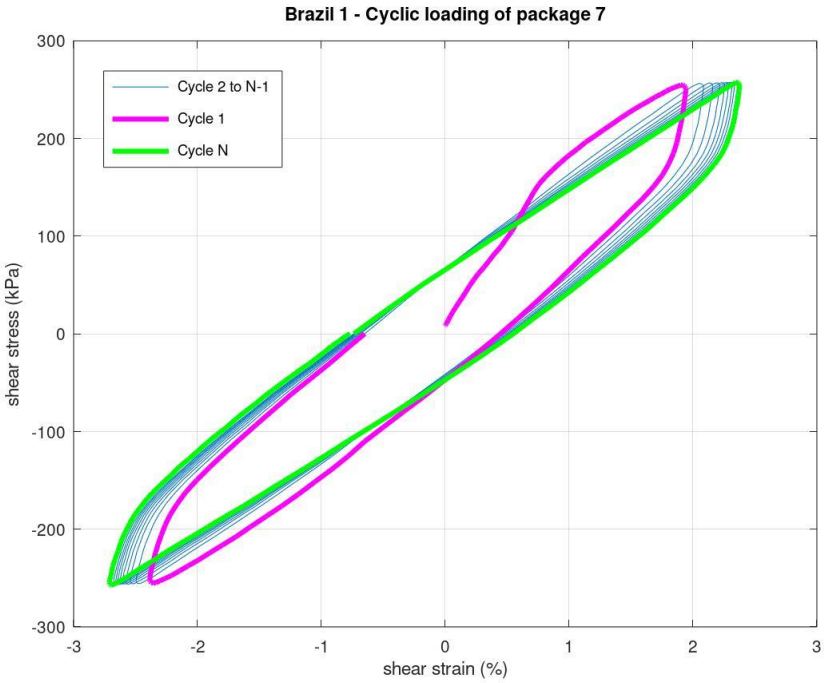

Figure A.59 - Cyclic loading of parcel 7.

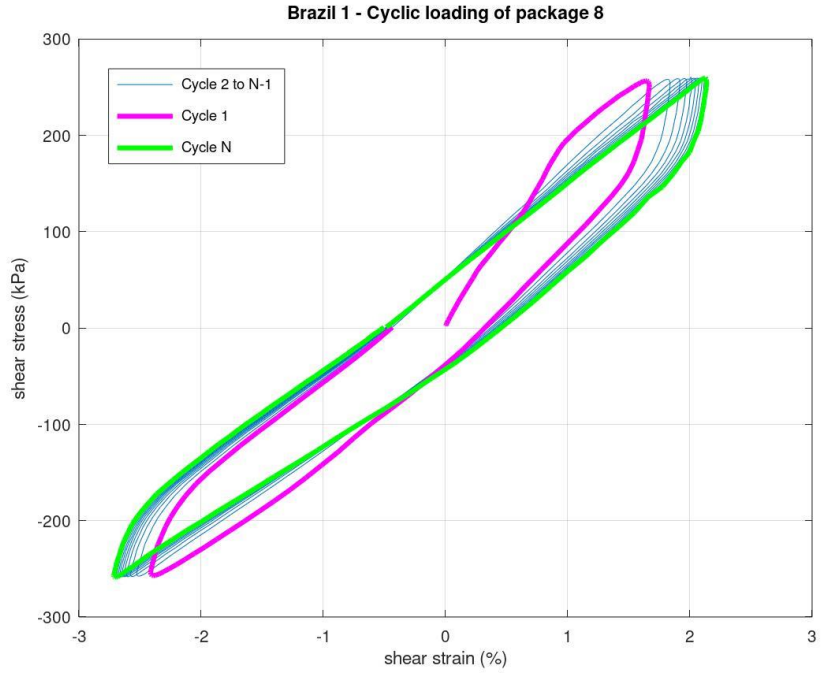

Figure A.60 - Cyclic loading of parcel 8.

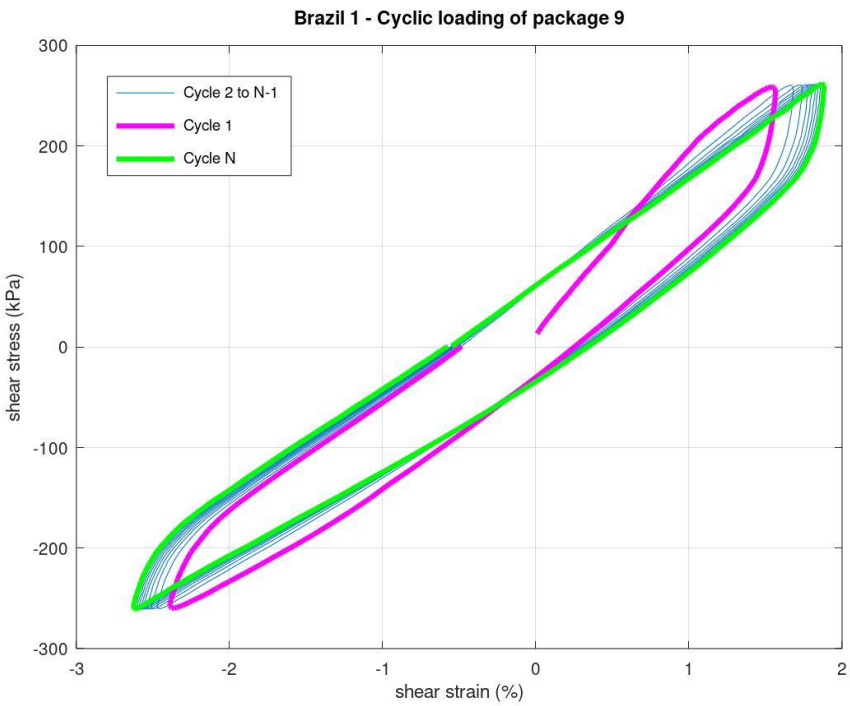

Figure A.61 - Cyclic loading of parcel 9.

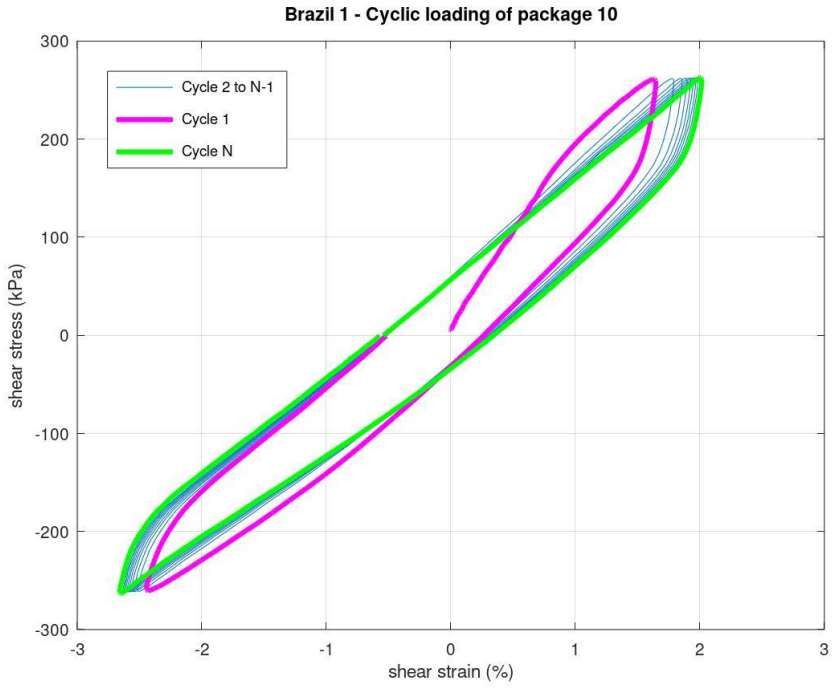

Figure A.62 - Cyclic loading of parcel 10.

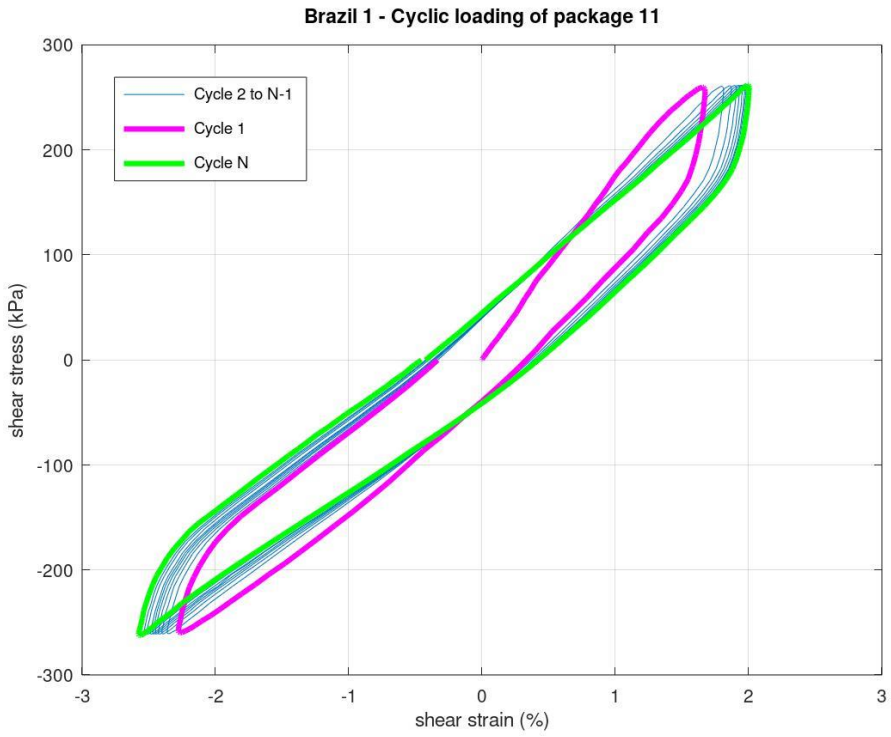

Figure A.63 - Cyclic loading of parcel 11.

Cyclic parameters

Parameters are calculated through the DLP-script, provided by NGI.

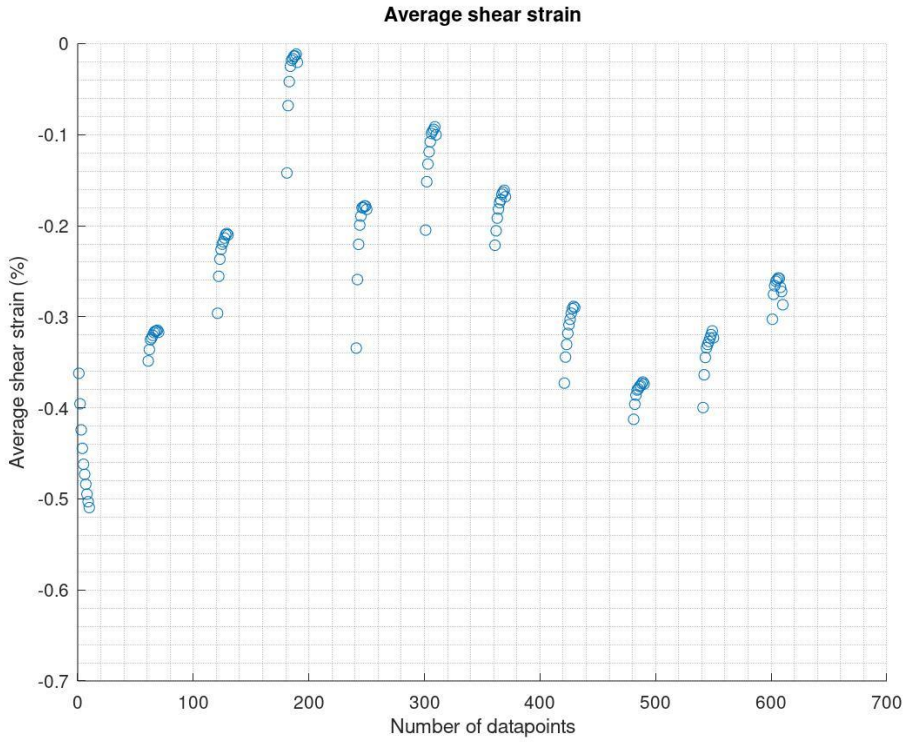

Figure A.64 - Average shear strain.

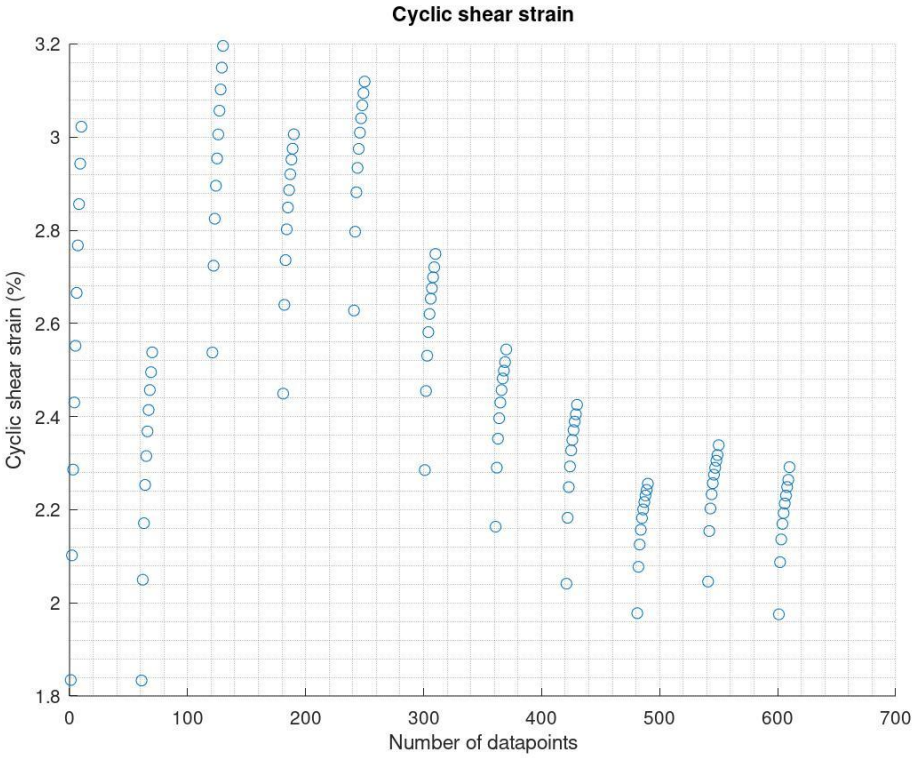

Figure A.65 – Cyclic shear strain.

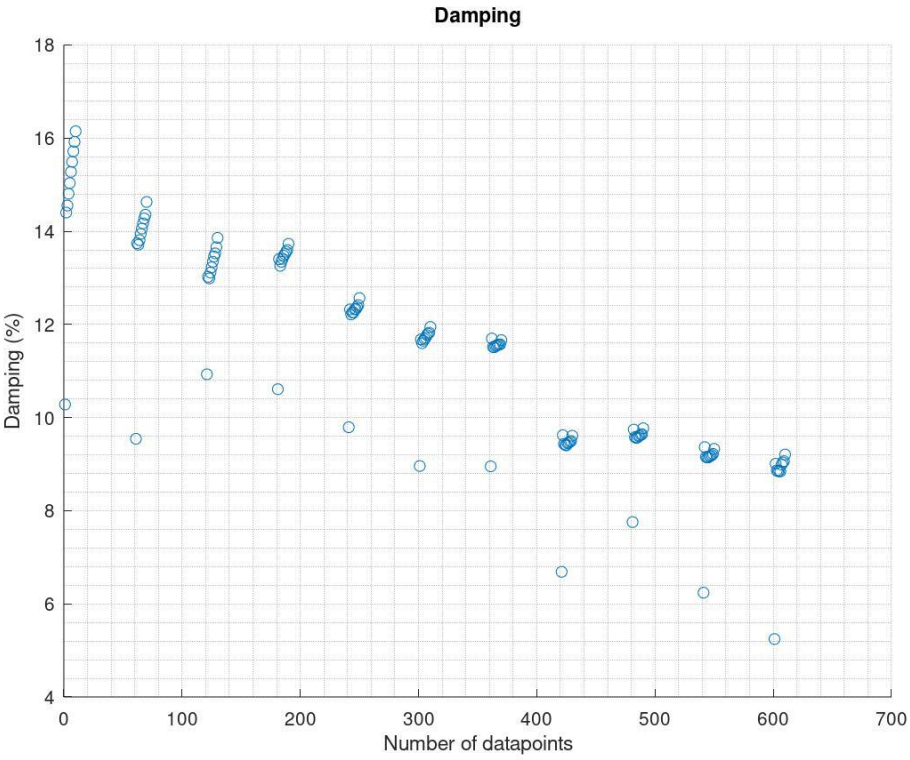

Figure A.66 – Damping.

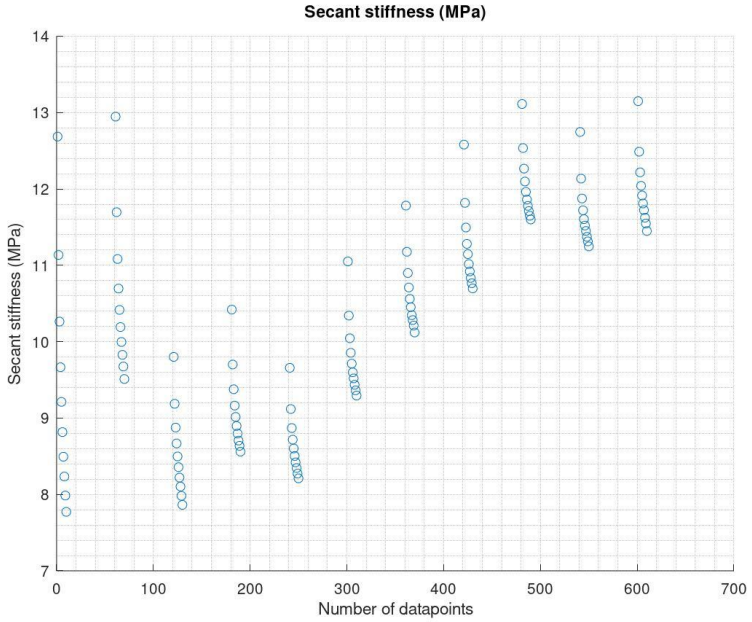

Figure A.67 – Secant stiffness.

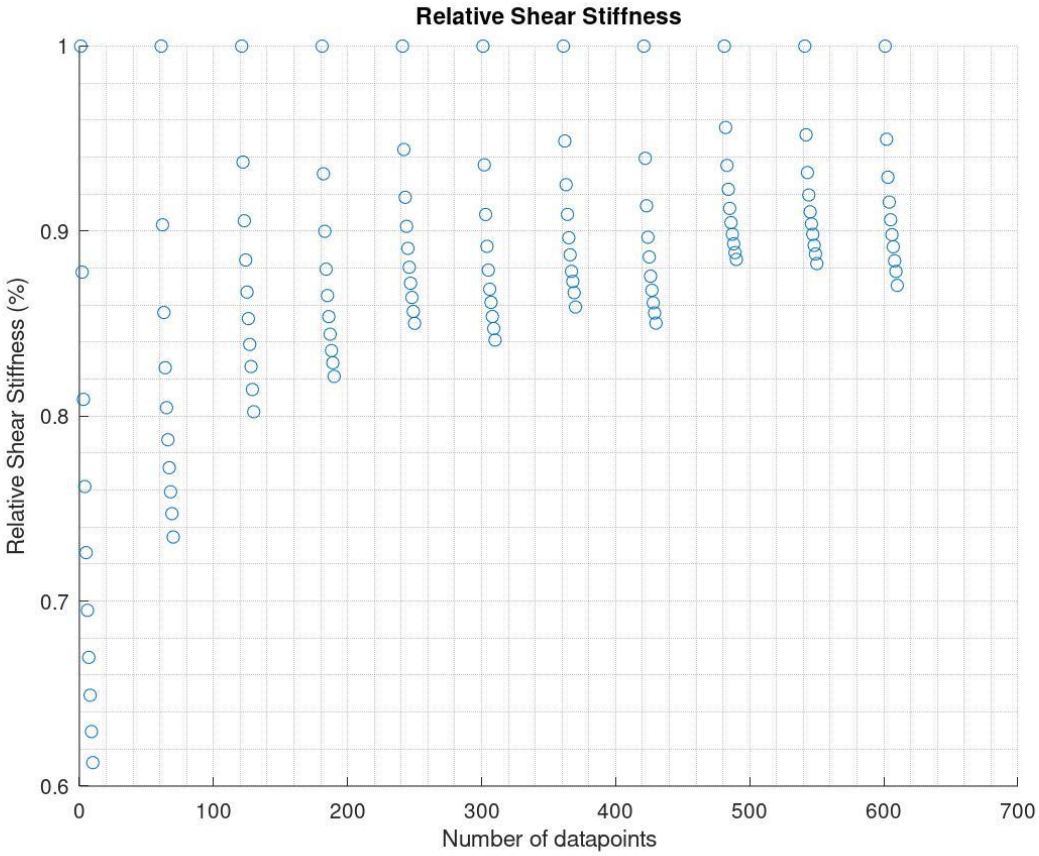

Figure A.68 – Relative shear stiffness.

Appendix A6 – Brazil_2

Cyclic loops and parameters for each cyclic parcel are included.

Cyclic loops

Each plot displays the cyclic behaviour of the kaolin-sample during cyclic loading. Axial consolidation is taken place alongside the cyclic loading.

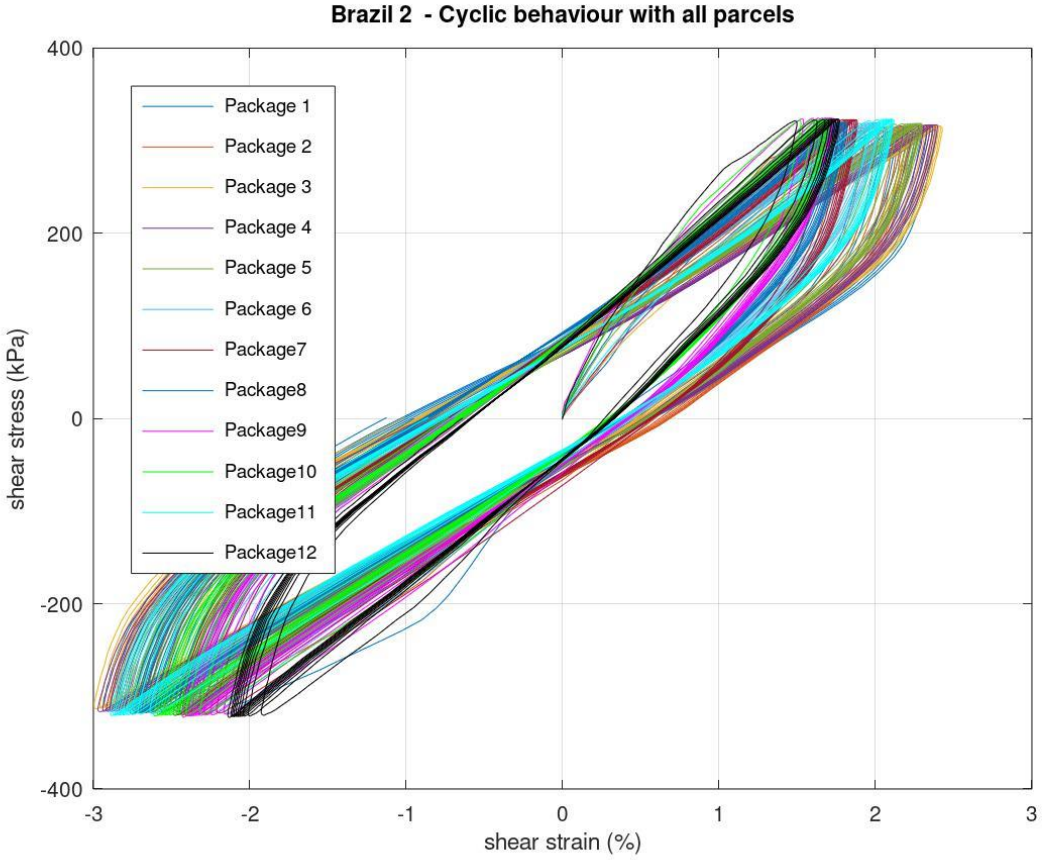

Figure A.69- Cyclic loading of all parcels.

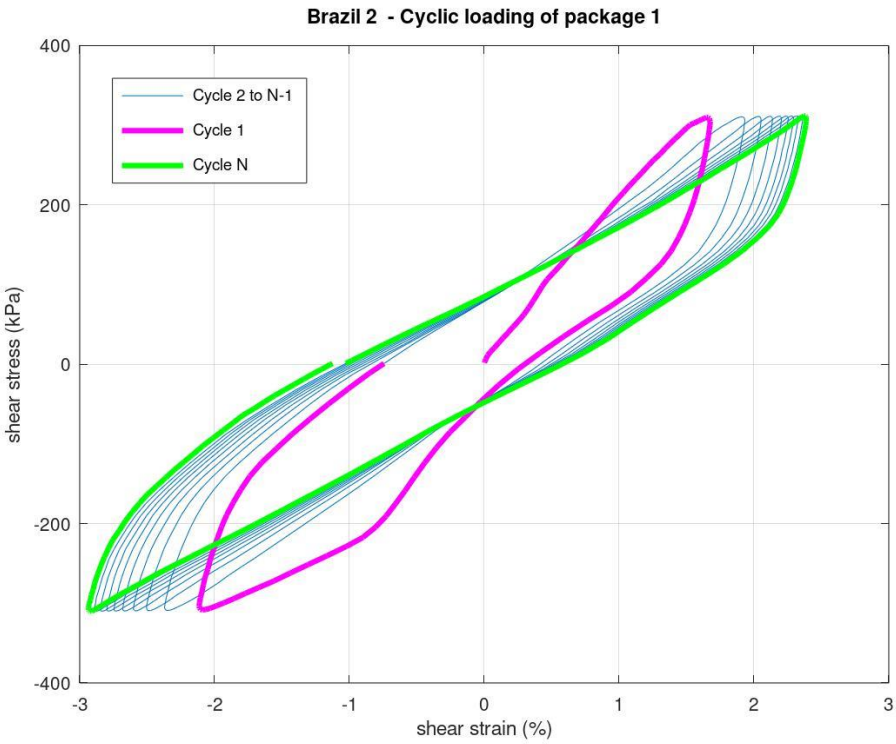

Figure A.70- Cyclic loading of parcel 1.

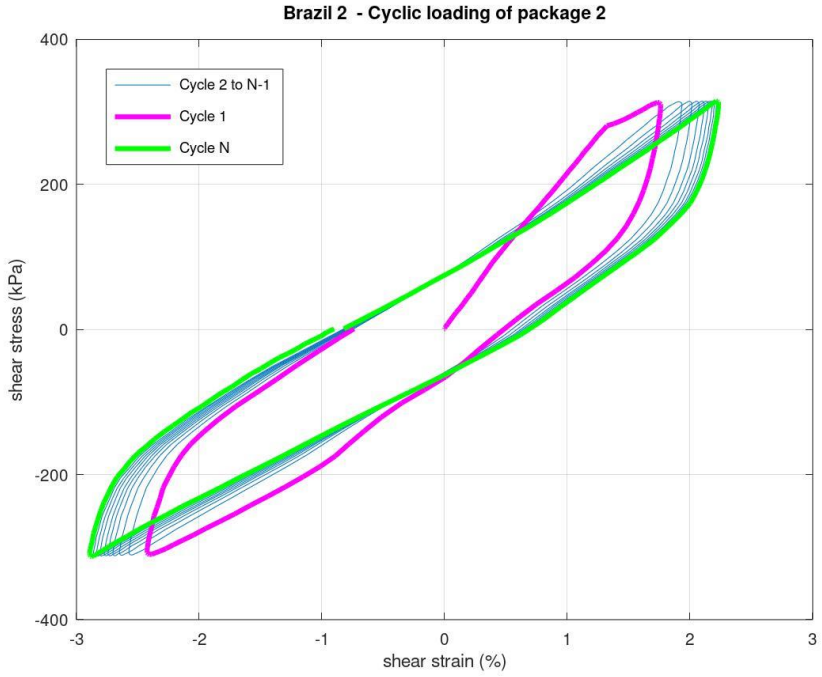

Figure A.71- Cyclic loading of parcel 2.

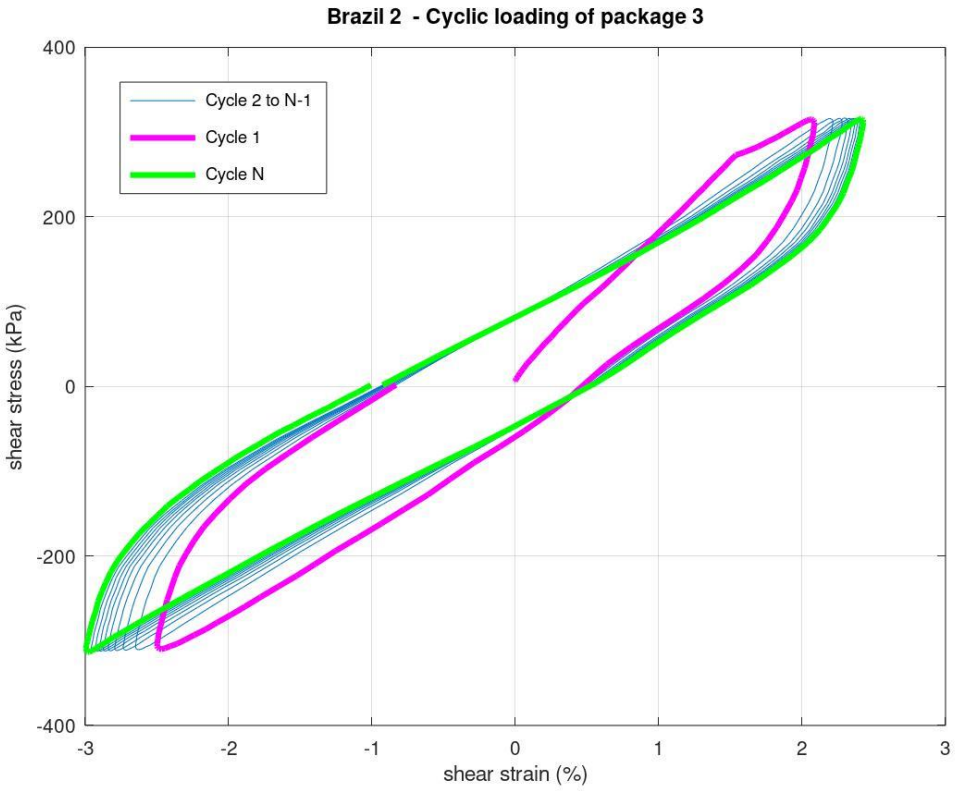

Figure A.72- Cyclic loading of parcel 3.

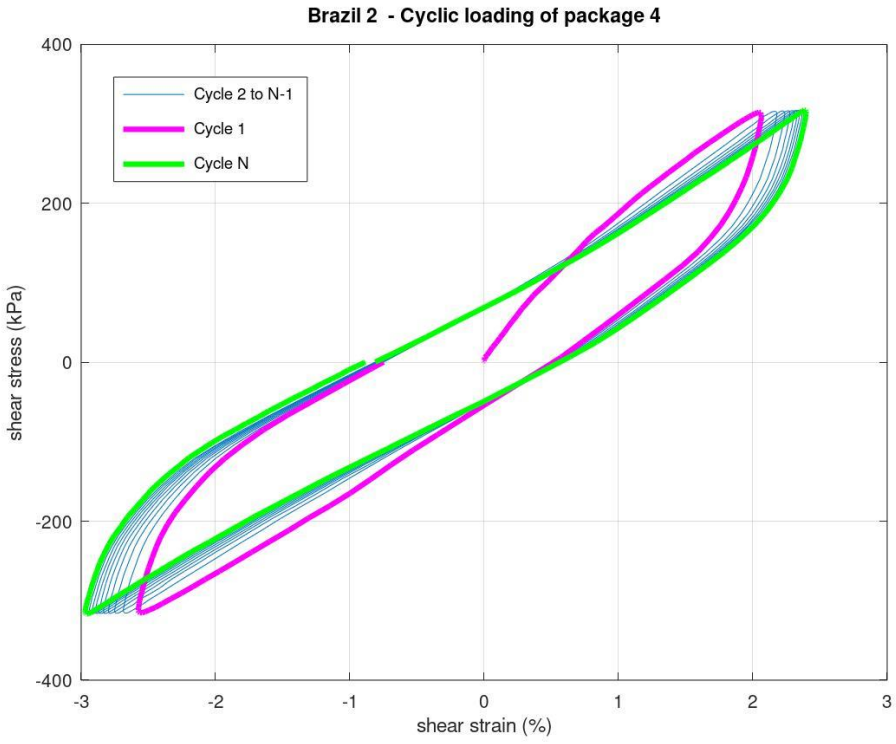

Figure A.73- Cyclic loading of parcel 4.

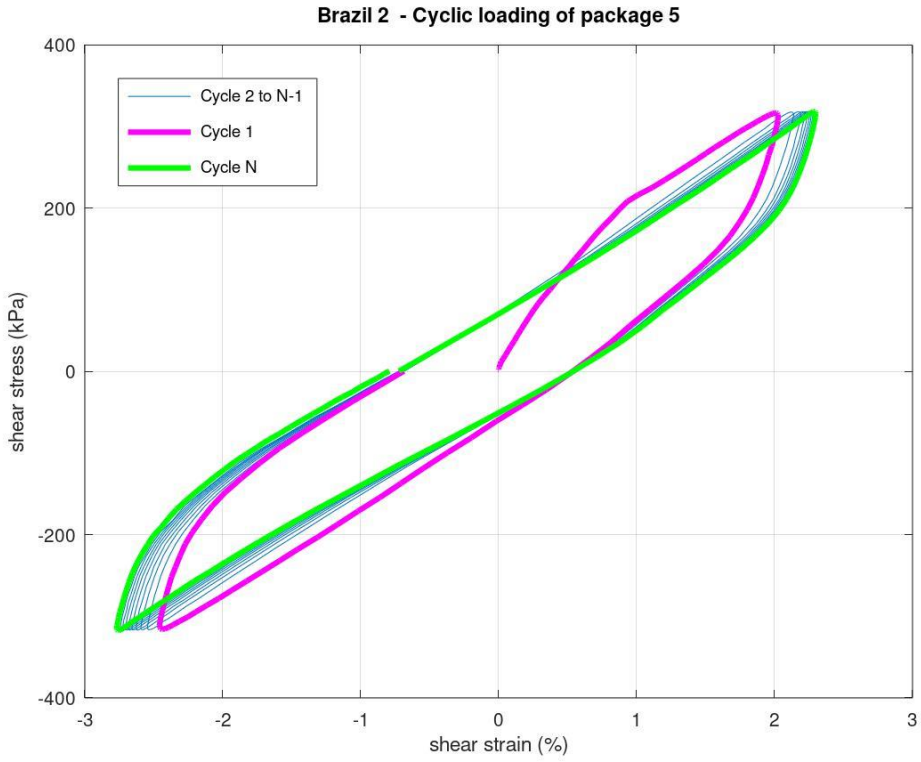

Figure A.74- Cyclic loading of parcel 5.

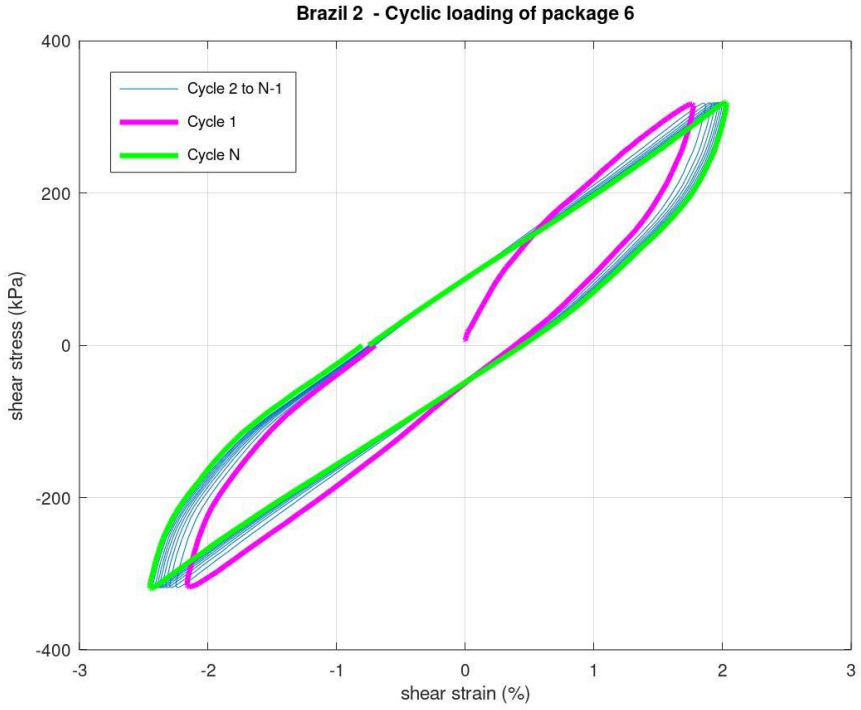

Figure A.75- Cyclic loading of parcel 6.

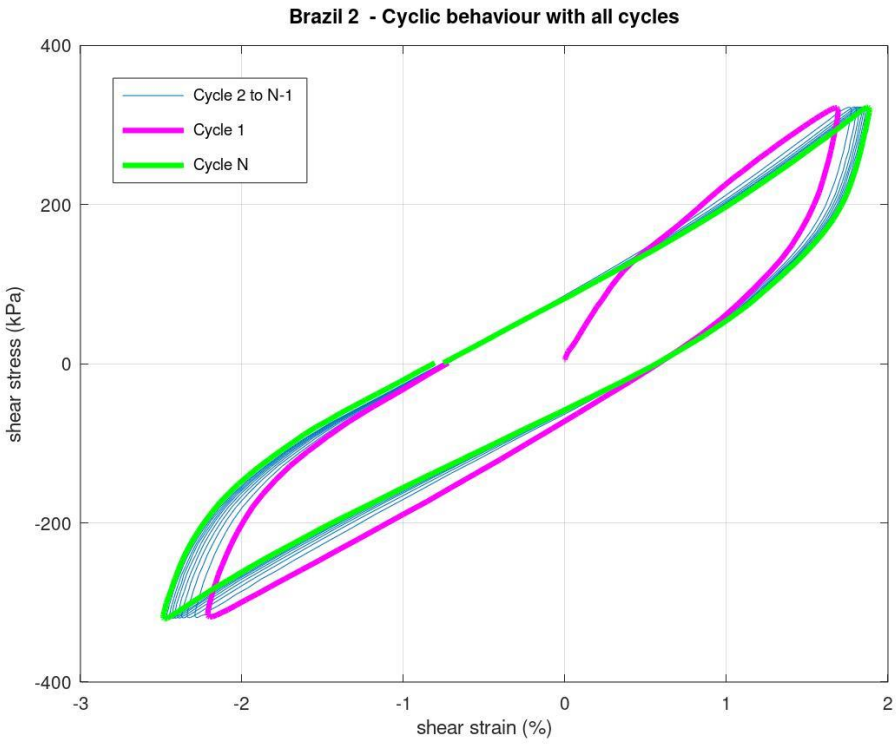

Figure A.76- Cyclic loading of parcel 7.

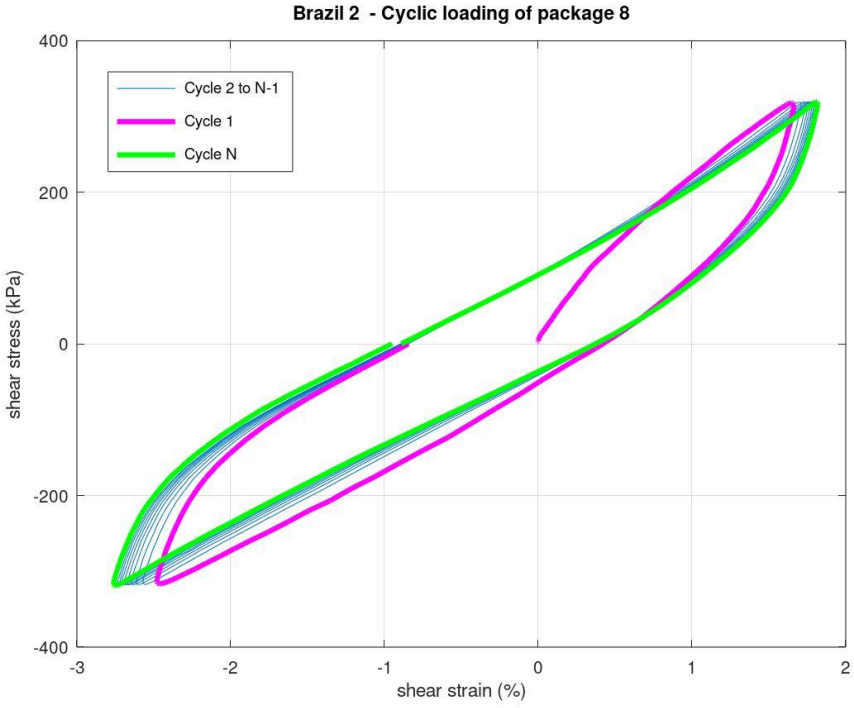

Figure A.77- Cyclic loading of parcel 8.

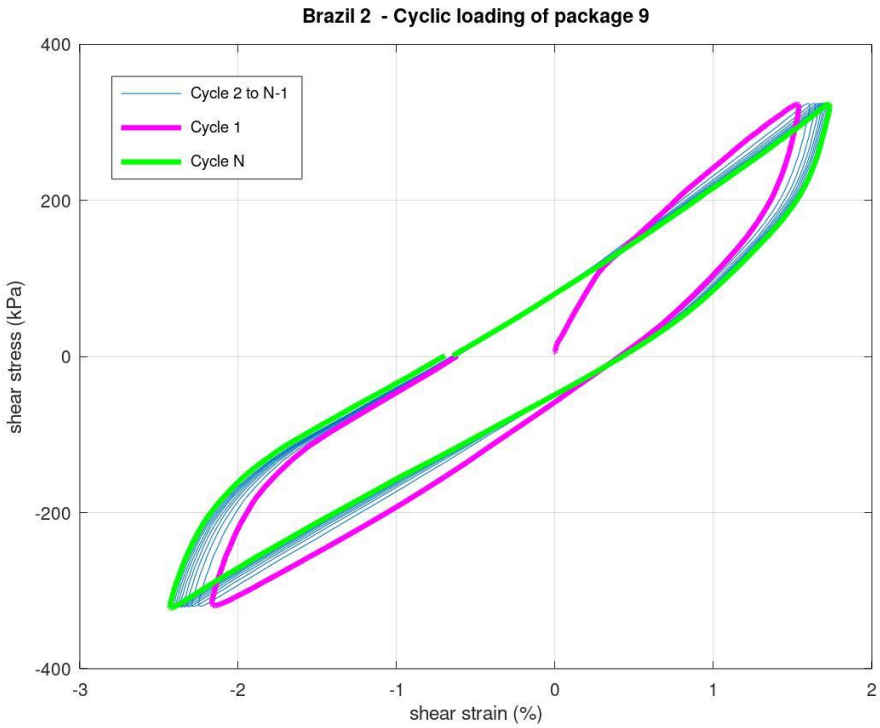

Figure A.78- Cyclic loading of parcel 9.

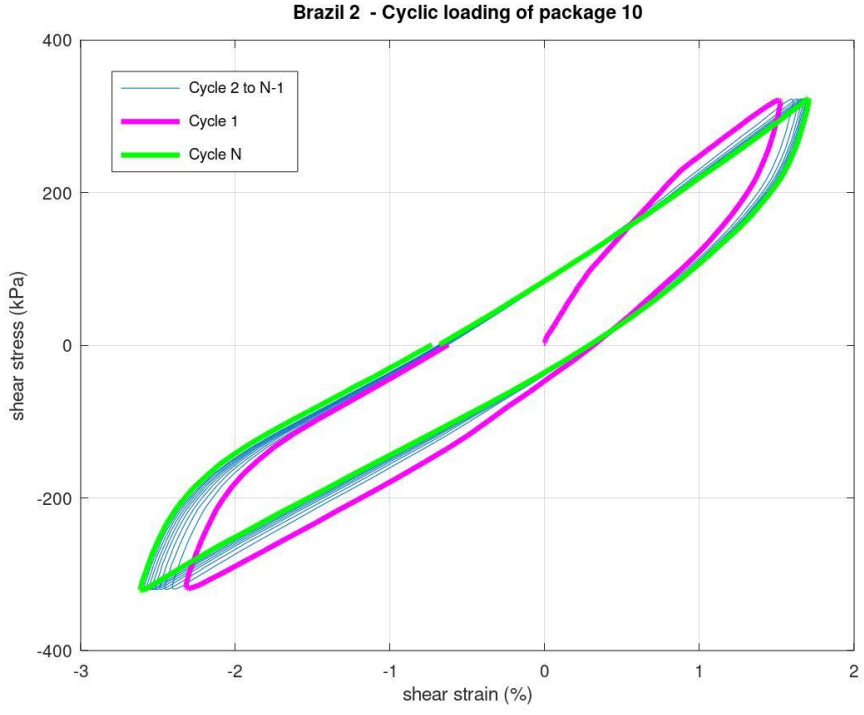

Figure A.79- Cyclic loading of parcel 10.

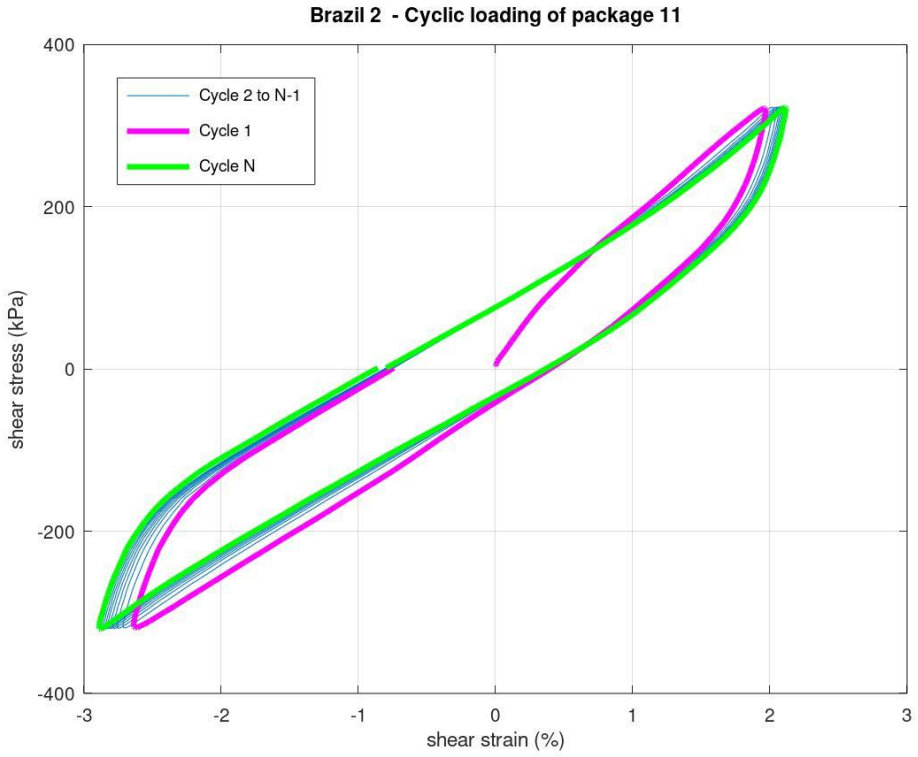

Figure A.80- Cyclic loading of parcel 11.

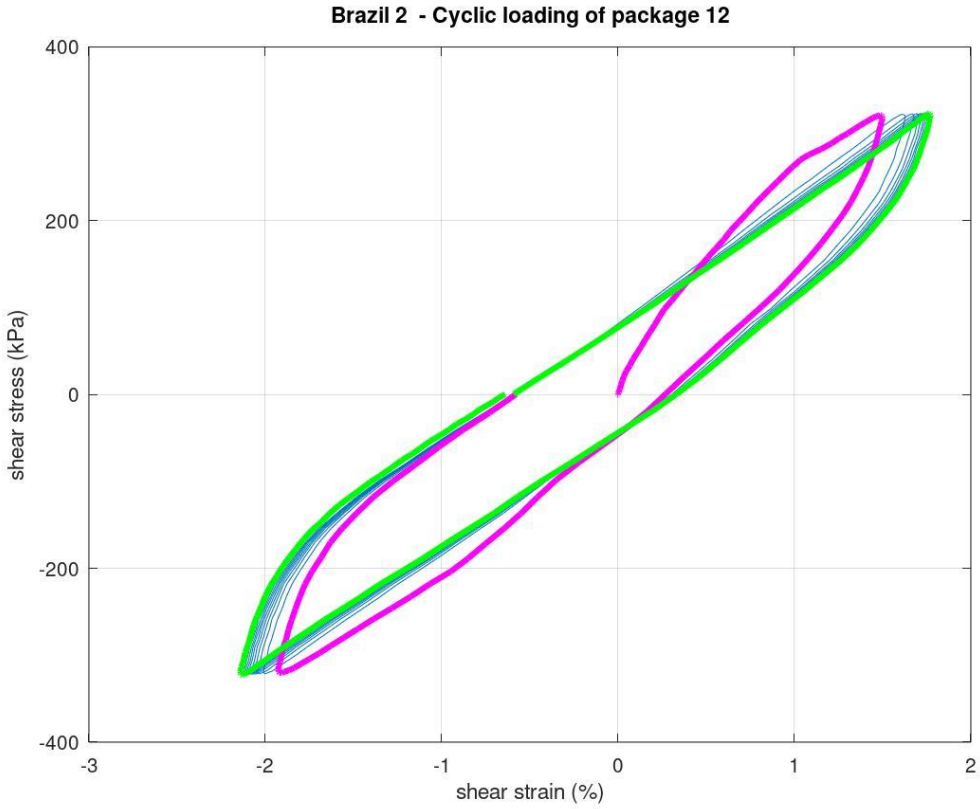

Figure A.81- Cyclic loading of parcel 12.

Cyclic parameters

Parameters are calculated through the DLP-script, provided by NGI.

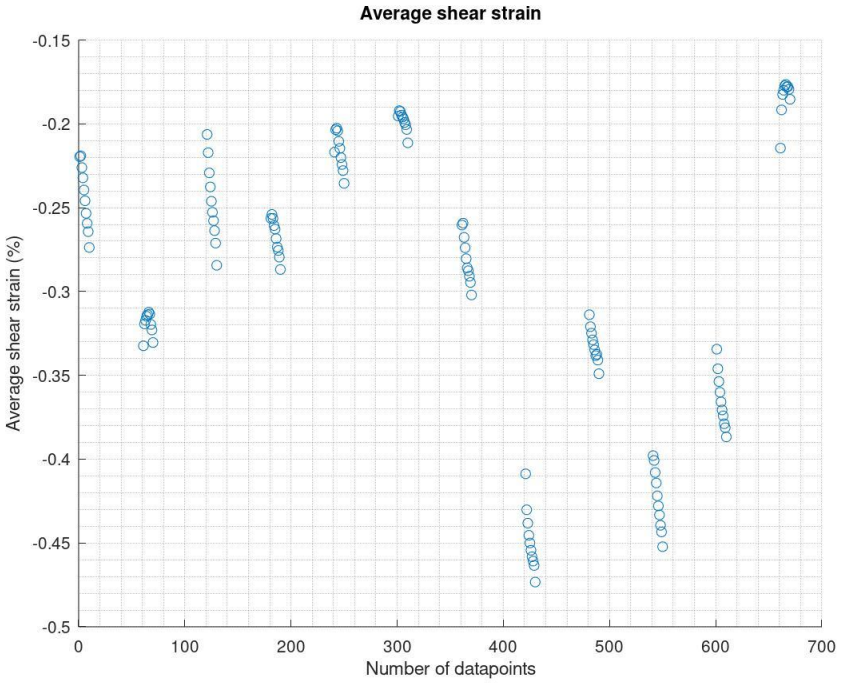

Figure A.82 - Average shear strain.

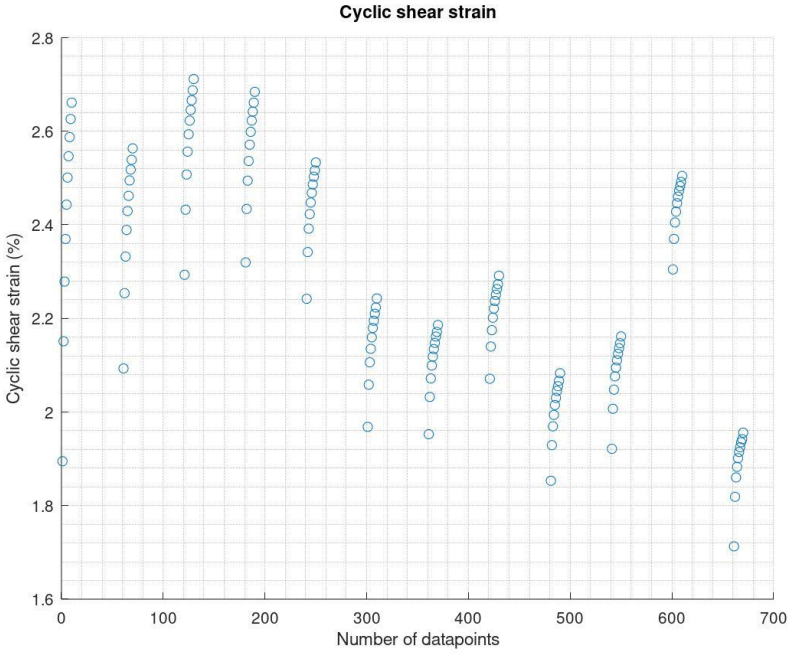

Figure A.83 – Cyclic shear strain.

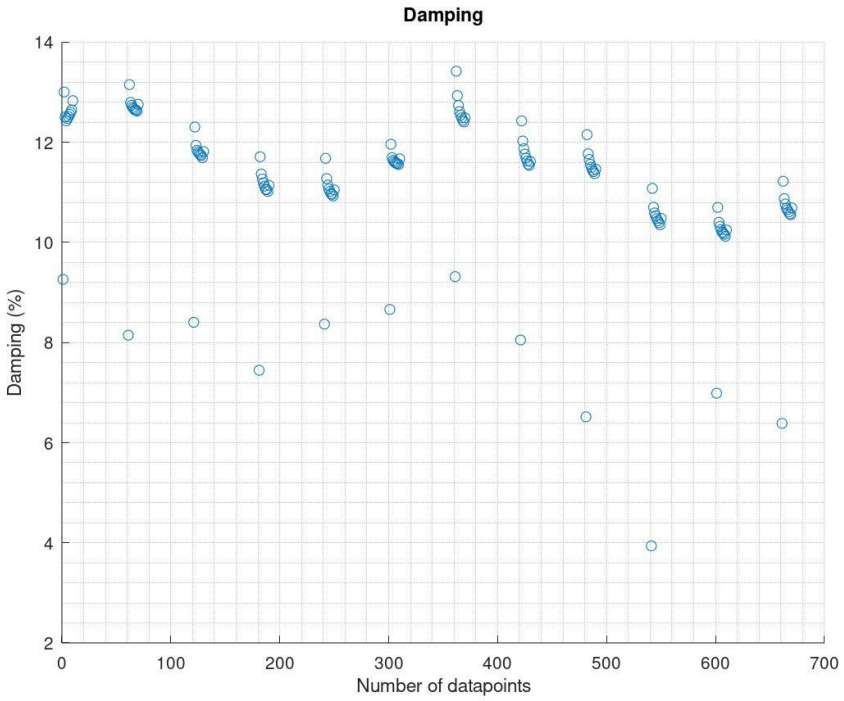

Figure A.84 – Damping.

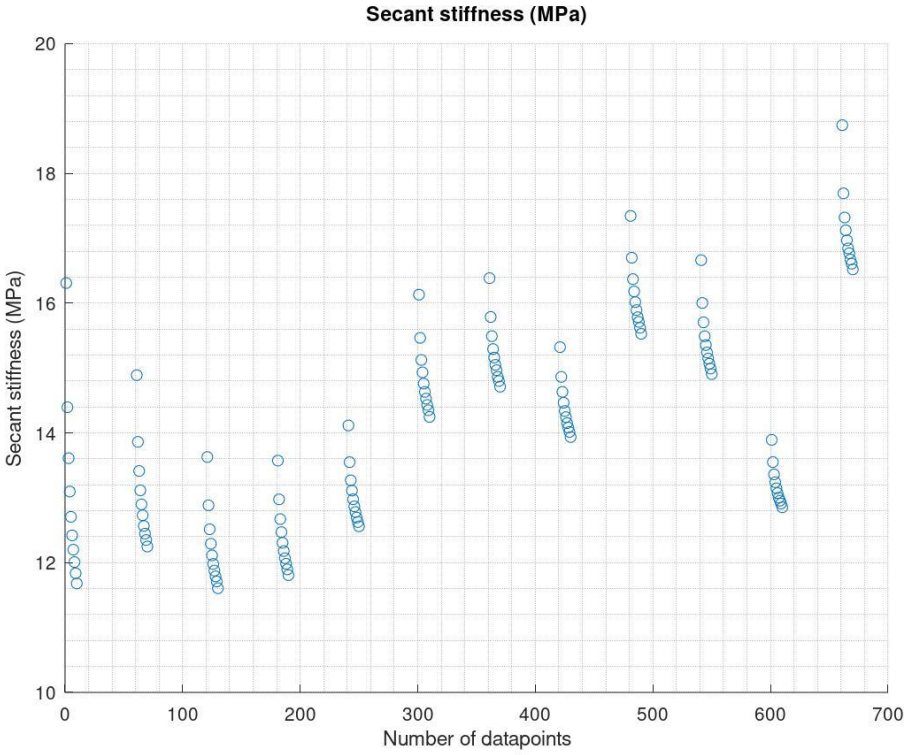

Figure A.85 – Secant stiffness.

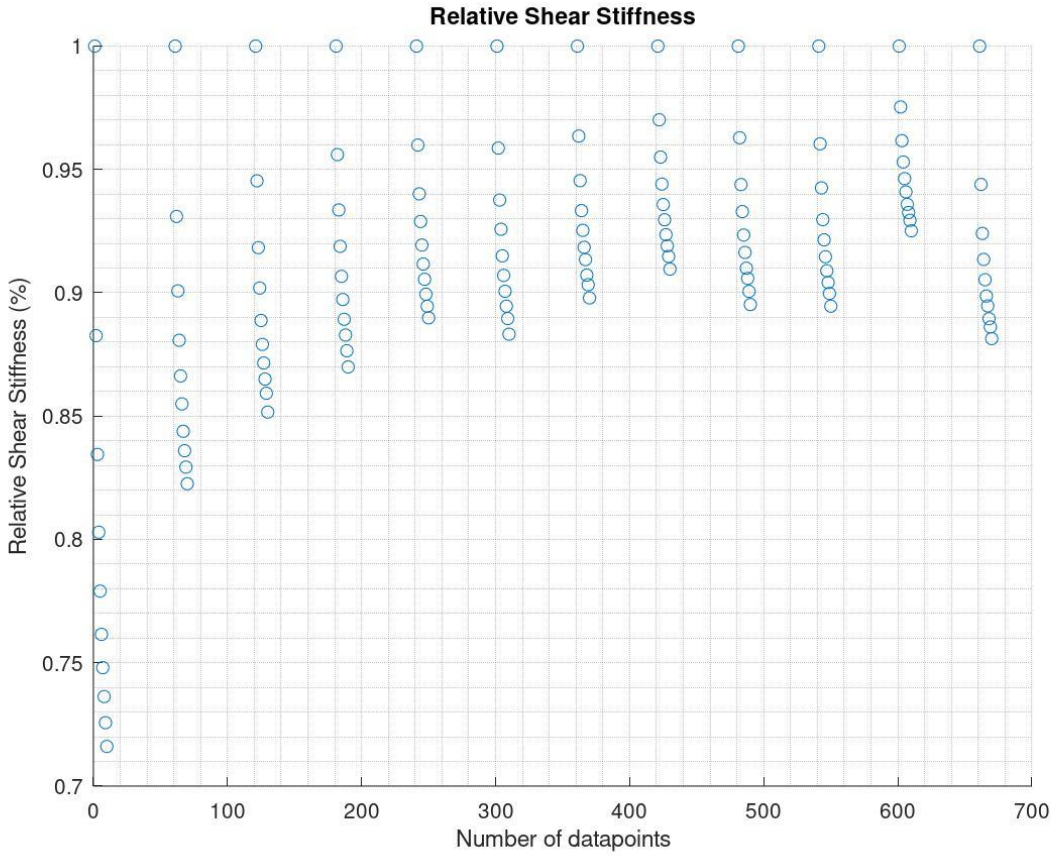

Figure A.86 – Relative shear stiffness.

Appendix B – Consolidation

This appendix includes the results of the consolidation for each test. Axial strain rates are only showed for tests with vertical consolidation during cyclic testing. Summary tables of specimen heights, for both kaolin-based and marine clay samples, are included in Table B1.

Table B1 - Height of samples before and after experiments.

Sample ID	Initial height (mm)	Final height (mm)	Axial strain (%)
Dummy test 1	101,5	95	5,9
Dummy test 2	101	94,2	6,7
KT1	101	91,5	9,4
KT2	101	93,5	7,4
Brazil_1	100	89,2	10,8
Brazil_2	100	90,9	9,1

Appendix B1 – DT1

Initial height of the sample was 101,5 mm.

The consolidation force is presented in Figure B1. The consolidation displacement and height-change of the specimen is found in Figures B2 and B3, respectively.

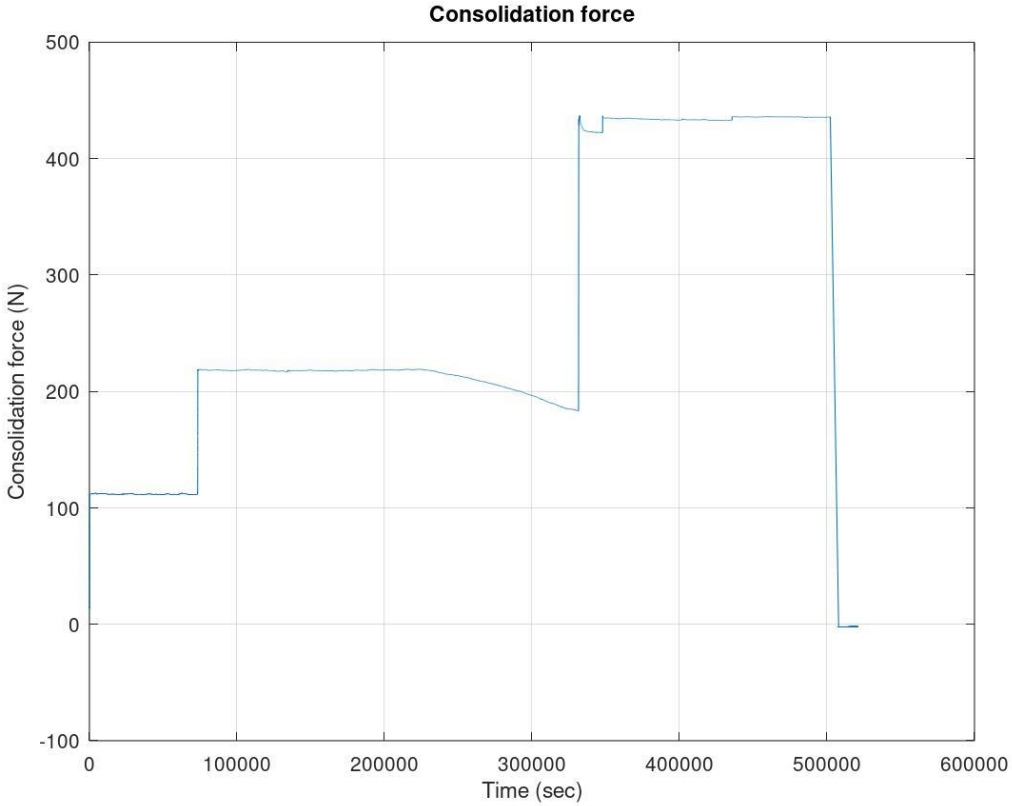

Figure B1 – Consolidation force over time.

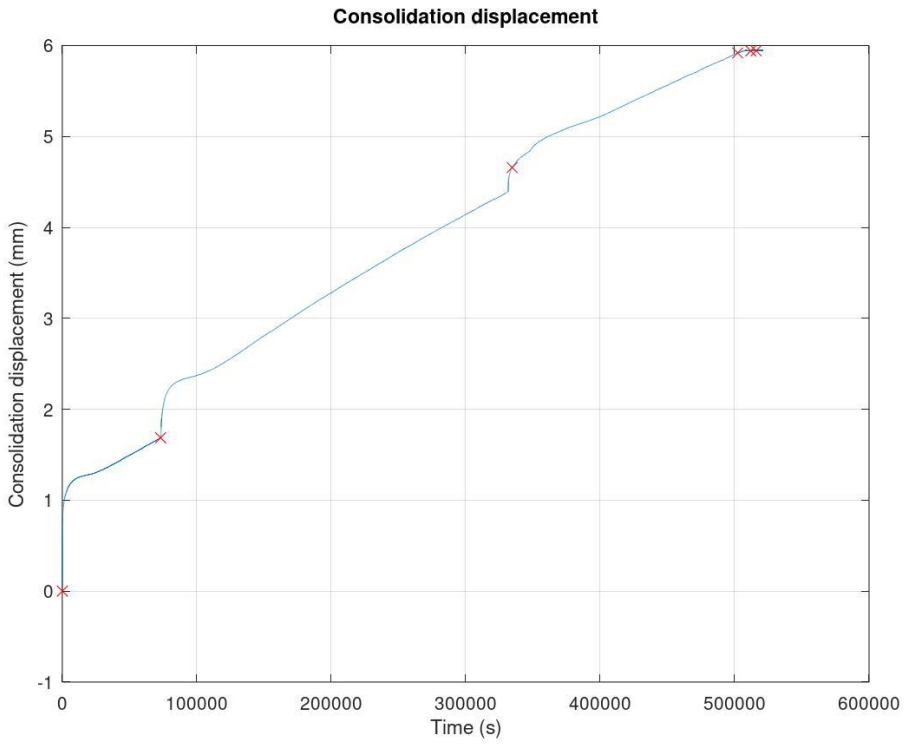

Figure B2 – Consolidation displacement over time. Crosses indicate the time mark for initiating consolidation-steps and cyclic testings.

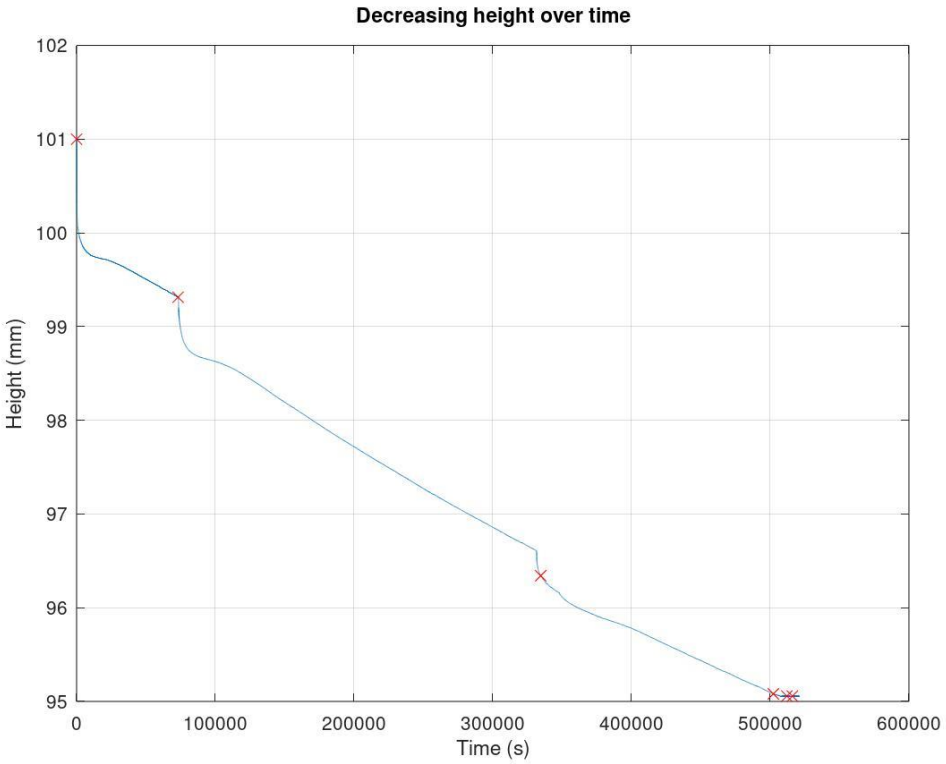

Figure B3 – Height change of specimen over time. Crosses indicate the time mark for initiating consolidation-steps and cyclic testings.

Appendix B2 – DT2

Initial height of the sample was 101 mm.

The consolidation force is presented in Figure B4. The consolidation displacement is found in Figure B5. The height-change of the specimen is found in Figure B6.

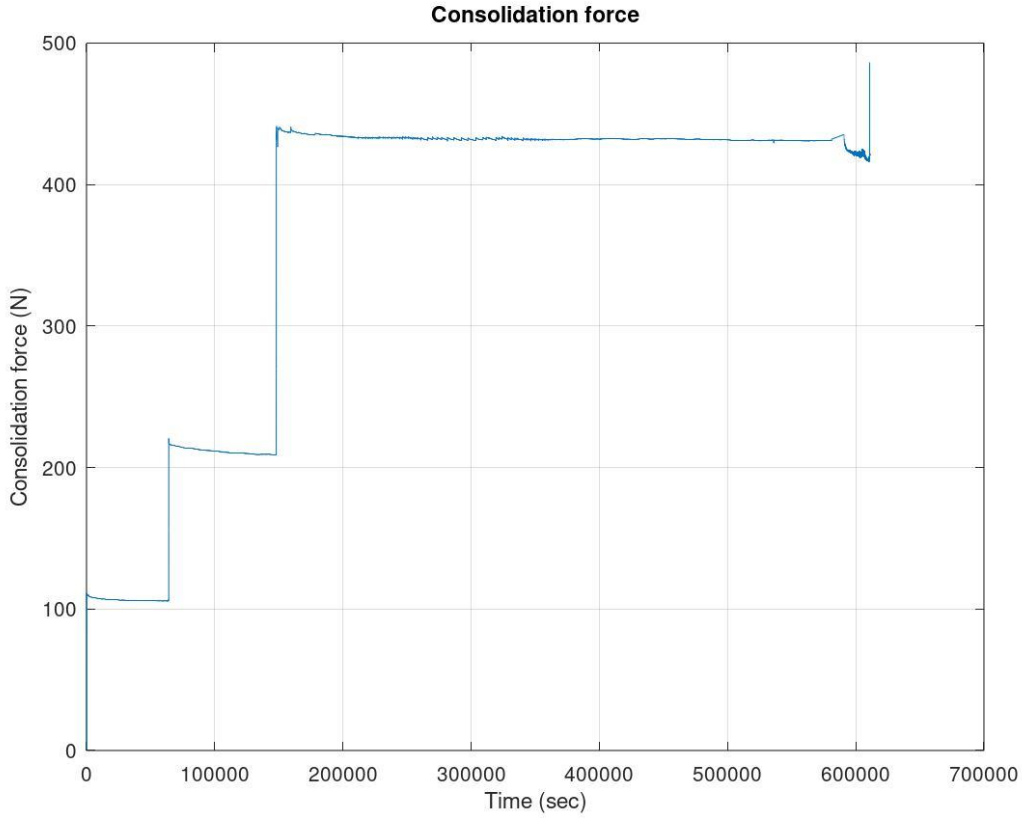

Figure B4 – Consolidation force over time.

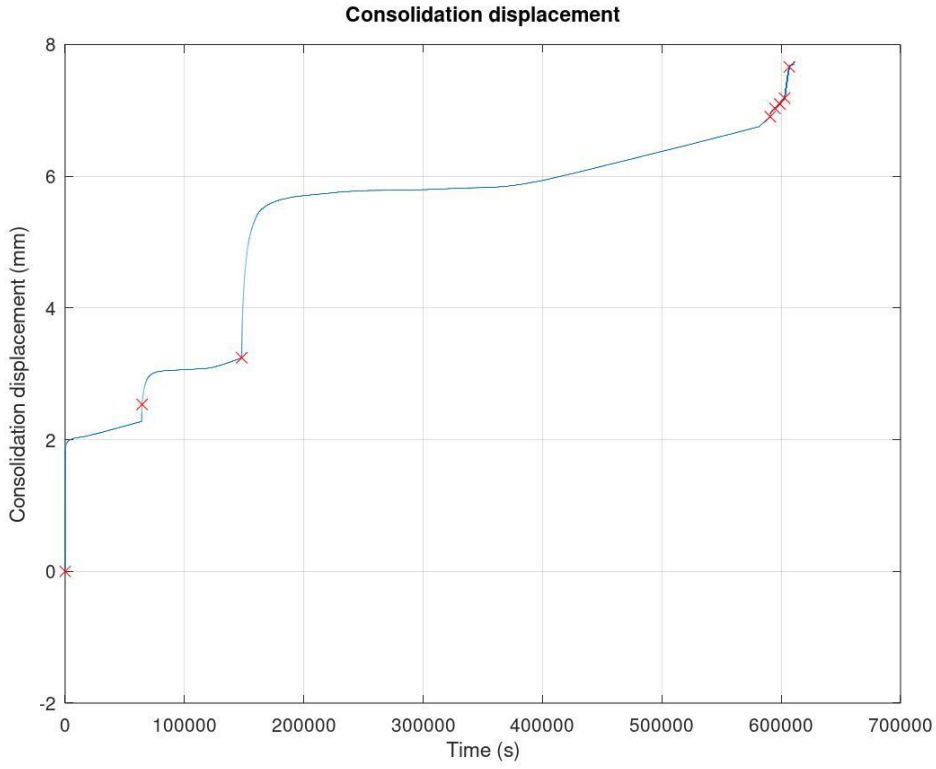

Figure B5 – Consolidation displacement over time. Crosses indicate the time mark for initiating consolidation-steps and cyclic testings.

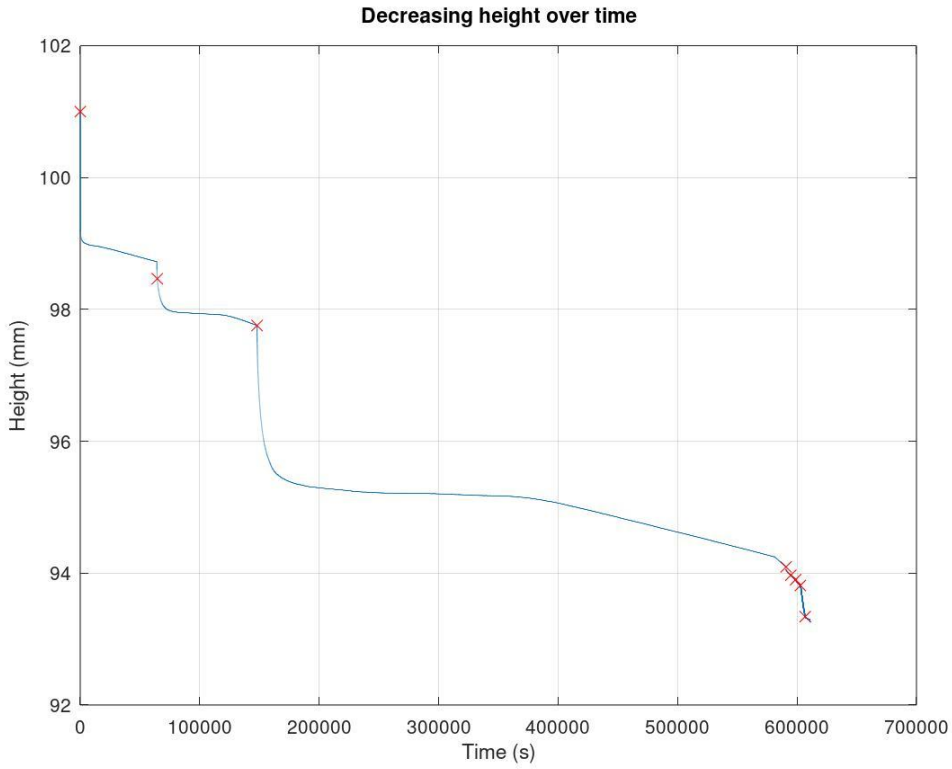

Figure B6 – Height change of specimen over time. Crosses indicate the time mark for initiating consolidation-steps and cyclic testings.

Appendix B3 – KT1

Initial height of the sample was 101 mm.

The consolidation force is presented in Figure B7. The consolidation displacement is found in Figure B8. The height-change of the specimen is found in Figure B9. The axial strain rates are found in Figure B10.

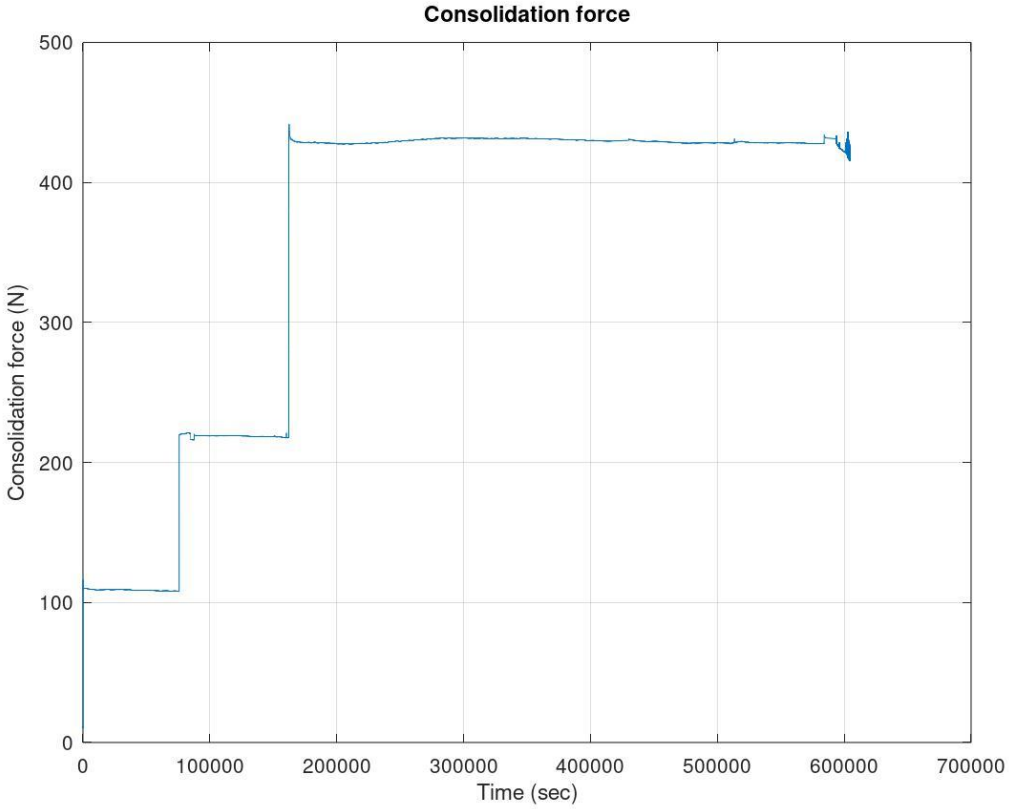

Figure B7 – Consolidation force over time.

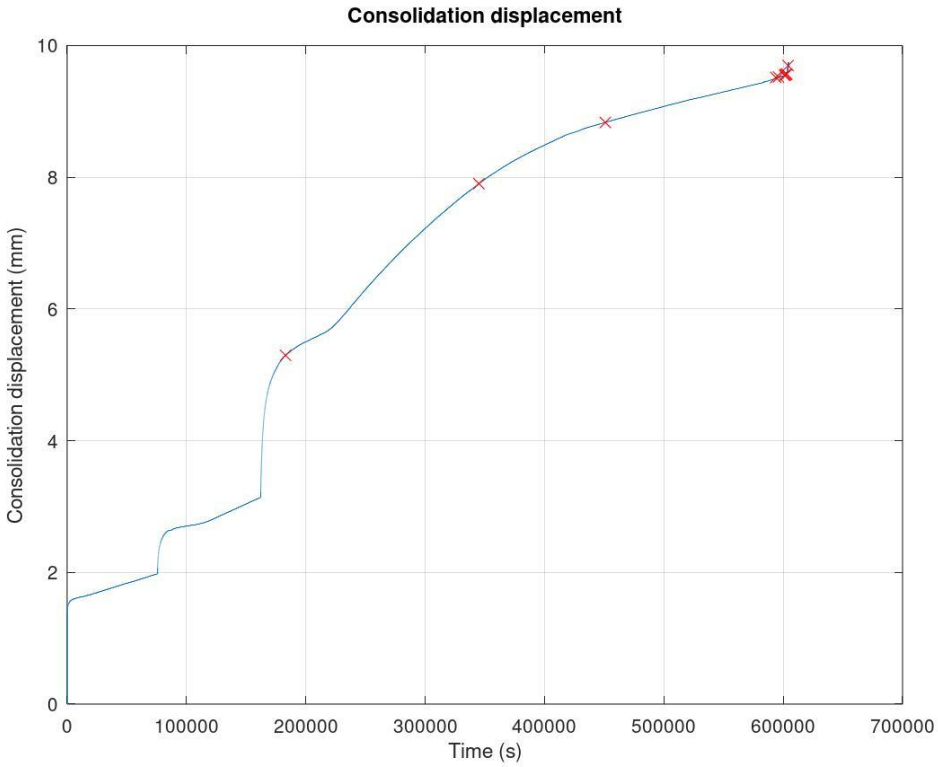

Figure B8 – Consolidation displacement over time. Crosses indicate the time mark for initiating consolidation-steps and cyclic testings.

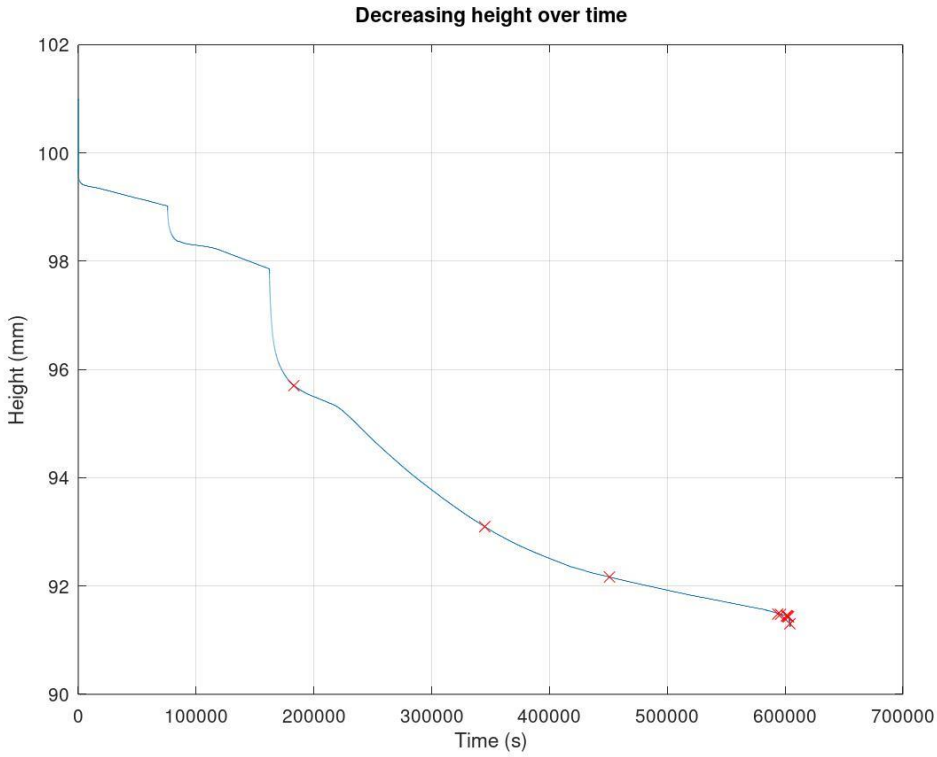

Figure B9 – Height change of specimen over time. Crosses indicate the time mark for initiating consolidation-steps and cyclic testings.

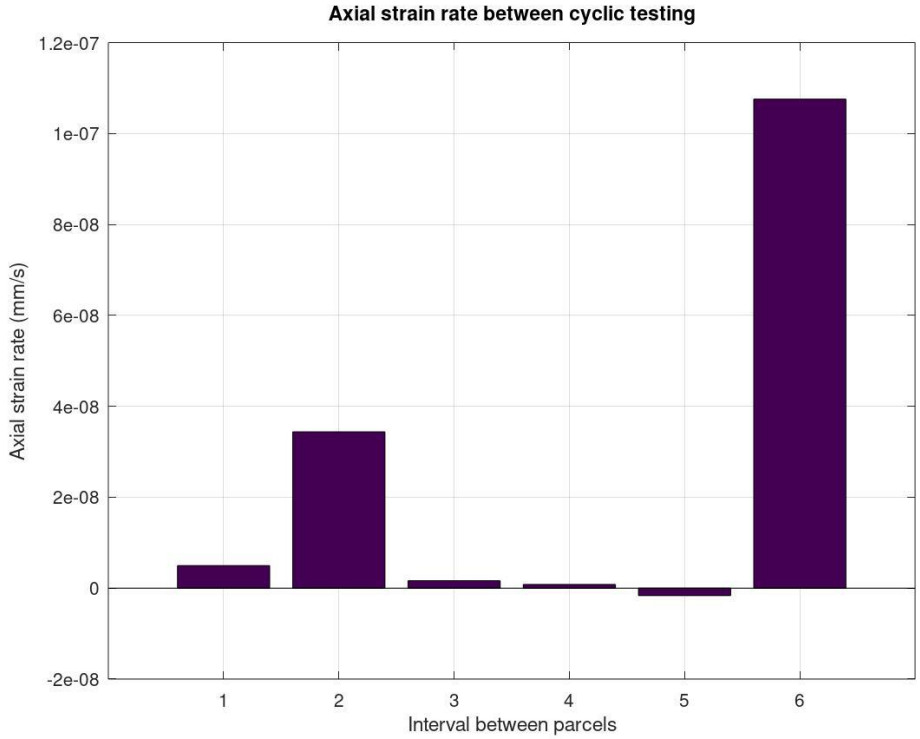

Figure B10 – Axial strain rates between each cyclic parcel.

Appendix B4 – KT2

Initial height of the sample was 101 mm.

The consolidation force is presented in Figure B11. The consolidation displacement is found in Figure B12. The height-change of the specimen is found in Figure B13. The axial strain rates are found in Figure B14.

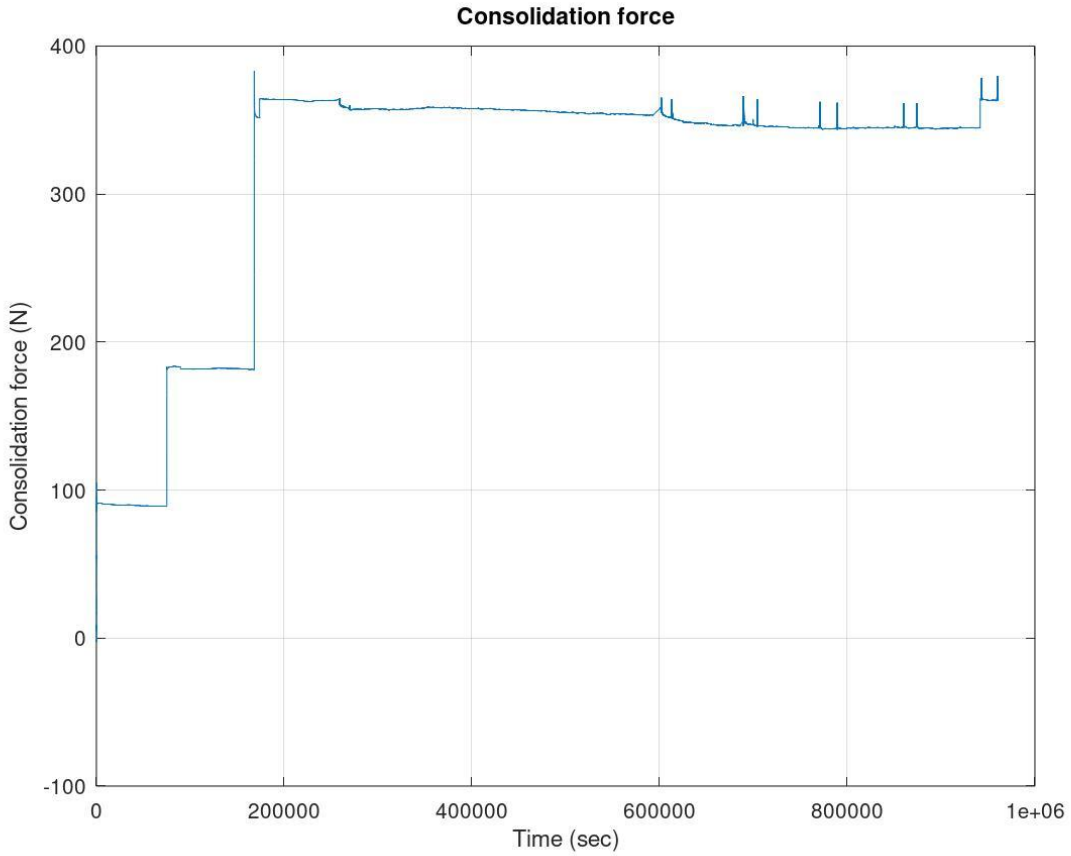

Figure B11 – Consolidation force over time.

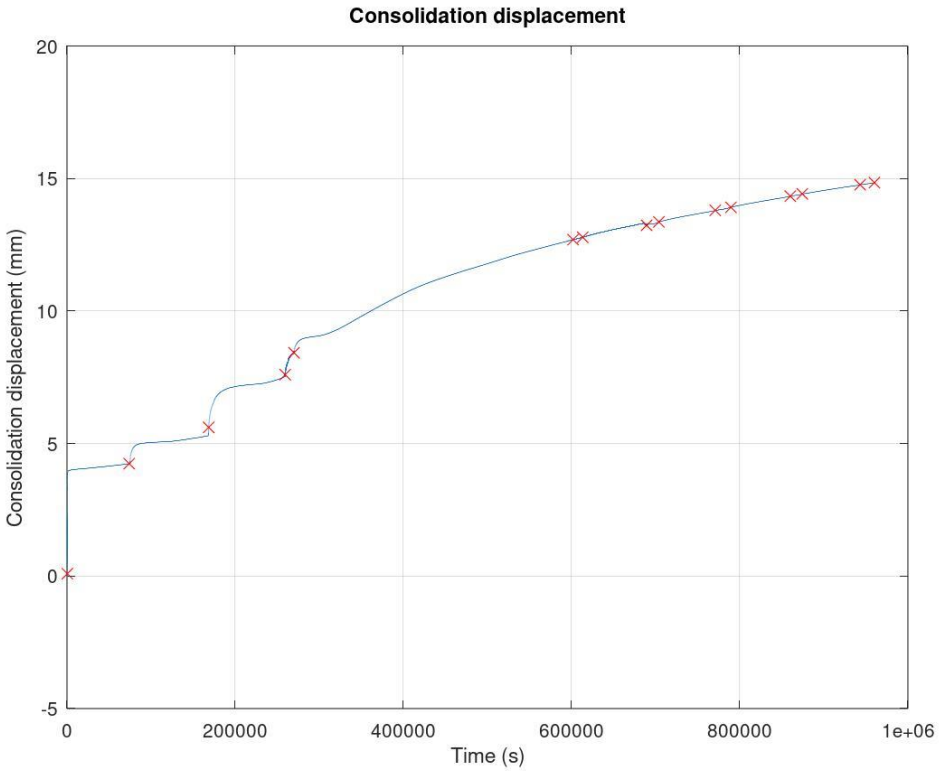

Figure B12 – Consolidation displacement over time. Crosses indicate the time mark for initiating consolidation-steps and cyclic testings.

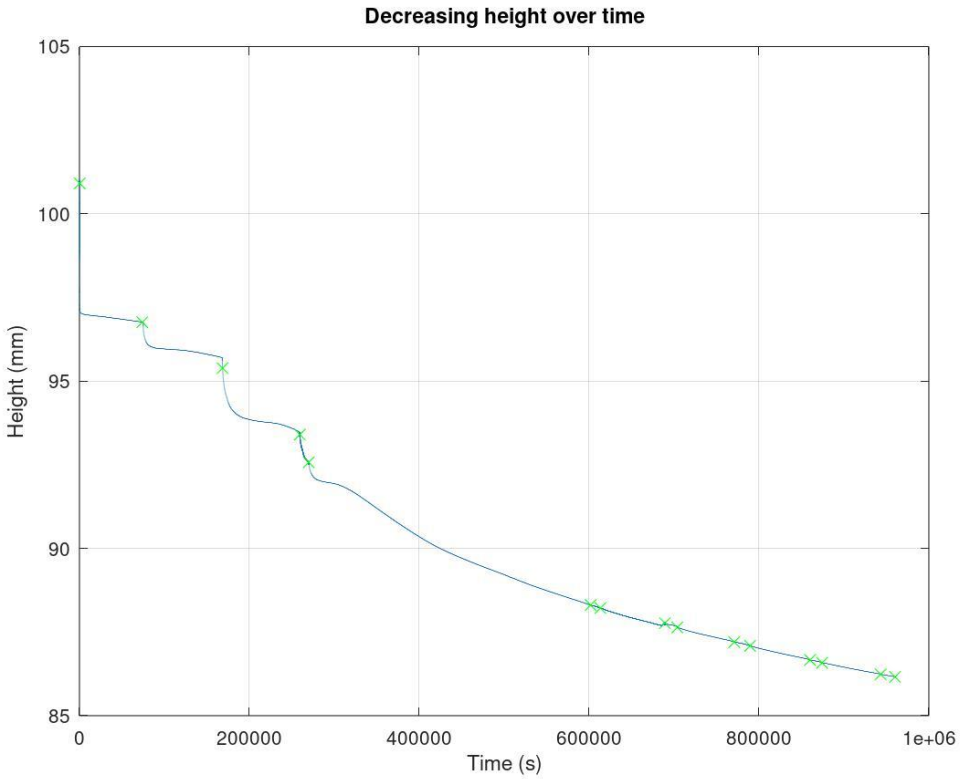

Figure B13 – Height change of specimen over time. Crosses indicate the time mark for initiating consolidation-steps and cyclic testings.

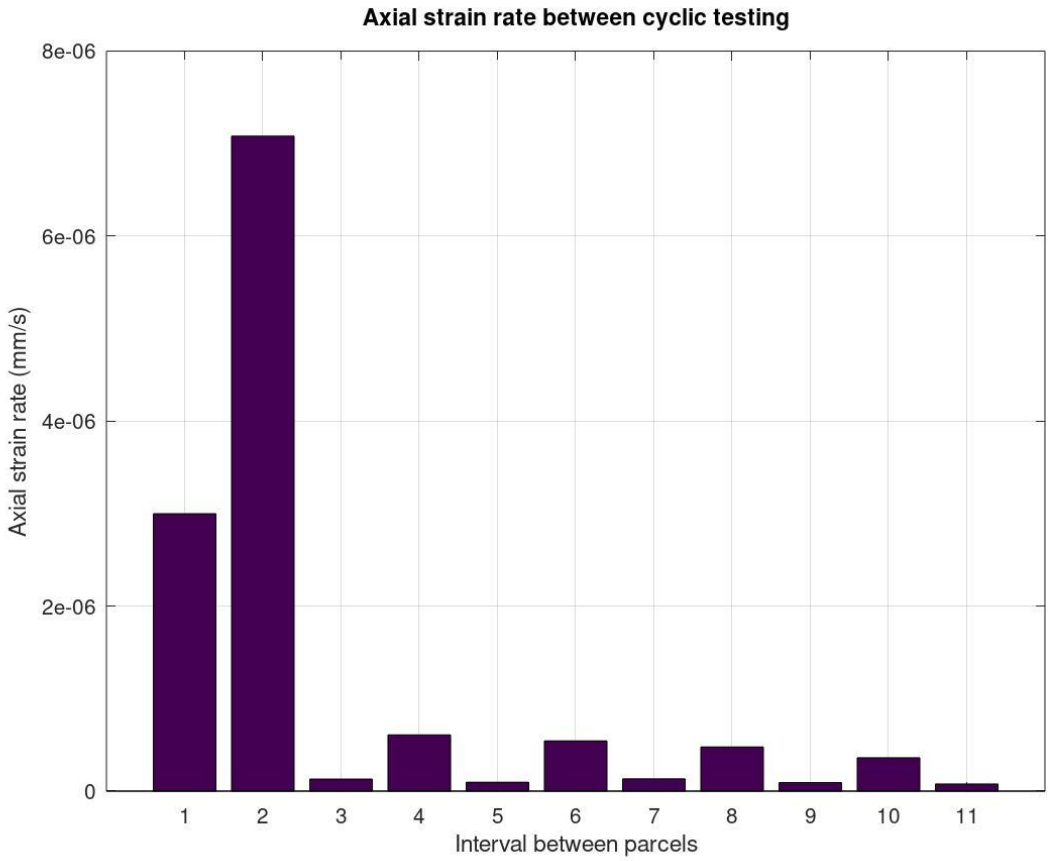

Figure B14 – Axial strain rates between each cyclic parcel.

Appendix B5 – Brazil_1

Initial height of the sample was 100 mm.

The consolidation force is presented in Figure B15. The consolidation displacement is found in Figure B16. The height-change of the specimen is found in Figure B16. The axial strain rates are found in Figure B18.

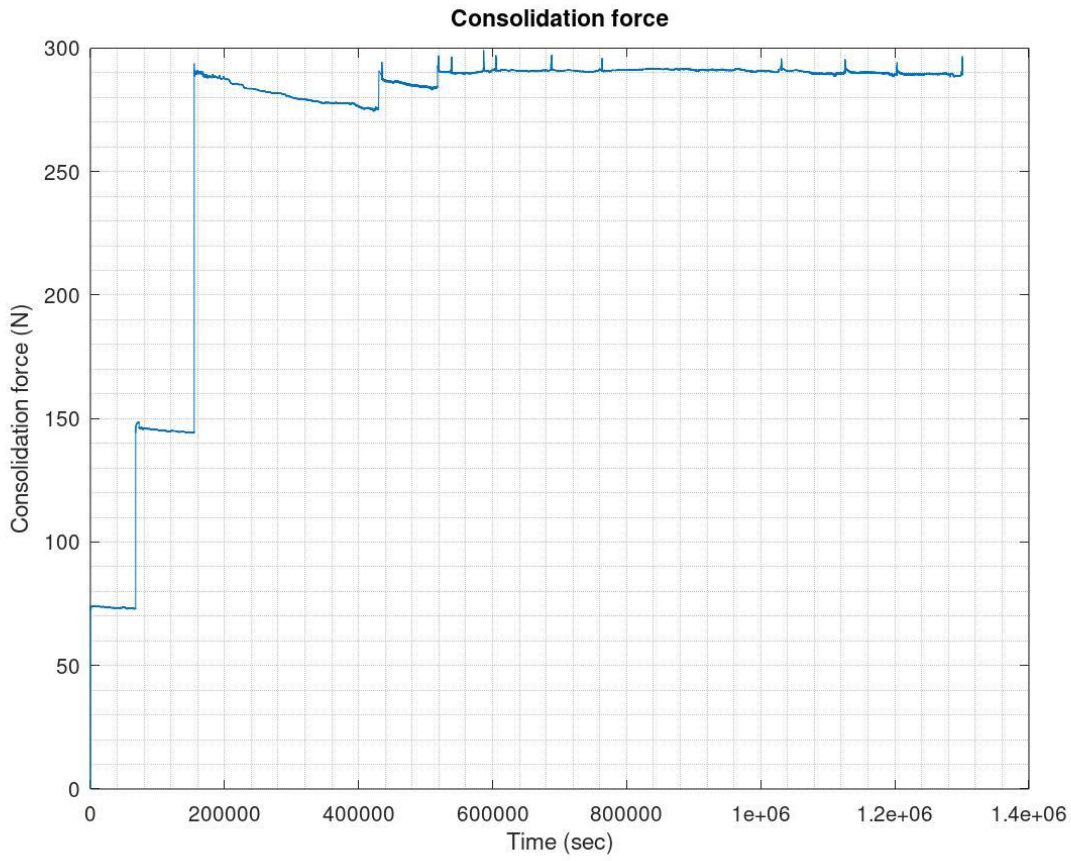

Figure B15 – Consolidation force over time.

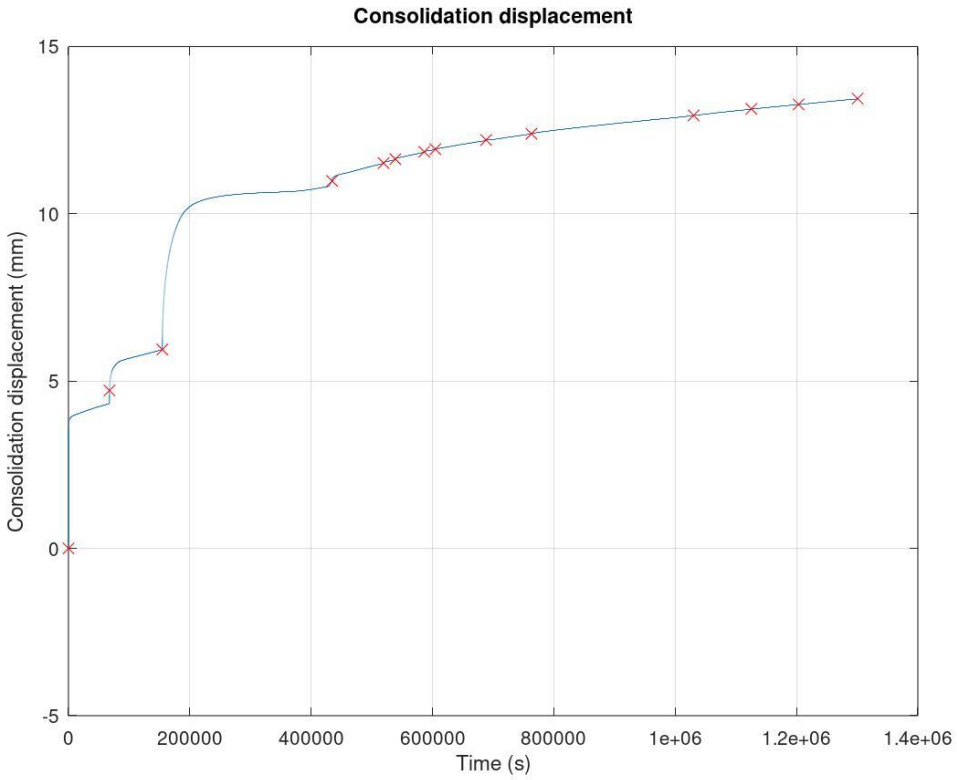

Figure B16 – Consolidation displacement over time. Crosses indicate the time mark for initiating consolidation-steps and cyclic testings.

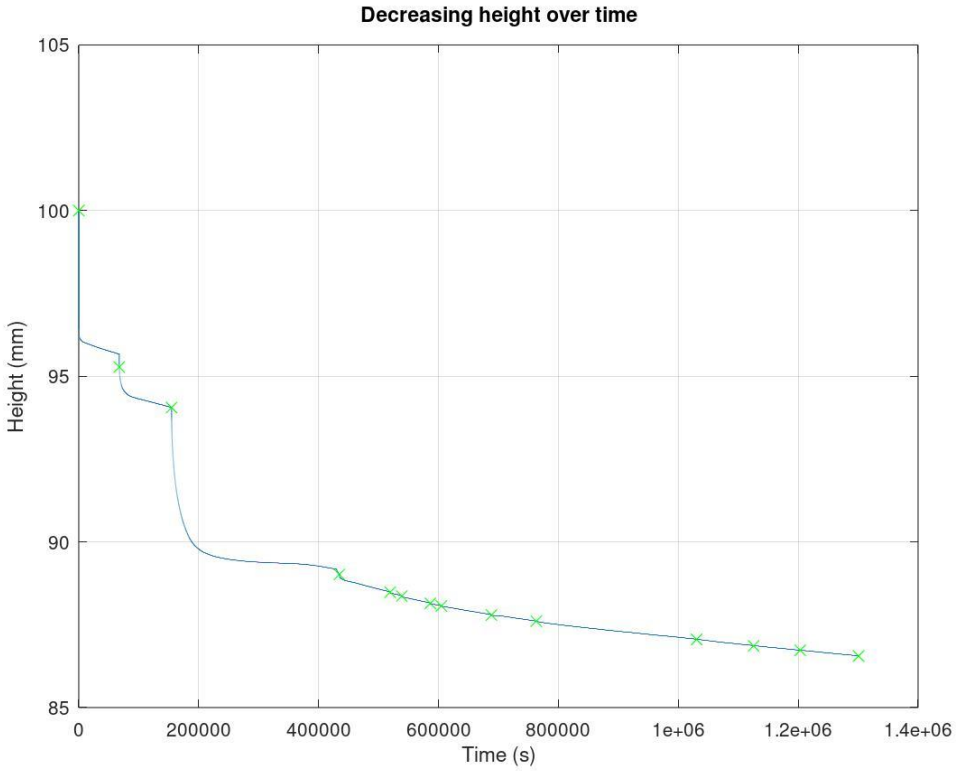

Figure B17 – Height change of specimen over time. Crosses indicate the time mark for initiating consolidation-steps and cyclic testings.

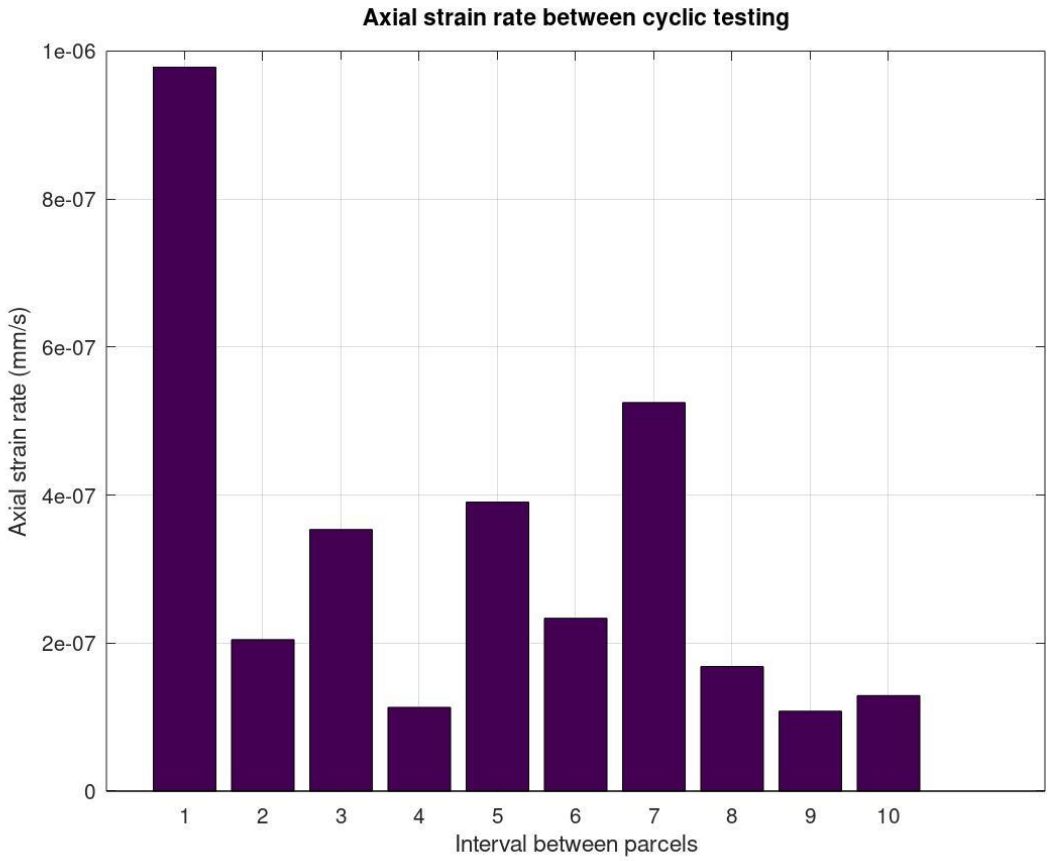

Figure B18 – Axial strain rates between each cyclic parcel.

Appendix B6 – Brazil_2

Initial height of the sample was 100 mm.

The consolidation force is presented in Figure B19. The consolidation displacement is found in Figure B20. The height-change of the specimen is found in Figure B21. The axial strain rates are found in Figure B22.

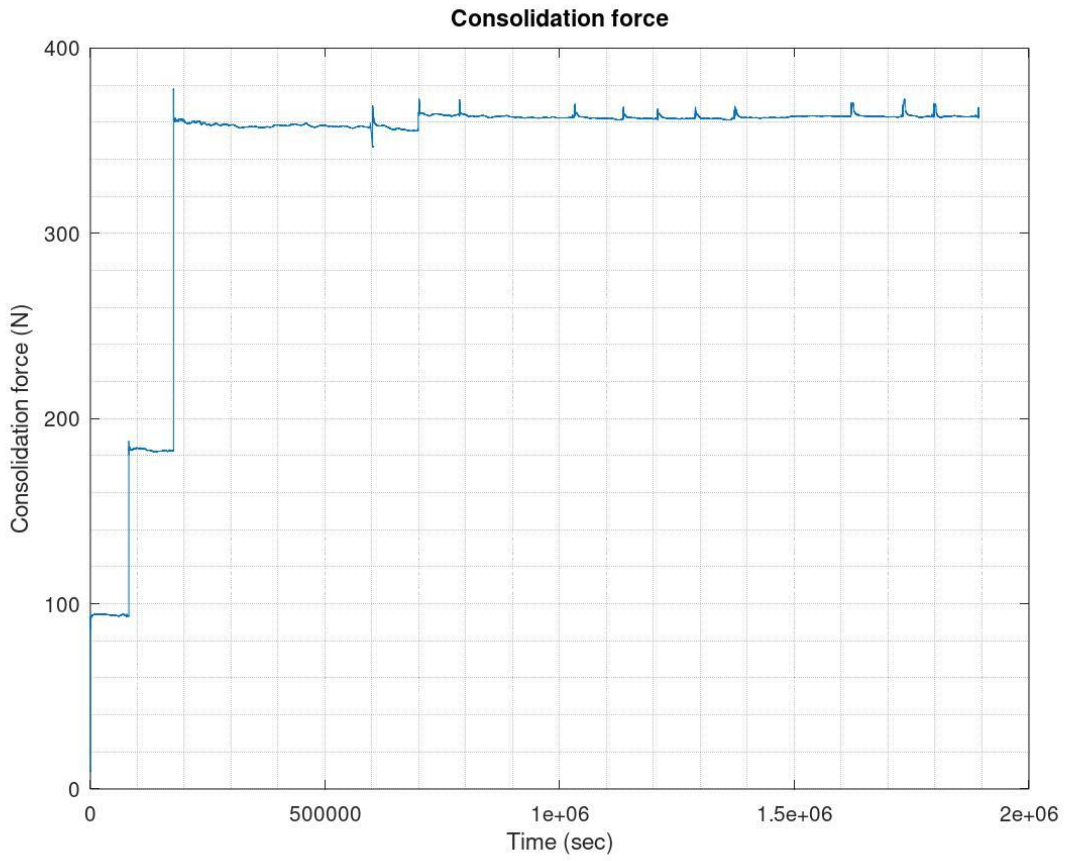

Figure B19 – Consolidation force over time.

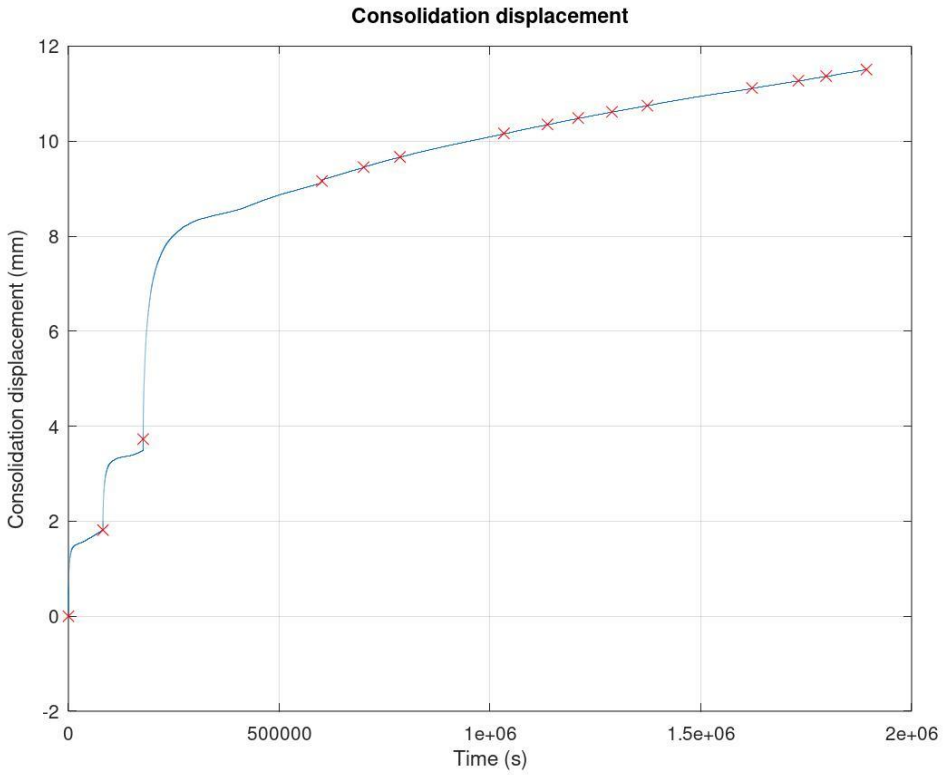

Figure B20 – Consolidation displacement over time. Crosses indicate the time mark for initiating consolidation-steps and cyclic testings.

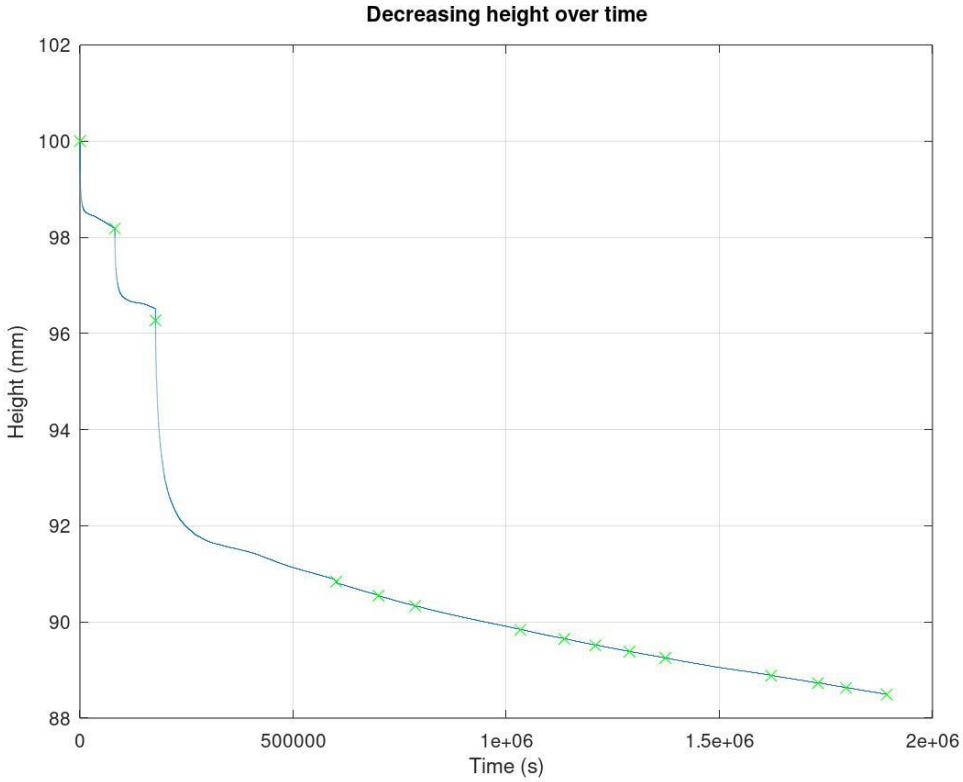

Figure B21 – Height change of specimen over time. Crosses indicate the time mark for initiating consolidation-steps and cyclic testings.

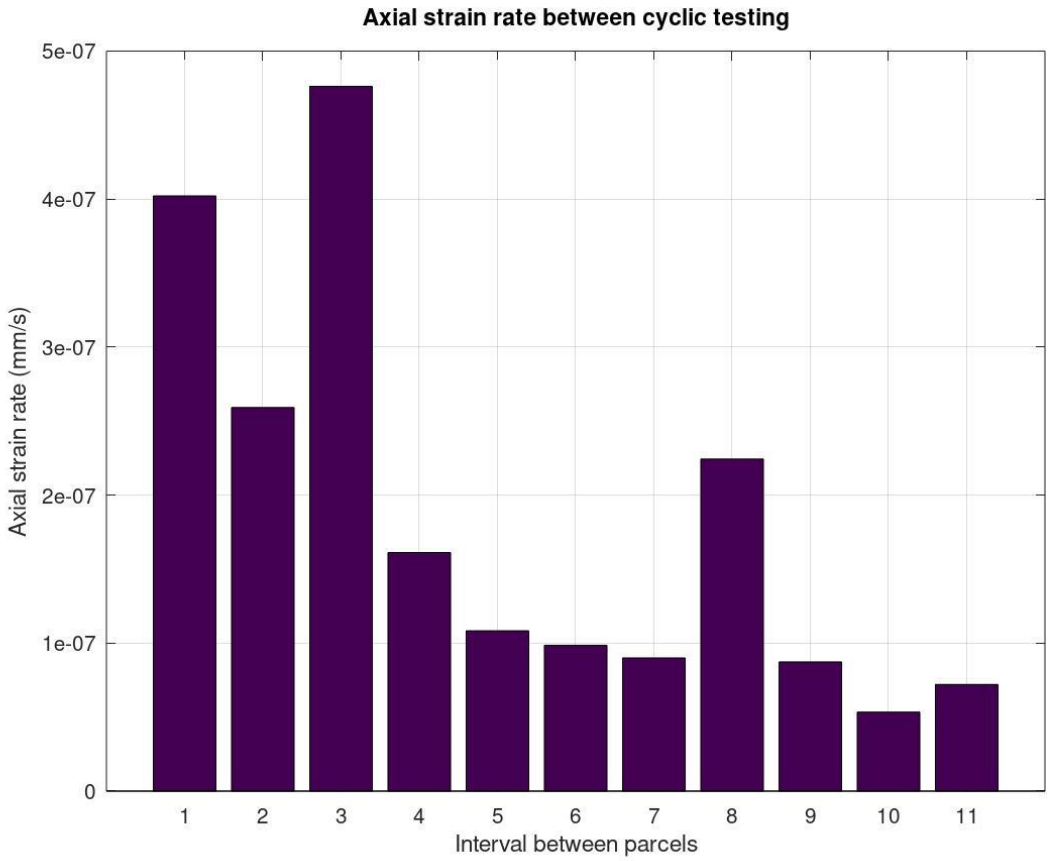

Figure B22 – Axial strain rates between each cyclic parcel.

Appendix C – Photographs

Photos of the samples are presented in this appendix. Only KT1, KT2, Brazil_1 and Brazil_2 are included. Some photos have corresponding cyclic direction indicated.

Appendix C1 – KT1

The left side (top of specimen), middle part and right side (bottom part of specimen) is shown in figures below.

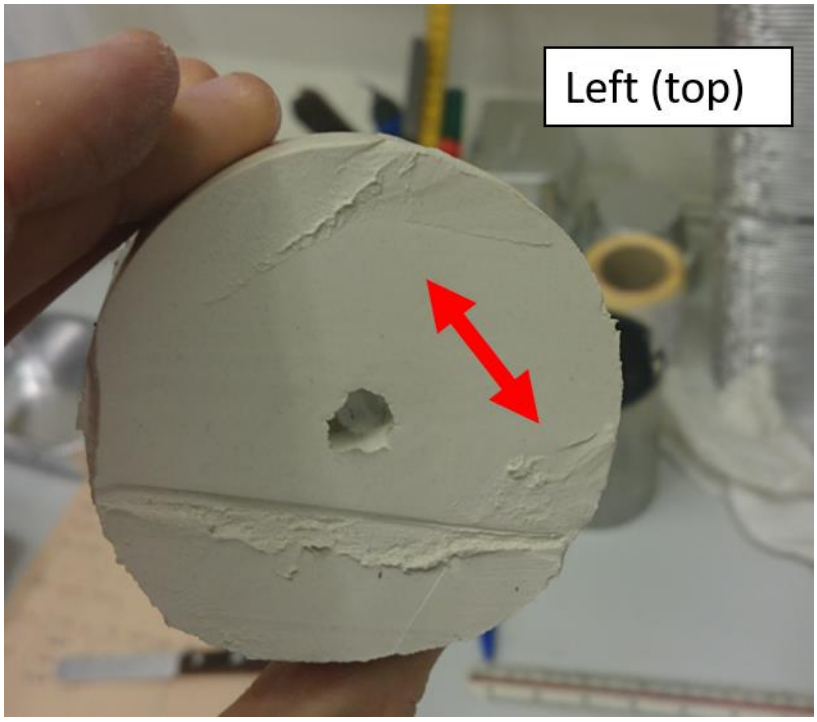

Figure C.1 – Left side (top) of KT1. Red arrows indicate direction of cyclic movement.

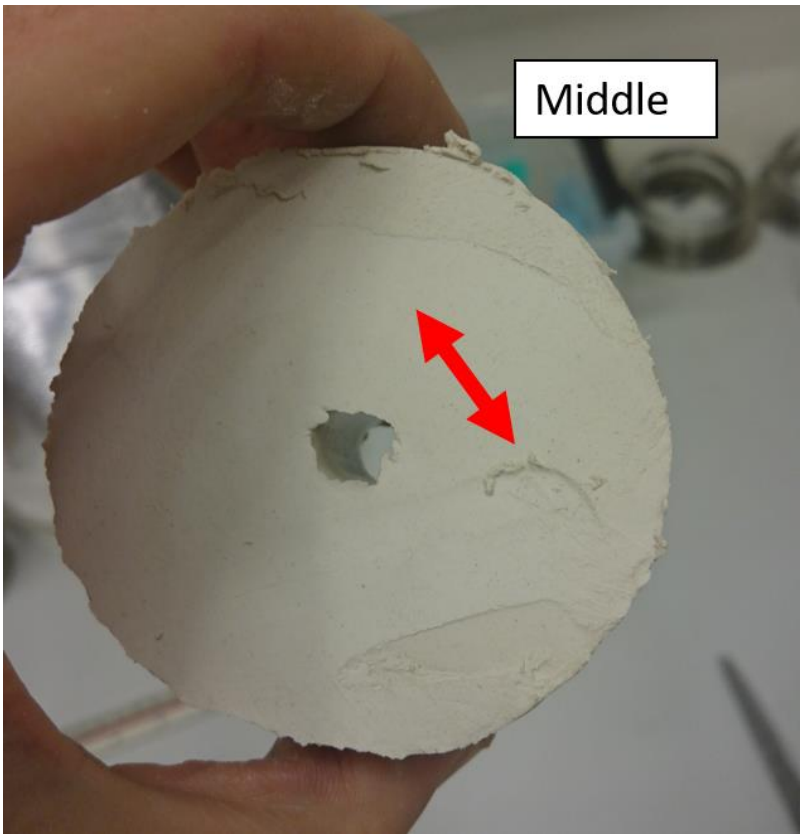

Figure C.2 – Middle part of the KT1. Red arrows indicate direction of cyclic movement.

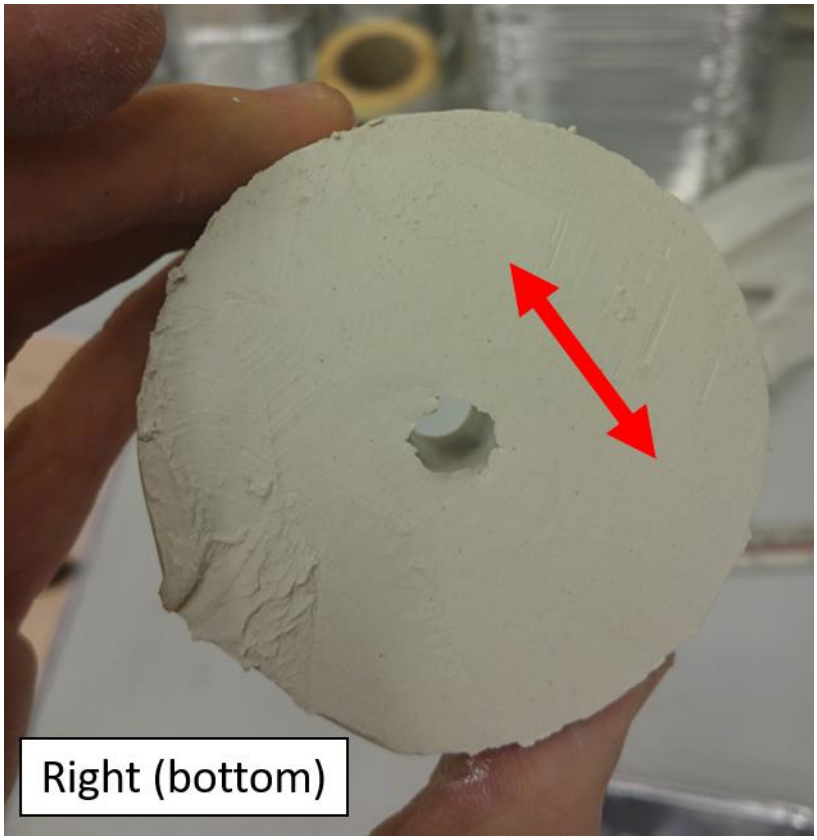

Figure C.3 - Right side (bottom) of KT1. Red arrows indicate direction of cyclic movement.

Appendix C2 – KT2

The left side (top of specimen), middle part and right side (bottom part of specimen) is shown in figures below.

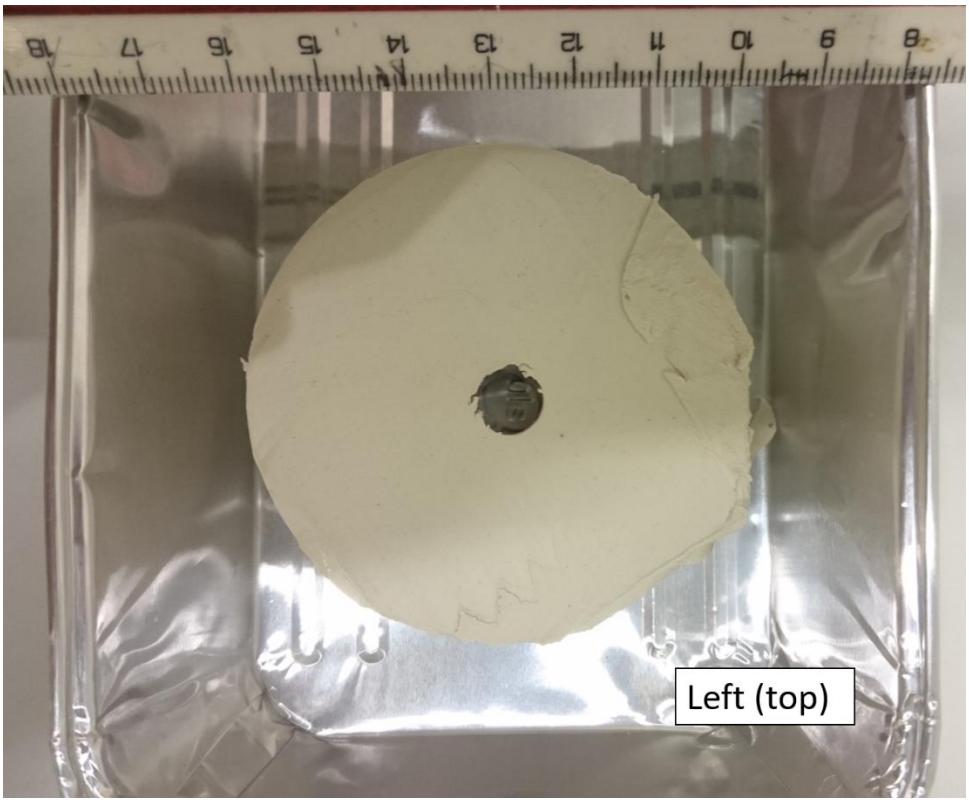

Figure C.4 - Left side (top) of KT2.

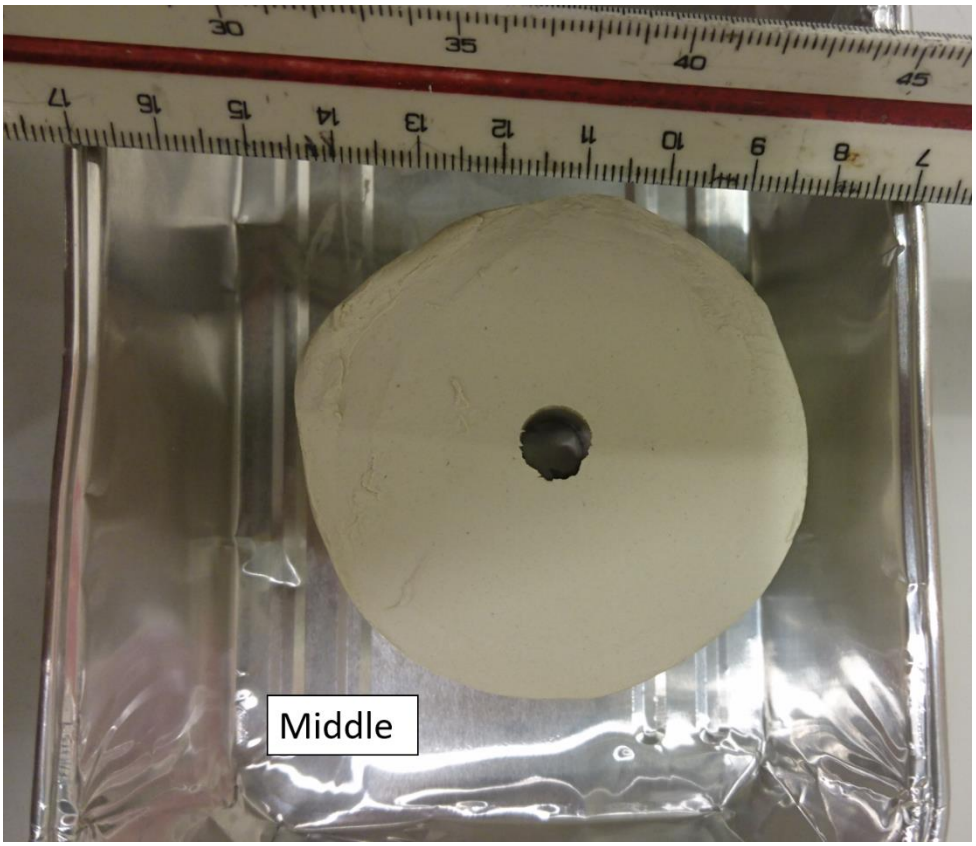

Figure C.5 – Middle part of KT2.

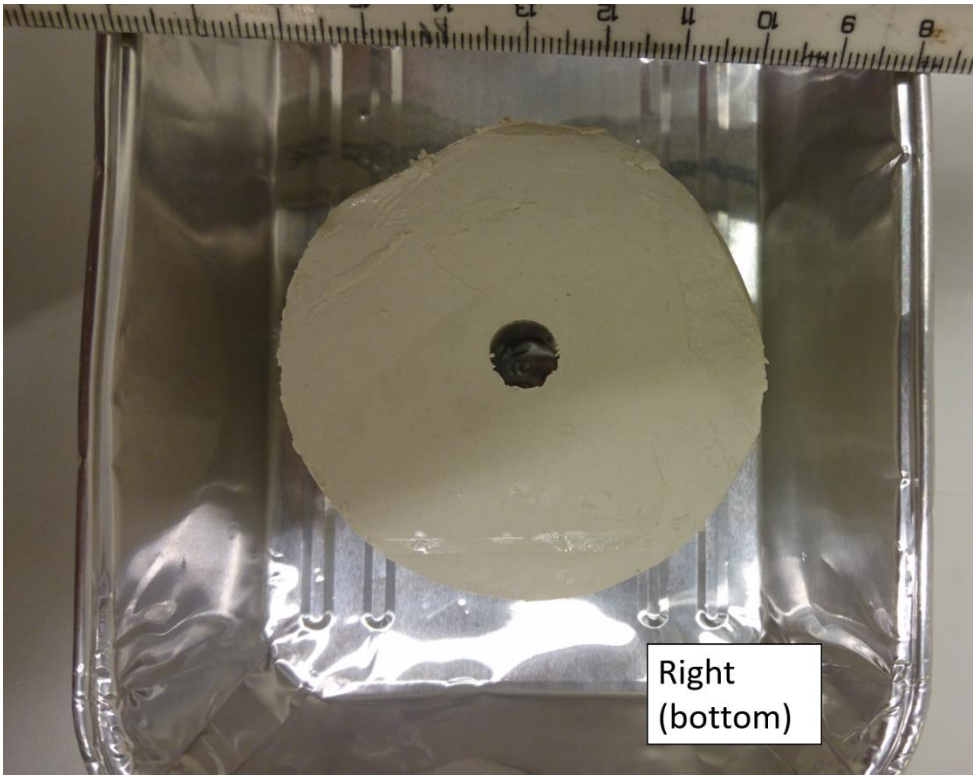

Figure C.6 – Right side (bottom) of KT2.

Appendix C3 – Brazil_1

The left side (top of specimen), middle part and right side (bottom part of specimen) is shown in figures below.

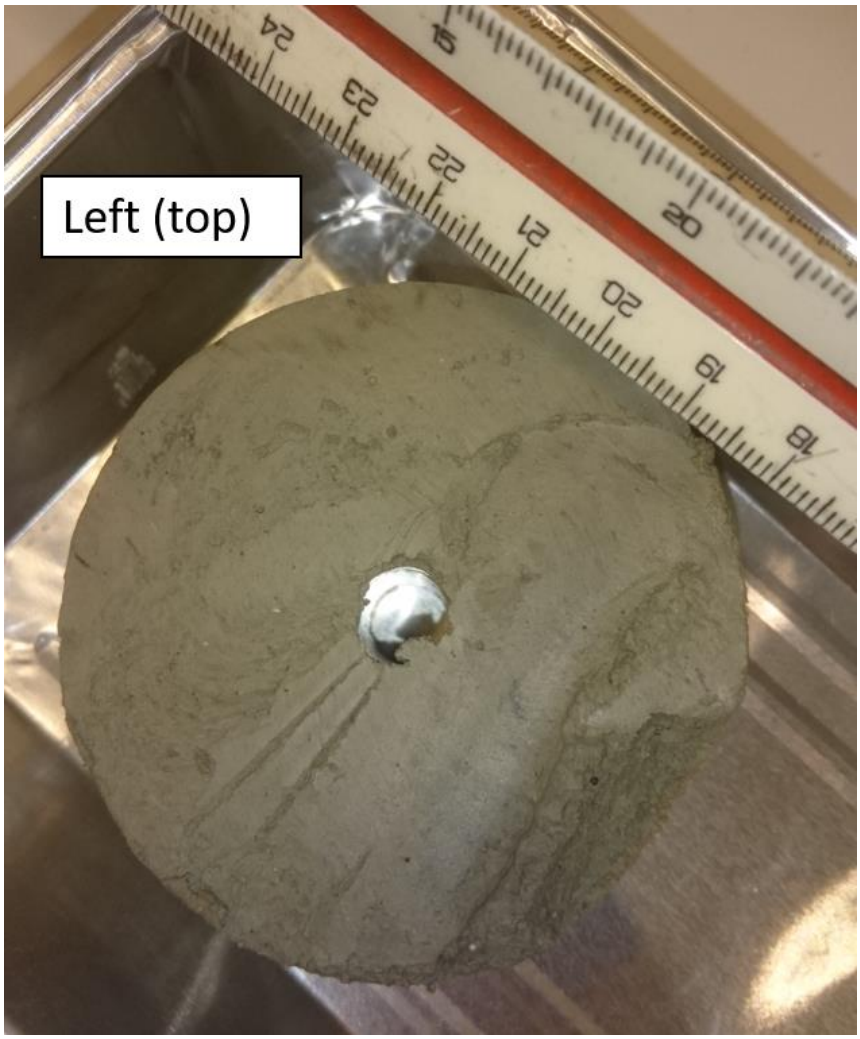

Figure C.7 – Left side (top) of Brazil_1..

Figure C.8 – Middle part of Brazil_1. Red arrows indicate direction of cyclic movement.

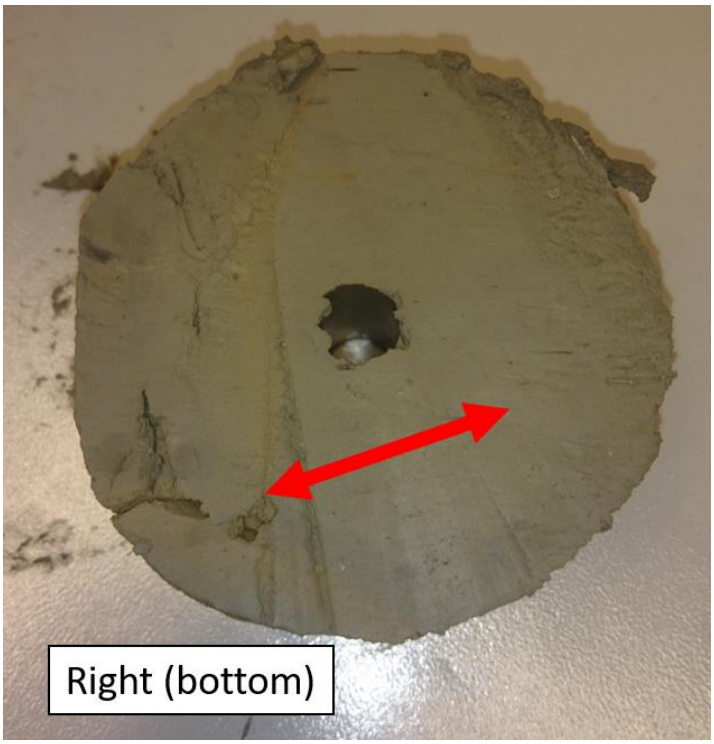

Figure C.9 – Right side (bottom) of Brazil_1. Red arrows indicate direction of cyclic movement.

Appendix C4 – Brazil_2

The left side (top of specimen), middle part and right side (bottom part of specimen) is shown in figures below.

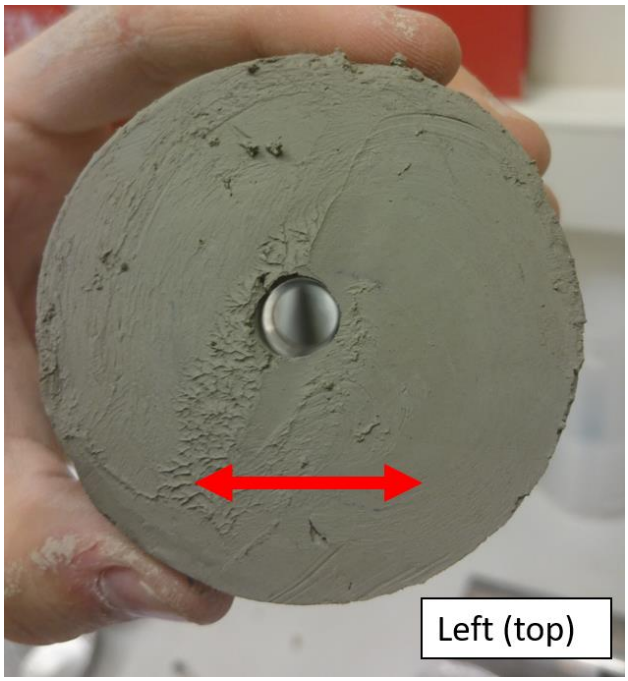

Figure C.10 – Left side (top) of Brazil_2. Red arrows indicate direction of cyclic movement.

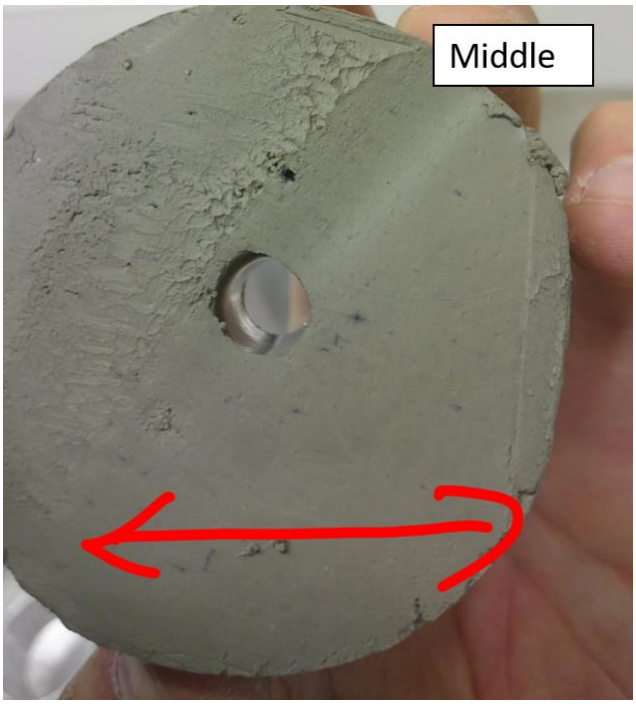

Figure C.11 – Middle part of Brazil_2. Red arrows indicate direction of cyclic movement.

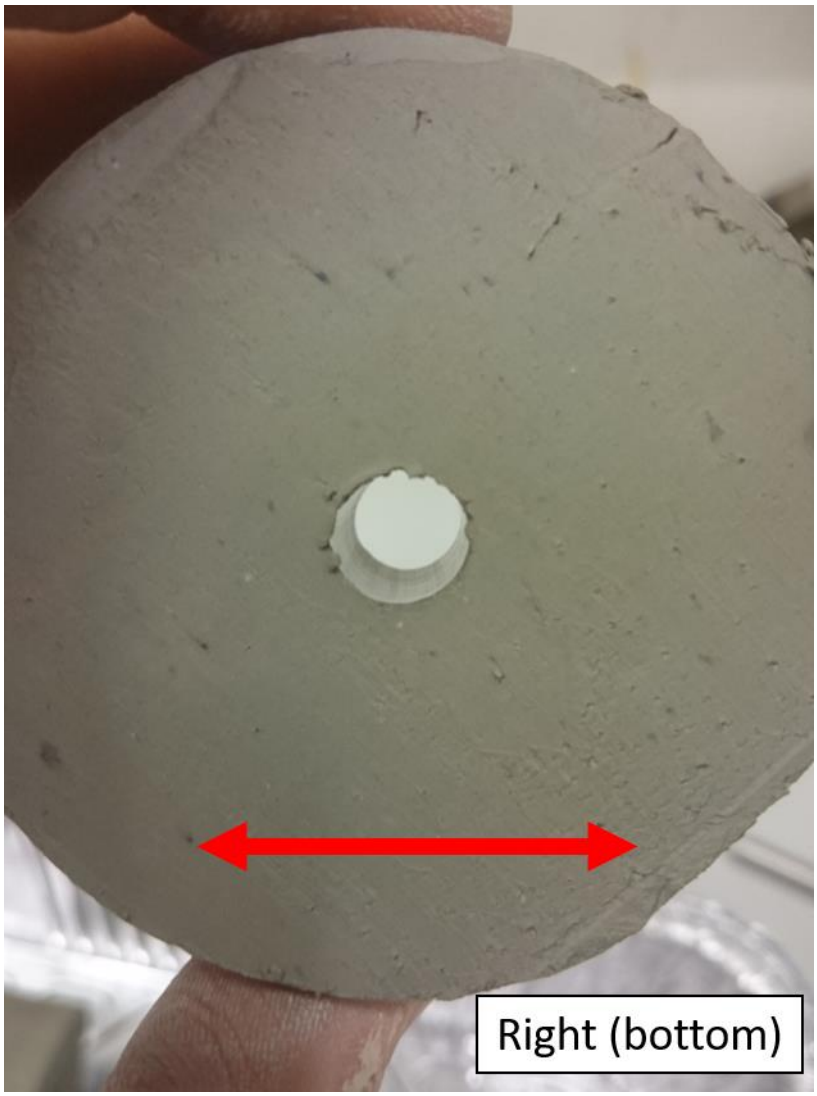

Figure C.12 – Right side (bottom) of Brazil_2. Red arrows indicate direction of cyclic movement.

Appendix D – Water content and material loss

The estimation of water content and is presented for each sample tested. This step is measured right after cyclic testing is fully complete. Material loss right after cyclic testing were also estimated for some of the samples.

Appendix D1 – Kaolin samples

Material loss of kaolin samples sample are found in Table D1. No material loss was estimated for samples DT1 and DT2.

Table D1 – Material loss of kaolin samples.

Sample ID	DT1	DT2	KT1	KT2
Weight of sample prior to testing (g)	-	-	633,71	630,41
Weight of sample after testing (g)	-	-	591,31	580,41
Estimated material loss (%)	-	-	6,69	7,93

The water content for kaolin samples are presented in Table D2.

Table D2 – Water content measurement of kaolin samples.

Sample ID	DT1	DT2	KT1	KT2
Reference-sample (initial water content, %)	32,82	33,11	33,30	32,58
Left side (top) (%)	33,70	30,59	29,74	28,27
Mid section (%)	31,20	30,77	30,03	28,31
Right-side (bottom) (%)	27,04	30,05	28,88	28,01
Average final water content (%)	30,65	30,47	29,55	28,20

Appendix D2 – Brazil samples

No material loss was estimated for Brazil_1, but for Brazil_2 the calculated loss is given in Table D3.

Table D3 – Material loss of Brazil-samples.

Sample ID	Brazil_1	Brazil_2
Weight of sample prior to testing (g)	-	553,71
Weight of sample after testing (g)	-	507,08
Estimated material loss (%)	-	8,42

The water content for Brazil_1 and Brazil_2 are presented in Table D4.

Table D4 – Water content measurement of Brazil-samples.

Sample ID	Brazil_1	Brazil_2
Reference-sample (initial water content, %)	44,67	46,17
Left side (top) – inner (%)	43,75	42,65
Left side (top) - outer (%)	42,30	42,09
Mid section - inner (%)	42,68	42,52
Mid section - outer (%)	43,24	42,99
Right-side (bottom) - inner (%)	40,65	41,89
Right-side (bottom) - outer (%)	42,35	37,36
Average final water content (%)	42,50	41,58